PEOPLE'S DEMOCRATIC REPUBLIC OF ALGERIA
Ministry of Higher Education and Scientific Research
University of Amar Telidji – Laghouat

Faculty of Technology
Department of Mechanical Engineering

DOCTORATE IN SCIENCES THESIS

Contribution to the modeling and optimization of a new solar hybrid Photovoltaic / thermal Bi-fluid collector

By:
Mr. Mohamed LEBBI

Thesis publicly defended on 04 /11/2021. In front of the jury composed of:

Prof. BOUABDALLAH Saïd	President	University of Amar Telidji, Laghouat, Algeria
Prof. TOUAFEK Khaled	Supervisor	Applied Research Unit in Renewable Energies of Ghardaïa, Algeria
Prof. BENCHATTI Ahmed	Co- Supervisor	University of Amar Telidji, Laghouat, Algeria
Prof. AOUISSI Mokhtar	Examiner	University of Amar Telidji, Laghouat, Algeria
Dr. HAMMO Abd-el-Kader Djilali	Examiner	University of Amar Telidji, Laghouat, Algeria
Prof. BOUARAOUR Kamel	Examiner	University of Ghardaïa, Algeria
Prof. BEKKOUCHE Sidi Mohammed El Amine	Examiner	Applied Research Unit in Renewable Energies of Ghardaïa, Algeria

2020/2021

بسم الله الرحمن الرحيم

Acknowledgements

The work presented in this thesis was carried out in collaboration between the **Mechanical Laboratory** of the University of Laghouat and the Applied Research Unit, **CDER / URAER** Ghardaïa, Algeria.

First, I would like to thank Almighty **God** for helping me and giving me the ability to do this modest work, which I hope will benefit all humans.

I would also like to thank my dear **parents** and my dear **wife**, who have given me all the support throughout my university studies.

I would like to thank my supervisor, **Mr. TOUAFEK Khaled**, Professor at the Applied Research Unit in Renewable Energies of Ghardaïa, for his supervision and patronage. Not only that, but I am very indebted to him for his continuous encouragement, unforgettable help, and kind feeling throughout the course of this study.

I would like to express my deepest gratitude to **Mr. BENCHATTI Ahmed**, Professor in the Mechanical Laboratory of the Faculty of Technology, University of Laghouat, for his supervision and effective guidance discussion and for giving me the opportunity to accomplish this modest work. Also, in terms of his effective advice, sharing experience and encouraging him to do the best of best work.

All my gratitude to **Mr. Saïd BOUABDALLAH**, Professor at the University of Laghouat, who honored us with chairing the jury, despite his many responsibilities.

All my gratitude to **Mr. AOUISSI Mokhtar**, Professor at the University of Laghouat, who honored us with his presence as a member of the jury.

I address my thanks to **Mr. HAMMO Abd-el-Kader Djilali**, Professor at the University of Laghouat who accepts to judge this work as a member of the jury.

I would like to express my thanks to **Mr. BOUARAOUR Kamel**, Professor, at the University of Ghardaïa, who did me the honor of accepting to participate in the jury for this thesis.

I would also like to thank **Mr. BEKKOUCHE Sidi Mohammed El Amine** Professor of Research at the URAER-Ghardaïa, for his participation as a member of the jury. as a member of the jury.

I also wish to express my gratitude to the **members of the Mechanics Laboratory** at the University of Laghouat. For their contribution to the achievement of this thesis.

My thanks also go to all **members of the Hybrid Solar Systems** / URAER / Ghardaïa team for their friendship and daily support throughout the development of this modest work, in particularly **Dr. Boutina Lyes**.

My thanks also to **Dr. Samir HASSANI** and **Saïd BENKACIALI** for their help and motivation to do this modest work.

My big thanks also go to all the **Workers** (research support) for their help during the experimental work, in particular Faisal, Mahfoud, Rabah, Suleiman, and Cheikh.

All expressions of appreciation and thanks to everyone who contributed and encouraged us during critical moments to achieve this modest work in its best form.

Dedicate

I dedicate this thesis in particular

To the Prophet Mohammad (صلى الله عليه وسلم)

To my dear parents Ali and Khoukha, who have enlightened me by giving me their hand throughout my years of study, "may God keep them".

I dedicate this work to the parents of my wife Mohamed and Hadda who supported me by their prayers.

To my wife Gherbi Z and my children Yacine, Rahma, Douaa and Loubna.

To my dear brothers and sisters, Said, Djamel, Elyakout and Naima.

To each of brother Ahmed chahat, his virtuous wife, and his children, without exception.

To my friends, Boutina, Hassani, Daimallah, Brihmat, Bezari, Abdelouhab , Benkaciali, Boutelhig, Fazani, Benkhlifa twins, Khelifa, Zarrit, khereur, Baissi, Daoud, Ghoubrini, Gama, Ghrissi, Laiourat, Rabah, Chuireb, and Hamli.

To my colleagues at work and all the distinguished professors

To all those who have contributed directly or indirectly to the achievement of this work.

To all scientists

Mohamed

Publications

1. **Lebbi, M**., Touafek, K., Benchatti, A., Boutina, L., Khelifa, A., Baissi, M. T., & Hassani, S. (2021). Energy performance improvement of a new hybrid PV/T Bi-fluid system using active cooling and self-cleaning: Experimental study. ***Applied Thermal Engineering,*** *182*, 116033. doi.org/10.1016/j.applthermaleng.2020.116033
2. Boutina L, **Lebbi M**, Touafek K, Khelifa A, Benchatti A. Numerical investigation of the natural air-cooling of photovoltaic modules in a new concept of hybrid system PVT mounted in stairs form (S-PVT). 2018 5th International Conference on Electrical and Electronic Engineering (ICEEE). IEEE, 2018. Doi:10.1109/ICEEE2.2018.8391383.
3. **LEBBI, Mohamed**, TOUAFEK, Khaled, BENCHATTI, Ahmed, *et al*. Channel gap effect on the passive cooling of the hybrid system PVT air collector. The 5th International Seminar on New and Renewable Energies, Renewable Energies Applied Research Unit, Ghardaïa – Algeria 24 - 25 Octobre 2018.
4. L. Boutina, A. Khelifa, K. Touafek, **M. lebbi**, M. T. Baissi, Improvement of PVT air-cooling by the integration of a chimney tower (CT/PVT), Applied Thermal Engineering. 129 (2018) 1181–1188. Doi.org/10.1016/j.applthermaleng.2017.10.097.
5. Boutina, L., Touafek, K., Khelifa, A., **Lebbi, M**., & Baissi, M. T. Etude numérique sur l'amélioration du refroidissement d'un module photovoltaïque par l'utilisation des nanofluides. The 5th International Seminar on New and Renewable Energies Renewable Energies Applied Research Unit, Ghardaïa – Algeria 24 - 25 Octobre 2018.
6. **Lebbi, M**., Touafek, K., Benchatti, A., Boutina, L., Benkaciali S, Hassani, S., Daimallah A. An innovative passive cooling system for photovoltaic modules. Energy journal, submitted.

Abstract

The accumulation of dust on the front faces of solar panels, the rise in the operating temperature of photovoltaic cells, and the low humidity levels recorded in semi-arid regions are considered major problems affecting negatively their performance. Therefore, over time, this leads to deteriorating and damaging PV cells. Hybrid photovoltaic/thermal systems are considered among the important technologies due to their efficiency in producing mainly electrical and thermal energy. This contribution is aimed to get a new hybrid system capable to reduce the PV cell's operating temperature with the use of passive and active cooling techniques. A self-cleaning technique suitable for the front face has also been incorporated. A numerical study of optimization of the geometrical and Thermo-hydrodynamic parameters using the CFD software Ansys Fluent was performed. After the simulation and optimization process, this new hybrid system was realized and tested under real climatic conditions in the Ghardaïa region. Thus, the PV module's backside is cooled by air, and flowing a thin film of water over its front side to cool and clean the system. The numerical results show that the optimal geometric parameters of the new hybrid PV / T air system (H_e = 0.05 m, W_e = 0.3 m, L_{che} = 0.735 m and d_{afp} = 0.03 m) enhancement of the average Nusselt number by about 20% compared to the case without AFP integration. Increasing the tilt angle of the PV / T air system improves the maximum flow velocity, especially for high Rayleigh number values (with and without AFP). With the use of the active air cooling technique, an improvement in the average Nusselt number was evaluated within 80% for the case of contra-current flow compared to in the co-current case. The experimental results showed a reduction of the PV module average temperature measured for the new hybrid system of around 15 °C, against the reference PV module. An improvement of approximately 5.7% in electrical efficiency compared to the reference case was obtained under the same operating conditions and at the peak of global solar irradiation, (G = 650 W / m^2). The overall energy efficiency and the average exergy efficiency are approximately 85.3% and 14.7%, respectively.

Keywords: Hybrid PV / T Bi-fluid system, Natural convection, cooling system, tilt angle, average Nusselt number, Rayleigh number, Solar heat gain, CFD, Energy performance, Experimental study, and Photovoltaic self-cleaning.

Résumé

L'accumulation de poussière sur les faces avant des panneaux solaires, l'élévation de la température de fonctionnement des cellules photovoltaïques et les faibles taux d'humidité enregistrées dans les régions semi-arides sont considérées comme des problèmes majeurs affectant négativement leurs performances. Par conséquent, cela peut entrainer des dégradations au cours du temps et même l'endommagement des cellules photovoltaïques. Les systèmes photovoltaïques/thermiques hybrides sont considérés parmi les technologies importantes en raison de leur efficacité à produire essentiellement de l'énergie électrique et thermique. L'objectif principal de cette contribution est d'obtenir un nouveau système hybride capable de réduire la température de fonctionnement des cellules photovoltaïques par des techniques de refroidissement passives et actives. Une technique de nettoyage appropriée de leurs faces avant a été également effectué. Une étude numérique d'optimisation des paramètres géométriques et thermo-hydrodynamiques utilisant le logiciel CFD Ansys Fluent a été abordée. Après les étapes de simulation et l'optimisation, ce système est réalisé et testé dans des conditions climatiques réelles de la région de Ghardaïa. Ainsi, la face arrière du module photovoltaïque est refroidi par l'air, et un écoulement d'un film d'eau sur sa face avant ont servi à refroidir et nettoyer le système. Les principaux résultats numériques montrent que les paramètres géométriques optimaux du nouveau système hybride PV/T air (He = 0,05 m, We = 0,3 m, L_{che} = 0,735 m et d_{afp}=0,03 m) ont amélioré le nombre moyen de Nusselt d'environ 20% par rapport au cas sans intégration AFP. En plus, l'augmentation de l'angle d'inclinaison du système PV/T air améliore la vitesse maximale de l'écoulement, en particulier pour les valeurs élevées du nombre de Rayleigh (avec et sans AFP). L'utilisation de la technique de refroidissement actif par air, et dans le cas d'écoulement à contre-courant, une amélioration du nombre de Nusselt moyen a été estimer à 80% pour le cas de l'écoulement à contre-courant par rapport au cas co-courant. Les résultats expérimentaux obtenus ont montré une réduction de la température moyenne mesurée pour le nouveau système hybride d'environ 15 °C, par rapport au module PV témoins (cas de référence). Une amélioration d'environ 5,7 % du rendement électrique par rapport au cas de référence a été obtenue dans les mêmes conditions de fonctionnement et au pic de l'irradiation solaire globale, (G = 650 W/m^2). L'efficacité énergétique globale et l'efficacité éxergétique moyenne ont été respectivement d'environ 85,3 % et 14,7 % respectivement.

Mots clés : Système hybride PV/T Bi-fluide, Convection naturelle, Système de refroidissement, Angle d'inclinaison, Nombre moyen de Nusselt, Nombre de Rayleigh, Gain de chaleur solaire, CFD, Performance énergétique, Étude expérimentale, Auto-nettoyage photovoltaïque.

ملخص

يعتبر تراكم الغبار على الوجوه الأمامية للألواح الشمسية، وارتفاع درجة حرارة تشغيل الخلايا الكهروضوئية، وانخفاض مستويات الرطوبة المسجلة في المناطق شبه القاحلة من المشاكل الرئيسية التي تؤثر سلباً على أدائها. لذلك مما يؤدي بمرور الوقت إلى تدهور حالة وحتى تلف الخلايا الكهروضوئية. تهدف هذه المساهمة إلى الحصول على نظام هجين جديد قادر على تقليل درجة حرارة تشغيل الخلية الكهروضوئية باستخدام تقنيات التبريد السلبي والنشط. كما تم ادراج تقنية تنظيف ذاتية مناسبة للوجه الأمامي. تم إجراء دراسة عددية لتحسين المعلمات الهندسية والحرارية الهيدروديناميكية باستخدام برنامج CFD Ansys Fluent. بعد عملية المحاكاة والتحسين، تم تحقيق واختبار هذا النظام الهجين الجديد في ظل ظروف مناخية حقيقية في منطقة غرداية. وبالتالي، يتم تبريد الجزء الخلفي من الوحدة الكهروضوئية عن طريق الهواء، وتدفق طبقة رقيقة من الماء على جانبها الأمامي لتبريد النظام وتنظيفه. أظهرت النتائج العددية أن المعلمات الهندسية المثلى لنظام الهواء الهجين الجديد PV / T (He = 0.05 m ،We = 0.3 m ،L_{che} = 0.735 m ،d_{afp} = 0.03 m) تعزيزًا لمتوسط رقم Nusselt بحوالي 20٪ مقارنة للقضية دون تكامل وكالة فرانس برس. تعمل زيادة زاوية إمالة نظام الهواء PV / T على تحسين سرعة التدفق القصوى، خاصة لقيم رقم Rayleigh العالية (مع وبدون AFP). باستخدام تقنية تبريد الهواء النشط، تم تقييم التحسن في متوسط رقم نسلت في حدود 80٪ لحالة تدفق التيار المعاكس مقارنةً بحالة التيار المشترك. تم الحصول على تحسن بنسبة 5.7 ٪ تقريبًا في الكفاءة الكهربائية مقارنة بالحالة المرجعية في نفس ظروف التشغيل وفي ذروة الإشعاع الشمسي الاجمالي، (G = 650 W/m^2). تبلغ الكفاءة الكلية للطاقة ومتوسط كفاءة الطاقة حوالي 85.3٪ و14.7٪ على التوالي.

الكلمات المفتاحية :

مجمع الطاقة الشمسية الكهروضوئية/حرارية ثنائي السوائل، الحمل الحراري الطبيعي والمختلط المضطرب، نظام التبريد، زاوية الميل، متوسط عدد نوسيلت، عدد رايليغ، اكتساب الحرارة الشمسية، الوحدة الكهروضوئية، النمذجة العددية، أداء الطاقة، كفاءة الطاقة، دراسة تجريبية، التنظيف الذاتي للوحدة الكهروضوئية،

Content

Chapter II:

General on CFD and numerical procedure

Chapter III:
Numerical modeling of hybrid PV/ T system by passive air-cooling

Chapter IV:
An innovative active single and Bi-fluid cooling system for photovoltaic modules

Chapter V: Study, Design and experimental realization of a new hybrid PV / T Bi-fluid system

List of figures

List of tables

Nomenclature

Symbols

P_{mp}	Electrical power at the maximum point, [W].
P_{PV}	PV module electrical power, [W].
P_{PVT}	PV/T Bi-fluid Electrical power, [W].
P_{STC}	Nominal electrical power, [W].
V	Output voltage, [V].
V_{oc}	Open circuit output voltage, [V].
V_{mp}	Voltage at maximum point, [V].
I_{mp}	Current at maximum point, [A].
I_{SC}	Current at Short-circuit, [A].
FF	Filling factor [-].
T_{amb}	Ambient temperature, [°C].
$T_{PV, avg}$	PV module average temperature, [°C].
$T_{PVT, avg}$	PV/T Bi-fluid average temperature, [°C].
T_{ref}	Temperature at standard testing conditions (STC), [°C].
$T_{air, in}$	Inlet air temperature, [°C].
$T_{air, out}$	Outlet air temperature, [°C].
$T_{w, in}$	Inlet water temperature, [°C].
$T_{w, out}$	Outlet water temperature, [°C].
G	Global solar radiation intensity, [W/m^2]
G_{avg}	Average solar radiation intensity, [W/m^2]
G_{STC}	Global solar radiation at (STC), [W/m^2].
A_c	Collecting area, [m^2].
A_{PV}	PV module area, [m^2].
L_{PV}	PV module length, [m].
W_{PV}	PV module depth, [m].
e_{glass}	Glass thickness of PV module, [m].
Nc	PV cells number, [-].
L_C	Length of the collector air channel, [m].
W_c	Depth of the collector air channel, [m].

S_C	Height of the collector air channel, [m].
L_e	Entrance sloped channel length, [m].
W_e	Entrance sloped channel depth, [m].
S_e	Entrance sloped channel height, [m].
L_{alm}	Aluminum flat plate length, [m].
W_{alm}	Aluminum flat plate depth, [m].
E_{alm}	Aluminum flat plate thickness, [m].
d_{alm}	Distance between (AFP) and the PV module, [m].
ϕ_t	Diameter of the transparent plastic tube, [m].
ϕ_n	Diameter of the water inlet nozzle pipe, [m].
ϕ_o	Diameter of the outlet water nozzle, [m].
P_{Fan}	DC fan electric power, [W].
I_{Fan}	DC fan operating current, [A].
V_{Fan}	DC fan operating voltage, [V].
L_{Fan}	Length of the DC fan, [m].
W_{Fan}	Depth of the DC fan, [m].
h_{Fan}	Thickness of the DC fan, [m].
P_{pump}	DC water pump electric power, [W].
I_{pump}	DC water pump operating current, [A].
V_{pump}	DC water pump operating voltage, [V].
L_{pump}	Length of the water DC pump, [m].
W_{pump}	Depth of the water DC pump, [m].
h_{pump}	Thickness of the water DC pump, [m].
$\phi_{in,\ pump}$	Inlet diameter of the water pump,[m]
$\phi_{out,\ pump}$	Outlet diameter of the water pump,[m]
H_{pump}	Maximum height (Head) Water DC pump
Q_{pump}	Volumetric flow rate,[L/min]
C_p	Specific heat capacity,[J/kg K]
m_a	Mass flow rate, [kg/s]
m_w	Mass flow rate, [kg/s]
v_n	Value of the measured variable, [-]
R	Uncertainty of the measuring value, [%]
w_n	Uncertainty intervals in variables, [%]

$W_{R,\ total}$	The total uncertainty in measurement value of any variable, [%]
AM	Air mass, [-]
Δp	The pressure difference produced by the fan, [Pascal]
g	gravitational acceleration, [m/s^2]
T_{amb}	Ambient temperature, [°C].
T_{ref}	Temperature at standard testing conditions (STC), [°C].
$T_{air,\ in}$	Inlet air temperature, [°C].
$T_{air,\ out}$	Outlet air temperature, [°C].
L_{Ch}	Length of the collector air channel, [m].
W_s	Depth of the collector air channel, [m].
L_{che}	Entrance sloped channel length, [m].
W_e	Entrance sloped channel depth, [m].
H_e	Entrance sloped channel height, [m].
L_{AFP}	Aluminum flat plate length, [m].
W_{AFP}	Aluminum flat plate depth, [m].
E_{AFP}	Aluminum flat plate thickness, [m].
d_{AFP}	Distance between (AFP) and the PV module, [m].
C_p	Specific heat capacity, [J/kg K].
M_{air}	Mass flow rate, [kg/s].
Pr	Prandtl number, [-].
Ra	Rayleigh number, [-].
Ra_L	Rayleigh's number based on PV module length, [-].
Ra_m	Modified Rayleigh number, [-].
Nu_{L_avg}	Average Nusselt number, [-].
g	Gravitational acceleration, [m/s^2] .

f	The friction coefficient, [-].
k_{in}	The input and output pressure drops, [-].
k_{out}	The output pressure drops, [-].
Dh	The hydraulic diameter of the rectangular channel, [m].
S	The gap size of the air channel spacing, [m].
H_{ch}	The difference of height between the inlet and the outlet of the air channel, [m].
V	Average magnitude velocity, [m/s].
P	The total pressure, [-].
σ_t	The stress tensor, [-].
G_k	The production of turbulent kinetic energy, [-].
K	The generation of turbulence kinetic energy, [-].
ε	The generation of turbulence dissipation energy,[-].

Acronyms

PV	Photovoltaic
PV/T	Photovoltaic/thermal
PV/T air	Systems with air as working fluid
PV/T Bi-fluid	Systems based on two working fluids
PV/T liquid	Systems with liquid as working fluid
PV/T water	Systems with water as working fluid
PV/T Combi	Systems that combines water and air as a working fluid
STC	Standard testing condition
SC	Self-cleaning
AFP	Aluminum flat plate
FEM	Finite element method
FDF	Finite difference method
FVM	Finite volume method

SEC	Sloped entrance channel

Greek symbols

α	The angle of tilt with respect to the horizontal plane, [°].
β	The thermal expansion coefficient, [1/K].
β_{ref}	Coefficient of the PV cell efficiency temperature, [1/K].
η_{o}	PV module nominal electric efficiency at (STC), [%].
$\eta_{el, PV}$	Electric efficiency of the PV module (reference case), [%].
$\eta_{el, PVT}$	Electric efficiency of the PV/T Bi-fluid, [%].
$\eta_{th, PVT}$	Thermal efficiency of the PV/T Bi-fluid, [%].
$\eta_{ex, PVT}$	Exergy efficiency of the PV/T Bi-fluid, [%].
η_{power}	Electrical-power generation efficiency of a conventional thermal power plant, [%].

Subscripts

amb	Ambient
O	Reference state
el	Electric
PV	Photovoltaic module
PVT	Photovoltaic/thermal
avg	Average
in	Inlet
out	Outlet
f	Fluid
air	Air
w	Water
th	Thermal
a	Air

General introduction

1. Context of the study

The exploitation of energy sources is an urgent necessity in human life, especially in today's world. Therefore, the search for these sources is a global challenge that researchers, politicians, and citizens must confront. However, the future holds sometimes-unexpected surprises due to the decrease in global stocks of primary sources (oil, gas, and coal). In this viewpoint, the ever-increasing demand for energy sources and the fear of the increasing spread of environmental pollution needs to search for an alternative related to renewable and clean energy sources. Therefore, the trend is scheduled towards harnessing renewable energies such as biomass, solar energy, and wind power, which represents the best and most efficient alternative. Where, the use of these sources of renewable energies plays an effective role in improving three categories of sustainable development: social, environmental, and economic. On the other hand, the promotion of renewable energies offers more independence and advantages, moving towards a global energy transition and reducing the use of fossil fuels.

Solar photovoltaic energy is one of the most widely used renewable energies in the world. It is based on the direct conversion of electromagnetic solar radiation into electricity through the photoelectric effect. Photovoltaic panels have the ability to convert photons into electrons, which provide energy in the form of a direct current (DC) that can be used immediately.

2. Problem statement

When solar radiation is fallen on the front side of PV panels, it is converted into electricity. However, a significant part of this solar energy is converted into thermal energy, which raises the operating temperature of the photovoltaic cells and thus deteriorates their electrical efficiency. Moreover, these panels are exposed to the accumulation of a lot of dust and dirt, which prevents the solar radiation from reaching the cells and decreases the output of electric energy. Therefore, the operating temperature rise and the dust accumulation on the front side of these solar panels, especially in arid and semi-arid desert areas, is a major issue that causes low performance and damage to photovoltaic cells.

Therefore, the challenge that we must raise in exploiting this energy is to improve the efficiency of these photovoltaic systems and reduce the cost of their production. Due to the nonlinear electrical properties of photovoltaic cells, the performance of the photovoltaic module can be improved by using passive or active cooling techniques. Thermal photovoltaic (PV/T) solar collectors are systems that use photovoltaic modules connected to heat exchangers to extract heat and use it in various fields. Where the extraction of the heat from PV modules using working fluids, and these hybrid solar collectors allow the production of thermal and electrical energy at the same time.

Although there are effective and integrated cooling mechanisms in hybrid PV/T systems, another major problem that reduces the performance and even damages the photovoltaic cells is the accumulation of dust on the photovoltaic module's front side.

Most of the previous work mentioned in the literature focused on the use of passive or active cooling systems with one or more coolants to reduce the temperature of the PV module, without taking into account the risk of dust accumulation on its front side.

3. Motivations

Following the huge increase in the demand for traditional fossil energy sources and the trend towards the exploitation of renewable energies, in particular, solar energy sources. It was found that the production of electrical energy by using solar panels has increased significantly in developing countries. However, high temperature and frequent sandstorms, especially in Arid and semi-arid areas, which are characterized by a large hour of the clear sky throughout the year, and negatively affect the efficiency of photovoltaic panels.

In light of these data, it appears that the solar hybrid Photovoltaic / Thermal Bi-fluid systems are the most appropriate solution for providing local electricity and providing citizens with air and hot water according to the following stimulating opportunities:

- ✓ Because of the vast area of Algeria and the tendency to build huge stations for the production of electric power, especially in the desert areas that are characterized by clear skies throughout the four seasons.
- ✓ If we consider the remote pastoral and agricultural areas, there is a common use of diesel generators to power independent installations, which pose a great threat to environmental pollution and thus pose a danger to plants, animals, and even to humans.
- ✓ Moreover, these desert areas face a factor of high temperature and sudden sandstorms. All these data were among the motivators that prompted us to take an interest in looking at it and what I can contribute to a better understanding of it.
- ✓ The low cost of making this hybrid PV/T Bi-fluid system due to the abundance of local materials and ease of maintenance.

- ✓ In addition, among the motivators that prompted us to find an innovative hybrid system, we have not yet registered any marketed hybrid system that cools and cleans itself in the world.

4. Scope and objectives

The main scope of the work presented in this thesis is to contribute to the improvement of the performance of solar panels through the optimization and the realization of a new simple and efficient Bi-fluid PV / T hybrid solar system. This new hybrid system able to reduce PV cells operating temperature by using passive and active cooling techniques, in more includes a technique that ensures continuous self-cleaning of the front side of PV modules.

Accordingly, two working fluids, i.e., water and air, were used in a new concept of the PV/T Bi-fluid hybrid system. In addition to generating electricity, this hybrid system provides useful hot water and air. This goal will be achieved through the following main axes:

- ✓ This work is aimed to optimize numerically and achieve experimentally a new solar hybrid PV/T system Bi-fluid solar collector, with a double role. The passive or active air-cooling of the PV module backside, and its front side that subject to flowing of water film to ensure self-cleaning and active water-cooling.
- ✓ This study is devoted to ensuring that the self and continuous cleaning of the PV module front side, from the accumulation of solid particles and bird droppings, especially in aerosol areas.
- ✓ To prevent dust deposition due to lack of moisture, dust, and dirt adhere to the front faces of solar panels.
- ✓ In the purpose to provide hot water, hot air, and electricity at the same time

5. Thesis contribution and organization

In this thesis, a new solar hybrid PV/T Bi-fluid system has been optimized numerically, fabricated, and tested experimentally under climatic conditions of arid regions to reduce the PV module operating temperature and to clean it from the soiling. This new hybrid PV/T Bi-fluid system contains a novel technique that ensures high performance and long life of the photovoltaic panels without interruption.

In fact, the cooling of stand-alone PV systems is a key factor that allows optimization of the output of the generated electrical energy required to supply the loads and its on-demand production.

In this context, the work of this thesis has been organized according to the following main points: It begins with a general introduction, followed by five chapters showing the methodology and the main results obtained, and ends with a general conclusion. Moreover, these points are explained in detail in this thesis as follows:

Firstly, this contribution started with a general introduction, which includes the context of the study, problem statement, motivations of this work, Scope and objectives, and thesis contribution.

- ✓ **Chapter 1:** Contains a generality on the hybrid solar systems and provides the state-of-the-art of cleaning techniques and cooling methods.
- ✓ **Chapter 2:** Comprises two parts. The first presents a generality on the CFD, and the second the numerical modeling procedure.
- ✓ **Chapter 3:** Contains numerical modeling of hybrid PV/ T system using passive air-cooling.
- ✓ **Chapter 4:** A novel concept of hybrid PV/T system using active air-cooling, and comparison of new hybrid PV/T system Bi-fluid system with current experimental data, has been presented.
- ✓ **Chapter 5:** This section focuses on the presentation of experimental results of a new solar hybrid PV/T Bi-fluid System.

Finally, a general conclusion of the main numerical and experimental results has been presented, as well as future works.

Chapter I

Generality on solar hybrid systems and literature reviews

I.1 Introduction

This section presents the general framework of the study conducted during the thesis and the importance of renewable energy use, in the climate change context and the energy crisis. These world crises involved fossil energy resource depletion that the world must confront with all available means and capabilities.

In this section, we will first provide the general focus for identifying solar PV thermal systems challenges. Besides, the state-of-the-art will be presented in a more specific and detailed way over a single and Bi-fluid hybrid solar system. In Fact, renewable energies improve efficiently three categories of sustainable development: social, environmental, and economic. On the other hand, promoting renewable energy offers more independence and advantage, by going towards a global energy transition and by reducing fossil fuel use. Renewable energy sources are inexhaustible and provided naturally from sunlight, biomass, waves, geothermal energy, wind, and hydraulic energy. Renewable energies are the best option for sustainable economic growth, coexistence between people and the environment **[1-4]**.

I.2 Sources of renewable energies

The most important renewable energy sources are mentioned, as follows **[5-6]**:

- ✓ Photovoltaic or thermal solar energy;
- ✓ Wind Energy;
- ✓ Geothermal energy;
- ✓ Marine energies;
- ✓ Hydraulic power;
- ✓ Energy from biomass.

Global electricity demand increases and renewable energy generation growth, 2019-2025, is plotted in **Figure. I.1. [7].**

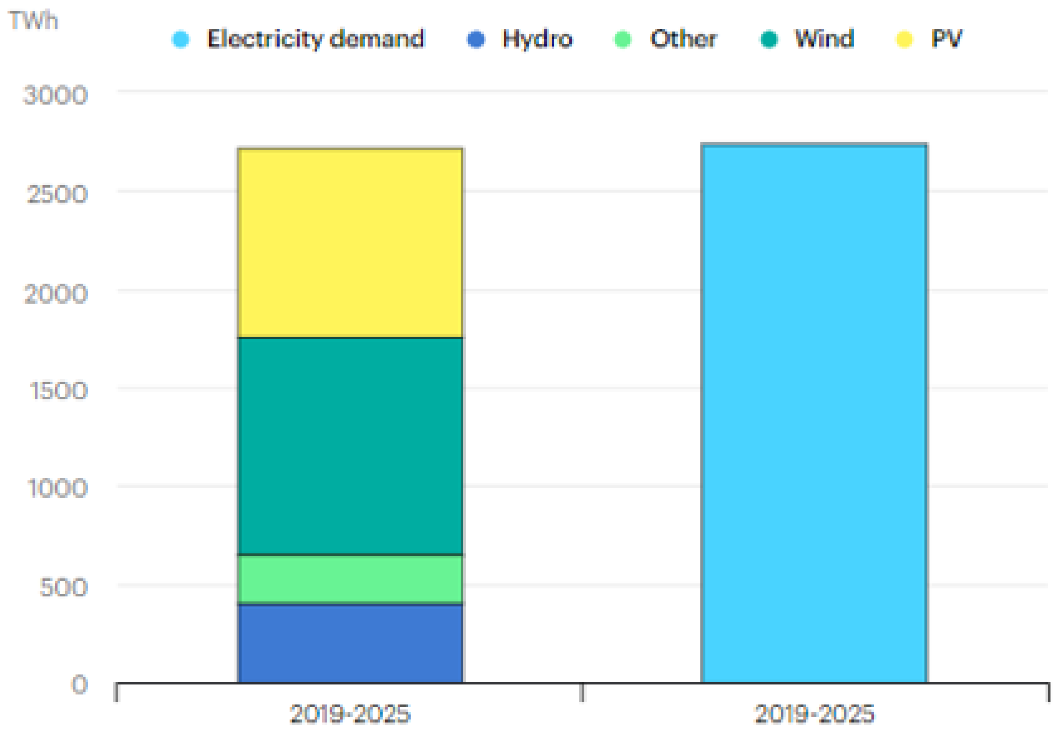

Figure I.1: *Global electricity demand increases and renewable energy generation growth, 2019-2025*

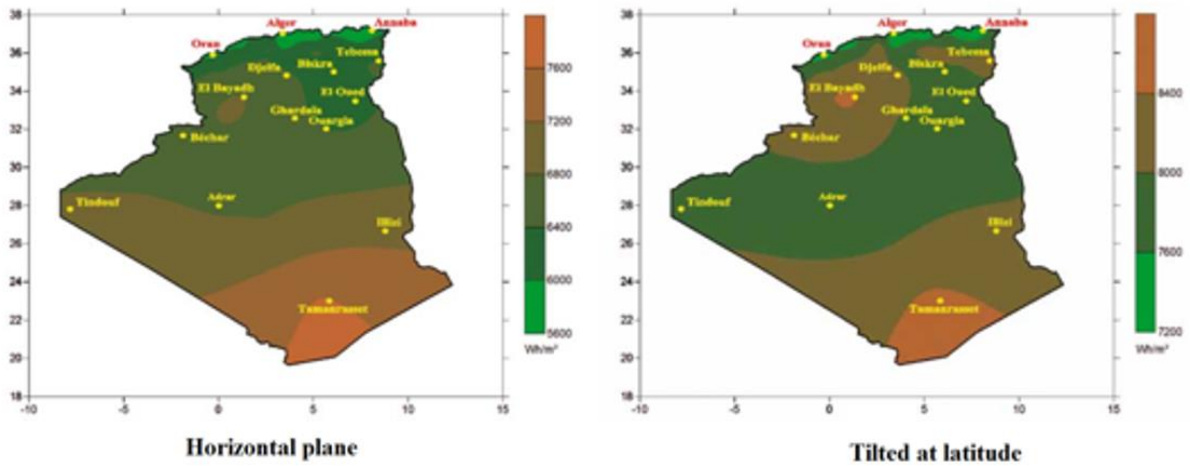

Figure I.2: *Annual average of the global irradiation full clear sky(GHI)*

Figure. I.2 presents the annual average of the global irradiation in the case of completely clear sky (GHI). Concerning the horizontal plane, GHI takes range values Algiers (latitude =36°N), 5000<GHI<6000Wh/m², Ghardaïa (latitude =32°N), 6400<GHI<6800Wh/m², Tamanrasset (latitude =23°) 5000<GHI<6000Wh/m².

Besides, for tilted at latitude case, GHI take range values Algiers (latitude =36°N), $5000<GHI<6000 Wh/m^2$, Ghardaïa (latitude =32°N), $6400<GHI<6800 Wh/m^2$, Tamanrasset (latitude =23°) $5000<GHI<6000 Wh/m^2$.

I.3 Limits and profits of using renewable energies

In the energy supply of any society, it is important to find a balance between three fundamental factors: competition, security of supply, and its impact on the environment and climate. It cannot find an ideal source of energy that includes all three aspects.

Table. I. 1: Advantage and limitations of renewable energies sources

RES Types	Advantages	Disadvantages
Solar energy	Solar energy is a form of renewable energy that is clean, secure, and unlimited.	Energy production depends on the bright sun but is intermittent and erratic, and is still expensive compared to other sources of electricity generation.
Energy biomass	Biomass is an even source of energy with geographically diverse assets and little political risk.	It may be difficult to provide large quantities and energy production is more expensive than using energy sources.
Wind energy	There are no carbon dioxide emissions during wind power production and is not necessary to use fuel.	Energy production depends on the presence of wind and Huge investment costs
Hydraulic energy	Hydropower does not affect by the climate and the environment and provides a stable and wide range of power generation.	Hydroelectric power plants greatly affect the landscape and the ecosystem and require large investments to build a hydroelectric power station.

It is mentioned in **Table.I.1** most of the major advantages and disadvantages of different renewable energy sources separately **[8-15]**.

I.4 Hybrid renewable energy systems structure

Hybrid energy systems combine two or more renewable energy sources, plus one or more conventional energy sources. Renewable energy sources, such as photovoltaics and wind turbines do not provide static energy, but by their integration, their connection allows for continuous electricity production.

Hybrid energy systems are generally self-sufficient from large interconnected grids and are often used in remote areas. The different sources in a hybrid system can be connected in two configurations, DC and AC installations.

In the literature, several classifications have been proposed according to well-defined criteria. In what follows, the classifications most used are presented. Hybrid energy systems can be grouped into two categories. The first category includes hybrid systems that are connected to the grid; they work in parallel with the network, these systems are connected to the network. In the second category, we find autonomous hybrid systems. These systems are isolated from the network.

I.5 Different types of hybrid photovoltaic systems structure

The structure of the hybrid system is classified into the systems types as shown in **Figure I.3** [16]. In the presence or absence of a conventional power source, a hybrid system can contain a conventional power source such as a diesel generator or a gas turbine or simply a complete installation of off-grid hybrid systems.

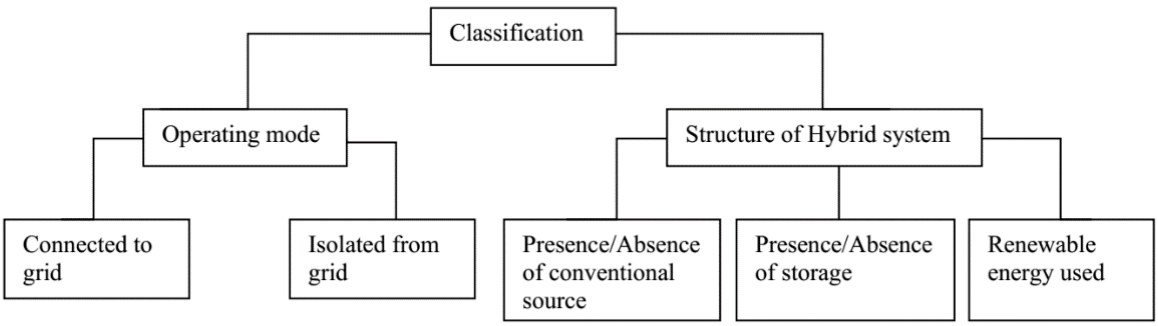

Figure I.3: *Classification of hybrid systems* ***[16]***

Whether there is storage capacity for standalone hybrid systems, a storage device is required. In case of an insufficient primary source, storage is load bearing. There are various storage methods. The most used are rechargeable batteries, flywheels. The renewable energy source used must include the structure of the hybrid renewable energy system on a renewable energy source, either a photovoltaic generator or wind turbine or a combination of its sources. The available energy potential (solar radiation, wind speed, etc.) is very important for source selection.

I.6 Photovoltaic systems with storage system

The photovoltaic installation must contain another source of energy, to meet the load demand during the night period or if there is a lack of solar radiation due to clouds or air pollution. This type of system is used to electrify homes and villages **[17, 18]**.

The ideal parameter is either the cost of the energy produced or the potential for the load loss **[19]**; the literature search examined the different types of storage: the author **[20]** addressed the ideal storage.

I.6.1 Hybrid photovoltaic/wind/storage systems

A hybrid PV/wind /battery system consists of a PV generator, a wind generator (WT), battery storage, a DC/DC converter, an AC/DC converter, and an inverter able to meet the peak load demand **[21]**.

I.6.2 Photovoltaic/wind/diesel systems

The photovoltaic and wind hybrid system must be designed as the basis for optimum capacity bearing the officially specified load. An optimized hybrid system should fulfill two main objectives: energy reliability and system cost **[22]**.

I.7 Solar energy harvest techniques

Solar energy is the main source of renewable energy that is tapped **[23-28]**. There are two basic passive or active technologies used to harvest solar energy by solar energy systems **[29-35]**.

I.7.1 Passive techniques

For passive solar energy harvesting techniques, such as windows, walls, roofs, and floors are used to collect and store solar radiation as thermal energy and to be a source of heating during cold days, especially at night **[37-42]**.

I.7.2 Active techniques

Likewise, solar energy can be recovered through active systems, for example, using photovoltaic panels, concentrating solar collectors, or thermal [43-47]. Solar thermal collectors convert solar radiation into heat through an absorbing plate, where the energy of sunlight is simultaneously absorbed and converted by gaseous or liquid fluids such as water or air [48-52].

I.8 Solar energy collector systems

Solar energy is a primary source of renewable energy, and therefore, it is the subject of much attention in research and development. Solar energy harvesting systems are divided into three main categories as shown below, thermal collectors, photovoltaics, and combined systems in hybrid systems Photovoltaics /thermal [53-60].

I.8.1 Solar thermal collectors

Solar thermal systems convert solar radiation into heat, where it is transferred by the heat exchanger through liquid fluids such as water or gaseous like air. These systems are a special type of heat exchangers that convert the energy of solar radiation into heat energy that is transferred through gaseous or liquid fluids to be stored for use when needed [61]. There are two main types of solar collectors: stationary and concentrated. An unfocused collector has the same area to intercept and absorb solar radiation, while a concentrated solar collector typically has concave reflective surfaces to intercept and focus solar radiation over a very small receiving area to increase the flux of radiation **[62]**. **Table I.**2 presents **s**olar energy collector types.

Table I.2 : Different type of Solar energy collectors [62]

Motion	**Collector type**	**Absorber type**	**Concentration ratio**	**Indicative temperature range (°C)**
Stationary	Flat plate collector (FPC)	Flat	1	30-80
	Evacuated tube collector(ETC)	Flat	1	50-200
	Compound parabolic collector (CPC)	Tubular	1-5	60-240
Single-axis tracking	Linear Fresnel reflector (LFR)	Tubular	5-15	60-300
	Parabolic trough collector(PTC)	Tubular	10-40	60-250
	Cylindrical trough collector(CTC)	Tubular	15-45	60-300
Two-axis tracking	Parabolic dish reflector(PDR)	Point	10-50	100-500
	Heliostat filed collector(HFC)	Point	10-50	150-2000

There are multiple applications of thermal solar collectors such as Building **[63]**, thermal storage systems **[64]**, and geothermal heat pumps **[65]** .etc.

I.8.2 Photovoltaics systems

Photo-electricity is the direct conversion of light into electricity, using materials that absorb photons of light and emit electronic charges. They can be used as electrical generators, and the main component of these generators is called the PV cell **[66]**. The solar PV system converts solar radiation into electricity that is used to power various devices. When it rains, very little electricity is produced due to the clouds, which block solar radiation. At night, no electricity is produced, even though the moon appears very bright. Since electricity is generally required at night, the electricity produced on sunny days is stored in batteries. The battery can be used at any time to do useful things such as powering lights, radios, and television **[67]**.

a) Operating principle

The word "photovoltaic" comes from the original Greek word "image", which means light, and from the word "voltage" derived from "volta", which represents the name of the Italian physicist Alessandro Volta, inventor of the first electric battery in the eighteenth century **[68]**. A photocell is a sensor made of a semiconductor material that absorbs light energy and then turns into an electric current. The principle of operation of this cell uses the properties of absorbing light radiation by semiconductor materials. So, the materials used in the design of photovoltaics are chosen according to the physical properties of some of their electrons that may be released from their atoms when excited by the photons **[69-73]**.

b) Photoelectric effect

The photoelectric effect is the production of electrical energy by a receiving system from the light flux. It is based on the principle, which, the silicone disc reinforced it positively. One of these faces is N-doped, so the PN junction is made. On both sides P and N, we have holes and stationary electrons. These static charges give rise to an electric field E that tends to push the mobile charges back and forth through the transition region. When the solar cell is illuminated, some photons hitting it are reflected and the other part enters the junction. The absorbed photons of sufficient energy release parts of the electron-hole pairs, which in turn move under the influence of the electric field in the crystal by the phenomenon of diffusion, which causes a voltage difference at these terminals **[74-78]**.

c) *Solar Photovoltaic technology*

This section gives a brief description of solar PV technology and the technical terms used. A solar photovoltaic installation is powered by many thin-film or crystalline photovoltaic modules. Individual PV cells are interconnected to form a PV module.

It takes the form of a panel for easy installation. Photovoltaic cells are made of light-sensitive semiconductor materials that use photons to dislodge electrons to drive an electric current **[79]**. There are two main categories of technologies used for photovoltaic cells, namely crystalline silicon, as shown in **Figure I.4,** which accounts for the majority of PV cell production; and thin film, which is newer and more and more popular.

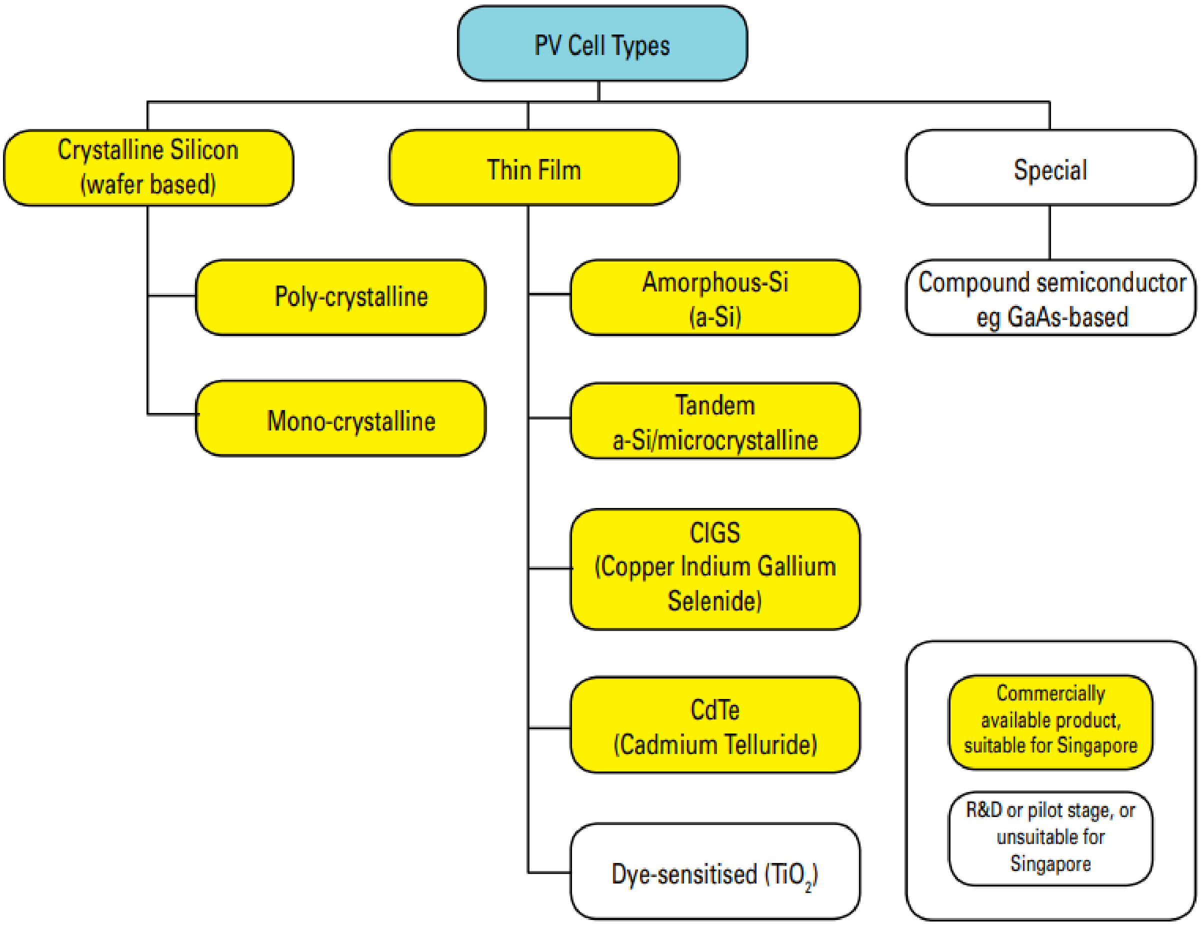

Figure I.4: *Family tree of PV technology* ***[79].***

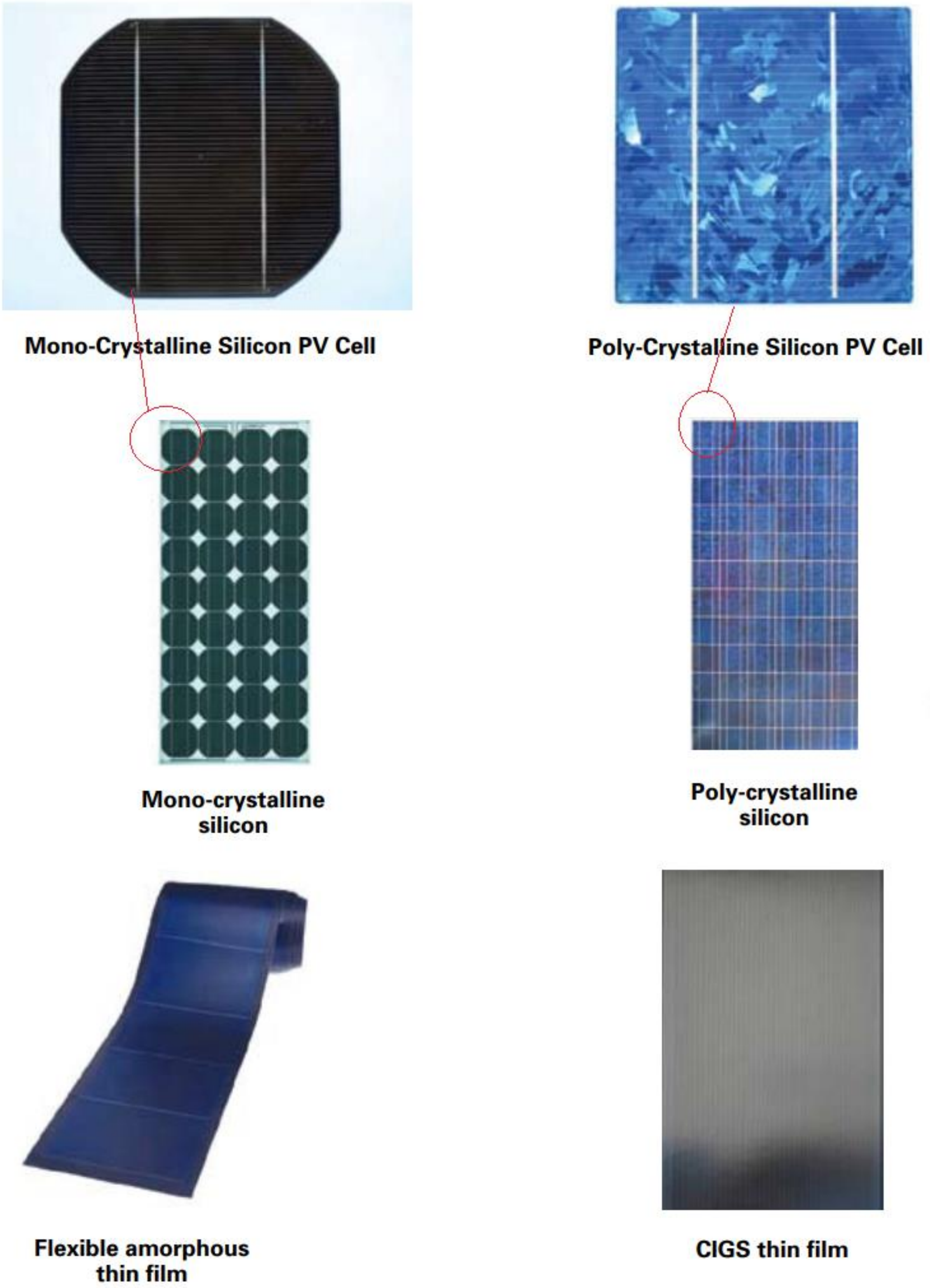

Figure I.5: ***Mono, polycrystalline silicon PV cell, and thin-film PV module technology [79].***

The family tree in **Figure I.5** provides an overview of these technologies available today and illustrate some of these technologies.

d) Shape of photovoltaic cells

Photovoltaic cells are electrically connected in series or in parallel to produce higher voltages and currents. In addition, mounting these photovoltaic cells interconnected to each other forming a module can provide electricity.

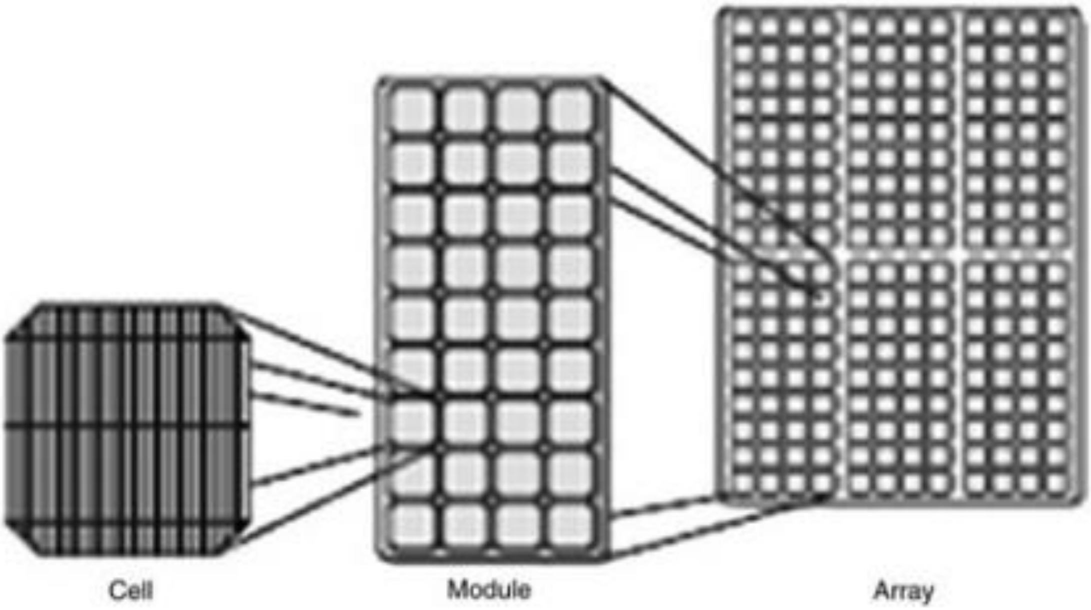

Figure I.6: *Photovoltaic cells, modules, and arrays* ***[80]***

When these photovoltaic panels are connected to each other in parallel or in series, it has allowed us to build a mini solar power plant of photovoltaic panels. The combination of these small solar power plants constituting several photovoltaic panels forms a large power plant for generating electricity that can power an entire city as shown in **figure I.6 [80]**.

I.9 External factors affecting the photovoltaic performance

Various factors must be taken into account to ensure optimum efficiency of solar photovoltaic modules. The main factors that can influence the efficiency of a photovoltaic module during its production process are as follows.

There are many factors that negatively affect the performance of PV systems, and they can be classified as follows, environmental factors, PV system factors, installation factors, cost factors **[81]**.

I.9.1 Environmental factors

The different environmental factors greatly affect the performance of PV systems and are represented in solar radiation, shadows, humidity, wind speed, temperature, and accumulated dust, and each of these factors will be discussed in detail **[82-85]**.

I.9.2 Direct solar radiation effect on the performance of PV panels

Solar irradiance is defined as the amount of energy from the solar source per unit area. Irradiance is usually affected depending on the weather and the position of the sun in the sky. The location of the sun changes throughout the day due to changes in the sun's altitude, which is the angle between the sun's rays and the horizontal plane, and the azimuth angle, which is the angle between true north and the projection of the sun's rays horizontally in the sky **[86]**.

So, the energy produced by a photovoltaic module is directly related to the availability of solar energy, and as a result, depends on the site of the installation of these systems **[87, 88]**.

I.9.3 Shading effect on the performance of PV panels

The performance of photovoltaic panels is strongly affected by the effect of shading from trees, passing clouds, neighboring buildings, and any other means as indicated in ref. **[89-93]**. Shading negatively affects the performance of photovoltaic panels. For this, all irregular shading conditions should be avoided as much as possible.

I.9.4 Wind speed effect on the performance of PV panels

Recently, it is reported that wind speed can also help to improve solar cell temperature performance due to its cooling effect **[94-96]**. There are other studies based on low wind speed in mostly sunny and less windy regions.

They showed that in very windy places, the contribution of wind speed could be more considered compared to less windy places **[97-101]**.

I.9.5 Relative humidity effect on the performance of PV panels

To analyze how humidity affects the performance of solar panels, it is necessary to know the extent to which water vapor particles influence the level of solar radiation. Moisture ions have seeped into the solar cell. For this reason, much work has been done to find the optimal solution to two major problems **[102-104]**.

I.9.6 Dust deposition effect on the performance of PV panels

Due to the accumulation of dust particles on the front surfaces of the PV modules and air pollution, the performance of the PV modules will inevitably be affected in a very bad way **[105-108]**.

I.9.7 Temperature effect on the performance of PV panels

Temperature affects the efficiency of the photovoltaic cell due to the properties of its component material, which is the semiconductor. The performance of the solar PV modules increases when the temperature reduced and drops at high temperatures, due to the voltage between the cells drops **[109-113]**.

It is known that the performance of photovoltaics is extremely sensitive to the temperature of the cells. Photovoltaic temperature is a function of various parameters such as meteorological variables (ambient temperature, wind speed, humidity, etc.), solar radiation, cell material, and system-dependent characteristics, the permeability of the cover in glass, plate absorption, etc. **[114-118]**.

I.10 Hybrid photovoltaic/thermal systems

Hybrid photovoltaic/thermal solar collectors are systems using photovoltaic (PV) modules as thermal absorbers. Much of the sun's radiation is not converted into electricity and increases their temperature, thus reducing their electrical efficiency. By recovering part of the heat dissipated by the PV modules using a heat transfer fluid, these hybrid solar collectors allow the simultaneous production of thermal and electrical energy **[119-125]**.

A photovoltaic/thermal hybrid solar system is obtained by combining solar thermal collectors with solar photovoltaic cells to enable the simultaneous generation of electricity and heat production. They are classified according to the type of fluids used to transfer the heat from the plate to the heat exchanger and then store them in the thermal tanks as shown in **figure I.7**.

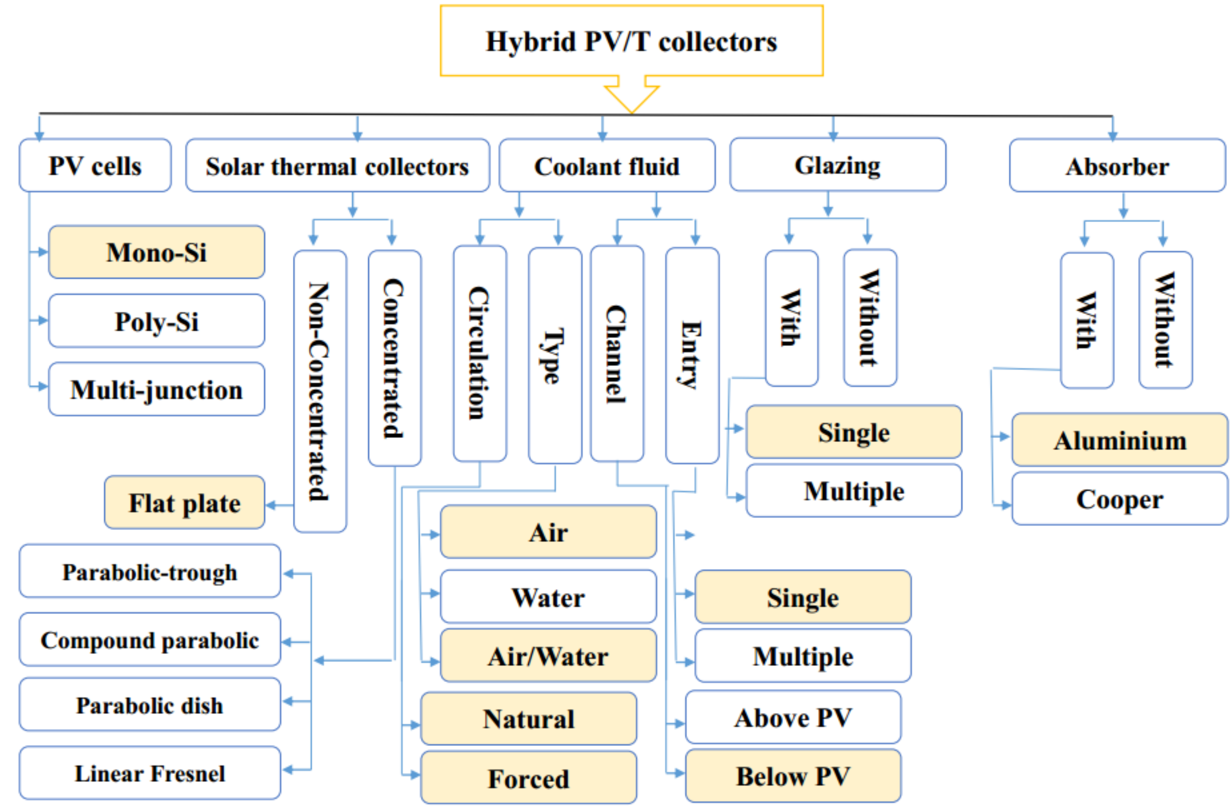

Figure I.7: *Classification of PV/T solar collectors* ***[126]***

PV/T hybrid thermal collectors are classified into three groups depending on the heat transfer fluid used, namely **[126].**

I.10.1 Hybrid system (PV/T) based air

Hybrid system (PV/T) solar collector-based air: This is an air circulation system that is installed under the PV module while allowing the unit to be cooled, with air heating, and it will be used for interior preheating or ventilation.

I.10.2 Hybrid system (PV/T) based water

This is a dedicated tube system for circulating water and antifreeze, and the tubes are located behind the PV module.

I.10.3 Combined hybrid system (Air/Water) (PV/T) - Bi-fluid

The hybrid PV/T Bi-fluid is a piping system intended for the circulation of water or antifreeze, and the tubes are located behind the PV module and a channel with or without fins that allow the circulation of air. In these hybrid systems, the cooling ensured by using two working fluids, air, and water.

I.11. Hybrid PV/T systems: A review

This part presents a review of scientific studies on the different types of PV / T hybrid collectors, with a description of the different configurations proposed in order to improve the performance of these systems. The first idea for a hybrid PVT system was discovered in the mid-1970s when Joshi and Dhoble [127] had carried out several studies.

In 1976, Wolf **[128]** studied the liquid-type PV/T solar collector in monitoring the performance of collectors for single-family homes over a full year. In 1979, Florschuetz **[129]** modified the original parameters of the "Hottel Whillier model" which is the thermal modeling of flat collectors and studied the electrical and thermal performances of PV/T collectors.

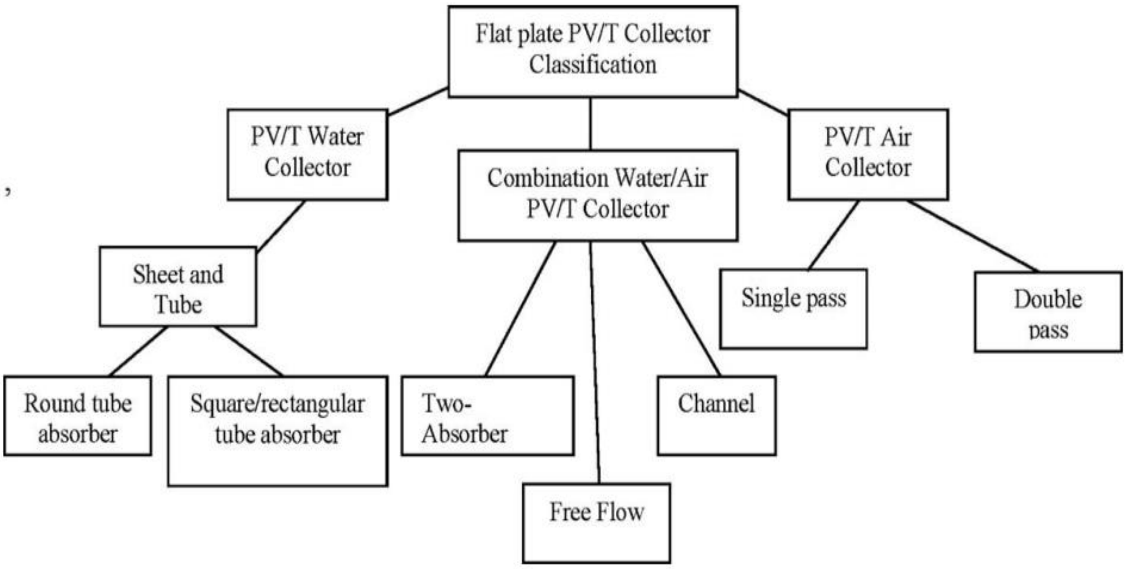

Figure I.8: *Classification of Flat plate Hybrid photovoltaic/thermal collector* ***[130]***

Despite the fact that the concept of PV/T solar collectors has been established for more than four decades, it is not yet fully commercialized. The flat plate PV/T collector can be classified as PV/air collector, PV/T water collector, and PV/T water/air collector mixture, depending on the type of working fluid used as shown in **figure I.8.**

In addition, the PV/T complexes can be determined by the presence of the absorbent collector beneath the flat plate. The complete design of the flat panel PV/T collector should consist of a glass cover (glaze or unglazed), a solar cell, encapsulated materials, and an absorbent collector underneath. The absorber plays an important function in a PV/T system. It cools the photovoltaic cell or module, and at the same time collects the thermal energy produced in the form of hot water or hot air. During the occurrence of this process, the efficiency of the cell or PV module increases.

I.11.1 Hybrid PV/T air solar collectors

Air PVTs are simple, less expensive, and the most widely used systems according to Michael et al., 2015 **[131]**. On the other hand, the air is passed through the bottom of the back surface of the PV, so that the recovered heat is used for heating or drying applications. A general review of studies on PV/T solar air collectors has been reviewed. Where different types of PV/T air collectors were designed and evaluated experimentally and theoretically. These collectors are classified according to the airflow pattern, i.e. below the absorber, whether the air flows over the absorber, on both sides of the absorber, in a single and double path. The performance of PV/T air collectors was evaluated through economic and environmental impact analyzes. Enviro-Economic and Exergy-Economic Analytics. The environmental - economic - energy - analyzes of these air collectors were studied and were reported during the years from 2010 to 2020 in **Table I. 3 [132-142]**.

Table I.3 : Some studies availed on hybrid PV/T system air collectors in 2010-2020

Authors and year	Contents	references
Sarhaddi et al.,(2010)	Energy–exergy analysis of theoretical and experimental study	[132]
Agrawal and Tiwari ,(2011)	Energy–exergy analysis of theoretical study	[133]
Amori and Al-Najjarv, (2012)	Energy analysis of theoretical study	[134]
Rojaria et al., (2013)	Energy–exergy–environmental analysis of experimental study	[135]
Kim et al., (2014)	Energy analysis of experimental study	[136]
Rajoria et al. ,(2015)	Energy–exergy–enviro-economic analysis of theoretical study	[137]
Tabet, et al. ,(2016)	Energy analysis of theoretical and experimental study	[138]
Zohri et al. ,(2017)	Energy analysis of experimental study	[139]
Nazri et al. ,(2018)	Energy-economic analysis of theoretical study	[140]
Fudholi et al.,(2019)	Exergy analysis of theoretical and experimental study	[141]
Tariq et al.,(2020)	Energetically, exergetically, and economically theoretical study	[142]

There are several types of PV/T air collectors, among these types, single pass and double pass where the air is the working fluid of heat transfer.

a) Single-pass PV/T air collector

There are three types of single-pass air PVT, with one side of the channel behind the PV module, the channel in one side front of the PV module, and with two channels in both side front and behind the module at the same time as cited in ref., **[143-146]**. A new PV/T model has been evaluated in terms of solar electric and thermal efficiency, which was proposed by Takashima et al., 1994 **[147]**. This system capable of keeping the cell at low temperature by placing a PV panel parallel to the solar collector, while keeping a space between the two is shown in f**igure I.9**.

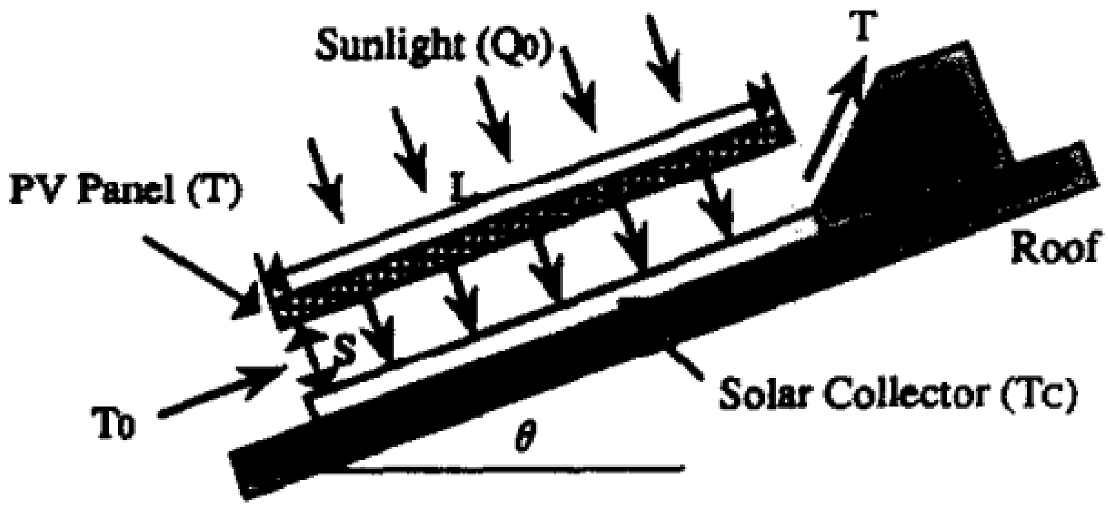

Figure I.9**: Proposed model of a hybrid PV / T system **[147]

They noted that they used natural convection as a way of cooling the cells. The main results show that the effect of temperature on yield is so small that the change in overall yield is small. On the other hand, the cooling effect of natural convection is effective in preventing PV overheating.

Tiwari et al. in 2006 **[148]** evaluated the performance of the BIPV module integrated into the building with the air duct for the climate of India. They demonstrated that the overall efficiency increased dramatically due to the extraction of thermal energy from below the PV module, as shown in f**igure I.10a**.

a)

b)

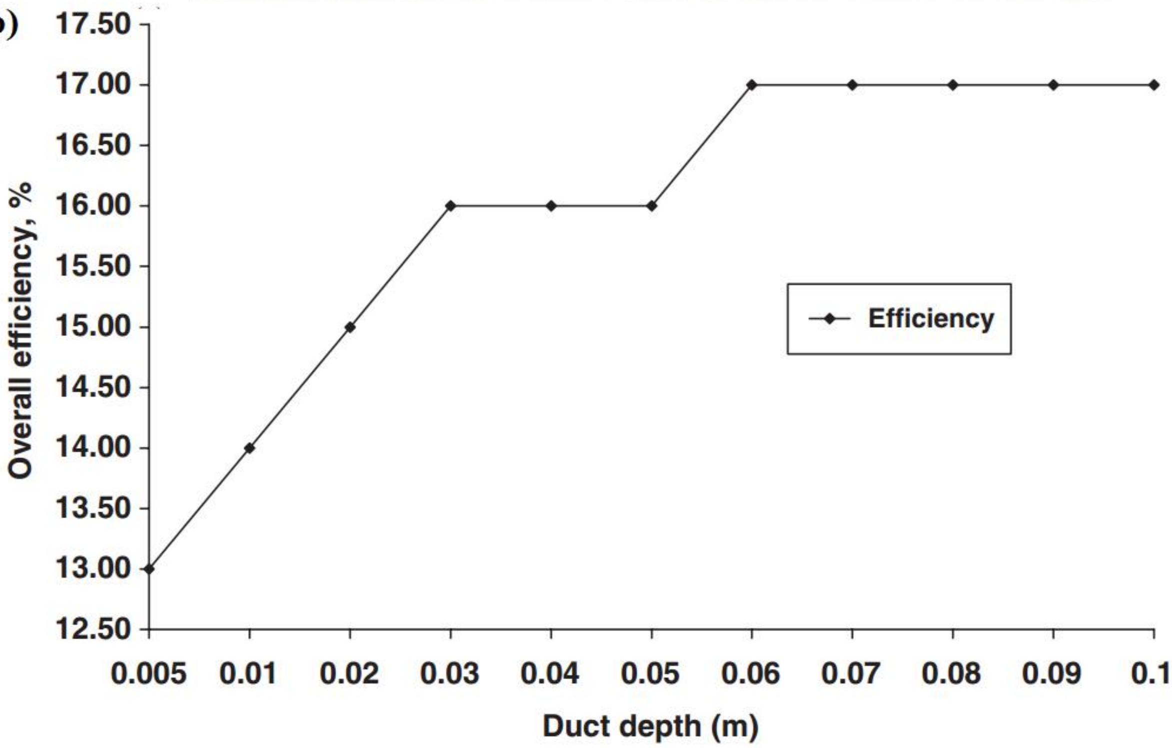

Figure I.10: ***a)*** *photograph of hybrid PV / T air system hybrid,* ***b)*** *duct depth effect on overall efficiency* ***[148].***

Additionally, the effect of duct depth on varying an overall efficiency as shown in f**igure I.10b** indicates that overall efficiency increases with increasing duct depth, as expected. The optimum values for the duct depth beyond 0.06 m were determined.

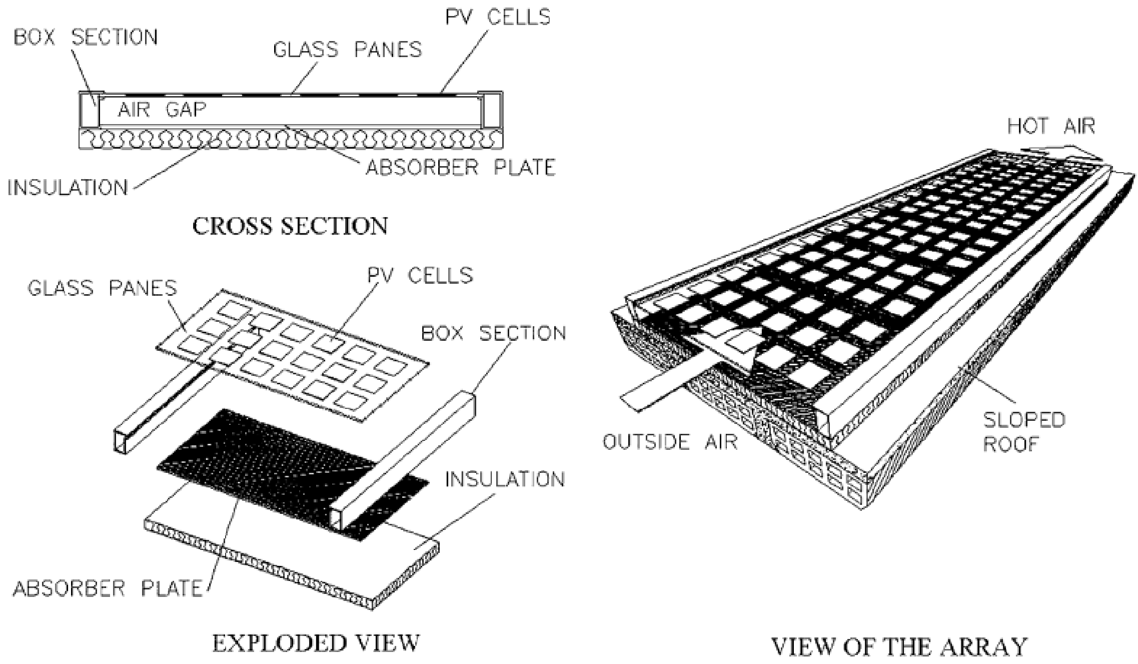

Figure I.11: *The preliminary conception of the design of an air collector PVT hybrid system* ***[149].***

Aste et al., 2008 [149] experimentally and theoretically examined a PV / T hybrid solar air collector, integrated into a roof collector, see f**igure. I.11**. The numerical analysis was carried out thanks to a program ensuring the possibility of updating technological innovation and its potential for application in buildings.

b) Double-pass PV/T air collector

A novel design to analyze the performance of a single-pass and double-pass PV / T system suitable for solar drying has been reviewed by Sopian et al., 1996 **[150]**. They identified important parameters to improve the performance of both types of systems, as they showed that the hybrid PV / T double air passage collector gives efficient performance (see **figure I.12 a**). f**igure I.12 b** shows the effect of mass flow on the yields (photovoltaic, thermal, and photovoltaic combined) of the collector. The increased flow rate improves the heat transfer coefficient, resulting in a lower PV panel temperature, hence increasing the efficiency of the collector.

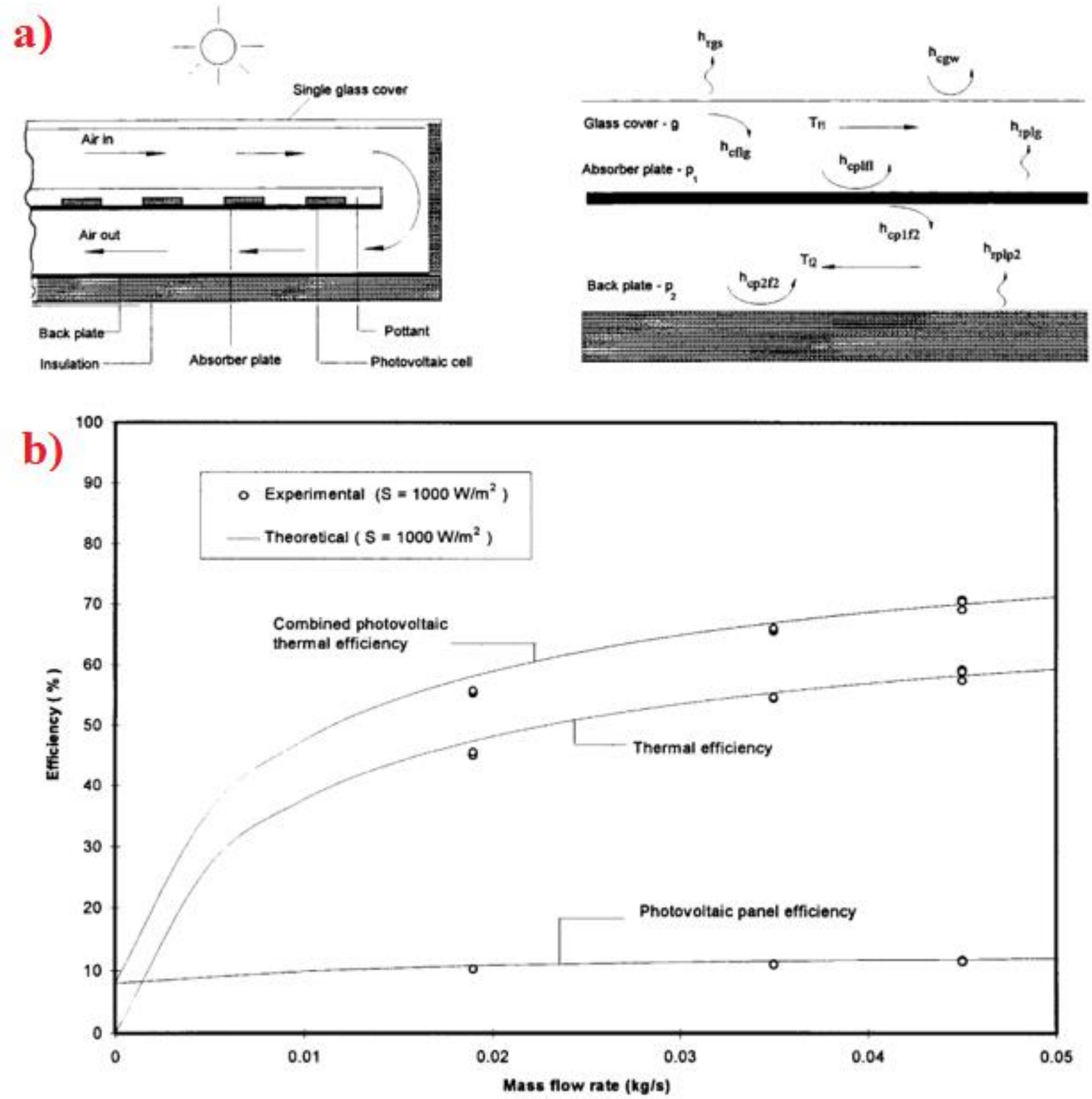

Figure I.12:* *a)* *Schematic of the double-pass photovoltaic solar collector with heat transfer coefficients.* ***b) *Effect of mass flow on the combined photovoltaic, thermal and photovoltaic thermal yields* ***[150].***

Hegazy, 2000 **[151]**, suggested four different models (see f**igure I.13 (a, b**)) aimed at comparing and evaluating the thermal and electrical performance of these four hybrid PVT air collectors. They noted that the performance of an air-powered PV/T hybrid solar collector depends on the maximum outlet air temperature, thermal and electrical yields, and the net electrical energy available after subtracting the energy required operating the system, fan, and other powered devices (see f**igure I.13 a**). The overall efficiency values calculated for the PV/T (I - IV) models are shown in f**igure I.13b** in the range $0.005 < G < 0.04$ (kg / s). In general, the overall efficiency of a particular PV / T model increases with an increase in the air mass rate G, reaches a maximum value, and then decreases with a further increase in G.

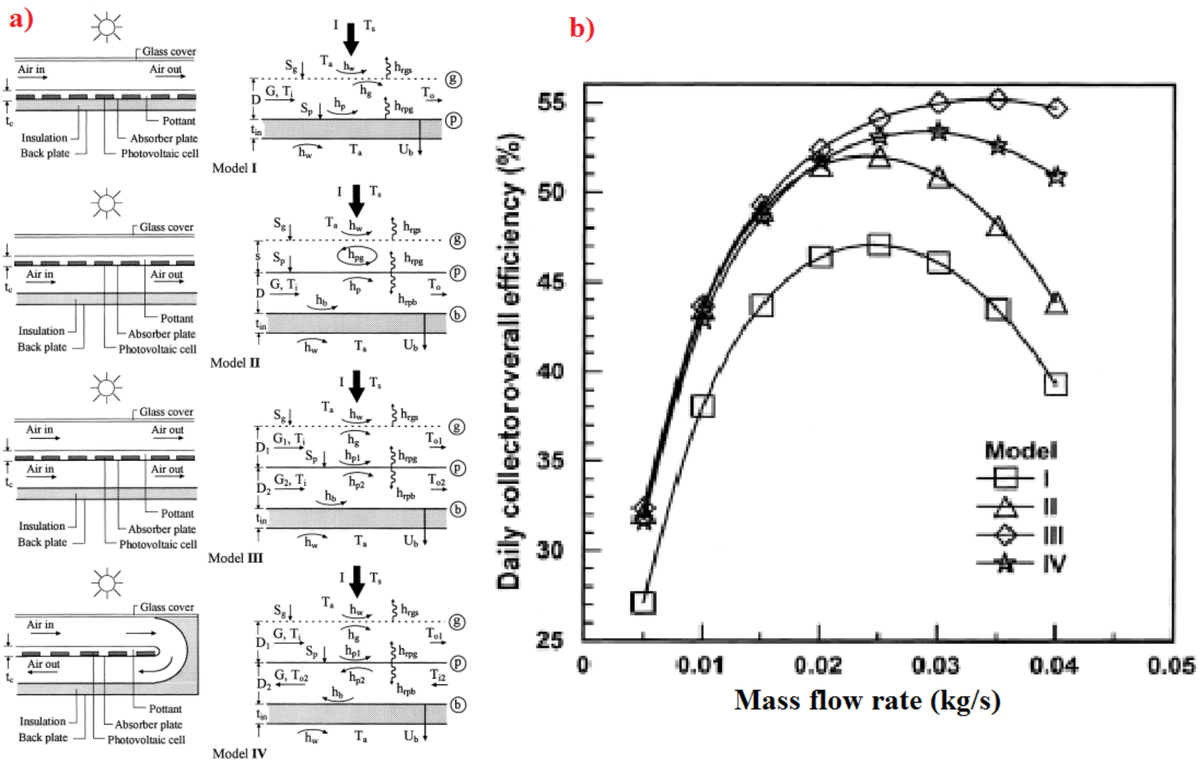

Figure I.13: ***a)*** *Diagram of the different PVT models with coefficients of heat transfer.* ***b)*** *Daily overall efficiency of the sensor for models (I – IV) as a function of the specific mass of the air* ***[151].***

Othman et al., 2005 **[152]**, studied a double pass system fabricated and set up with a parabolic element, a concentrator, and fins, the concentration reflectors were used to increase the power produced by the solar cells (**see figure I.14(a, b)).** They proved that using fins on the back of the manifold improves heat transfer from the manifold. In addition, it has been shown that the total efficiency of the PV/T system has been improved with a double pass collector and fins. Air was made to flow through an upper channel and then under the absorption plate or the lower channel of the manifold as shown **in figure I.14b**. Nevertheless, f**igure I.14b** shows some contribution of electrical efficiency to the total system efficiency. The combined efficiency ranges from 39-70% at a mass flow rate of 0.015-0.16 kg / s and radiation intensity of 500 W / m^2. It was observed that the experimental results were slightly better than those predicted in the mathematical model were. This characteristic may be due to the effect of IR radiation emitted by tungsten halogen lamps during the test.

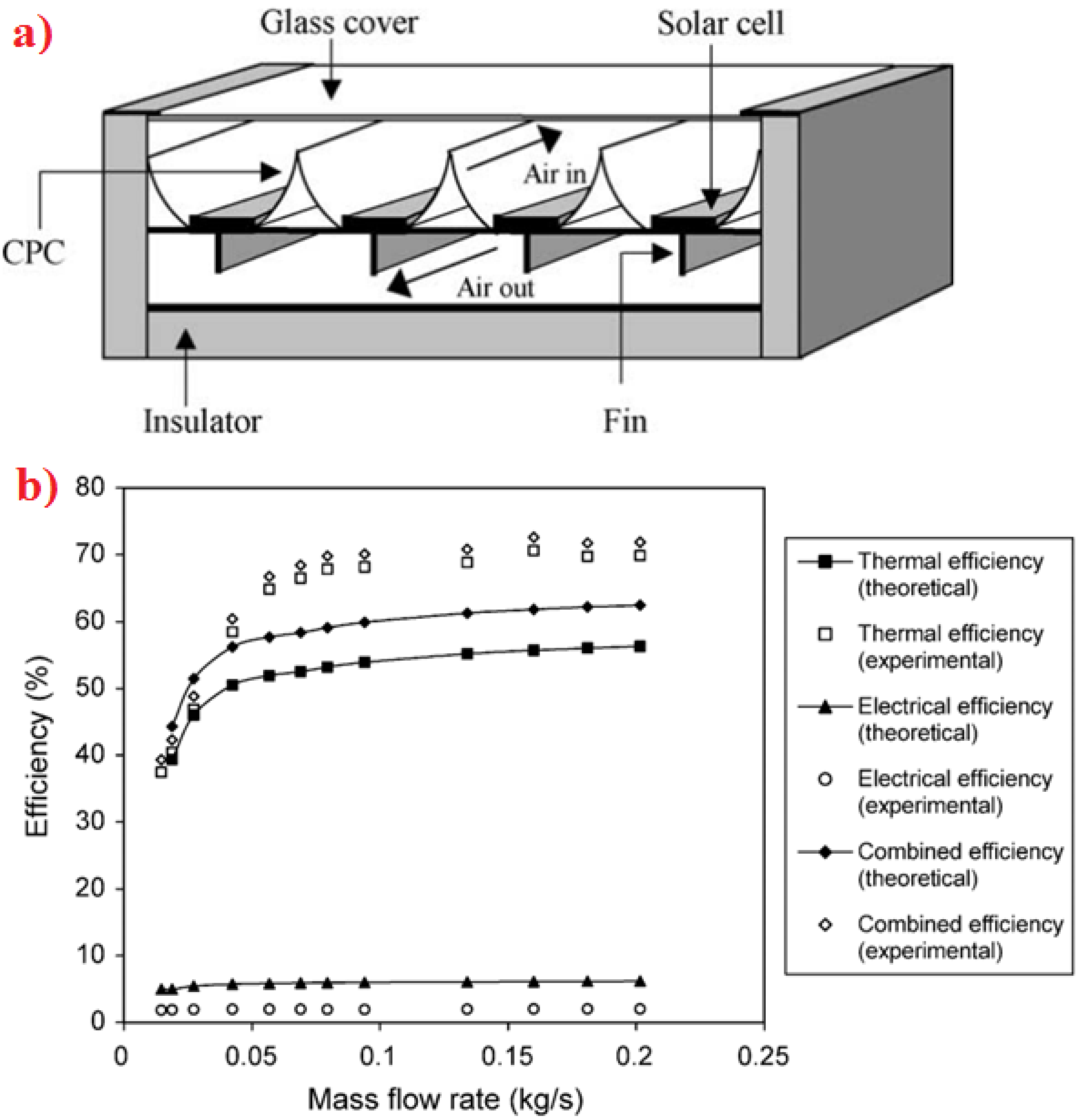

Figure I.14:* *a)* *The schematic model of a double pass photovoltaic solar thermal collector with CPC and fins*, b)* *The effect of mass flow on solar radiation yields of 500 (w / m2), (d1-16.5cm, d2 = 3cm, Ti = Ta = 31-32C °)* ***[152].

A new design of a double pass thermal photovoltaic air collector with a compound parabolic concentrator and fins has been studied as shown in **figure I.15a,** is reported also by Othman et al., **[153]**.

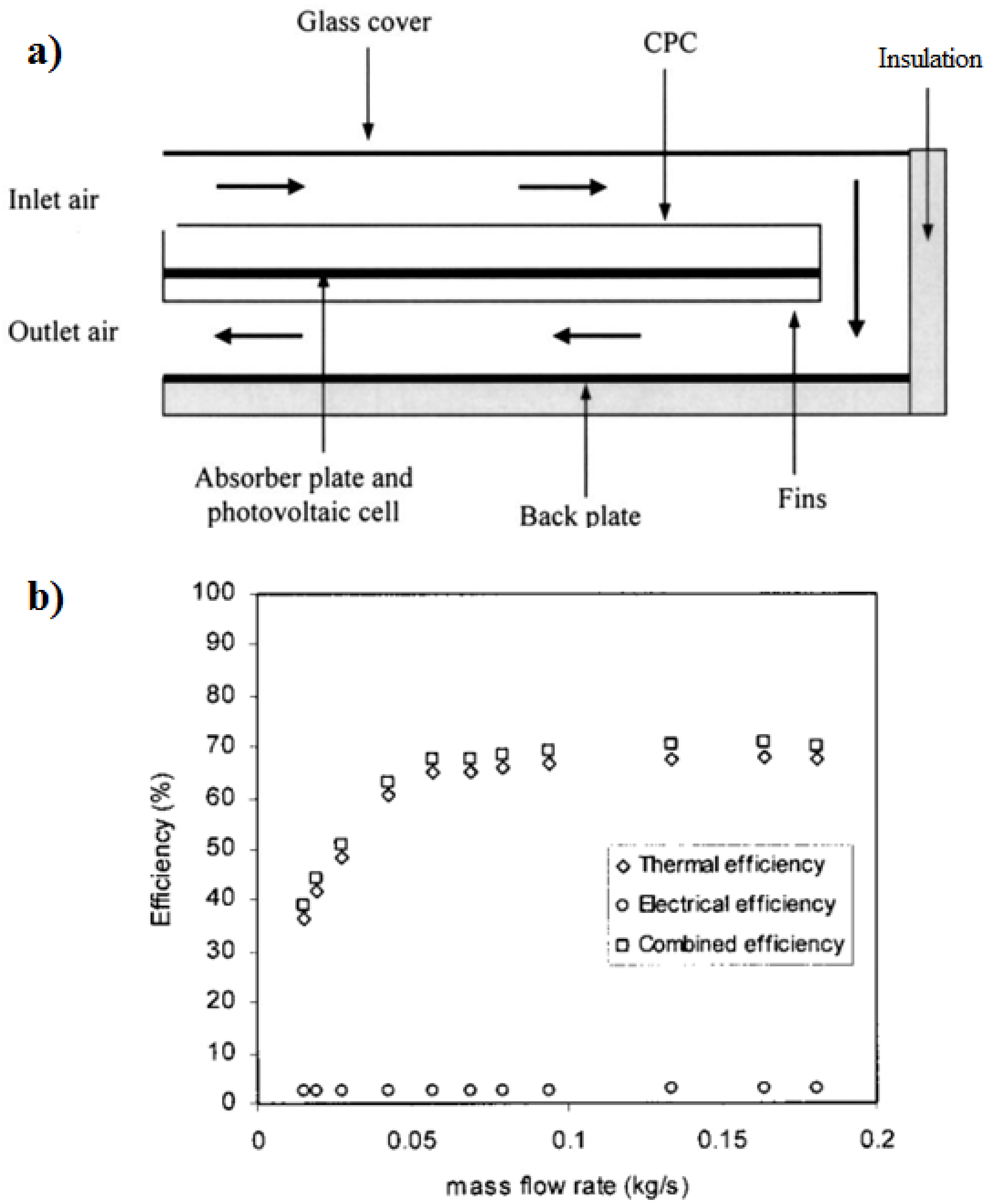

Figure I.15: ***a)*** *Design of a double-pass thermal photovoltaic solar air heater with CPC and fins,* ***b)*** *Effect of mass flow on solar radiation yields of 600 W/m*^{2}*), (d1-16.5cm, d2 = 3cm , Ti = Ta = 31-32C °)* ***[153].***

The air enters through the upper channel formed by the glass cover and the photovoltaic panel and is heated directly by the sun. Then it enters the lower channel formed by the backside and the photovoltaic panel. Compound parabolic concentrators concentrate solar radiation on the photovoltaic cells. Electricity from the collector can be used to drive the fan. A stand-alone solar collector can be produced if appropriate sizing has been carried out. The fins on the back of the photovoltaic panel increase heat transfer to the air and improve the efficiency of the system.

Figure I.15b shows the effect of mass flow on photovoltaic, thermal, and photovoltaic yields combined with solar radiation of 600 W/m^2. The combined efficiency of 70% can be achieved with a higher mass flow. In the figure, it is indicated that a state of saturation has been reached at a mass flow rate of 0.0568 kg/s and Re = 6.269. The efficiency of the system could be improved by using a higher fin density at the rear of the absorbent plate.

I.11.2 PV/T water-based collector

Flat plate PV/T water-based technology has many advantages in overall performance and space-saving than PV modules and solar thermal collectors installed separately.

a) Working fluid is pure water

Hottel-Whillier's well-known model for thermal analysis of flat panels is extended to the analysis of photovoltaic/thermal collectors. It has been combined in such a way that, with a simple modification of the conventional parameters of the original model, all existing relationships and information available in the literature still apply has been reviewed by Florschuetz et al. **[154]**.

Besides, the basic assumptions of the original model, it is necessary to assume that the local electrical efficiency of the solar cell array (absorber) is a decreasing linear function of the local temperature of the absorber over the operating temperature range. Based on the extended model, thermal and electrical performance examples of the combined manifold are shown and discussed based on the collector design parameters as shown in the normal cross-section and with the direction of the flow direction of the manifold fluid in f**igure I.16 a.**

The configuration is shown in the normal cross-section and towards the direction of flow of the collecting fluid as shown in f**igure I.16a**.The solar cells are bonded to the surface of the plate, this cell/plate composite will be called absorber and below this plate, the tubes are installed and are well insulated. The degradation of the electrical performance of glazed collectors operating at higher temperatures compared to bare collectors operating at lower temperatures is also visible in f**igure I.16b**. The resulting magnitude of this degradation depends both on the transmittance of the glazing system and on the difference in operating temperature levels.

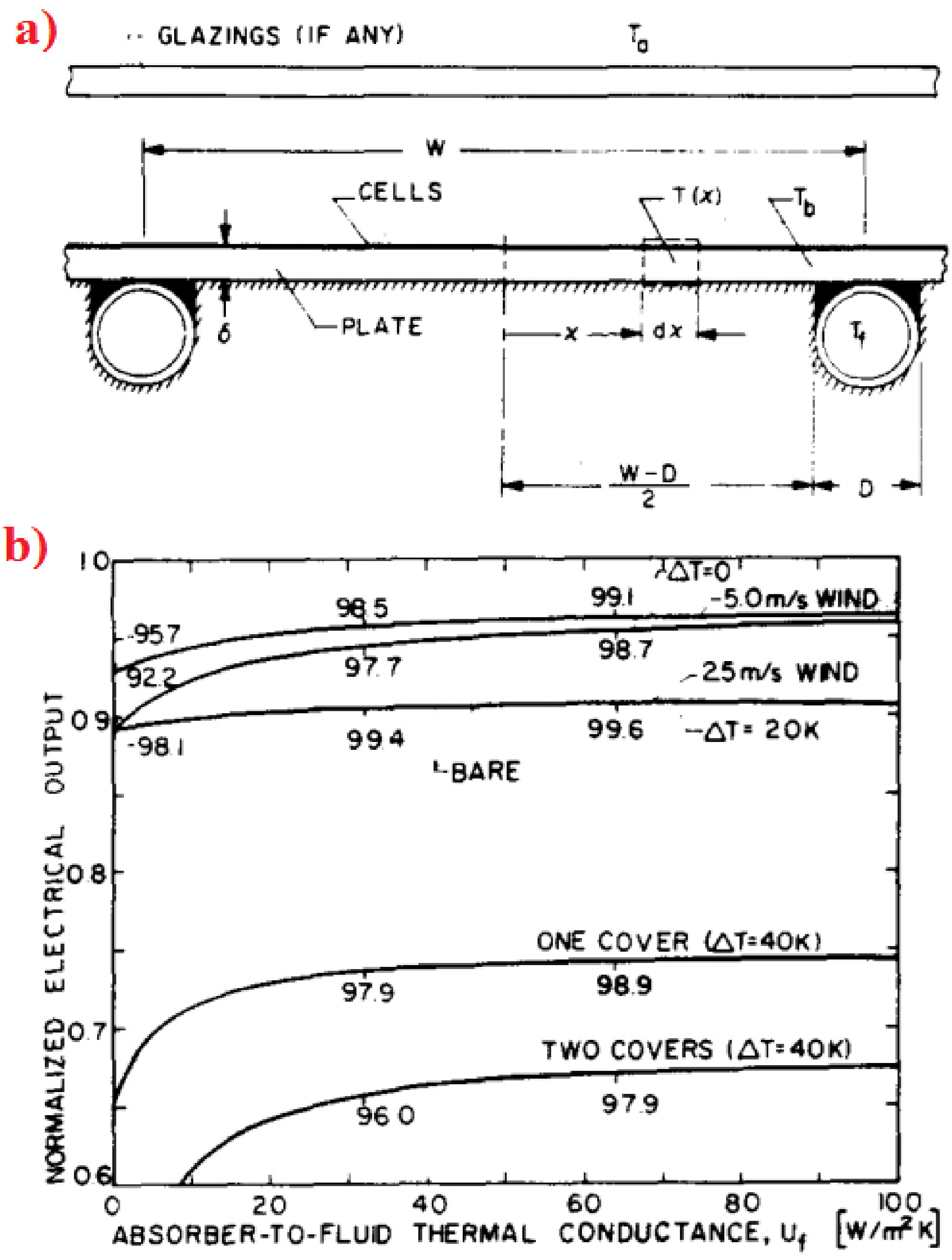

Figure I.16: ***a)*** *Normal cross-section and towards the direction of flow of the collecting fluid,* ***b)*** *Normalized Electrical output power as a function of the overall thermal conductance of the absorber to the collecting fluid for the combined collectors* ***[154].***

Although the performance of hybrid thermal photovoltaic PV/T collectors has been studied both experimentally and numerically for a few years, the thermal models developed in previous studies were mostly steady-state models that only predicted annual yields, evaluated by Chow et al. **[155]**. The operation of a PV / T collector is inherently dynamic. A steady-state model is not suitable for predicting the operating temperatures of the PV module and the coolant during periods of fluctuating illumination or intermittent fluid flow. Based on the volume control finite difference method, an explicit dynamic model was developed for a single glazed flat plate water heater PV / T collector. The proposed model is suitable for dynamic systems, it allows a detailed analysis of the transient energy flowing between different components of the collector and the instantaneous energy yields. **Figure I.17a** shows the front view of a PV water heater collector, and a cross-section through a water tube between two mid planes of the absorbent plate. The front glass cover is separated from the photovoltaic plate by airspace. The PV plate is fixed to the absorbent plate by a thin adhesive layer. This adherent layer is a compound that also includes the EVA (ethylene vinyl acetate) layer and the Tedlar layer. The absorber plate platforms the fins of the heat exchanger water tubes, which are equally spaced across the width of the panel. The water tubes are boned on the absorbent plate.

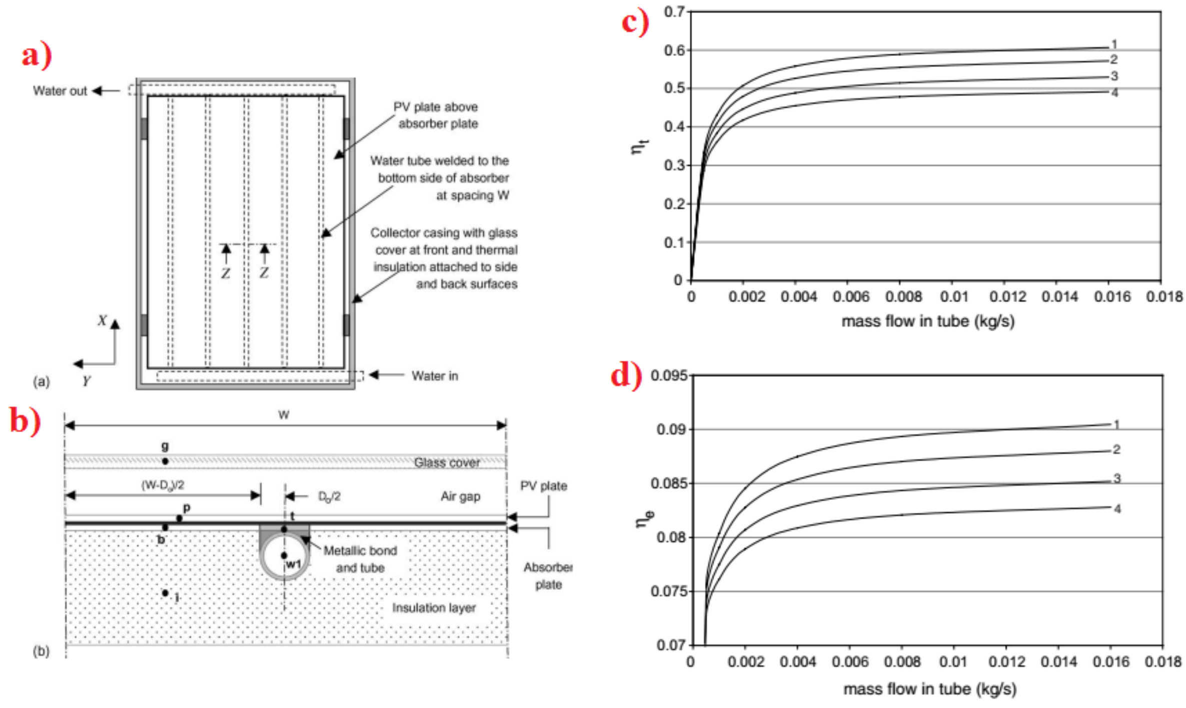

Figure I.17: ***a)*** *Simple glazed PV / T collector, a) front view and,* ***b)*** *Z - Z section (through a water tube). Evolution of thermal and electrical efficiency with a mass flow rate of water at each tube,* ***c)*** *thermal efficiency,* ***d)*** *electrical efficiency* ***[155].***

The arrangement of the two common heads at the upper and lower ends allows balanced water flow in all the tubes and thermally renders the plane of symmetry halfway between two adjacent water tubes. There will be no heat flow through this plane at any time under correct operation. The edges and the lower surface of the panel are inserted with thermal insulation. The thermal behavior of the entire panel is then well-defined by analyzing the heat transfer near a single water tube, as in section Z - Z of **figure I.17b**.

As shown in **figure I.18a,** the first node represents the glass cover. The second node is for the PV plate. The third 'b' concerns the tinplate absorber. For hybrid water collectors, most of the studies focused on the circulation of a pumped fluid through mini channels (sheet and tube) or else, as proposed by Nahar et al. **[156]**; a channel attached directly behind the PV cells. As can be seen in **figures I.18b**, the heat collector without an absorbent plate gives slightly better thermal performance; therefore, the thermal sensor excluding the absorbent plate may offer a better solution for heat removal in the PV / T module.

Therefore, all subsequent evaluations in the present research were carried out without the absorbent plate. This elimination of the absorbent plate will not only reduce the weight and cost but also alleviate some technical problems such as the generation of leakage current in the PV/T system, which is one of the reasons for potential induced degradation (PID).

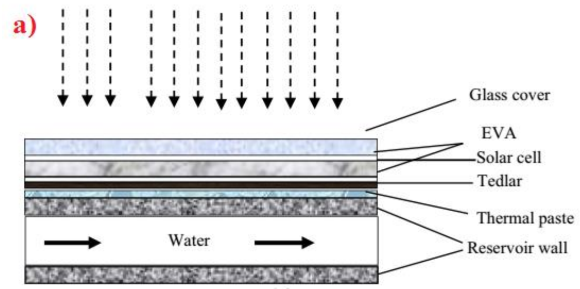

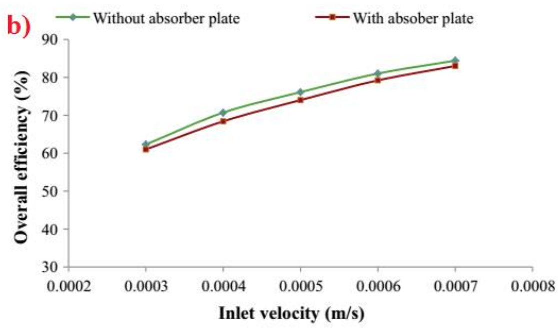

Figure I.18:* *a)* *Sketch of PV/T water-based flat plate solar collector.* *b)* *Comparison of PV/T overall efficiencies with and without absorber plate* *[156].

It observed that the overall efficiencies were best for the case without an absorber plate, which indicated that integrating an absorber plate serves a role negative as shown in **figure I.8b**.

b) Working fluid is water concentrated with nanofluid

The nanoparticle is an assembly of a few hundred to a few thousand atoms of Nano-metric size (1 to 100 nm). Suspensions of nanoparticles in a fluid often called nanofluid, have interesting thermal characteristics compared to traditional base fluids. The thermal conductivity of nanofluid can be significantly higher than that of pure liquids according to the study reviewed by Gladès Bachir in 2010 **[157]**. Also cited the most used nanoparticles to obtain nanofluid are aluminum oxide, Al2O3, aluminum, Al, copper, Cu, copper oxide, CuO, gold, Au, silver, Ag, carbon nanotubes, silicon, Si and titanium dioxide, TiO2. The most commonly used base liquids are water, ethylene glycol, EG, oils, and Toluene. Due to its renewable and non-polluting nature, solar energy is often used in applications such as power generation, thermal heating, and chemical processing. The most economical solar water heaters are of the "flat-plate" type, but these suffer from relatively low efficiency and outlet temperatures. Taylor et al. **[158]** present recent work indicating that optical filters can be constructed from suspensions of specialized nanoparticles. Specifically, this paper describes the theoretical optimization process for the design of Nanofluid-based filters for solar photovoltaic/thermal applications. This particular application is suitable because nanofluid used as solar energy absorbers and as circulating heat transfer fluids. The Nano-fluidic filters described in this work compare favorably with the optical filters of five alternatives to PV cells: InGaP, CdTe, InGaAs, Si, and Ge. This study demonstrates that nanofluid create efficient, compact, and potentially inexpensive optical filters. A general diagram of this type of PV/T system is shown in **figure I.19a**.

The spectral quench efficiency for the selection of the particle options calculated using the above (see **figure I.19b)**.

The extinction efficiency is a non-dimensional parameter that is defined as the cross-section of light extinction divided by the geometric cross-section. It can be seen that the particle options are available in the UV to near-infrared wavelengths (0.25-2 mm).

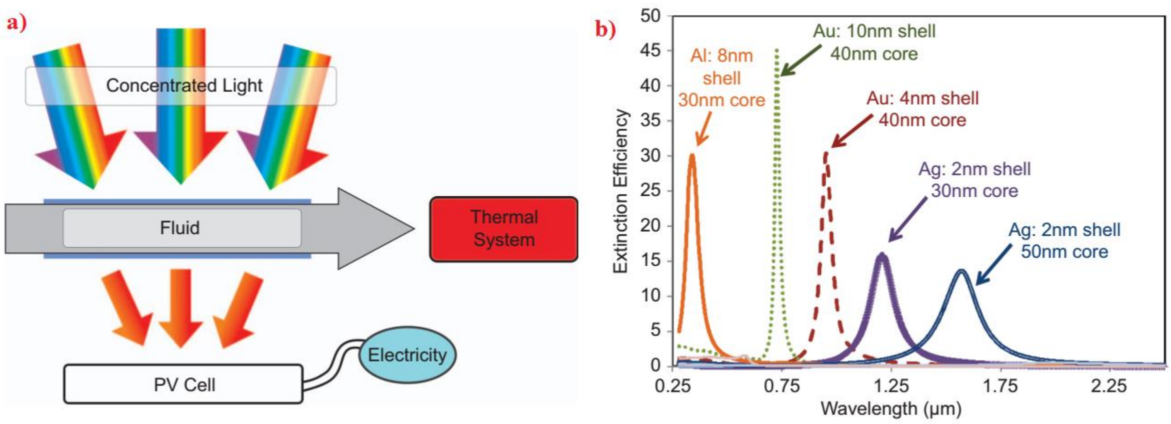

Figure I.19: ***a)*** *The experimental installation of a hybrid PV / T based-nanofluid system solar collector,* ***b)*** *A selection from the wide range of particle options used to creating nanofluid band-pass filters in this study* ***[158].***

In recent years, nanofluid has been proposed as efficient refrigerants and optical filters for PV/T systems, for this reason, Hassani et al., **[159]** theoretically studied the life cycle exergy of three different configurations of Nanofluid-based PV/T hybrid systems and compared their performance to that of a standard PV and PV/T system (see **figure I.20a**).

They found that life cycle exergy analysis revealed that the Nanofluid-based PV / T system performed better compared to standard PV and PV / T systems. At the optimum value of solar concentration C, the Nanofluid-based PV/T configuration with optimized optical and thermal properties produces 1.3 MW h / m^2 of high-quality exergy per year with exergy return time the lowest of 2 years, when they are 0.36, 0.79 MW h / m^2.

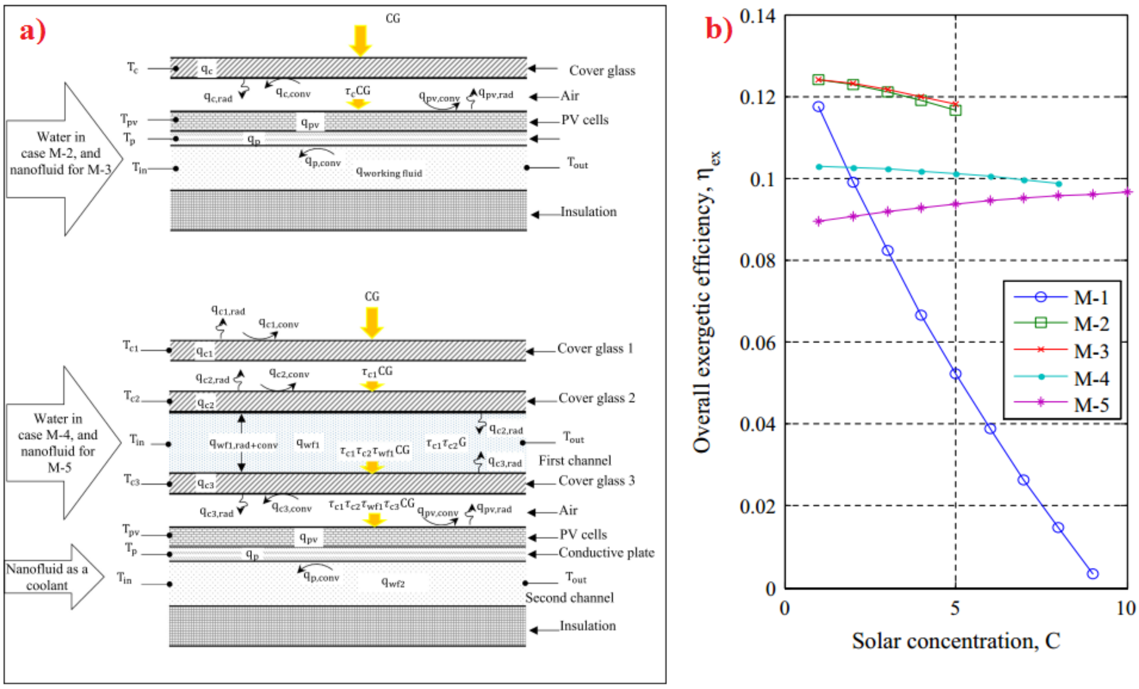

Figure I.20: *Hybrid PV / T system diagram used for the four configurations studied;* ***(a)*** *M-2 and M-3,* ***(b)*** *M-4 and M-5,* ***b)*** *Overall efficiency exergy produced by the corresponding collector versus a solar concentration* ***[159].***

Overall, it has been found that Nanofluid-based PV/T with optimized optical and thermal properties has potential for development in a high concentration solar system, as shown in **figure I.20b**.

I.11.3 PV/T Bi-fluid solar collector

Known as a photovoltaic/thermal (PV/T) solar collector, this type of hybrid solar collector involves the integration between conventional PV cells and a solar thermal component.

Up to now, all researches in this field has focused on either air or water as the working fluid. When both water and air are utilized under the same PV/T solar collector, it is seen as more appealing due to its space-saving design and range of potential applications. Known as a Bi-fluid-type PV/T solar collector, this type of hybrid system is the subject of this research.

Air-cooled or water-cooled systems supplying most of the electricity and hot air or hot water, and recover infrared heat radiated from the cell, so dual fluid hybrid collectors can extract more heat and achieve better overall efficiency.

Table.I.4: Nine different design concepts of PV/T Combi collectors cited in Ref. **[161]**.

PV/T collectors classifications	Design concepts	
(a)	Sheet-and tube :	1. Uncovered sheet-and-tube PV/T collector.
		2.Single/one –cover sheet –and –tube PV/T collector
		3.Double/two-cover sheet-and-tube PV/T collector
(b)	Channel :	4. Channel above PV
		5.channel underneath opaque PV
		6.channel underneath transparent PV
(c)	Free flow	7. Free flow PV/T collector
(d)	Two-absorber	8.Insulated two absorber PV/T collector
		9.Insulated two absorber PV/T collector

Different concepts of combined PV/Thermal collectors are possible. These concepts differ in their approach to obtaining maximum yields, and it is not easy to say whether the yield of a complicated design will be significantly higher than the yield of a simpler one. In order to better understand the expected performance of the different concepts, nine different designs have been proposed **[160]**.

Abdul Hamid et al. **[161]**, reviewed different derived designs of hybrid systems PV/T Combi, as shown in **Table 2**. This study showed that the use of photovoltaic thermal combination technology (PV/T Combi) to cover the limitations and weaknesses of the PV/T water or PV/T air collector systems use.

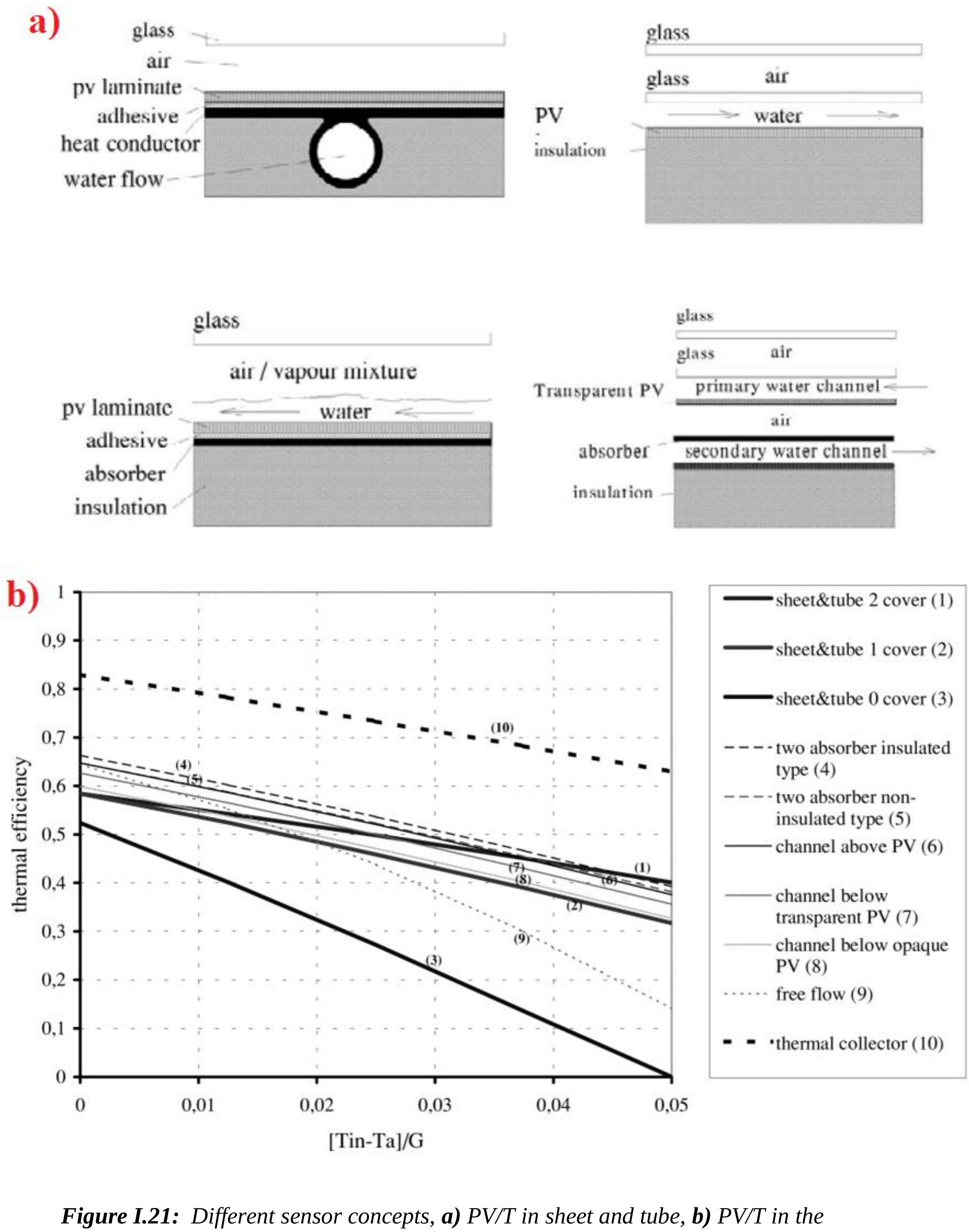

Figure I.21: *Different sensor concepts,* ***a)*** *PV/T in sheet and tube,* ***b)*** *PV/T in the channel,* ***c)*** *PV/T with free flow,* ***d)*** *PV/T with two isolated absorbers, e) Thermal efficiency for the case with power generation different PV/T Bi-fluid* ***[162].***

In 2003, Zondag et al. **[162]**, wanted to obtain a clearer vision on the performance of the different concepts of a hybrid system, a comparative study on four configurations of the hybrid system was launched as mentioned in **figure I.21 (a,b).** The Numerical analysis showed that the overall efficiencies of most configurations are over 50%. They found that the single blanket sheet and tube design seemed the most promising of the concepts examined for hot water production. Two absorber PV/T Sensors have an additional complication in that the condensate on the top glass layer will cause additional reflection of the radiation, which will reduce the efficiency at high temperatures even faster than that shown in **figure I.21b**. One of the advantages of the free-flow concept is its inherent prevention against overheating due to the very large increase in the rate of evaporation towards higher temperatures.

In 2007, Tripanagnostopoulos **[163]** studied several modifications aimed at improving the performance of the hybrid PV/T Bi-fluid system. A new type of PV/T collector with either double heat extraction, water, or air circulation (**see figure I.22a**). This system is simple and suitable for integrating buildings, providing hot water, or air depending on the season and the thermal needs of the building.

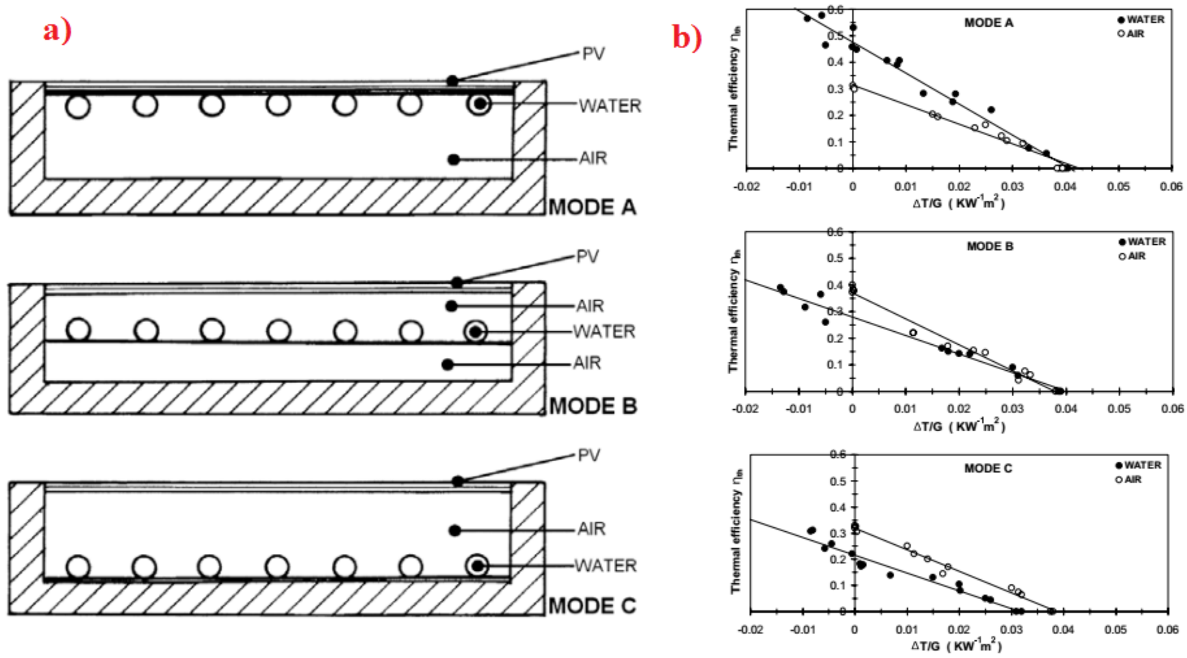

Figure I.22: ***a)*** *Design of three alternative PV/T dual designs used to determine the optimum arrangement of the water and air heat exchangers,* ***b)*** *Thermal efficiencies for the three centers* ***[163].***

Experiments with double-type PV/T models of another arrangement of the heat exchange elements of water and air were carried out. The most efficient design has been further explored, making low-cost modifications to improve the extraction of heat from the air. These modifications include a thin metal foil placed in the middle of the air channel, mounting the fins on the wall opposite the PV back surface of the air channel, and placing the combined foil with small ribs on the wall of the opposite air channel. In the double PV/T collector, the heat of the water and the air exchangers are together in the same device and there are three main layout modes as shown in **figure I.22a**. The results of the PV/T/dual manifold experimental tests concerning the three modes of placement of the water heat exchanger in the air channel are shown. These results relate to the thermal efficiency η_{th} of the PV/T/dual system for the extraction of water and heat from the air, with regard to the DT/G ratio. The thermal efficiency of the PV/water sub-collector is extended to the negative DT/G axis, certain experiments having been carried out for the ambient temperature being higher than the temperature of the water at the inlet of the system (Ta> Ti).

From the results shown in **figure I.22b**, it can be seen that the first PV/T mode/dual design (MODE A) with the water heat exchanger on the PV back surface, has the highest thermal performance of the system. High for water heating, while air heating is considered satisfactory. The second design mode (MODE B) has superior thermal performance for air heating and moderate for water heating. The latest design mode (MODE C) has moderate performance for air heating, but the performance for water heating is poor because the whole is far from the PV back surface.

Assoa et al. **[164]** studied a collector that combines air preheating and hot water production in addition to the conventional electrical function of solar cells. The alternative positioning of the section of this solar thermal collector and the PV section allows water to be produced at higher average temperatures than most existing hybrid collectors. These higher temperatures will allow the coupling of components such as solar coolers during the summer and, of course, a direct domestic hot water (DHW) system without the need for additional auxiliary heating systems. A two-dimensional mathematical model was simplified and developed in a steady state of a Bi-fluid PV/T collector (air and water) which consists of a metal absorber. Then, a parametric study (numerical and experimental) is undertaken to determine the effect of various factors such as the mass flow of water on the thermal performance of the solar collector. Finally, the results of an experimental test bench and the first simulation results obtained on large-scale experiments are compared. The studied photovoltaic solar air collector is shown schematically in **figure I.23a**. It consists of a ribbed sheet steel absorber on which a PV plate is fixed through a thin layer of Tedlar. Each PV plate consists of a 240 mm x1980 mm polycrystalline photovoltaic module. The electrical efficiencies of the solar collector were studied to vary the mass airflow rates for three different collector lengths (see **figure I.23b**).

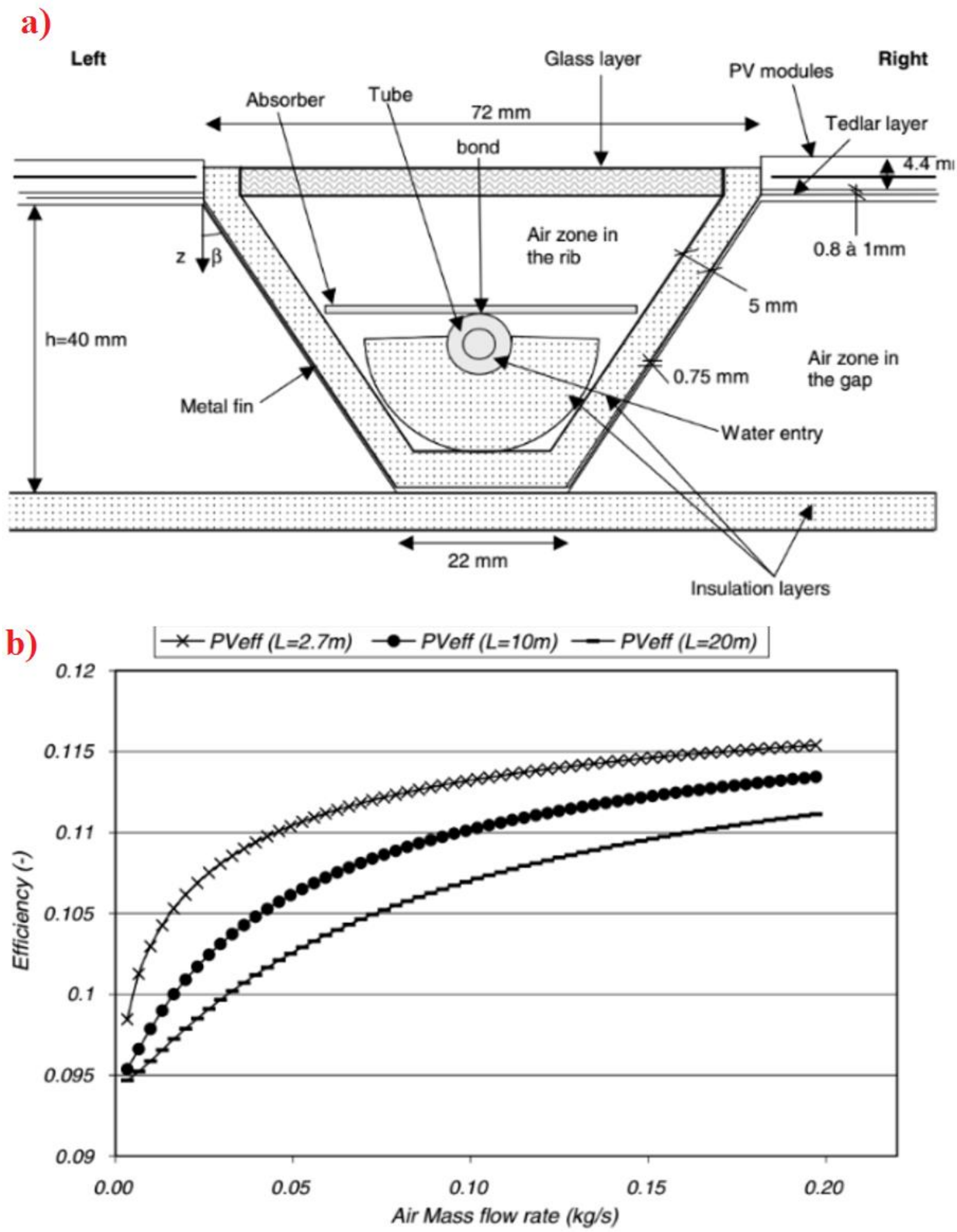

Figure I.23:* *a)* *Cross-section of PV / T hybrid collector,* *b)*Estimated efficiency of PV modules as a function of air mass flow and sensor length, (T_e = T_{sk} = 36.3C °, T_{fin} = 24.7,Twin = 25.5C °) *[164].

A 2D steady-state energy balance method for a Bi-fluid PV/T solar collector, using a serpentine tube configuration was developed and validated, for a range of mass flow rates of water and air as shown in **figure I.24b** evaluated by ref. **[165]**.

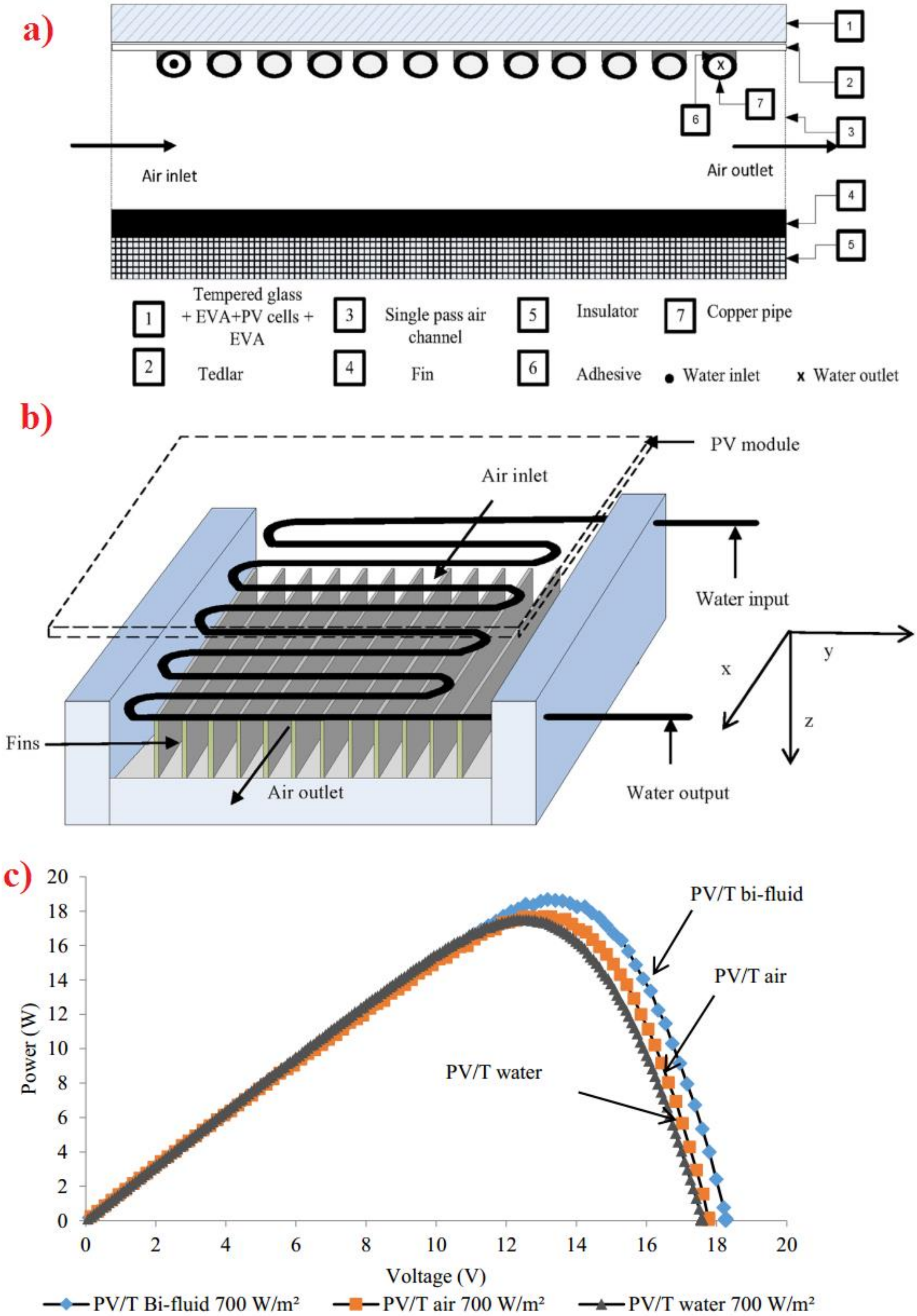

Figure I.24: ***a)*** *Side-view cross-section and* ***(b)*** *front and top-view cross-section of the designed Bi-fluid PV/T solar collector),* ***c)*** *Power against voltage or PV curve for PV/T air, water, and Bi-fluid with a mass flow rate of water and air at 0.0066 kg/s and 0.0262 kg/s respectively* ***[165].***

As illustrated in **figure I.24c**, for the same set of solar radiation, the increase in the peak Power and the open-circuit voltage for the panel during the simultaneous mode of fluid operation is higher than the independent model. The increase in the open-circuit voltage is observed owing to the low mean temperature of PV cells during the simultaneous mode of fluid operation.

From the above-mentioned graph, it can be concluded that using both working fluids simultaneously is one of the effective electricity enhancement techniques for a PV module. The collector is capable of producing three different modes of fluid operation: air mode, water mode, and simultaneous mode. The feasibility of the designed Bi-fluid PV/T solar collector was demonstrated based on experimental results obtained indoors and outdoors [166].

I.11.4 Effect of dust deposition on the PV modules energy performance

In the long term, dust deposition on the front side of the PV module is an important factor that negatively affects their energy performance. Besides, the reduced value of measured irradiance creates an overall performance ratio error from PV power generation, due to the radiation sensors afflicting similar types of soils covering the PV systems **[167]**.

Figure I.25 (A-F) displays real photographs of different dust deposition on PV modules contains different materials such as minerals, bird droppings, engine gas exhaust, and agricultural emissions **[168]**. The PV module energy performance is more degraded by dust deposition, which affects directly the optical, thermal, and electrical characteristics of the PV module [169].

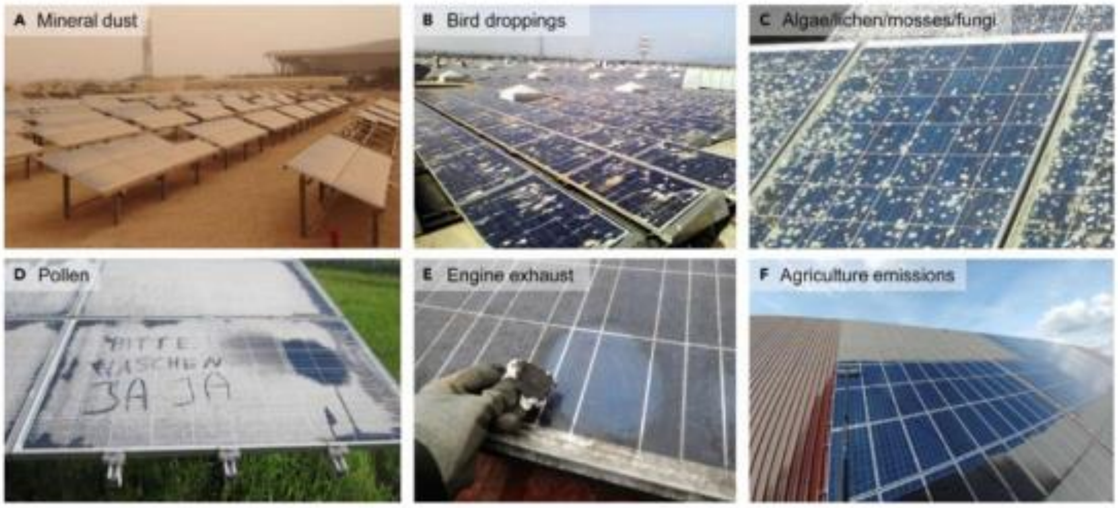

Figure I.25: *Overview of various pollution photographs types by (A) mineral dust in a desert area, (B) bird droppings, (C) algae, lichen, mosses, and (D) pollen in wet and moderate climates, (E) engine exhaust from an industrial area, and (F) agricultural emissions* ***[168].***

A relatively low ash deposition, equal to 0.06 mg / cm^2, can lead to a decrease in energy production of 2.5 %[170].

I.11.5 Factors affecting the dust accumulation

The characteristics of the dust particles vary depending on the location, as the sand grains are scattered in arid desert areas, while in the coastal region, salts and dirt resulting from the rain are prevalent. According to studies that have been conducted, the Middle East, and North Africa, have some of the worst regions of dirt accumulation in the world, where peak losses can be as high as 70% **[171, 172]**. Human activities and natural processes generate dust, which is present in the air as suspended solid particles (PM). These particles deposited on PV surfaces typically range in size from 1 to 50 microns **[173]**.

Wind speed and direction all play an important role in dust deposition on PV module surfaces. For example, a low wind speed allows dust accumulation, on the contrary, High wind speed has the potential to remove dust from the photovoltaic surface **[174]**. The presence of humidity on the PV module front area creates a cohesive force between the particles, which causes the particles to adhere to the PV surface **[175, 176]**. The accumulation of dust is strongly influenced when the adhesive force between the PV surfaces and the dust particles is strong enough. Indeed, this presence of humidity in the atmosphere promotes high adhesive forces.

Light rains usually promote the dust deposition process, while heavy rains with the potential to eliminate dust from the photovoltaic surface. It was found that below 20 mm of rain the PV surface was not properly cleaned in a dry Californian climate **[177, 178]**.

The front surface of the PV module includes glass for conventional modules and various transparent polymer-based acrylics for lightweight structures. Acrylic materials are characterized by a stronger ability to adhere to higher dust than the glass cover **[179]**. An increase in the tilted angle of the PV module affects the stability of dust particles.

The stability of dust particles on the front surfaces of PV modules affected by the increased tilt angle of these systems, up to a critical angle of 23.4° **[176]**. For a fixed exposure period, increasing the tilt angle reduces the density of deposited dust. At a constant tilt angle, the density of dust deposition increases with the number of days of exposure **[180]**. In urban settlements in the regions of South Asia and the Middle East, the average dust reduction of 1.11% to 0.11% when the tilt angle of the PV system is varied from 0° to 90° **[181]**.

I.11.6 Cleaning of PV module systems

To maintain the efficiency of the solar panels, they must be cleaned continuously. However, this process requires hard work and is very costly, especially for large solar arrays. The phenomenon of dust precipitation due to the surrounding environment on the glass PV panels is a major impediment to the maintenance and operating costs of solar power plants **[182]**.

Mazumder et al. **[183]**, reported that the deposition of only 4 g/m^2 of dust (particle diameter between 0.5 and 10 µm) reduces the output power by about 40%. There are several methods for removing dust, sand, and bird residues, such as natural means, mechanical means, self-cleaning Nano-film, and electrostatic methods **[184]**.

The self-cleaning technology can enhance the efficiency of electricity produced and protect the solar cell. Scientific researchers have presented several methods of self-cleaning of the PV module, such as the mechanical method, electrostatic method, and coating method **[185]**.

The performance of the PV modules deteriorates due to the deposition of the artificial dust on the panels when their surface is dry and wet. In addition, most results showed that particularly artificial pollution on the wet front side of the PV modules causes serious deterioration in electrical performance **[186, 187]**.

I.12 Gaps and challenges of solar hybrid PV/T systems collectors

It is important to note that necessary to improve integrated solar PV/T hybrid systems for buildings, house roofs, industrial factories, or in the field of solar water pumping. Several authors studied hybrid PV/T Bi-fluid in buildings, but these systems remain unaesthetic and therefore unattractive to the citizens and other users. For this reason, the improvement of hybrid PV/T systems and the way to design different configurations with a beautiful interface are fundamental needs.

Works of literature show that these systems rest generally on experimental platforms (strip of the test) and only mounted on the ceiling; therefore, without proper design, it is difficult to challenge the world PV/T market. For this reason, it is highly recommended that an appropriate study be conducted on these systems not only to improve the aesthetic but also to optimize different configurations and increase their performance.

I.13 Conclusion

In this chapter, and based on the state of the art of PV/T hybrid systems presented in the literature, there are no theoretical and experimental studies on the combination of cooling and cleaning techniques at the same system.

In order to obtain hot air, hot water, electric power and protect the photovoltaic panels for a long time, it is necessary to make an effective optimization of new hybrid PV/T Bi-fluid systems.

Accordingly, this study will focus on the combination of both cooling and self-cleaning technologies in a single hybrid system.

The continuous self-cleaning of the PV module front side ensures that the build-up of solid particles and bird droppings is removed, especially in arid and semi-arid regions, where sandstorms occur frequently. While the PV module backside is cooled by passive or active air-cooling.

References

[1] A. Şencan, (Ed.). Modeling and optimization of renewable energy systems. BoD–Books on Demand. (2012).

[2] K. Chhnang. Promotion of the Efficient Use of Renewable Energies in Developing Countries. (2009).

[3] D. Connolly, H. Lund, B. V. Mathiesen, M. Leahy. The first step towards a 100% renewable energy-system for Ireland, Applied Energy. 88 (2011) 502-507. https://doi.org/10.1016/j.apenergy.2010.03.006

[4] Z. Dostál, L. Ladányi. Demands on energy storage for renewable power sources, Journal of Energy Storage. 18 (2018) 250-255. https://doi.org/10.1016/j.est.2018.05.003

[5] M. Gross, R. Mautz. Renewable energies, Routledge. (2014).

[6] P. D. Dunn. Renewable energies: sources, conversion and application. (1986).

[7] https://www.iea.org/reports/world-energy-outlook-2020

[8] M. D. Esteban, J. M. Espada, J. M. Ortega, J. S. López-Gutiérrez, V. Negro. What about Marine Renewable Energies in Spain?, Journal of Marine Science and Engineering. 7 (2019) 249. https://doi.org/10.3390/jmse7080249

[9] M. Mediavilla, C. De Castro, I. Capellán, L. J. Miguel, I. Arto, F. Frechoso. The transition towards renewable energies: Physical limits and temporal conditions, Energy Policy. 52 (2013) 297-311. https://doi.org/10.1016/j.enpol.2012.09.033

[10] M. Pehnt. Dynamic life cycle assessment (LCA) of renewable energy technologies, Renewable energy. 31 (2006) 55-71. https://doi.org/10.1016/j.renene.2005.03.002

[11] L. Abdelhamid, L. Bahmed, A. Benoudjit. Impact of renewable energies–environmental and economic aspects. Management of Environmental Quality. 23 (2012) 6-22. https://doi.org/10.1108/14777831211191566

[12] H. M. Wee, W. H. Yang, C. W. Chou, M. V. Padilan. Renewable energy supply chains, performance, application barriers, and strategies for further development, Renewable and Sustainable Energy Reviews. 16 (2012) 5451-5465. https://doi.org/10.1016/j.rser.2012.06.006

[13] Z. Abdmouleh, A. Gastli, L. Ben-Brahim. Survey about public perception regarding smart grid, energy efficiency & renewable energies applications in Qatar. Renewable and Sustainable Energy Reviews. 82 (2018) 168-175. https://doi.org/10.1016/j.rser.2017.09.023

[14] S. O. Ganiyu, C. A. Martínez-Huitle. The use of renewable energies driving electrochemical technologies for environmental applications, Current Opinion in Electrochemistry. 22 (2020) 211-220. https://doi.org/10.1016/j.coelec.2020.07.007

[15] C. Dögl, D. Holtbrügge, T. Schuster. Competitive advantage of German renewable energy firms in India and China: An empirical study based on Porter's diamond. International Journal of Emerging Markets. 7 (2012) 191-214. https://doi.org/10.1108/17468801211209956

[16] J. Kartite, M. Cherkaoui. Study of the different structures of hybrid systems in renewable energies: A review, Energy Procedia. 157 (2019) 323-330. https://doi.org/10.1016/j.egypro.2018.11.197

[17] G. Mulder, F. De Ridder, D. Six. Electricity storage for grid-connected household dwellings with PV panels, Solar energy. 84 (2010) 1284-1293. https://doi.org/10.1016/j.solener.2010.04.005

[18] I. Vosseler, E. Ramírez, X. Vallvé, T.T. SL, J. M. Carreras, S.E.B.A. Asociación. PV HYBRID VILLAGE ELECTRIFICATION IN SPAIN: 6 YEARS EXPERIENCE WITH MSG (MULTI-USER SOLAR HYBRID GRIDS), In Paper presented at the 19th European Photovoltaic Solar Energy Conference and Exhibition. 7 (2004) 11.

[19] A. Fragaki, T. Markvart. Stand-alone PV system design: results using a new sizing approach, Renewable Energy. 33 (2008) 162-167. https://doi.org/10.1016/j.renene.2007.01.016

[20] A. Zahedi. Development of an electrical model for a PV/battery system for performance prediction, Renewable energy. 15 (1998) 531-534. https://doi.org/10.1016/S0960-1481(98)00219-5

[21] G. Notton, S. Diaf, L. Stoyanov. Hybrid photovoltaic/wind energy systems for remote locations, Energy Procedia. 6 (2011) 666-677. https://doi.org/10.1016/j.egypro.2011.05.076

[22] S. Sinha, S. S. Chandel. Review of recent trends in optimization techniques for solar photovoltaic–wind based hybrid energy systems, Renewable and Sustainable Energy Reviews. 50 (2015) 755-769. https://doi.org/10.1016/j.rser.2015.05.040

[23] J. L. Bobin, E. Huffer, H. Nifenecker. L'énergie de demain: techniques, environnement, économie. EDP Sciences. (2005).

[24] N. Kannan, D. Vakeesan. Solar energy for future world: A review, Renewable and Sustainable Energy Reviews. 62 (2016) 1092-1105. https://doi.org/10.1016/j.rser.2016.05.022

[25] P. H. Chou, S. Kim. Techniques for maximizing efficiency of solar energy harvesting systems, In Proceedings of the fifth conference on mobile computing and ubiquitous networking (ICMU 2010), Seattle, WA, USA. (2010).

[26] L. Mateu, F. Moll. Review of energy harvesting techniques and applications for microelectronics, In VLSI Circuits and Systems II, International Society for Optics and Photonics. 5837 (2005) 359-373.

[27] H. Sharma, A. Haque, Z. A. Jaffery. Modeling and optimisation of a solar energy harvesting system for wireless sensor network nodes. Journal of Sensor and Actuator Networks, 7 (2018) 40. https://doi.org/10.3390/jsan7030040

[28] S. Sojan, R. K. Kulkarni. A Comprehensive Review of energy harvesting techniques and its potential applications. International Journal of Computer Applications, 139 (2016) 14-19.

[29] N. Ashraf, M. Faizan, W. Asif, H. K. Qureshi, A. Iqbal, M. Lestas. Energy management in harvesting enabled sensing nodes: Prediction and control, Journal of Network and Computer Applications. 132 (2019) 104-117. https://doi.org/10.1016/j.jnca.2019.01.015

[30] O. V. Ekechukwu, B. Norton. Review of solar-energy drying systems II: an overview of solar drying technology, Energy conversion and management. 40 (1999) 615-655. https://doi.org/10.1016/S0196-8904(98)00093-4

[31] S. Mekhilef, R. Saidur, A. Safari. A review on solar energy use in industries, Renewable and sustainable energy reviews. 15 (2011), 1777-1790. https://doi.org/10.1016/j.rser.2010.12.018

[32] E. Kabir,P. Kumar, S. Kumar, A. A. Adelodun, K. H. Kim. Solar energy: Potential and future prospects, Renewable and Sustainable Energy Reviews. 82 (2018) 894-900. https://doi.org/10.1016/j.rser.2017.09.094

[33] S. A. Kalogirou. Solar energy engineering: processes and systems, Academic Press. (2018).

[34] N. J. Guilar, T. J. Kleeburg, A. Chen, D. R. Yankelevich, R. Amirtharajah. Integrated solar energy harvesting and storage, IEEE Transactions on Very Large Scale Integration (VLSI) Systems. 17 (2009) 627-637. DOI**:** 10.1109/TVLSI.2008.2006792

[35] Z. Abdin, M. A. Alim, R. Saidur, M. R. Islam, W. Rashmi, S. Mekhilef, A. Wadi. Solar energy harvesting with the application of nanotechnology, Renewable and sustainable energy reviews. 26 (2013) 837-852. https://doi.org/10.1016/j.rser.2013.06.023

[36] A. M. Omer. Focus on low carbon technologies: The positive solution, Renewable and Sustainable Energy Reviews. 12 (2008) 2331-2357. https://doi.org/10.1016/j.rser.2007.04.015

[37] M. M. E. Van Esch, R. H. J. Looman, G. J. de Bruin-Hordijk. The effects of urban and building design parameters on solar access to the urban canyon and the potential for direct passive solar heating strategies, Energy and Buildings. 47 (2012) 189-200. https://doi.org/10.1016/j.enbuild.2011.11.042

[38] L. G. Valladares-Rendón, G. Schmid, S. L. Lo. Review on energy savings by solar control techniques and optimal building orientation for the strategic placement of façade shading systems, Energy and Buildings. 140 (2017) 458-479. https://doi.org/10.1016/j.enbuild.2016.12.073

[39] X. Cao, X. Dai, J. Liu. Building energy-consumption status worldwide and the state-of-the-art technologies for zero-energy buildings during the past decade, Energy and buildings. 128 (2016) 198-213. https://doi.org/10.1016/j.enbuild.2016.06.089

[40] V. Bhatnagar, P. Owende. Energy harvesting for assistive and mobile applications, Energy Science & Engineering. 3 (2015) 153-173.

[41] M. K. Singh, S. Mahapatra, S. K. Atreya. Solar passive features in vernacular architecture of North-East India, Solar Energy. 85 (2011) 2011-2022. https://doi.org/10.1016/j.solener.2011.05.009

[42] A. Buonomano, F. Calise, A. Palombo. (2018). Solar heating and cooling systems by absorption and adsorption chillers driven by stationary and concentrating photovoltaic/thermal solar collectors: Modelling and simulation, Renewable and Sustainable Energy Reviews. 82 (2018) 1874-1908. https://doi.org/10.1016/j.rser.2017.10.059

[43] V. Devabhaktuni, M. Alam, S. S. S. R. Depuru, R. C. Green II, D. Nims, C. Near. Solar energy: Trends and enabling technologies, Renewable and Sustainable Energy Reviews. 19 (2013) 555-564. https://doi.org/10.1016/j.rser.2012.11.024

[44] R. Foster, M. Ghassemi, A. Cota. Solar energy: renewable energy and the environment. CRC press. (2009).

[45] A. Kasaeian, F. Rajaee, W. M. Yan. Osmotic desalination by solar energy: A critical review, Renewable Energy. 134 (2019) 1473-1490. https://doi.org/10.1016/j.renene.2018.09.038

[46] E. Akrami, A. Gholami, M. Ameri, M. Zandi. Integrated an innovative energy system assessment by assisting solar energy for day and night time power generation: Exergetic and Exergo-economic investigation, Energy Conversion and Management. 175 (2018) 21-32. https://doi.org/10.1016/j.enconman.2018.08.075

[47] F. Assilzadeh, S. A. Kalogirou, Y. Ali, K. Sopian. Simulation and optimization of a LiBr solar absorption cooling system with evacuated tube collectors, Renewable energy. 30 (2015), 1143-1159. https://doi.org/10.1016/j.renene.2004.09.017

[48] Y. Tian, C. Y. Zhao. A review of solar collectors and thermal energy storage in solar thermal applications, Applied energy. 104 (2013) 538-553. https://doi.org/10.1016/j.apenergy.2012.11.051

[49] P. Raj, S. Subudhi. A review of studies using nanofluids in flat-plate and direct absorption solar collectors, Renewable and Sustainable Energy Reviews. 84 (2018) 54-74. https://doi.org/10.1016/j.rser.2017.10.012

[50] J. Liu, Z. Ye, L. Zhang, X. Fang, Z. Zhang. A combined numerical and experimental study on graphene/ionic liquid nanofluid based direct absorption solar collector, Solar Energy Materials and Solar Cells. 136 (2015) 177-186. https://doi.org/10.1016/j.solmat.2015.01.013

[51] X. Li, G. Zeng, X. Lei. The stability, optical properties and solar-thermal conversion performance of SiC-MWCNTs hybrid nanofluids for the direct absorption solar collector (DASC) application, Solar Energy Materials and Solar Cells. 206 (2020) 110323. https://doi.org/10.1016/j.solmat.2019.110323

[52] S. A. Kalogirou. Solar thermal collectors and applications, Progress in energy and combustion science. 30 (2004) 231-295. https://doi.org/10.1016/j.pecs.2004.02.001

[53] C.C. Arbogast. Solar energy recovery system, U.S. Patent No. 4,476,853. Washington, DC: U.S. Patent and Trademark Office. (1984).

[54] J. C. McDonald, T. R. Winston, M. S. Rohr. A heterophile system in human renal transplantation. VII. The antigen is an intrinsic component of several human tissues, Transplantation. 26 (1978) 191-193.

[55] H. F. Funk. System for solar energy collection and recovery, U.S. Patent No. 4676068. Washington, DC: U.S. Patent and Trademark Office. (1987).

[56] A. Herez, M. Ramadan, B. Abdulhay, M. Khaled. Short review on solar energy systems, In AIP Conference Proceedings, AIP Publishing LLC. 1758 (2016) 030041. https://doi.org/10.1063/1.4959437

[57] A. J. L. Ferreira. Briefing: Recent developments in pavement energy harvest systems, In Proceedings of the Institution of Civil Engineers-Municipal Engineer, Thomas Telford Ltd. 165 (2012) 189-192.

[58] J. M. Lemos, R. Neves-Silva, J. M. Igreja. Adaptive control of solar energy collector systems. Springer. 253 (2014). https://doi.org/10.1007/978-3-319-06853-4

[59] R. Kicsiny, I. Farkas. Improved differential control for solar heating systems, Solar energy. 86 (2012) 3489-3498. https://doi.org/10.1016/j.solener.2012.08.003

[60] J. M. Lemos, R. Neves-Silva, J. M. Igreja. Adaptive control of solar energy collector systems. Springer International Publishing. (2014).

[61] S. Kalogirou. The potential of solar industrial process heat applications, Applied Energy. 76 (2003) 337-361. https://doi.org/10.1016/S0306-2619(02)00176-9

[62] M. S. Buker, S. B. Riffat. Building integrated solar thermal collectors–A review, Renewable and Sustainable Energy Reviews. 51 (2015) 327-346. https://doi.org/10.1016/j.rser.2015.06.009

[63] Y. Tian, C. Y. Zhao. A review of solar collectors and thermal energy storage in solar thermal applications. Applied energy, 104 (2013) 538-553. https://doi.org/10.1016/j.apenergy.2012.11.051

[64] V. Trillat-Berdal, B. Souyri, G. Achard. Coupling of geothermal heat pumps with thermal solar collectors, Applied Thermal Engineering. 27 (2007) 1750-1755. https://doi.org/10.1016/j.apenergy.2012.11.051

[65] D. Rekioua, E. Matagne. Optimization of photovoltaic power systems: modelization, simulation and control, Springer Science & Business Media. (2012).

[66] H. A. Wade. Solar photovoltaic systems technical training manual, Unesco. (2003).

[67] H. Mathieu, H. Fanet. Physique des semiconducteurs et des composants électroniques, Paris: Dunod. 5 (2001).

[68] S. Fonash. Solar cell device physics, Elsevier. (2012).

[69] A. G. Aberle, R. Hezel, Progress in low-temperature surface passivation of silicon solar cells using remote-plasma silicon nitride, Progress in photovoltaics: research and applications. 5 (1997) 29-50.

[70] T. Kirchartz, U. Rau. What makes a good solar cell?, Advanced Energy Materials. 8 (2018) 1703385.

[71] J. L. Gray. The physics of the solar cell, Handbook of photovoltaic science and engineering, 2 (2011) 82-128.

[72] Nelson, J. A. The physics of solar cells. World Scientific Publishing Company. (2003).

[73] C. R. Dickson, B. J. Johnson, D. B. Gerhardt. U.S. Patent No. 4,892,592. Washington, DC: U.S. Patent and Trademark Office. (1990).

[74] M. A. Green. Solar cells: operating principles, technology, and system applications, Englewood Cliffs. (1982).

[75] S. Fonash. Solar cell device physics, Elsevier. (2012).

[76] B. M. Kayes, H. A. Atwater, N. A. Lewis. Comparison of the device physics principles of planar and radial p-n junction nanorod solar cells, Journal of applied physics. 97 (2005) 114302. https://doi.org/10.1063/1.1901835

[77] C. Brabec, U. Scherf, V. Dyakonov. Organic photovoltaics: materials, device physics, and manufacturing technologies, John Wiley & Sons. (2011).

[78] J. A. Nelson. The physics of solar cells, World Scientific Publishing Company. (2003).

[79] D. Tan, A. K. Seng. Handbook for solar photovoltaic (PV) systems, Singapore: Energy Market Authority. (2011).

[80] P. Mohanty, T. Muneer, M. Kolhe. Solar photovoltaic system applications, a guidebook for off-grid electrification. Springer, (Eds.). (2015).

[81] A. K. M. Zakzouk, A. R. M .Alamoud, B. H. Khoshaim. Factors affecting the performance of a photovoltaic power system (PVPS), International journal of solar energy. 5 (1987) 67-81. https://doi.org/10.1080/01425918708914410

[82] M. M. Fouad, L. A. Shihata, E. I. Morgan. An integrated review of factors influencing the perfomance of photovoltaic panels, Renewable and Sustainable Energy Reviews. 80 (2017) 1499-1511. https://doi.org/10.1016/j.rser.2017.05.141

[83] S. A. Said, G. Hassan, H. M. Walwil, N. Al-Aqeeli. The effect of environmental factors and dust accumulation on photovoltaic modules and dust-accumulation mitigation strategies, Renewable and Sustainable Energy Reviews. 82 (2018) 743-760. https://doi.org/10.1016/j.rser.2017.09.042

[84] M. Santhakumari, N. Sagar. A review of the environmental factors degrading the performance of silicon wafer-based photovoltaic modules: Failure detection methods and essential mitigation techniques, Renewable and Sustainable Energy Reviews. 110 (2019) 83-100. https://doi.org/10.1016/j.rser.2019.04.024

[85] P. Jayakumar. Resource assessment handbook, Asia and Pacific Center for Transfer of Technology of the United Nations. (2009).

[86] J. D. Mondol, Y. G. Yohanis, B. Norton. The impact of array inclination and orientation on the performance of a grid-connected photovoltaic system, Renewable Energy. 32 (2007) 118-140. https://doi.org/10.1016/j.renene.2006.05.006

[87] D. L. King, W. E Boyson, J. A. Kratochvil. Analysis of factors influencing the annual energy production of photovoltaic systems. In Conference Record of the Twenty-Ninth IEEE Photovoltaic Specialists Conference, IEEE. (2002) 1356-1361. DOI: 10.1109/PVSC.2002.1190861

[88] A. Tabanjat, M. Becherif, D. Hissel. Reconfiguration solution for shaded PV panels using switching control, Renewable Energy. 82 (2015) 4-13. https://doi.org/10.1016/j.renene.2014.09.041

[89] M. Al-Chaderchi, K. Sopian, T. Salameh, D.Zhang, M. A. Alghoul. Enhancing the Performance of PV Panel Undergoing Shading Effects, International Journal of Power Electronics and Drive Systems. 9 (2018) 1937.

[90] A. Jahanfar, J. Drake, B. Sleep, L. Margolis. Evaluating the shading effect of photovoltaic panels on green roof discharge reduction and plant growth, Journal of Hydrology. 568 (2019) 919-928. https://doi.org/10.1016/j.jhydrol.2018.11.019

[91] F. Bayrak, H. F. Oztop. Effects of static and dynamic shading on thermodynamic and electrical performance for photovoltaic panels, Applied Thermal Engineering. 169 (2020) 114900. https://doi.org/10.1016/j.applthermaleng.2020.114900

[92] D. Wang, T. Qi, Y. Liu, Y. Wang, J. Fan, Y. Wang, H. Du. A method for evaluating both shading and power generation effects of rooftop solar PV panels for different climate zones of China, Solar Energy. 205 (2020) 432-445. https://doi.org/10.1016/j.solener.2020.05.009

[93] N. Gökmen, W.Hu, P. Hou, Z. Chen, D. Sera, S. Spataru. Investigation of wind speed cooling effect on PV panels in windy locations, Renewable Energy. 90 (2016) 283-290. https://doi.org/10.1016/j.renene.2016.01.017

[94] J. K. Kaldellis, M. Kapsali, K. A. Kavadias. Temperature and wind speed impact on the efficiency of PV installations. Experience obtained from outdoor measurements in Greece, Renewable Energy. 66 (2014) 612-624. https://doi.org/10.1016/j.renene.2013.12.041

[95] H. Salimi, A. M. Lavasani, H. Ahmadi-Danesh-Ashtiani, R. Fazaeli. Effect of dust concentration, wind speed, and relative humidity on the performance of photovoltaic panels in Tehran, Energy Sources, Part A: Recovery, Utilization, and Environmental Effects. (2019) 1-11. https://doi.org/10.1080/15567036.2019.1677811

[96] G. Xydis. The wind chill temperature effect on a large-scale PV plant—an exergy approach. Progress in Photovoltaics: Research and Applications. 21 (2013) 1611-1624.

[97] T. Bhattacharya, A. K. Chakraborty, K. Pal. Effects of ambient temperature and wind speed on performance of monocrystalline solar photovoltaic module in Tripura, India, Journal of Solar Energy. 2014 (2014). https://doi.org/10.1155/2014/817078.

[98] E. Kaplani, S. Kaplanis. Thermal modelling and experimental assessment of the dependence of PV module temperature on wind velocity and direction, module orientation and inclination, Solar Energy. 107 (2014) 443-460. https://doi.org/10.1016/j.solener.2014.05.037

[99] T. Huld, A. M. G. Amillo. , A. M. G. Estimating PV module performance over large geographical regions: The role of irradiance, air temperature, wind speed and solar spectrum, Energies. 8 (2015), 5159-5181. https://doi.org/10.3390/en8065159

[100] A. Vasel, F. Iakovidis. The effect of wind direction on the performance of solar PV plants, Energy Conversion and Management. 153 (2017) 455-461. https://doi.org/10.1016/j.enconman.2017.09.077

[101] A. Sohani, M. H. Shahverdian, H. Sayyaadi, D. A. Garcia. Impact of absolute and relative humidity on the performance of mono and poly crystalline silicon photovoltaics; applying artificial neural network, Journal of Cleaner Production. 276 (2020) 123016. https://doi.org/10.1016/j.jclepro.2020.123016

[102] I. Mesquita, L. Andrade, A. Mendes. Effect of relative humidity during the preparation of perovskite solar cells: Performance and stability, Solar Energy. 199 (2020) 474-483. https://doi.org/10.1016/j.solener.2020.02.052

[103] L. J. Piotrowski, M. G. Simões, F. A. Farret. Feasibility of water-cooled photovoltaic panels under the efficiency and durability aspects, Solar Energy. 207 (2020) 103-109. https://doi.org/10.1016/j.solener.2020.06.087

[104] L. Xu, S. Li, J. Jiang, T. Liu, H. Wu, J. Wang, X. Li. The influence of dust deposition on the temperature of soiling photovoltaic glass under lighting and windy conditions, Solar Energy. 199 (2020) 491-496. https://doi.org/10.1016/j.solener.2020.02.036

[105] Y. N. Chanchangi, A. Ghosh, S. Sundaram, T. K. Mallick. Dust and PV performance in Nigeria: A review, Renewable and Sustainable Energy Reviews. 121 (2020) 109704. https://doi.org/10.1016/j.rser.2020.109704

[106] T. M. Alnasser, A. M. Mahdy, K. I. Abass, M. T. Chaichan, H. A. Kazem. Impact of dust ingredient on photovoltaic performance: An experimental study, Solar Energy. 195 (2020) 651-659. https://doi.org/10.1016/j.solener.2019.12.008

[107] H. Wang, X. Meng, J. Chen. Effect of air quality and dust deposition on power generation performance of photovoltaic module on building roof, Building Services Engineering Research and Technology. 41 (2020), 73-85. https://doi.org/10.1177/0143624419868806

[108] A. Shukla, K. Kant, A. Sharma, P. H. Biwole. Cooling methodologies of photovoltaic module for enhancing electrical efficiency: A review, Solar Energy Materials and Solar Cells. 160 (2017) 275-286. https://doi.org/10.1016/j.solmat.2016.10.047

[109] A. Maleki, A. Haghighi, M. E. H. Assad, I. Mahariq, M. A. Nazari. A review on the approaches employed for cooling PV cells, Solar Energy. 209 (2020) 170-185. https://doi.org/10.1016/j.solener.2020.08.083

[110] L. J. Piotrowski, M. G. Simões, F. A. Farret. Feasibility of water-cooled photovoltaic panels under the efficiency and durability aspects, Solar Energy. 207 (2020) 103-109. https://doi.org/10.1016/j.solener.2020.06.087

[111] A. Hassan, A. Wahab, M. A. Qasim, M. M. Janjua, M. A. Ali, H. M. Ali, T. R. Jadoon, E. Ali, A. Raza, N. Javaid. Thermal management and uniform temperature regulation of photovoltaic modules using hybrid phase change materials-nanofluids system, Renewable Energy. 145 (2020) 282-293. https://doi.org/10.1016/j.renene.2019.05.130

[112] F. Bayrak, H. F. Oztop, F. Selimefendigil. Experimental study for the application of different cooling techniques in photovoltaic (PV) panels, Energy Conversion and Management. 212 (2020) 112789. https://doi.org/10.1016/j.enconman.2020.112789

[113] H. Jabari, M. Azzeh. Investigate the Effect of Dust, Air Velocity and Temperature on Photovoltaic Cells Performance. (2016). http://scholar.ppu.edu/handle/123456789/1481

[114] E. P. J. A. Skoplaki, J. A. Palyvos. (2009). Operating temperature of photovoltaic modules: A survey of pertinent correlations, Renewable energy. 34 (2009) 23-29. https://doi.org/10.1016/j.renene.2008.04.009

[115] S. Dubey, J. N. Sarvaiya, B. Seshadri. Temperature dependent photovoltaic (PV) efficiency and its effect on PV production in the world–a review, Energy Procedia. 33 (2013) 311-321. https://doi.org/10.1016/j.egypro.2013.05.072

[116] A. U. Obiwulu, M. A. Chendo, N Erusiafe, S. C. Nwokolo. (2020). Implicit meteorological parameter-based empirical models for estimating back temperature solar modules under varying tilt-angles in Lagos, Nigeria, Renewable Energy. 145 (2020) 442-457. https://doi.org/10.1016/j.renene.2019.05.136

[117] S. Gowid, A. Massoud. A robust experimental-based artificial neural network approach for photovoltaic maximum power point identification considering electrical, thermal and meteorological impact, Alexandria Engineering Journal. 59 (2020) 3699-3707. https://doi.org/10.1016/j.aej.2020.06.024

[118] Y. Tripanagnostopoulos, T. H. Nousia, M. Souliotis, P. Yianoulis. Hybrid photovoltaic/thermal solar systems, Solar energy. 72 (2002) 217-234. https://doi.org/10.1016/S0038-092X(01)00096-2

[119] P. G. Charalambous, G. G. Maidment, S. A. Kalogirou, K. Yiakoumetti. Photovoltaic thermal (PV/T) collectors: A review, Applied thermal engineering. 27 (2007) 275-286. https://doi.org/10.1016/j.applthermaleng.2006.06.007

[120] P. Dupeyrat, C. Ménézo, M. Rommel, H. M. Henning. Efficient single glazed flat plate photovoltaic–thermal hybrid collector for domestic hot water system, Solar Energy. 85 (2011) 1457-1468. https://doi.org/10.1016/j.solener.2011.04.002

[121] N. Amrizal, D. Chemisana, J. I. Rosell. Hybrid photovoltaic–thermal solar collectors dynamic modeling, Applied energy. 101 (2013) 797-807. https://doi.org/10.1016/j.apenergy.2012.08.020

[122] A. Herez, H. El Hage, T. Lemenand, M. Ramadan, M. Khaled. Review on photovoltaic/thermal hybrid solar collectors: Classifications, applications and new systems, Solar Energy. 207 (2020) 1321-1347. https://doi.org/10.1016/j.solener.2020.07.062

[123] A. Zarei, M. Liravi, M. B. Rabiee, M. Ghodrat. A Novel, eco-friendly combined solar cooling and heating system, powered by hybrid Photovoltaic thermal (PVT) collector for domestic application, Energy Conversion and Management. 222 (2020) 113198. https://doi.org/10.1016/j.enconman.2020.113198

[124] M.A. Obalanlege, Y. Mahmoudi, R. Douglas, E. Ebrahimnia-Bajestan, J. Davidson, D. Bailie. Performance assessment of a hybrid photovoltaic-thermal and heat pump system for solar heating and electricity, Renewable Energy. 148 (2020) 558-572. https://doi.org/10.1016/j.renene.2019.10.061

[125] A. L. Abdullah, S. Misha, N. Tamaldin, M. A. M. Rosli, F. A. Sachit. Theoretical study and indoor experimental validation of performance of the new photovoltaic thermal solar collector (PVT) based water system, Case Studies in Thermal Engineering. 18 (2020) 100595. https://doi.org/10.1016/j.csite.2020.100595

[126] A. Herez, H. El Hage, T. Lemenand, M. Ramadan, M. Khaled. Review on photovoltaic/thermal hybrid solar collectors: Classifications, applications and new systems, Solar Energy. 207 (2020) 1321-1347. https://doi.org/10.1016/j.solener.2020.07.062

[127] S. S. Joshi, A. S. Dhoble. Photovoltaic-Thermal systems (PVT): Technology review and future trends, Renewable and Sustainable Energy Reviews. 92 (2018) 848-882. https://doi.org/10.1016/j.rser.2018.04.067

[128] M. Wolf. Performance analyses of combined heating and photovoltaic power systems for residences, Energy Conversion. 16 (1976) 79-90. https://doi.org/10.1016/0013-7480(76)90018-8

[129] L. W. Florschuetz. Extension of the Hottel-Whillier model to the analysis of combined photovoltaic/thermal flat plate collectors, Solar energy. 22 (1979) 361-366. https://doi.org/10.1016/0038-092X(79)90190-7

[130] A. Ibrahim, M. Y. Othman, M. H. Ruslan, S. Mat, K. Sopian. Recent advances in flat plate photovoltaic/thermal (PV/T) solar collectors, Renewable and sustainable energy reviews. 15 (2011) 352-365. https://doi.org/10.1016/j.rser.2010.09.024

[131] J. J. Michael, S. Iniyan, R. Goic. (2015). Flat plate solar photovoltaic–thermal (PV/T) systems: A reference guide, Renewable and sustainable energy reviews. 51 (2015) 62-88. https://doi.org/10.1016/j.rser.2015.06.022

[132] F. Sarhaddi, S. Farahat, H. Ajam, A. Behzadmehr. Exergetic performance assessment of a solar photovoltaic thermal (PV/T) air collector, Energy and Buildings. 42 (2010) 2184-2199. https://doi.org/10.1016/j.enbuild.2010.07.011

[133] S. Agrawal, G. N. Tiwari. Energy and exergy analysis of hybrid micro-channel photovoltaic thermal module, Solar energy. 85 (2011) 356-370. https://doi.org/10.1016/j.solener.2010.11.013

[134] K. E. Amori, H. M. T. Al-Najjar. Analysis of thermal and electrical performance of a hybrid (PV/T) air based solar collector for Iraq, Applied Energy. 98 (2012) 384-395. https://doi.org/10.1016/j.apenergy.2012.03.061

[135] C. S. Rajoria, S. Agrawal, G. N. Tiwari. Exergetic and enviroeconomic analysis of novel hybrid PVT array. Solar energy, 88 (2013) 110-119. https://doi.org/10.1016/j.solener.2012.11.018

[136] J. H. Kim, S .H. Park, J. T. Kim. Experimental performance of a photovoltaic-thermal air collector, Energy Procedia. 48 (2014) 888-894. https://doi.org/10.1016/j.egypro.2014.02.102

[137] C.S. Rajoria, S. Agrawal, G. N. Tiwari, G. S. Chaursia. Exergetic and enviroeconomic analysis of semitransparent PVT array based on optimum airflow configuration and its comparative study, Solar Energy. 122 (2015) 1138-1145. https://doi.org/10.1016/j.solener.2015.10.020

[138] J. C. Mojumder, W. T. Chong, H. C. Ong, K. Y. Leong, A. Al-mamoon. An experimental investigation on performance analysis of air type photovoltaic thermal collector system integrated with cooling fins design, Energy and buildings. 130 (2016) 272-285. https://doi.org/10.1016/j.enbuild.2016.08.040

[139] M. Zohri, A. Fudholi, M. H. Ruslan and K. Sopian. Performance analysis of photovoltaic thermal (PVT) with and without V-groove collector, Journal of Engineering and Applied Sciences. 12 (2017) 6029-6032. DOI: 10.36478/jeasci.2017.6029.6032

[140] N. S. Nazri, A. Fudholi, B. Bakhtyar, C. H. Yen, A. Ibrahim, M. H. Ruslan, S. Mat, K. Sopian. Energy economic analysis of photovoltaic–thermal-thermoelectric (PVT-TE) air collectors, Renewable and Sustainable Energy Review. 92 (2018) 187-197, 2018. https://doi.org/10.1016/j.rser.2018.04.061

[141] A. Fudholi, M. Zohir, N. S. B. Rukman, N. S. Nazri, M. Mustapha, C. H. Yen, M. Mohammad, K. Sopian. Exergy and sustainability index of photovoltaic thermal (PVT) air collector: a theoretical and experimental study, Renewable and Sustainable Energy Reviews. 100 (2019) 44-51. https://doi.org/10.1016/j.rser.2018.10.019

[142] R. Tariq, J. Xamán, A. Bassam, L. J. Ricalde, M. E. Soberanis. (2020). Multidimensional assessment of a photovoltaic air collector integrated phase changing material considering Mexican climatic conditions, Energy. 209 (2020) 118304. https://doi.org/10.1016/j.energy.2020.118304

[143] E. M. A. Alfegi, K. Sopian, M. Y. H. Othman, B. B. Yatim. Transient mathematical model of both side single pass photovoltaic thermal air collector. 2 (2007) 22-26.

[144] M. E. A. Alfegi, K. Sopian, M. Y. H. Othman, B. B. Yatim. Experimental investigation of single pass, double duct photovoltaic thermal (PV/T) air collector with CPC and fins, American Journal of applied sciences. 5 (2008) 866-871.

[145] E. M. A. Alfegi, K. Sopian, M. Y. H. Othman, B. B. Yatim. The effect of flow rates on the performance of finned single pass, double duct photovoltaic thermal solar air heaters, European journal of scientific research. 25 (2009) 339-344.

[146] J. C. Franklin, M. Chandrasekar. Performance enhancement of a single pass solar photovoltaic thermal system using staves in the trailing portion of the air channel, Renewable Energy. 135 (2019) 248-258. https://doi.org/10.1016/j.renene.2018.12.004

[147] T. Takashima, T. Tanaka, T. Doi, J. Kamoshida, T. Tani, T. Horigome. New proposal for photovoltaic-thermal solar energy utilization method, Solar energy. 52 (1994) 241-245. https://doi.org/10.1016/0038-092X(94)90490-1

[148] A. Tiwari, M. S. Sodha, A. Chandra, J. C. Joshi. (2006). Performance evaluation of photovoltaic thermal solar air collector for composite climate of India. Solar energy materials and solar cells, 90(2006), 175-189. https://doi.org/10.1016/j.solmat.2005.03.002

[149] N. Aste, G. Chiesa, F. Verri. Design, development and performance monitoring of a photovoltaic-thermal (PVT) air collector, Renewable energy. 33 (2008) 914-927. https://doi.org/10.1016/j.renene.2007.06.022

[150] K. Sopian, K. S. Yigit, H. T. Liu, S. Kakac, T. N. Veziroglu. Performance analysis of photovoltaic thermal air heaters, Energy Conversion and management. 37 (1997), 1657-1670. https://doi.org/10.1016/j.renene.2007.06.022

[151] A. A. Hegazy. Comparative study of the performances of four photovoltaic/thermal solar air collectors, Energy Conversion and management. 41 (2000) 861-881. https://doi.org/10.1016/S0196-8904(99)00136-3

[152] M. Y. H. Othman, B. Yatim, K. Sopian, M. N. A. Bakar. Performance analysis of a double-pass photovoltaic/thermal (PV/T) solar collector with CPC and fins, Renewable energy. 30 (2005) 2005-2017. https://doi.org/10.1016/j.renene.2004.10.007

[153] M. Y. Othman, B. Yatim, K. Sopian, M. N. A. Bakar. Double-pass photovoltaic-thermal solar air collector with compound parabolic concentrator and fins, Journal of energy engineering. 132 (2006) 116-120.

[154] L. W. Florschuetz. Extension of the Hottel–Whillier model to the analysis of combined photovoltaic/thermal flat plate collectors, Solar Energy. 22 (1979) 361–366. https://doi.org/10.1016/0038-092X(79)90190-7

[155] T. T. Chow. Performance analysis of photovoltaic-thermal collector by explicit dynamic model, Solar Energy. 75 (2003) 143-152. https://doi.org/10.1016/j.solener.2003.07.001

[156] A. Nahar, M. Hasanuzzaman, N. A. Rahim. Numerical and experimental investigation on the performance of a photovoltaic thermal collector with parallel plate flow channel under different operating conditions in Malaysia, Solar energy. 144 (2017) 517-528. https://doi.org/10.1016/j.solener.2017.01.041

[157] G. Bachir. Contribution à l'étude de la convection naturelle dans les nanofluides en configuration de Rayleigh-Bénard (Doctoral dissertation, Université de Toulouse, Université Toulouse III-Paul Sabatier). (2010).

[158] R. A. Taylor, T. Otanicar, G. Rosengarten. Nanofluid-based optical filter optimization for PV/T systems. Light: Science & Applications, 1 (2012) 1-34. https://doi.org/10.1038/lsa.2012.34

[159] S. Hassani, R. Saidur, S. Mekhilef, R. A. Taylor. Environmental and exergy benefit of nanofluid-based hybrid PV/T systems, Energy Conversion and Management. 123 (2016) 431-444. https://doi.org/10.1016/j.enconman.2016.06.061

[160] Y. B. Assoa. Performances de capteurs solaires PV/T hybrides bi-fluides intégrables à l'enveloppe des bâtiments, Doctoral dissertation, Lyon, INSA. (2008).

[161] S. A. Hamid, M. Y. Othman, K. Sopian, S. H. Zaidi. An overview of photovoltaic thermal combination (PV/T Combi) technology, Renewable and Sustainable Energy Reviews. 38 (2014) 212-222. Doi.org/10.1016/j.rser.2014.05.083

[162] H. A. Zondag, D. W. de Vries, W. G. J. van Helden, R. J. C. van Zolingen, A. A. van Steenhoven. The yield of different combined PV-thermal collector designs, Solar energy. 74 (2003) 253-269. https://doi.org/10.1016/S0038-092X(03)00121-X

[163] Y. Tripanagnostopoulos. Aspects and improvements of hybrid photovoltaic/thermal solar energy systems, Solar energy. 81 (2007) 1117-1131. https://doi.org/10.1016/j.solener.2007.04.002

[164] Y. B. Assoa, C. Menezo, G. Fraisse, R. Yezou, J. Brau. Study of a new concept of photovoltaic–thermal hybrid collector, Solar energy. 81 (2007), 1132-1143. https://doi.org/10.1016/j.solener.2007.04.001

[165] H. Jarimi, M. N. A. Bakar, M. Othman, M. H. Din. Bi-fluid photovoltaic/thermal (PV/T) solar collector: Experimental validation of a 2-D theoretical model, Renewable Energy. 85 (2016) 1052-1067. https://doi.org/10.1016/j.renene.2015.07.014

[166] H. Jarimi, M. N. A. Bakar, M. Othman, M. H. Din. Bi-fluid photovoltaic/thermal PV/T solar collector with three modes of operation: Experimental validation of a theoretical

model, In: Sayigh A. (eds) Mediterranean Green Buildings & Renewable Energy. Springer, Cham. (2017) 445-464. https://doi.org/10.1007/978-3-319-30746-6_33

[167] G. P. Smestad, T. A. Germer, H. Alrashidi, E. F. Fernández, S. Dey, H. Brahma, N. Sarmah, A. Ghosh, N. Sellami, I. A. I. Hassan, M. Desouky, A. Kasry, B. Pesela, S. Sundaram, F. Almonacid, K. S. Reddy, T. K. Mallick, L. Micheli. Modelling photovoltaic soiling losses through optical characterization, Scientific reports. 10 (2020) 1-13. https://doi.org/10.1038/s41598-019-56868-z

[168] K. Ilse, L. Micheli, B. W. Figgis, K. Lange, D. Dabler, H. Hanifi, F. Wolfertstetter, V. Naumann, C. Hagendorf, R. Gottschalg, J. Bagdahn. Techno-economic assessment of soiling losses and mitigation strategies for solar power generation, Joule. 3 (2019) 2303-2321. https://doi.org/10.1016/j.joule.2019.08.019

[169] Y. N. Chanchangi, A. Ghosh, S. Sundaram, T. K. Mallick. An analytical indoor experimental study on the effect of soiling on PV, focusing on dust properties and PV surface material, Solar Energy. 203 (2020) 46-68. https://doi.org/10.1016/j.solener.2020.03.089

[170] J. K. Kaldellis, P. Fragos. Ash deposition impact on the energy performance of photovoltaic generators, Journal of cleaner production. 19 (2011) 311-317. https://doi.org/10.1016/j.jclepro.2010.11.008

[171] S. Ghazi, A. Sayigh, K. Ip. Dust effect on flat surfaces–A review paper, Renewable and Sustainable Energy Reviews. 33 (2014) 742-751. https://doi.org/10.1016/j.rser.2014.02.016

[172] Y. N. Chanchangi, A. Ghosh, S. Sundaram, T. K. Mallick. Dust and PV Performance in Nigeria: A review, Renewable and Sustainable Energy Reviews. 121 (2020) 109704. https://doi.org/10.1016/j.rser.2020.109704

[173] B. Weber, A. Quiñones, R. Almanza, M. D. Duran. Performance reduction of PV systems by dust deposition, Energy Procedia. 57 (2014) 99-108. https://doi.org/10.1016/j.egypro.2014.10.013

[174] S. A. Said, G. Hassan, H. M. Walwil, N. Al-Aqeeli. The effect of environmental factors and dust accumulation on photovoltaic modules and dust-accumulation mitigation strategies, Renewable and Sustainable Energy Reviews. 82 (2018) 743-760. https://doi.org/10.1016/j.rser.2017.09.042

[175] R. Albert, I. Albert, D. Hornbaker, P. Schiffer, A. L. Barabási. Maximum angle of stability in wet and dry spherical granular media, Physical Review E - Statistical Physics,

Plasmas, Fluids, and Related Interdisciplinary Topic. 56 (1997) R6271-R6274. https://doi.org/10.1103/PhysRevE.56.R6271

[176] N. S. Beattie, R. S. Moir, C. Chacko, G. Buffoni, S. H. Roberts, N. M. Pearsall. (2012). Understanding the effects of sand and dust accumulation on photovoltaic modules, Renewable Energy. 48 (2012) 448-452. https://doi.org/10.1016/j.renene.2012.06.007

[177] J. Ascencio-Vásquez, I. Kaaya, K. Brecl, K. A. Weiss, M. Topič. (2019). Global climate data processing and mapping of degradation mechanisms and degradation rates of PV modules, Energies. 12 (2019) 47-49. https://doi.org/10.3390/en12244749

[178] J. Ascencio-Vásquez, K. Brecl, M. Topič, M. Methodology of Köppen-Geiger-Photovoltaic climate classification and implications to worldwide mapping of PV system performance, Solar Energy. 191 (2019) 672-685. https://doi.org/10.1016/j.solener.2019.08.072

[179] H. K. Elminir, A. E. Ghitas, R. H. Hamid, F. El-Hussainy, M. M. Beheary, K. M. Abdel-Moneim. Effect of dust on the transparent cover of solar collectors, Energy conversion and management. 47 (2006), 3192-3203. https://doi.org/10.1016/j.enconman.2006.02.014

[180] R. Xu, K. Ni, Y. Hu, J. Si, H. Wen, D. Yu, D. (2017). Analysis of the optimum tilt angle for a soiled PV panel, Energy Conversion and Management. 148 (2017) 100-109. https://doi.org/10.1016/j.enconman.2017.05.058

[181] A. Ullah, A. Amin, T. Haider, M. Saleem, N. Z. Butt. Investigation of soiling effects, dust chemistry and optimum cleaning schedule for PV modules in Lahore, Pakistan, Renew. Energy. 150 (2020) 456–468. https://doi.org/10.1016/j.renene.2019.12.090

[182] M. K. Mazumder, R. Sharma, A. S. Biris, J. Zhang, C. Calle, M. Zahn. Self-cleaning transparent dust shields for protecting solar panels and other devices, Particulate Science and Technology. 25 (2007) 5-20. https://doi.org/10.1080/02726350601146341

[183] G. He, C. Zhou, Z. Li. Review of self-cleaning method for solar cell array, Procedia Engineering. 16 (2011) 640-645. https://doi.org/10.1016/j.proeng.2011.08.1135

[184] A. Syafiq, A. K. Pandey, N. N. Adzman, N. Abd Rahim. Advances in approaches and methods for self-cleaning of solar photovoltaic panels, Solar Energy. 162 (2018) 597-619. https://doi.org/10.1016/j.solener.2017.12.023

[185] A. M. Pavan, A. Mellit, D. De Pieri. The effect of soiling on energy production for large-scale photovoltaic plants, Solar energy. 85 (2011), 1128-1136. https://doi.org/10.1016/j.solener.2011.03.006

[186] C. Santoro, F. B. Abad, A. Serov, M. Kodali, K. J. Howe, F. Soavi, P. Atanassov. Supercapacitive microbial desalination cells: new class of power generating devices for reduction of salinity content, Applied energy. 208 (2017) 25-36. https://doi.org/10.1016/j.apenergy.2017.10.056

[187] S. A. Kalogirou, R. Agathokleous, G. Panayiotou. On-site PV characterization and the effect of soiling on their performance, Energy. 51 (2013) 439-446. https://doi.org/10.1016/j.energy.2012.12.018

Chapter II

Generality on CFD and numerical procedure

II.1 Introduction

Computational science depends on the use of computer systems to be able to solve particularly simple and complex problems and to reach effective solutions in the fastest time and at the lowest cost, and this makes it more widely used and popular in the scientific world. Moreover, due to the massive advancement of computers, the resulting simulations became better and faster. The future of all scientific experiments and engineering analyzes lies in arithmetic and simulation, which in turn complements and facilitates all theoretical sciences for their realization on the ground. This section of the study consists of two parts, the first part is generalizations about CFD simulation, and the second part presents the numerical methods and steps used to solve the governing equations that describe our physical problem.

Computational Fluid Dynamics often referred to as CFD, focuses to find a numerical solution of partial differential equations (PDEs) to any problem. The definition of computational fluid dynamics is cited in the dictionary as “**The prediction of the behavior of fluids and of the effects of fluid motion past objects by numerical methods rather than model experiments**"[1].

II.2 Historic of CFD and applications domain

Computational Fluid Dynamics CFD was originally started to appear from pioneering research by scientists such as Richardson (1910), **[2]**. Over the past two decades, models have been generally and widely used for computational fluid dynamics CFD to predict the parameters that control internal environments **[3]**. The rapid development of computer systems and capabilities has greatly contributed to the support and development of scientific research using CFD **[4]**. Obtaining a reliable model is one of the most difficult modeling tasks, and therefore, once achieved, can be an efficient and flexible method that can be combined with experimental data to provide useful information on airflow patterns inside and outside an energy system **[5]**.

CFD has become an essential numerical tool for many industrialists in the engineering field **[6]**. The application of CFD modeling as an engineering tool can only be justified because of its accuracy and the level of confidence in its results, **[7]**. In addition, can use the CFD for Clinical Practice in Human Nose **[8]**. The CFD science serves to develop and permit a reliable and accessible method for wind environmental studies. This is satisfied by a novel methodology for architectural wind environment study and wind engineering by integrating CFD simulation, multiple parametric tools, and evaluation Criteria **[9, 10]**.

The CFD also witnessed the development of several models in different buildings in order to create or restore ideal plans, such as offices, historic establishments, and stadiums **[11, 12]**. Besides, some applications of Computational Fluid Dynamics in biomedical applications are reviewed in Ref. **[13]**. Shahab et al. Reviewed and implemented CFD-DEM applied to chemical process systems **[14]**. Computational Fluid Dynamics (CFD) has been recognized as a very useful tool for predicting the movement of air in various locations of the indoor environment to ensure proper ventilation.

These numerical techniques have been used for decades and years, as the best research tool **[15, 16]**. The strategies of the sustainable ventilation strategies applied in buildings by using CFD tools are examined by Erdem et al. **[17]**. Bournet et al. **[18]** reviewed numerical and experimental studies of the effect of ventilator design on the distributed climate of greenhouses: A review of experimental and CFD studies. Furthermore, CFD has been applied to deal with problems in the environment and architecture. **Table II.1** summarizes the application area of CFD in the different fields **[19]**.

Table II.1 : CFD applications in various area **[19]**

Industrial applications	Aerospace, Architecture, Automobile ,Biomedical, Combustion
	Chemical and process, Electronics and computers, Nuclear Glass, manufacturing, HVAC(heat, ventilation and cooling), petroleum
	Power, Marine, Mechanical, Metallurgical, Train design, Water, Turbo machinery
Environmental applications	Atmospheric pollution, Climate calculations, Oceanic flows, pollution of natural waters, safety
physiological applications	Cardiovascular flows (heart, major vessels)
	Flow in lungs breathing passages

II.3 Principles and Fundamentals of CFD simulation

The CFD simulations solve the governing equations, which compose of many nonlinear differential equations combined to describe conservation laws, by discretizing them into a set of algebraic equations with high capacity computers. Widely implemented discretization methods during CFD simulation include the Finite Volume Method (FVM) **[20, 21]**, Finite Element Method (FEM), **[22]** and Finite Difference Method (FDM), **[23]**. The procedure that represents the fundamentals of using CFD software to model flow problems numerically is shown in the flowchart schematically in **figure II.1.**

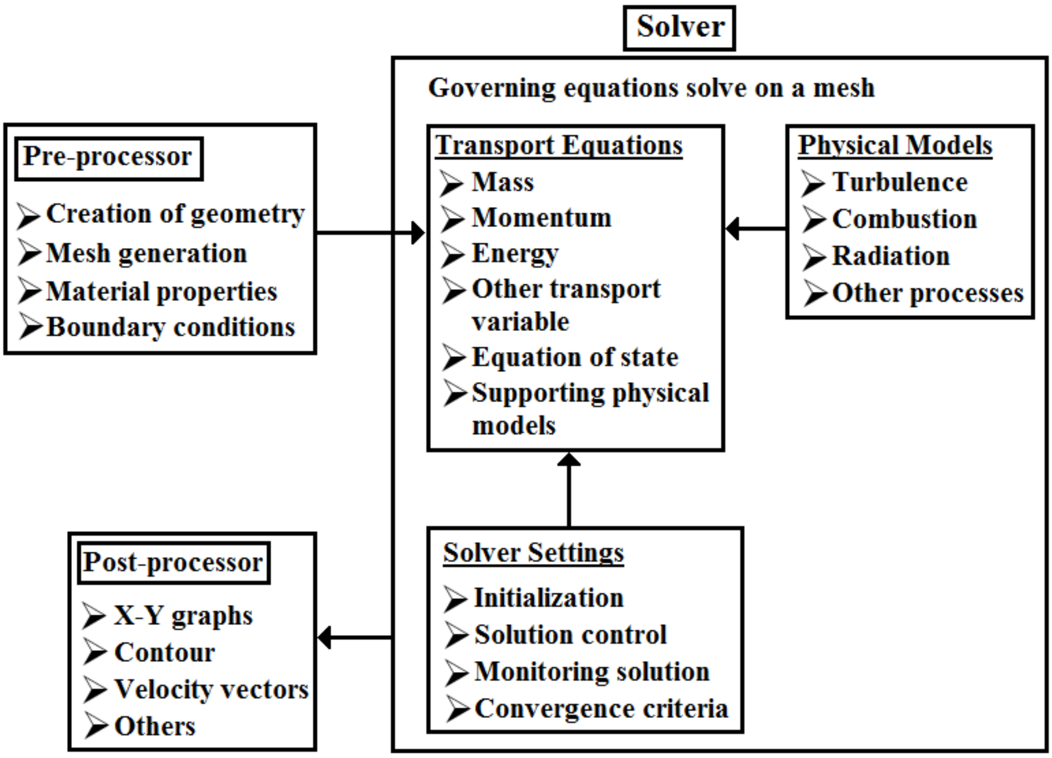

Figure II.1: *A representative scheme of main Fundamentals of CFD simulation and different procedure that used their software* ***[24]***

There are three main steps for modeling a physical problem with CFD, first starts with the preprocessor in which the creation of the geometry and the generation of the mesh and exported forms a geometry with well-defined boundaries. The second step is the choice of the solver or the choice of the numerical methods, models, and the discretization schemes as well as the type of transient or permanent phenomenon or can solve with iterative methods the transport equations in a continuous medium or medium porous. Third, by the post-processor or we can do the processing of the results obtained, and the plot is formed of a graph or visualizations by outlines.

II.3.1 Conservation of governing equations

The Computational fluid dynamic CFD is built on three basic principles of physic **[25]**, mass conservation, and momentum and energy conservation. The governing equations are as the following form:

a) Mass conservation equations

The continuity equation, which is based on the principle of conservation of mass, is shown in the equation. (II.1):

$$\frac{\partial \rho}{\partial t}+\frac{\partial(\rho u)}{\partial x}+\frac{\partial(\rho v)}{\partial y}+\frac{\partial(\rho w)}{\partial z}=0 \qquad \text{(II.1)}$$

Where (u, v, w) are the velocities of the fluid in the (x, y, z) directions, ρ is the fluid density, and t is the time.

✓ ***Momentum conservation***

The Navier-Stokes equations, which based on the principle of conservation of momentum in the directions (x, y, w) are mentioned in equations (II.2), (II.3) and (II.4) respectively:

X-direction

$$\frac{\partial(\rho u)}{\partial t}+\nabla.\left(\rho u\vec{U}\right)=-\frac{\partial p}{\partial x}+\frac{\partial \tau_{xx}}{\partial x}+\frac{\partial \tau_{yx}}{\partial y}+\frac{\partial \tau_{zx}}{\partial z}+\rho f_x \qquad \text{(II.2)}$$

Y-direction

$$\frac{\partial(\rho v)}{\partial t}+\nabla.\left(\rho v\vec{U}\right)=-\frac{\partial p}{\partial y}+\frac{\partial \tau_{xy}}{\partial x}+\frac{\partial \tau_{yy}}{\partial y}+\frac{\partial \tau_{zy}}{\partial z}+\rho f_y \qquad \text{(II.3)}$$

Z-direction

$$\frac{\partial(\rho w)}{\partial t}+\nabla.\left(\rho w\vec{U}\right)=-\frac{\partial p}{\partial z}+\frac{\partial \tau_{xz}}{\partial x}+\frac{\partial \tau_{yz}}{\partial y}+\frac{\partial \tau_{zz}}{\partial z}+\rho f_z \qquad \text{(II.4)}$$

For the symbol, P is the pressure is the velocity vector $U=\left(u_i,v_j,v_k\right)$, $f = f_i + f_j + f_k$ is the body force vector.

Body force vector, and $\tau=\begin{bmatrix}\tau_{xx}\tau_{xy}\tau_{xz}\\ \tau_{yx}\tau_{yy}\tau_{yz}\\ \tau_{zx}\tau_{zx}\tau_{zz}\end{bmatrix}$, the symbol τ is the shear stress tensor.

If the non-Newtonian fluid, the volumetric effect of viscosity is considered negligible. For the case where the fluid is a Newtonian fluid, it can calculate the shear stress with equation (5) as follows:

$$\tau_{ij}=\mu\left(\frac{\partial u_i}{\partial x_j}+\frac{\partial u_j}{\partial x_i}-\delta_{ij}\left(\frac{2}{3}\right)\frac{\partial u_k}{\partial x_k}\right) \qquad \text{(II.5)}$$

While the symbol τ_{ij} is the Kronecker delta; µ is the dynamic viscosity; and the indices j, k and I refer to the linear dimensions x, y and z.

✓ ***Energy conservation***

The equation that is based on the principle of conservation of total energy is expressed below. To obtain the total energy conservation equation, it subtracts the product of the momentum conservation equation by their velocities vector from the energy equation, which can be written in Eq. (II.6) equation as this way:

$$\frac{\partial(\rho e)}{\partial t}+\nabla.\left(\rho e\vec{U}\right)=\rho\dot{q}+\frac{\partial}{\partial x}\left(k\frac{\partial p}{\partial x}\right)+\frac{\partial}{\partial y}\left(k\frac{\partial p}{\partial y}\right)+\frac{\partial}{\partial z}\left(k\frac{\partial p}{\partial z}\right)-$$
$$p\frac{\partial}{\partial y}\left(\frac{\partial u}{\partial x}-\frac{\partial v}{\partial y}-\frac{\partial w}{\partial z}\right)+\lambda\frac{\partial}{\partial y}\left(\frac{\partial u}{\partial x}-\frac{\partial v}{\partial y}-\frac{\partial w}{\partial z}\right)^2+ \qquad \text{(II.6)}$$
$$\mu\left(2\left(\frac{\partial u}{\partial x}\right)^2+2\left(\frac{\partial v}{\partial y}\right)^2+2\left(\frac{\partial w}{\partial z}\right)^2+\left(\frac{\partial u}{\partial x}+\frac{\partial v}{\partial y}\right)^2+\left(\frac{\partial u}{\partial z}+\frac{\partial w}{\partial x}\right)^2+\left(\frac{\partial v}{\partial z}+\frac{\partial w}{\partial y}\right)^2\right)^2$$

Where $\vec{U}$ the velocities vector, e is total energy and $\dot{q}$ is heat source.

II.3.2 Numerical methods

An analytical solution of a set of partial differential equations is only possible with very simple flows. For most practical applications, numerical methods (such as finite differences, finite elements, or the finite size method) should be used to obtain an approximate solution of the discretized equations with imposed initial and boundary conditions.

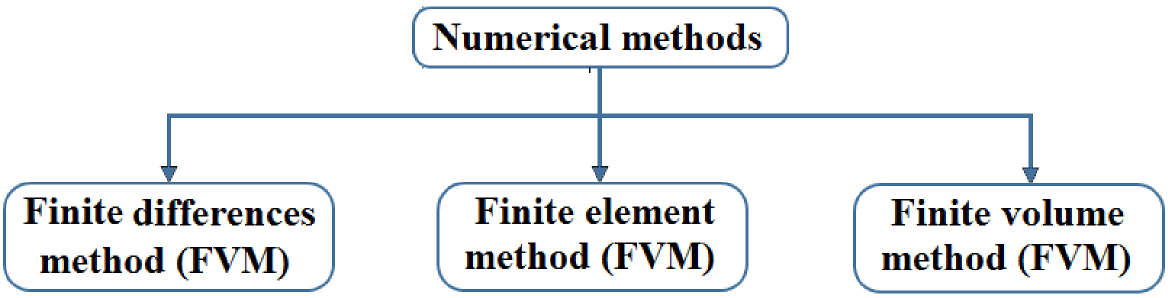

Figure II.2: *Representative different procedure of CFD workflow simulation.*

The discretization process consists of transferring the governing equations into the discrete equivalents **[26, 27]** and transforming the partial differential function PDFs into algebraic equations that can be solved by different numerical methods. There is many numerical methods we can cite, the more used for the thermos-hydrodynamic flow as mentioned in **figure II.2**.

a) Finite element method

The finite element method (FEM) is a technique based on the discretization and the resolution of systems of nonlinear partial differential equations. The principle of the finite element method requires that a certain number of points in space called nodes define the geometry of the system. Each node has a set of degrees of freedom (temperature, speed, pressure, etc.). These nodes are interconnected by elements that define the mathematical interactions of the degrees of freedom. The degrees of freedom are estimated by numerical integration on the element.

All the individual elements of the model are combined to create a set of equations that represent the system to be analyzed. Finally, these equations are solved to reveal useful information about the behavior of the system **[28]**. The real advantage of finite element analysis lies in the ability to solve arbitrarily complex problems for which analytical solutions are not available or which would be excessively long and expensive to solve by hand **[29]**.

The main basic steps in any finite element analysis. The first one trades by the creation of the geometry of the solid model and then with a grid. The choice of the type of element and the definition of the material properties **[30]**. Indeed, FEM finite element methods are versatile in applications to multidimensional complex irregular geometries. Primary applications of FEM began with structural analysis in the late 1950s and were primarily based on principles of variation **[31]**. Early in the development of FEM, applications were made only for simple flow problems, starting with Zienkiewicz and chneug **[32]**, followed by Oden and Wellford **[33]**, and Chung **[34]**.

b) Finite Difference method

This method consists of converting partial derivative equations by dividing the returns of the point values of the function into a finite number of discrete points. This numerical technique approximates the derivatives occurring in equations using the Taylor series development **[35]**.

The finite difference method is based on an idea of such simple ones that, partial differential equations are written in terms of discrete quantities of dependent and independent variables. This makes it possible to transform these non-linear equations into simultaneous algebraic equations with all the unknowns prescribed at discrete mesh points for the whole domain **[36]**.

c) Finite volume method

The finite volume method FVM is a numerical technique for solving the governing equations for fluid flow and mass transport, which calculate the values of variables kept on average over a control volume **[37]**. Obviously, the most ordinary way to achieve the representation of conservation laws in their exact integral form is to define the integral form of the equations and not the differential form, which is the basis of the finite size method. The term cell is used in the Finite Volume Method FVM instead of the term element, used in the Finite Element Method FEM **[38]**.

The finite volume method (FVM) is very popular in computational fluid dynamics (CFD) due to the high flexibility that stems from their discretization **[39, 40]**. The FVM has played an important role in the simulation of fluid flow problems thanks to the work carried out by the CFD group of Imperial College in the early 1970s under the direction of Professor Spalding **[41]**, with such contributors as Patankar **[42]**, and Gosman **[43]**. Due to the adaptability of structured and unstructured meshes and conservative numerical rigor, FVM is used in a wide range of engineering applications for complex engineering design **[44-46]**.

II.3.3 Turbulent models

The majority of fluid flows encountered in nature that are of practical interest in engineering are turbulent, very complex, and unstable based on a number of Reynolds numbers. To know the nature of the flow, laminar or turbulent, we define a dimensionless number, the Reynolds number of a flow, as a function of a characteristic velocity and length. Industry flows, like those found in nature, are predominantly turbulent. Although there is no universal definition of turbulence to date, its main properties are known. Turbulence results in the presence of vortex movements continuously distributed over a wide range of scales. In the space-time domain, turbulence is characterized by its non-linear three-dimensional dynamics, subjected to energy transfer mechanisms between large and small structures.

Turbulence is the state of a fluid whose flow is irregular and is characterized mainly by the presence of movements of all different sizes, which appear when the forces of inertia are large compared to the viscous forces **[47, 48]**. The Navier-Stokes equations do not present an exact analytical solution in the general case. It is, therefore, necessary to use a digital resolution capable of rendering an account of all the scales involved in the case of turbulent flow turbulence.

The complexity of the dynamics of turbulent flows and its strong nonlinearity can lead to consider different simulation approaches, more or less expensive in terms of computational operations, which lead to models of which the degree of complexity varies. Three very distinct approaches can be used in this study. For this, there are several approaches to model turbulent flows whether at large scales, Direct numerical simulation, DNS and; Large eddy simulation, LES, or at small scales, Reynolds average Navier stocks simulation, RANGS.

a) Direct Numerical simulation (DNS)

Indeed, the number of points needed to perform a DNS (Direct Numerical Simulation) is directly related to the Reynolds number of the flow. DNS-type simulations are therefore limited to "academic" calculations of the small-side cubic box type, or too low Reynolds number flows. Even if it is not excluded that one day, the means of calculation will allow such simulations.

In DNS simulations, the Navier-Stokes equations are fully solved: turbulence is calculated for all of its scales and no longer modeled. These simulations are therefore very precise but have a calculation cost that is far too high for it to be possible (at least to date) to simulate an industrial configuration in DNS. The DNS approach: A complete solution of the Navier-Stokes equations involves discretization in space and time. It thus has the advantage of giving access to all instantaneous quantities considered in the flow **[49]**.

b) Large Eddy simulation (LES)

LES simulations solve spatially filtered Navier-Stokes equations; only small structures are modeled, while all others are calculated. In practice, spatial filtering is imposed by the mesh: only the structures larger than the mesh size will be solved. The LES (Large Eddy Simulation) approach: This is a numerical method intermediate between DNS and statistical methods. In fact, it consists of filtering the small scales that are modeled and directly calculating the large scales of the turbulent cascade intended only for the three-dimensional geometries **[50]**.

In addition, models, known as sub-mesh models, are introduced to simulate small-scale turbulence. With this kind of simulation, it is possible to obtain average quantities but also fluctuating quantities, which is of interest to the LES in comparison to RANS simulations. The calculation costs, admittedly higher than for RANS simulations, remain reasonable and allow the simulation of complex geometries on refined meshes.

c) Statistical Modeling of Turbulence (RANS)

RANS simulations solve the averaged Navier-Stokes equations. In other words, the turbulence is here fully modeled. As a result, the results obtained are not always representative of reality, especially if the simulated configurations are complex (in a reactive situation in particular). However, this type of simulation makes it possible to obtain a good order of magnitude of the average flow, in terms of speed, temperature, or pressure. This is why many of the industrial codes currently on the market are based on this principle.

The cost of computation (in CPU time) is indeed relatively low, which makes it possible to simulate very complex configurations on refined meshes. In order to considerably reduce the cost of a simulation, it is possible to envisage modeling all or part of the turbulent structures present in the flow.

The RANS approach (Reynolds Averaged Navier-Stokes) has the principle to solve the Navier-Stokes equations for the average quantities so that the only movement average is calculated. This method consists of breaking down each quantity of the Navier-Stocks equations into an average quantity and the other as a fluctuating one. The averaged equations show correlation terms double fluctuating. These terms come from the non-linearity of the balance equations and are called Reynolds tensions, reflecting the effect of turbulence on the evolution of the mean motion and making the systems of equations open (the number of unknowns more than the number of equations). It is the consequence of taking the average of the instantaneous equations, which introduces a loss of information. Arises then the problem of the closure of the system, that is to say of the link between the double correlations and the mean-field **[51, 52]**.

The objective of the turbulence models for the RANS equations is to compute the Reynolds stresses, which can be done by three main categories of RANS-based turbulence models, Linear eddy viscosity models **[53]**, Nonlinear eddy viscosity models **[54]**, and Reynolds stress model (RSM) **[55]**. In this context, the study is focused on linear eddy viscosity models, which are widely used in CFD software and solar energy applications.

d) Linear eddy viscosity models

The Reynolds stresses, as obtained from a Reynolds averaging of the Navier-Stokes equations, are modeled by a linear constitutive relationship with the mean flow-straining field in these turbulence models. This linear relationship is also known as the Boussinesq hypothesis. There are several subcategories for the linear eddy-viscosity models, depending on the number of (transport) equations solved to compute the eddy viscosity coefficient, such as Algebraic models, One-equation models, and two-equation models.

In this study, attention has been given to listing more pieces of information for models with two equations. Among these models, Two-equation turbulence models are one of the most common types of turbulence models. Models like the **K-ε** model and the k-ω model have become industry-standard models and are commonly used for most types of engineering problems. Two equation turbulence models are also very much still an active area of research and new refined two-equation models are still being developed. By definition, two-equation models include two extra transport equations to represent the turbulent properties of the flow. This allows a two-equation model to account for historical effects like convection and diffusion of turbulent energy.

However, most if not all flows in practical applications are turbulent and therefore the study of turbulent flow is not purely theoretical. In engineering, it is therefore essential to have valid theoretical physical models taking into account turbulence with its various scales and methods of solving their differential equations, which are unfortunately nonlinear and strongly coupled. The greatest difficulty, in solving the stored Navier equations, remains the use of an indispensable turbulence scheme, for the simulation of turbulent flow. It is then a question of finding a model, which can take into account with precision, the physical reality of the flow.

A turbulence model is a numerical procedure for closing the equations of the mean flow so that several varieties of flow can be calculated **[56]**. There are also many derivatives of this type of turbulence models particularly, algebraic turbulence models **[57, 58]**, one-equation turbulence models **[59]**, and two-equation turbulence models **[60, 61]**. Among these turbulence models, we were interested in the most used model in thermo-hydrodynamic work and solar energy is the two-equation models. Two-equation models are models more used in many research works. These models consist of three categories, which are as follows, Realizability issues turbulence models **[62, 63]**, k-omega turbulence models **[64, 65]**, and K-epsilon turbulence models **[66, 67]**.

e) K-ε turbulence model

The k-ε turbulence model proposed by Harlow and Nakayama in 1968 **[68]** is by far the most widely used two-equation eddy-viscosity-using turbulence model. These models have been popular, widely used, and both their capabilities and limitations have been highlighted, which are well documented in the literature. PHOENICS provides the standard High-Reynolds-number form of the k-ε model, as presented by Launder and Spalding (1974), **[69]**, with the inclusion of allowance for buoyancy effects. It is a two-equation model that gives a general description of turbulence by means of two transport equations (PDE) one for turbulent kinetic energy (k) and the other for dissipation (ε). Turbulent dissipation is the rate at which fluctuations in speed dissipate. The coefficients are derived empirically; Valid only for turbulent flows. In the standard k-ε model, the turbulent viscosity is determined from a single turbulence length scale, so the calculated turbulent diffusion is that which only occurs at the specified scale when in reality all scales of motion will contribute to the turbulent diffusion. The k-ε model uses the gradient diffusion assumption to relate Reynolds stresses to mean velocity gradients and turbulent viscosity. The k-ε model is one of the most common turbulence models, although it just does not perform well in cases of large adverse pressure gradients **[70]**. It is a two-equation model, which means, it includes two extra transport equations to represent the turbulent properties of the flow. This allows a two-equation model to account for historical effects like convection and diffusion of turbulent energy.

This model consisting of three models such as the Standard k-ε model, the Realizable k-ε model, and the RNG k-ε model. This model proves to be inefficient for currents involving a reverse pressure gradient, separation, and strong curvature of the pipes. The most troubling weakness is the lack of sensitivity to negative pressure gradients; another disadvantage is the numerical rigidity when the equations are integrated through the viscous under layer, which is processed with damping functions that have stability problems **[71, 72]**.

The two-equation turbulence closures of the Reynolds-Averaged Navier-Stokes equations are applied widely in such engineering applications. This model contains four types of turbulence models which are, k-ε standard model, k-ε Realizable models, k-ε RNG models, and Low Reynolds turbulence models **[73, 74]**.

- **K-ε Standards model**

The k-ε model is a turbulent viscosity group model, based on the Boussinesq gradient hypothesis, which relates the turbulent stresses to the mean-field, as in the case of viscous stresses. The constraints, which appear in the preceding equations. One of the advantages of this method is taking into account the spatial variability of turbulent agitation and its simplicity of implementation. It turns out to be one of the most popular models in practical applications. In a turbulent flow, if we assume that the turbulence responds rather quickly to changes in the mean flow **[75, 76]**. Launder and Spalding (1972), **[77]** first proposed the standard k-ε model.

Regarding the model, the transport equation for kinetic turbulent energy (k), is derived from the exact equation, but the transport for ε was obtained using physical reasoning and is therefore similar to the transport equation derived mathematically from kinetic turbulent energy k, but is not correct. The turbulent kinetic energy, k, and its dissipation rate ε, for this model, are obtained by the following equations.

- ✓ Turbulent kinetic energy, k

$$\frac{\partial(\rho k)}{\partial t}+\frac{\partial}{\partial x_j}(\rho k u_i)=\frac{\partial}{\partial x_j}\left[\left(\mu+\frac{\mu_t}{\sigma x_j}\right)\frac{\partial k}{\partial x_j}\right]+G_k+G_b-\rho\varepsilon-Y_M+S_k \qquad \text{(II.7)}$$

- ✓ Dissipation rate ε

$$\frac{\partial(\rho\varepsilon)}{\partial t}+\frac{\partial}{\partial x_i}(\rho\varepsilon u_i)=\frac{\partial}{\partial x_j}\left[\left(\mu+\frac{\mu_t}{\sigma_\varepsilon}\right)\frac{\partial\varepsilon}{\partial x_j}\right]+C_{1\varepsilon}\frac{\varepsilon}{k}(G_k+c_{3\varepsilon}G_b)-C_{2\varepsilon}\rho\frac{\varepsilon^2}{k}+S_\varepsilon \qquad \text{(II.8)}$$

While G_k is the generation of turbulent kinetic energy that occurs due to average velocity gradients, G_b is the generation of turbulent kinetic energy that occurs due to buoyancy, and Y_M represents the incompressible fluctuating expansion turbulence that contributes to the overall dissipation rate.

Table II.2 : presentations of Turbulent variable and constant appears in equations k-ε standard

Symbol	signification	Formulation or values
G_k	Generation of turbulent kinetic energy due to average velocity gradients	$G_k=\rho\overline{u_i u_j}\frac{\partial u_j}{\partial x_j}$
G_b	generation of turbulent kinetic energy that occurs due to buoyancy	$G_b=\beta g_j\frac{\mu_t}{\mathrm{Pr}_t}\frac{\partial T}{\partial x_i}$
Y_M	incompressible fluctuating expansion turbulence that contributes to the overall dissipation rate	$Y_M=2\rho\varepsilon M_t^2$
S_ε	Source created by turbulent kinetic energy	$S_\varepsilon=\sqrt{2S_{ij}S_{ij}}$
S_k	Source created by turbulent kinetic energy	$S_k=\sqrt{2S_{ij}S_{ij}}$
$C_{1\varepsilon}$	Constant determined experimentally	$C_{1\varepsilon}=1.44$
$C_{2\varepsilon}$	Constant determined experimentally	$C_{2\varepsilon}=1.92$

C_μ	Constant determined experimentally	$C_\mu = 0.09$
σ_k	turbulent Prandtl numbers for the turbulent kinetic energy	$\sigma_k = 1.0$
σ_ε	turbulent Prandtl numbers for the turbulent dissipation rate	$\sigma_\varepsilon = 1.3$
μ_t	Turbulent kinetic energy and its dissipation rate	$\mu_t = \rho C\mu \frac{k^2}{\varepsilon}$

S_ε and S_k are source terms defined by the user. $C_{1\varepsilon}$, $C_{2\varepsilon}$, and Cμ are constants, which have been determined experimentally and are taken to have the following values. These entire symbols were summarized in **table II.2.**

- **Realizable k-ε model**

A recent development is the Realizable k-ε model that Shih and others have developed. This model contains a new transport equation for the turbulent dissipation rate. Additionally, a critical model coefficient is expressed as a function of the average flow and turbulence properties, rather than an assumed constant as in the standard model. This procedure allows the model to satisfy certain mathematical constraints on the normal constraints compatible with the physics of turbulence (feasibility). The concept of variation is also consistent with experimental observations in boundary layers.

The **Realizable** k-ε model is significantly better than the standard k-ε model for many applications and can generally be used to give answers that are at least as precise. Both standard and workable models have been implemented in STAR-CCM + with a two-layer approach, which enables them to be used with a fine mesh that resolves the viscous under layer **[78-81]**. The most recently developed model is achievable by Shih (1995), **[82]** comparatively of the three variants of k-ε and has two main differences from the standard k-ε model. It expresses a new equation for the turbulent viscosity, and the dissipation rate transport equation was derived from the equation for the transport of the mean square vortex fluctuation.

The form of the turbulent viscosity equations is based on the feasibility constraints; the positivity of the normal Reynolds stresses and the Schwarz inequality for the turbulent shear stresses. This is neither satisfied by the standard or by the RNG k-ε models that make the feasible model more accurate than the two models in predicting flows such as separate flows and flows with complex secondary flow characteristics. In terms of modifications improved by Shih (1995), appeared in the transport equations become:

$$\frac{\partial(\rho k)}{\partial t}+\frac{\partial}{\partial x_j}(\rho k u_i)=\frac{\partial}{\partial x_j}\left[\left(\mu+\frac{\mu_t}{\sigma_k}\right)\frac{\partial k}{\partial x_j}\right]+G_k+G_b-\rho\varepsilon-Y_M+S_k \qquad \text{(II.9)}$$

$$\frac{\partial(\rho\varepsilon)}{\partial t}+\frac{\partial}{\partial x_j}(\rho\varepsilon u_i)=\frac{\partial}{\partial x_j}\left[\left(\mu+\frac{\mu_t}{\sigma_\varepsilon}\right)\frac{\partial\varepsilon}{\partial x_j}\right]+\rho C_1 s\varepsilon-\rho C_2\frac{\varepsilon^2}{k+\sqrt{\nu\varepsilon}}+C_{1\varepsilon}\frac{\varepsilon}{k}\rho C_{3\varepsilon}G_b+S_\varepsilon \qquad \text{(II.10)}$$

Table II.3: Presentations of the Turbulent variable and constant for k-ε Realizable turbulent model.

Symbol	signification	Formulation
G_k	Represents the generation of turbulent kinetic energy that arises due to mean velocity gradients.	$G_k=\rho\overline{u_i u_j}\frac{\partial u_j}{\partial x_j}$
G_b	Represents generation of turbulent kinetic energy the arises due to buoyancy	$G_b=\beta g_j\frac{\mu_t}{\Pr_t}\frac{\partial T}{\partial x_i}$
Y_M	represents the fluctuating dilation in compressible turbulence that contributes to the overall dissipation rate	$Y_M=2\rho\varepsilon M_t^2$
S_ε	source terms defined by the user dissipation	$S_\varepsilon=\sqrt{2S_{ij}S_{ij}}$
S_k	source terms defined by the user kinetic energy	$S_k=\sqrt{2S_{ij}S_{ij}}$
$C_{1\varepsilon}$	Constant determined experimentally	$C_{1\varepsilon}=1.44$
$C_{2\varepsilon}=1.9$	Constant determined experimentally	$C_{2\varepsilon}=1.9$
C_μ	Constant determined experimentally	$C_\mu=\frac{1}{(A_0+A_s\frac{kU^*}{\varepsilon})}$
C_v	Constant determined experimentally	$C_v=100$
U^*	Constant determined experimentally	$U^*=\sqrt{S_{ij}S_{ij}+\tilde{\Omega}_{ij}\tilde{\Omega}_{ij}}$
$\tilde{\Omega}_{ij}$	Constant determined experimentally	$\tilde{\Omega}_{ij}=\overline{\Omega}-\varepsilon_{ijk}\omega_k-2\varepsilon_{ijk}\omega_k$
A_0	Constant determined experimentally	$A_0=4.04$
A_s	Constant determined experimentally	$A_s=\sqrt{6}\cos\phi$
ϕ	Constant determined experimentally	$\phi=\frac{1}{3}cos^{-1}\left(\sqrt{6}\frac{S_{ij}S_{jk}S_{ki}}{\tilde{S}^3}\right)$
$\tilde{S}$	Constant determined experimentally	$\tilde{S}=\sqrt{S_{ij}S_{ij}}$

S_{ij}	Constant determined experimentally	$S_{ij}=\frac{1}{2}\left(\frac{\partial u_j}{\partial x_j}+\frac{\partial u_i}{\partial x_j}\right)$
$\sigma_k=1.0$	Inverse effective Prandtl numbers for the turbulent kinetic energy	$\sigma_k=1.0$
σ_ε	Inverse effective Prandtl numbers for the turbulent kinetic energy dissipation rate	$\sigma_\varepsilon=1.2$
μ_t	Turbulent kinetic energy and its dissipation rate	$\mu_t=\rho C\mu\frac{k^2}{\varepsilon}$

- **RNG k-ε model**

Similar to the standard k-ε model, the RNG k-ε model was derived from the Navier Stokes instantaneous equations, except that it uses a technique called renormalization group theory described by Yakhot and Orszag, (1986) **[83]**. This derivation produces a model with constants different from those used in the k-epsilon standard model, and adds new terms to the transport equations for the turbulent kinetic energy and its dissipation. The effect of the vortex is also taken into account in the RNG k-ε model, improving the precision of the swirling flows. An analytical formula for turbulent Prandtl numbers is provided in this model while the standard model relies on user-specific constant values.

Finally, assuming proper treatment of the near-wall region, the RNG k-ε model uses an analytically derived differential formula for the effective turbulent viscosity, which accounts for the low Reynolds number of streams. The RNG k-ε model is, therefore, more precise and more reliable than the standard k-ε model for a wider range of flow rates **[84, 85]**.

The RNG k-ε model is, therefore, more precise and more reliable than the standard k-ε model for a wider range of flow rates. Due to these differences, the transport equations appear as follows.

- ✓ Turbulent kinetic energy, k

$$\frac{\partial(\rho k)}{\partial t}+\frac{\partial}{\partial x_i}(\rho k u_i)=\frac{\partial}{\partial x_j}\left[(\alpha_k\mu_{eff})\frac{\partial k}{\partial x_j}\right]+G_k+G_b-\rho\varepsilon-Y_M+S_k \quad \text{(II.11)}$$

- ✓ Dissipation rate ε

$$\frac{\partial(\rho\varepsilon)}{\partial t}+\frac{\partial}{\partial x_j}(\rho\varepsilon u_i)=\frac{\partial}{\partial x_j}\left[(\alpha_\varepsilon\mu_{eff})\frac{\partial\varepsilon}{\partial x_j}\right]+C_{1\varepsilon}\frac{\varepsilon}{k}\rho(G_bC_3\varepsilon+G_k)-\rho C_{2\varepsilon}\frac{\varepsilon^2}{k}-R_\varepsilon+S_\varepsilon \quad \text{(II.12)}$$

The RNG k-ε model theory has a scale removal method that defines the effective viscosity, which is expressed by the following equation:

$$\partial\left(\frac{\rho^2 k}{\sqrt{\varepsilon\mu}}\right)=1.72\frac{\hat{v}}{\sqrt{\hat{v}-1+C_v}}d\hat{v} \qquad \text{(II.13)}$$

Table II. 4 represented the turbulent variable and constant appears in each equation.

Table II.4: Presentations of the turbulent variable and constant appear in each equation for RNG.

Symbol	Signification	Formulation
G_k	Represents the generation of turbulent kinetic energy that arises due to mean velocity gradients.	$G_k = \rho\overline{u_i u_j}\frac{\partial u_j}{\partial x_j}$
G_b	Represents generation of turbulent kinetic energy the arises due to buoyancy	$G_b = \beta g_j \frac{\mu_t}{\mathrm{Pr}_t}\frac{\partial T}{\partial x_i}$
Y_M	represents the fluctuating dilation in compressible turbulence that contributes to the overall dissipation rate	$Y_M = 2\rho\varepsilon M_t^2$
S_ε	source terms defined by the user dissipation	$S_\varepsilon = \sqrt{2S_{ij}S_{ij}}$
S_k	source terms defined by the user kinetic energy	$S_k = \sqrt{2S_{ij}S_{ij}}$
$C_{1\varepsilon}$	Constant determined experimentally	$C_{1\varepsilon} = 1.42$
$C_{2\varepsilon}$	Constant determined experimentally	$C_{2\varepsilon} = 1.68$
C_μ	Constant determined experimentally	0.0845
C_v	Constant determined experimentally	100
σ_ε	Inverse effective Prandtl numbers for the turbulent kinetic energy	$\sigma_\varepsilon = 1.2$
σ_k	Inverse effective Prandtl numbers for the turbulent kinetic energy dissipation rate	$\sigma_k = 1.0$
μ_t	Turbulent kinetic energy and its dissipation rate	$\mu_t = \rho C_\mu \frac{k^2}{\varepsilon}$

II.3.4 Comparison of different K-ε turbulent models and their applications

Computational fluid dynamics (CFD) for wind and environmental engineering continues to rely on the conventional Reynolds-averaged Navier–Stokes (RANS) methods. Their simplicity, robustness, and computational economy have not yet been seriously challenged by any other turbulence simulation methods, and it is likely that RANS methods, in the present or improved form or in combination, will continue to dominate the industrial and environmental CFD for Some time to come.

However, industrial CFD tends to use overly simplistic turbulence models, which are unable to reproduce some major phenomena encountered by wind and environmental engineering such as flow collision, illusory body awakening, instability, and 3D boundary layer separation, buoyancy effects, and others **[86]**.

The RANS-based modeling approach therefore greatly reduces the computational effort and resources required and is widely adopted for practical engineering applications. A whole hierarchy of closure models is available in FLUENT, including Spalart-Allmaras (one equation), feasible k-ε (2 equations) and its variants, standard k-ω(2 equations), transitional shear stress transport (SST k-ω) and the Reynolds stress model (RSM). All these turbulence models have been compared according to their description, behavior, and uses **[87-89]**.

The standard model k-ε is the basic model with two transport equations solving k and **ε**, this is the default **k-ε** model. The coefficients are calculated empirically; it is only valid for fully turbulent flows. The options to account for viscous heating, buoyancy and compressibility are shared with other **k-ε** models. It is robust, widely used despite the known limitations of the model. Performs poorly for complex flows involving a severe pressure gradient. It is suitable for initial iterations, initial screening of alternative designs, and parametric studies.

The RNG k-ε model is a variation of the standard **k-ε** model. The equations and the coefficients are derived analytically. Significant changes in equation e improve the ability to model highly stressed flows. Additional options help predict swirling and low Reynolds number flows. It is suitable for complex shear flows involving rapid deformation, moderate vortex, vortices, and locally transient flows.

The Realizable k-ε model is a variant of the standard **k-ε** model. Its "feasibility" results from changes that make it possible to obey certain mathematical constraints, which ultimately improves the performance of this model.

Table II.5 : RANS model description, behavior and capabilities **[90]**

Models	**Description**	**Behavior and use**
Standard k-ε	The baseline two-transport-equation model solving for k and ε. This is the default k–ε model.	Robust and widely used despite the known limitations of the model. Performs poorly for complex flows involving severe pressure gradient, separation, and strong line curvature.
RNG k–ε	A variant of the standard k–ε model. Significant changes in the ε equation improve the ability to model highly strained flows.	More suitable for complex shear flows involving rapid strain, moderate vortex, vortices, and locally transient flows.
Realizable k–ε	A variant of the standard k–ε model. Its "Realizability" stems from changes that allow certain mathematical constraints to be obeyed which ultimately improves the performance of this model.	Provides many of the same benefits and has similar applications to RNG k-ε model Maybe more precise and easier to converge than RNG k-ε model.

It offers many of the same benefits, has similar applications to RNG k-ε model, and perhaps it is more accurate and easier to converge than RNG k-ε model. The t**able II.5** summarize the description, behavior and capabilities different k-epsilon models.

II.3.5 Radiation models

The procedure for setting up and solving a radiation problem is described below and described in detail in the following sections. There are five radiation models that allow you to include radiation, with or without a participating medium, in your heat transfer simulations that are built into fluent software.

For modeling, issues causing the heating or cooling process of surfaces due to radiation and/or heat sources or sinks due to radiation in the fluid phase can be included in your model using one of the following radiation models.

- Discrete Transfer Radiation Model (DTRM) **[91, 92]**
- P-1 Radiation Model **[93, 94]**
- Rosseland Radiation Model **[94]**
- Surface-to-Surface (S2S) Radiation Model **[94]**
- Discrete Ordinates (DO) Radiation Model **[95, 96]**

Table II.6 : Radiation model advantages and limitations **[97]**

Models	**advantages**	**limitations**
DTRM	The primary advantages of the DTRM are threefold: it is a relatively simple model, you can increase the accuracy by increasing the number of rays, and it applies to a wide range of optical thicknesses.	DTRM assumes that all surfaces are diffuse. This means that the reflection of incident radiation at the surface is isotropic with respect to the solid angle.
P-1 Model	The P-1 model has a diffusion equation, which is easy to solve with little CPU demand. The model includes the effect of scattering. In addition, the P-1 model can easily be applied to complicated geometries with curvilinear coordinates.	P-1 model considers that all surfaces are diffuse, where the reflection of incident radiation at the surface is isotropic with respect to the solid angle and The implementation assumes gray radiation.
Rosseland Model	The Rosseland model does not solve an extra transport equation for the incident radiation, and is very faster than the P-1 model and requires less memory.	The Rosseland model can be used only for optically thick media and for the optical thickness exceeds 3. It is not available for the pressure-based solver, only.
DO Model	The DO model covers the full range of optical thicknesses and the current implementation is limited to either gray radiation or non-gray radiation using a gray band model. It also allows the solution of radiation at semi-transparent walls, the computational cost is moderate, and memory requirements are modest.	The weighted-sum-of-gray-gases model (WSGGM) cannot be used for the Do model to specify the absorption coefficient in each band, and the emissivity is assumed constant within each band.
S2S Model	The surface-to-surface (S2S) radiation model is good for modeling the enclosure radiative transfer without participating media.	The use of the S2S radiation model requires the surface are diffuse, gray radiation, not applicable for model participating radiation problems, and cannot be used with periodic and symmetry boundary conditions.

For the use of radiation models, there are advantages and limitations, which must be taken into consideration, and are summarized in **table II.6**.

II.3.6 Modeling fluid a free surface

A study of the cooling of the PV module by the flow of water flowing over the surface before modeling a two-phase problem (air and water) consists of simulating the flow of a situation leading to solving a free surface problem (air-water). The free surface is implemented as an asymmetry limit which means that no flow occurs across this border (i.e. normal speed is, therefore, zero at the border) **[98]**.

In problems with free or mobile interfaces, the area of study has unknown boundaries, the determination of which is part of the solution. There are three methods for modeling the

problem of the free surface (Volume of fluid (VOF) **[99-101]** model, level set model **[102]**, and hybrid model, **[103, 104]**.
The phenomena encountered for free surface flow are very varied:

- ✓ The flow of immiscible fluids (fluid-fluid interface)
- ✓ Unsteady fluid-structure interaction (peristaltic flow)
- ✓ Flow with the propagation of a phase change front
- ✓ Atomization of jets...

The importance of industrial issues motivate the dynamism of research carried out in this field, where the difficulties are of several types:

- ✓ Taking into account the physical interface phenomena (capillary voltage ...)
- ✓ Treatment of singular points
- ✓ Spatial discretization and the evolution of interfaces
- ✓ Imposition of boundary conditions

It is generally distinguished here the Eulerian method and the Lagrangian method, although mixed methods combining the two strategies have also been proposed.

II.3.6 .1 Eulerian method

There are many types of research that were examined in this context, which reported in Ref. **[105, 106]**. In this approach, the volume fractions of each phase are considered mathematically as continuous functions in time and space and whose sum is equal to unity. The balance equations for each phase make it possible to obtain a set of equations with a similar structure for all phases. This method consists of giving the velocity fields ‘u’ and the pressure ‘p’ at any point at a given instant ‘t ’: $u = u(x, y, z, t)$; $p = p(x, y, z, t)$
This approach allows several phenomena to be taken into account; it includes the VOF (Volume Of Fluid) model as well as other methods:

- ✓ Forehead tracking method
- ✓ Marker and cell type method (MAC)
- ✓ Level line method

II.3.6 .2 Lagrangian method

In the Lagrangian description of flows, we follow the movement of these particles over time. The flow is described by giving their positions according to the starting one: x = x (x0, y0, z0, t). The Lagrangian representation is linked to the notion of the trajectory. Many types of research were implemented in The Lagrangian approach **[107,108]**.

II.3.6 .3 Euler-Lagrange Multiphasic technique

The Discrete Phase Model (DPM) adopts this approach. In this model, the fluid phase is treated as a continuous phase approximated by the Euler-Euler method by solving the Navier - Stokes equations. For the dispersed phase, a number of particles, bubbles, or drops are followed by a Lagrangian method. The DPM model simulates the exchange of energy, mass, and momentum between the dispersed phase and the fluid **[109,110]**.

II.3.6 .4 Selecting the right Multiphasic method

The VOF (Volume Of Fluid) model is the most appropriate in the case of stratified or free-surface flows, the Euler model and the mixed model are adopted for flows in which the volume fraction of a dispersed phase exceeds 10%. The VOF model is a surface tracking technique applied to a fixed Eulerian mesh. It is designed for two or more immiscible fluids when the position of the interface between the fluids is of interest. It is an appropriate model for stratified, free surface, or gravity flows. In flows in which the volume fraction of the dispersed phase is less than or equal to 10%, the DPM model is suitable **[111]**.

II.3.6 .5 Principle of the VOF method

The VOF method is based on meshes that cover the entire computational domain (which contains both liquid and gas). During a computation iteration, the resolution of the Navier-Stokes equations is carried out only in cells full of liquid (or full of gas). Cells that are liquid correspond to cells intersected by the free surface **[112,113]**.

II.3.6 .6 The equations used in the VOF model

This section presents the adopted equations by the fluent calculation code in the VOF model, which governs the flow, and is given below. The capture of the interface between the phases is ensured by solving the equation of the continuity of the volume fraction of the phase, "q", considered among "n" phases **[114]**:

$$\frac{\partial(\alpha_q)}{\partial t} + u_i \frac{\partial(\alpha_q)}{\partial x_i} = \frac{S_q}{\rho_a} + \sum(\dot{m}_{pq} - \dot{m}_{pq}) \tag{II.13}$$

Temporal variation of fluid volume + Flow balance = Source of masses + Phase transfer αq is the volume fraction of the phase number to be checked for a mixture with n phases in the following equations:

$$\sum_{q=1}^{n}\alpha_q = 1; \rho = \sum_{q=1}^{n}\rho_q \qquad \text{(II.14)}$$

II.3.6 .7 Geometric reconstruction of the interface

Interface checking is the selection of the free area from the fluid volume fractions of mixed cells. There are two methods are as follows.

a) The linear interpolation scheme

Youngs **[115,116]** generalized this method assuming that the interface follows a linear slope between two successive meshes. This method consists of linearly connecting the neighboring mixed cells as follows: For each mixed cell, the height of the fluid is determined, which corresponds to its fraction of fluid volume (h = | C | α / x). Place a point at this height and equidistant from the vertical edges of the cell. By connecting the dots like this defined from a cell to these neighbors, we obtain a definition of the free surface as shown in f**igure II. 3**.

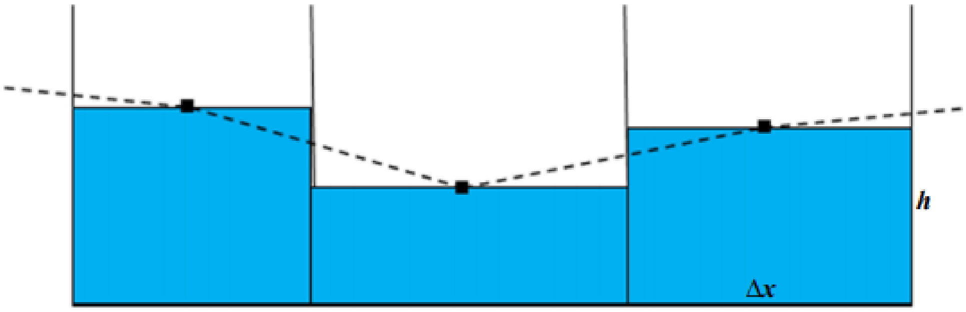

Figure II. 3. *Linear interpolation of free surface**[116]***

However, the method previously described can pose an important problem If the meshes (supposed to be rectangular: the assumption of Cartesian mesh) are not of equal dimensions according to x, it can pose problems of conservation of the mass. This is why very particular care must be taken in the quality of the mesh.

b) Donor-acceptor scheme

As the name suggests, this method works on all mixed cells to identify which ones will "donor" a quantity of fluid and neighboring cells that will "accept" this quantity of the fluid. The volume of fluid that will pass through advection through the facets of the cells corresponds to the minimum of the two following values: the volume of fluid existing in the "donor" cell and the free volume in the "acceptor" cell **[117]**.

II.3.6 .8 Surface tension and wall adhesion

The VOF model can also include the effects of surface tension along with the interface between each pair of phases. The model can be further improved by the specification of the contact angles between the phases and the walls. There is a pressure difference between the liquid and the gas, equal to the local curvature of the surface "k" multiplied by a coefficient "σ", the value of the surface tensions. This coefficient depends on the two fluids present **[118-120]**. The strongest pressure reigns in the fluid whose surface is convex:

$$P_2 - P_1 = 2.\sigma.k \tag{II.15}$$

Where k is the mean curvature of the surface. The importance of surface tensions is assessed through knowledge of the Reynolds number and one of these two dimensionless quantities: the number of capillaries and the number of Weber.

The effect of surface tension is determined on the basis of the Reynolds number (Re = UL/ν), where L is the characteristic length. If Re is less than 1, the next parameter to be considered is the capillary number (Ca=ρU/σ), where σ is the surface tension of the liquid, and, if Re is greater than 1, the next parameter to be considered is the Weber number.

If Re << 1, then we are interested in the capillary constant,

$$C_a = \frac{\mu U}{\sigma} \tag{II.16}$$

If Re >> 1, we are more interested in the Weber number:

$$W_e = \frac{\rho.L.U^2}{\sigma} \tag{II.17}$$

U is the speed of the free surface, and the length L corresponds in our case to the air gap d. In both cases, the surface tension forces are considered negligible for Ca >> 1 or We >> 1.

II.3.7 Commercial CFD packages

A variety of CFD trading codes have been developed and are currently available. For decades, various challenges in this field have led to notable competition among the developers of these CFD codes. These CFD codes, applicable to the fields of modeling Newtonian and non-Newtonian fluids, two-phase flows, flow-dependent properties, phase change and flow through porous media, have gained great popularity.

Table II.7 : Some commonly used commercial CFD codes and their important features

CFD Code	provider	Solver	Parameters	Features/capabilities
CFX and Fluent	ANSYS.inc www.ANSYS.com	FVM	Temperature, flux, convection, radiation, heat surce	Inbuilt geometry, meshing, pre-and post-processing features, Enthalpy and latent heat-base phase change models available and CAD compatible.
COMSOL multiphasic	COMSOL www.comsol.com	FEM, FVM, and PTM	Temperature, flux, convection, radiation, electromagnetic	Inbuilt geometry, pre-and post-processing features, Enthalpy and latent heat-base phase change models available and CAD compatible. and live link feature for matlab, and excel.
Star-CCM **Star-CD**	CD-adapco Group www.cd-adapco.com	FVM	Temperature, convection, radiation,	Inbuilt geometry, pre-and post-processing features, Enthalpy and latent heat-base phase change models available and CAD compatible.
PHONECS	CHAM Ltd. www.chamo.co.uk	FEM and FVM	Temperature, convection, radiation,	Inbuilt geometry, pre-and post-processing features, Enthalpy and latent heat-base phase change models available and CAD compatible. and live link feature for matlab, and excel.

OpenFAOM (open source)	OpenFAOM CFD	FVM/FEM	Temperature, flux, convection, radiation, heat surce	Inbuilt geometry, meshing, pre-and post-processing features. CAD compatible.
Flow 3D	Flow Science.inc. www.flow3d.com	FVM	convection, radiation, heat surce, Temperature, radiation,	Inbuilt geometry, pre-and post-processing features. CAD import and edit feature.
SOLIDWORKS Flow simulation	Dassault systems SOLIDWORKS corps www.solidworks.com	FVM	convection, radiation, flux, Temperature,	Inbuilt geometry, pre-and post-processing features. CAD import and edit feature.
CFD-DEM coupling LIGGHTS(open source)	CFDEM @ project www.cfdm.com	DEM	convection, radiation, flux, Temperature,	. CAD import and edit feature. Inbuilt geometry, pre-and post-processing features.

A CFD code consists of input parameters, a temporal section, a discretization section, a space discretization section, and an output parameter section **[121,122]**. Among these commonly used commercial CFD codes are mentioned in **Table II.7 [123]**.

II.4 Numerical procedure

II.4.1 Physical problem model description

Fluid flows, whether laminar or turbulent, are described by the system of partial differential equations (P.D.E). Thus, all physical phenomena are governed by this system formed by the equations of continuity, of the quantity of motion and energy that must be solved to know the characteristics of the thermal field and the flow field. Unfortunately, it is practically impossible to find an analytical and exact solution to such systems because the above equations are very complex, that is to say, nonlinear on the one hand and coupled on the other hand. In this case, the use of numerical resolution is necessary and prompts us to choose the appropriate numerical method to obtain the best approximations. Theoretically, any study of turbulent flow must be done by solving the Navier-Stokes equation and the continuity, which governs instantaneous velocities. However, this view has proved to be very complicated, even impossible. Therefore, it is preferable to approach turbulent flows by an approach that consists of breaking down any physical quantity (velocity, pressure, temperature with zero-time average. Only incompressible flows will be developed here.

The numerical calculation was carried out using the “FLUENT 16" calculation software, based on the finite volume method. First, the problem is addressed by considering the case of a natural convection airflow passing through an inclined channel of an upper wall being heated. The second case is a forced convection airflow in an inclined channel at a different inclination angle and different Reynolds number with the objective of optimizing the hydrodynamic parameters in terms of heat transfer rate such as Nusselt number. The third case is the mixed convection of air and water flow, i.e. flow with a free surface in a channel cooled from below by air and from above with a film of water flows on the front surface of the channel.

In this chapter, we will present the finite volume method, because it is reliable, its adaptation to the problem, its guarantee for the conservation of mass and momentum, and of any transportable scalar on each control volume and in any of the computational domain. The calculation in question is performed on a PC machine equipped with a Pentium 4HT microprocessor with a clock frequency of 3 GHz and 1 GB of RAM.

The use of FLUENT software allows us to build a numerical model capable of processing and solving transport equations. We have treated three configurations in two-dimensional and three-dimensional cases.

- ✓ The first configuration is a question of simulating the case of turbulent natural convection in a channel inclined by 60°C is heated upwards as shown in **figure II. 1.**
- ✓ The second configuration it constitutes an inclined channel provided with turbulent forced convection of different angle and for different Reynolds number **figure II.2.**
- ✓ The third configuration is an inclined channel with an angle of 60 heated from the top to cool from the bottom with the ambient air and upwards with a film of water flowing over the front surface of the can see **figure II.3.**

The current study is developed in order to simulate, the evolution of the turbulent flow of air and water in an inclined channel in natural convection in order to optimize the geometric parameters as well as the parameters hydrodynamic. To better assess the critical values characterizing the transfer modes, the mesh test must comply with certain requirements. Then, the modeling passes by a judicious choice of the various parameters of the computer code. With the good settings being found, we will launch the simulations. Each time, one will wait for the convergence of the solution to be able to process the results and deduce the mean Nusselt number as well as the tracing of the contours of thermal fields and of velocities fields.

This study aims to optimize the geometric parameters, such as the effect of the gap, the effect of the length of the input channel, the effect of the input/output ratio of the input channel, and the effect of the distance of the aluminum plate from the upper wall (PV module). This study is done to understand the behavior of the airflow in turbulent natural convection of the Rayleigh number $Ra_L > 10^9$.

Regarding the second configuration, the choice was based on the optimal configuration obtained by the first configuration studied. In this study, we have simulated the forced convection flow for different Reynolds numbers at different tilt angles. With the aim of knowing the effect of the Reynolds number and the angle of inclination on the transfer rate and the thermo-hydrodynamic flow behavior.

The third configuration was based on the comparison of a numerical model with current experimental data, a fixed tilt angle DFC fans with varied velocity as a function of solar irradiance. In this section, the modeling of the problem with a free surface by using the VOF model. The water mass flow rate is fixed to mw=0.034kg/s.

II.4.2 Numerical method

The numerical calculation CFD is a tool that allows the numerical resolution of conservation equations written in a local form. The latter are, generally, partial differential equations whose solution depends on two to four variables: the time variable with one to three spatial coordinates. This system of equations only very rarely has an analytical solution. It is, therefore, necessary to resolve them by an adequate numerical method. In this context, the choice of the software used to solve the non-linear transport equations is more essential.

In our problem, the choice is on the Ansys fluent software, which is based on the finite volume method. In this section, we present the presentation of the software used and the different steps used for the modeling by the use of fluent software as well as a representation of the principle and procedure of the finite volume method.

Numerical flow simulation software can be considered as true "digital experiments" when done with care. The advantage of "numerical methods" is that all the physical quantities related to the flow (velocity field, pressure field, stresses, etc.), are immediately available at any point of flow. In an experiment, obtaining these physical quantities at any point in the field is often impossible or very difficult to put into practice.

II.4.2.1 Various step for numerical modeling

The numerical resolution by Ansys FLUENT software, in general, is done by two pre-software gambit software for the creation of the geometry, the definition of borders, and the generation of the mesh. On the other hand, the fluent solver does the resolution where we can choose the different appropriate models and the corresponding method and processing of the results:

- Creation of the geometry using the GAMBIT software,
- Choice of the mesh strategy and creation of several grids,
- Definition of the boundary conditions in GAMBIT,
- Definition of the problem using the FLUENT software,
- Calculation with FLUENT for the different cases selected,
- Analysis of the obtained results in post treatment

The creation of the geometry as well as the choice of the adapted mesh is done by the software package "Gambit. This mesh generator offers extended solutions for the most complicated geometries. It is able to realize geometries in 2D or 3D and to build the mesh. It generates files with an *. mesh extension and for FLUENT.

Gambit gathers three main essential functions one cites the tomorrow of computation by the construction of the geometry, the generation and the checking of the quality of the selected mesh and as well as the definitions of the borders and the precision of the type of fluid or solid tomorrow. For the current case, the generation of the mesh constitutes an important phase knowing that the precision and the accuracy of the numerical results depend on it. Under Gambit, we can choose the three types of mesh mentioned below:

- Structured mesh (quadra / hexa)
- Unstructured mesh (tri / tetra.)
- Hybrid mesh

II.4.2.2 Mesh generation techniques

The generation of a very good mesh quality is essential for obtaining an accurate and meaningful calculation result. Practically, there is no standard rule for creating a valid mesh; however, different approaches lead to an acceptable mesh grid. We can summarize these rules as follows [124]:

- Maintain good quality of the elements,
- Ensure good Resolution in regions with strong gradients,
- Ensure good Smoothness in the transition zones between the fine-meshed parts and the coarse meshed parts,
- Minimize the Total number of elements (reasonable calculation time).

In the present work, the choice fell on a structured mesh (Quadra / hexahedral).

II.4.2.3 Calculation by the FLUENT solver

Once the loading of the mesh file (carried out with the GAMBIT software) is carried out under "FLUENT", we must scale the geometry (in our case, we use the millimeter).

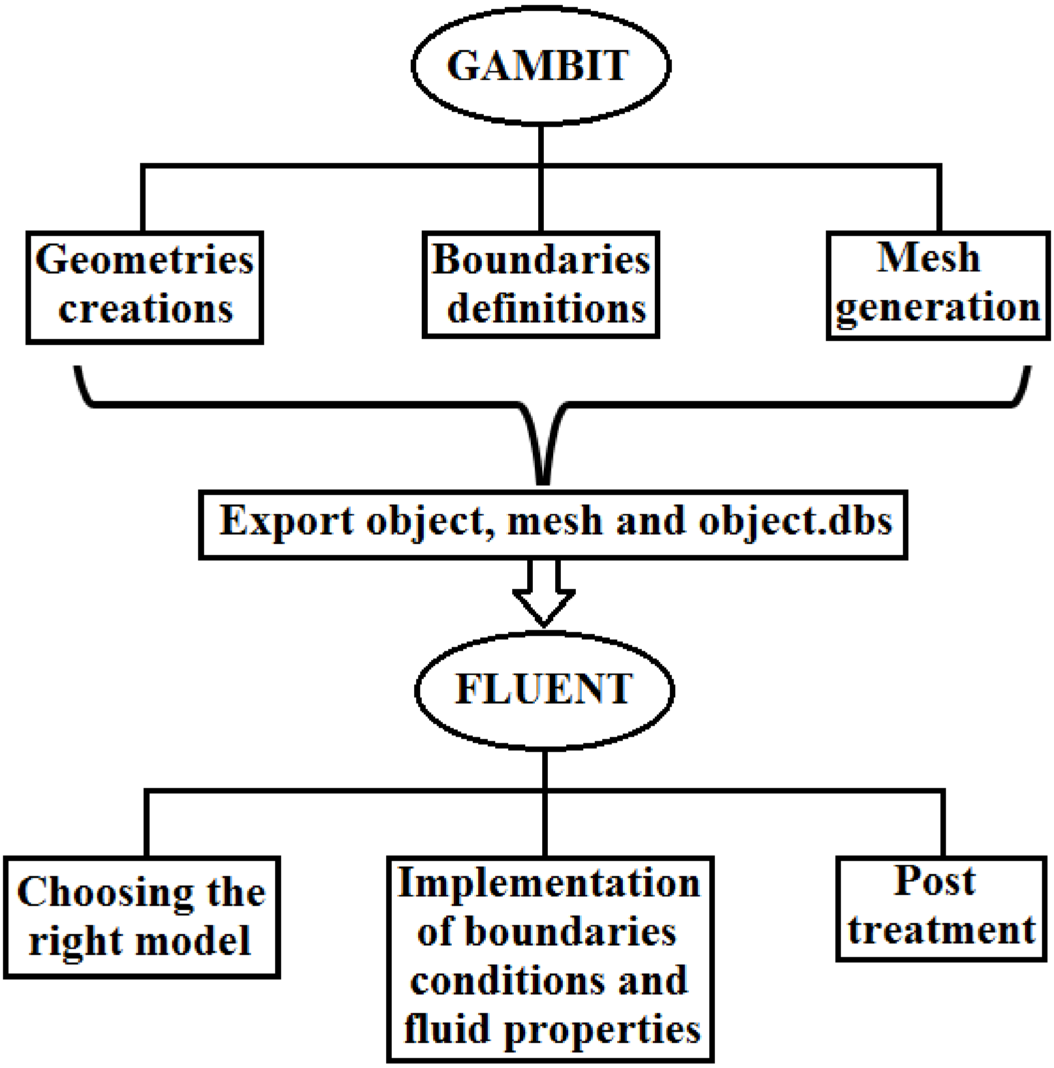

Figure II. 4 : *Procedure and steps follows in Gambit masher and Fluent solver*

The "FLUENT" software makes it possible to reorder the nodes, the surfaces, and the cells in memory, so that they have the same arrangement in the grid and in the memory, in order to improve the performance of calculation. **Figure II.4** represents the different steps that used to solve a problem by using Ansys Fluent.

II.4.2.4 FLUENT solver presentation

FLUENT is a computer code for modeling fluid flows and heat transfers within or around complex geometries. This software is widely used in industry (aerospace, automotive, nuclear, chemical, biomedical, environment, weather, etc.). Capable of solving flow problems using Structured mesh for simple or unstructured geometries, for complex geometries. The types of mesh, which are supported, are:

- 2D, triangular or quadrilateral meshes,
- 3D mesh, tetrahedral/hexahedral/pyramidal,
- Mixed (hybrid) meshes

FLUENT is written in the C programming language and makes full use of the flexibility and power offered by this language (dynamic memory allocation). In addition, it uses an architecture that allows it to run multiple processes simultaneously on the same workstation or on separate workstations for more efficient execution.

It is operated through a graphical interface and the advanced user can adapt or augment, as needed, the interface by writing macros and menu functions in order to automate certain procedures. On the other hand, FLUENT has the capacity to model the various problems of the following flow fields:

- Cases of two-dimensional (2D) or three-dimensional 3D flows;
- Permanent or unsteady flow
- Incompressible or compressible fluids (subsonic, transonic,
- Supersonic or hypersonic);
- Viscous or non-viscous, laminar or turbulent flows;
- Newtonian or non-Newtonian fluid;
- Forced heat transfer mode, by conduction, convection, or radiative;
- Mono or multi-physical flow with or without phase changes;
- Flow in a partially or very filled with porous medium.

The FLUENT software is based on the numerical modeling method known for its computing power and simplicity of implementation; finite volume method. Patankar and Spalding [125] first described it.

II.4.2.5 Principle of the finite volume method (FVM)

This method is used to numerically solve partial differential equations such as the finite difference method and the finite element method, but unlike the finite difference method, which uses derived approximations. The finite element method is used by approximation of integrals. In it, the conservation laws (of mass, momentum, and energy) are expressed locally in integral form. The computed domain is divided into a specified number of main subdomains called control volumes, each of which includes a node called a master node. The finite volume method consists of integrating the partial differential equations described in the previous chapter on each control volume.

The principle of this method is based on a discretization technique that converts nonlinear partial differential conservation equations into linear algebraic equations and the latter is solved numerically **[126,127]**. The control volumes technique consists of integrating partial differential equations on each control volume to obtain discretized equations that keep all the physical quantities on a control volume, as shown in **figure II. 5**.

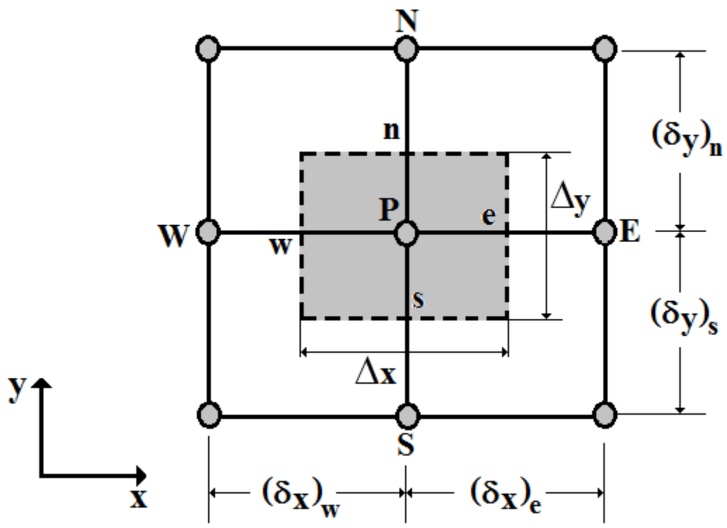

Figure II. 5 : *Control volume* ***[128]***

For a principal node P, the points E and W (E = East, W = West) are neighbors in the x-direction, while N and S (N = North, S = South) are neighbors in the y-direction. The conservation equations presented in the previous chapter can be written in a common form, this formulation allows not reiterating the work of discretization for each equation. The studied variable, each of the equations can be reduced to a single general equation according to the form:

$$\frac{\partial}{\partial t}(\rho\phi)+\sum\frac{\partial}{\partial x_i}(\rho x_i\phi)=\sum\frac{\partial}{\partial x_i}\left(\Gamma_\phi\frac{\partial\phi}{\partial x_i}\right)+S_\phi \tag{II.18}$$

$$\underbrace{\frac{\partial\phi}{\partial\tau}}_{(1)}+\sum_{j=1}\underbrace{\frac{\partial}{\partial X_i}\left(U_j\phi\right)}_{(2)}=\sum_{j=1}\underbrace{\frac{\partial}{\partial X_j}\left(\Gamma_\phi\frac{\partial\phi}{\partial X_J}\right)}_{(3)}+\underbrace{S_\phi}_{(4)} \tag{II.19}$$

(1): transient term

(2): convection transport term

(3): the term of transport by diffusion

(4): source term

Where ϕ is the transported property, Γ indicates the diffusion coefficient and S_ϕ the source term.

Table II.8 : List of transports equations terms

Equations	**Variable**	**Diffusive term**	**Source term**
Equation type	ϕ	Γ	S
Continuity equation	1	0	0
Momentum x-direction	U	μ+μt	-
Momentum y-direction	V	μ+μt	-
Momentum z-direction	W		-
Energy equation	T	α	0
Turbulent Kinetic energy	k	-	-
Turbulent dissipation energy	ε	-	-

All of these terms are listed in **Table II.8**. Only this equation is discretized and the system of partial differential equations is solved for each successive value of ϕ.

II.4.2.6 The general concept of the finite volume method

Uses of the finite volume method to solve a problem follows the following steps [129]:

- Clearly define the area of study and divide this area of calculation into a finite number and discrete control volumes whose sum is exactly equal to the volume of the computational domain. We say that we generate a mesh.
- Discretization of the differential equations governing the phenomenon. In the end, we get a system of algebraic equations.
- Solve the final algebraic system by a solving method (method iterative or direct).

a) Velocity- pressure coupling

If we notice the momentum equations, we note the presence of pressure in the source term as a gradient. These equations can only be solved if the pressure p is known or estimated. In case the correct pressure is known, the velocity field obtained after solving the linear algebraic system will satisfy the continuity equation. As the pressure is not known, it is necessary to use a procedure for the pressure calculation. The velocity pressure coupling is achieved by using the equation to derive an equation for the pressure from the discretized continuity equation; we have the choice between three velocity pressure-coupling algorithms, SIMPLE (Semi Implicit Method for Pression-linked Equation), SIMPLEC (Semi Implicit Method for Pression-linked Equation Consistent), et PISO (Pression - Implicit with Splitting of Operators) **[130]**.

b) SIMPLE algorithm Flowchart based on FVM

In order to better explain the operation of the SIMPLE algorithm based on the finite volume method FVM, the flowchart of the numerical simulation of the steady-state process has been developed and presented in figure 4. The sequence of essential operations constituting the SIMPLE algorithm is and all step of work the algorithm simple is mentioned in the following main points.

- Give a pressure field P *
- solve the momentum equations to obtain the velocities U * and V *
- solve the pressure correction equation P '
- correct the pressure P, P * and P '
- correct the speeds according to relations III.74
- solve the discretized equations of other dependent variables such as temperature
- replacing the old pressure field with the new one and returned to step (2)

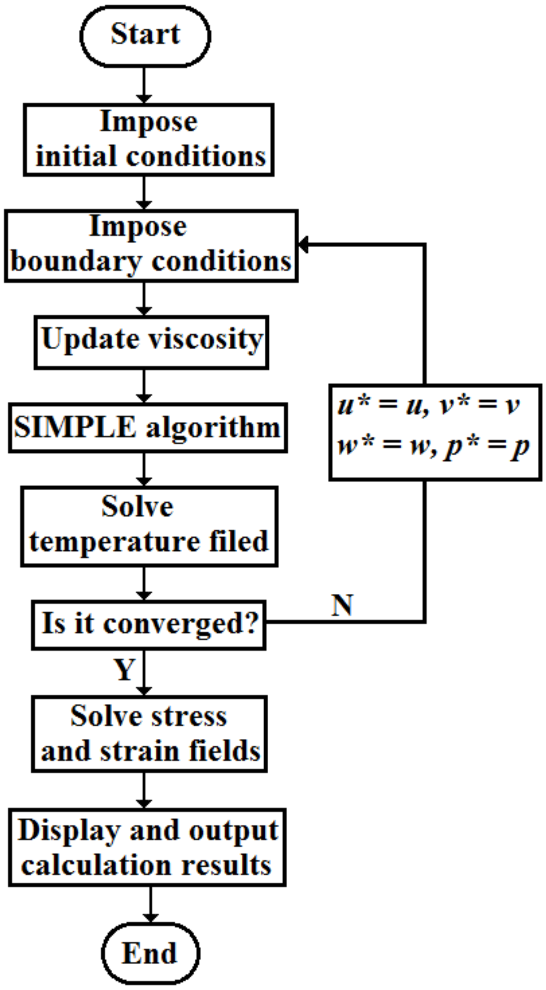

Figure II. 6. *Flowchart of numerical simulation based on FVM* ***[130]***

- The calculations will be repeated until reaching convergence
- Firstly, put the values of the initial conditions, such as the pressure fields, the speeds, and the temperature.
- Implement the boundary conditions for the walls and the entrances and exits.
- Calculate the dynamic viscosity value as a function of the speed and temperature fields defined by the initial conditions and the limit conditions.
- Calculate the velocity and pressure fields with the SIMPLE algorithm, then calculates the temperature field according to a law of conservation of energy.
- Judge if the current iteration is satisfied with the predefined convergence criterion.

c) CFD FLUENT model and scheme setup

In this 3D CFD analysis, the VOF model of multiphase flow with an implicit volume fraction parameter was used. For boundary conditions, the top surface was treated as a zero-shear a wall to remove the friction of air at the top wall, causing it to behave as open to the atmosphere. On all solid boundaries, the no-slip boundary condition was applied. The non-equilibrium wall function was used for near-wall treatment because the non-equilibrium wall function partly accounts for non-equilibrium effects neglected in the standard wall function. The RNG k-ε turbulence model was adopted because it is an appropriate choice when the turbulence transfer among the phases plays a dominant role (ANSYS, 2016). The inlet and outlet faces were considered the pressure inlet and pressure outlet, respectively. The bounded gradient maximization (BGM) scheme was applied for volume fraction discretization to get a sharp interface of water. The height of the wall roughness was considered $h=1.5 *10^{-06}$ m for Perspex glass as the experimental channel was fabricated using a Perspex glass sheet.

- Single precision or double-precision, in "double precision" mode: floating-point numbers are represented using 64 bits, while "single-precision" mode: uses a 32-bit representation.
- The formulation based on the pressure, "Pressure based", or sequential (implicit): This formulation makes it possible to solve the transport equations separately sequentially, i.e. isolated from each other (implicit by default). The isolated solver is classic for incompressible flows, therefore, it is the formulation that we have chosen to use for our case since it requires less memory capacity and offers flexibility in the resolution procedure.
- Choice of the discretization scheme, there are several discretization schemes such as first-order, second-order, third-order MUSCL, Power-law, QUICK, hybrid. These diagrams are integrated into Fluent to interpolate to the faces of the control volume the variables stored in the center of the cell.
- In Choice of the interpolation diagram of the pressure on the faces, there are several diagrams, in particular, standard diagrams, Body-Force-Weighted, PRESTO ", Linear, and Second Order. These diagrams are integrated into FLUENT and the choice is dealing with the second-order schemes as it is more recommended.
- Choice of pressure-velocity coupling method, "FLUENT" offers three methods for pressure-velocity coupling (only with the "Pressure based" formulation) we recall, SIMPLE, SIMPLEC, and PISO algorithm. The choice of the algorithm is carried over to SIMPLE because it is more suited to our problem.
- Choice of under relaxation, in case of convergence (criteria convergence take value of 10^{-07}) difficulties and because of the non-linearity of the transport equations, it is

necessary to make a change of the variable φ by accelerating or slowing down from one iteration to another the variation of the considered variable.

- Choice of interpolation methods (Gradients), the gradients of the variables are necessary to evaluate the diffusive fluxes, the derivatives speed, and for high order discretization schemes. The gradients, which are as follows, Green-Gauss cell-Based, Green-Gauss Node-Based, and Least-Squares cell-Based.
- Choice of the temporal step for the case of unsteady flows, at each stage of computation, the solver reiterates until convergence before advancing to the following step. The initialization of the solution defines the initial solution and must be realistic. Δt must be small enough to solve the time-dependent characteristics and ensure that convergence is reached in the maximum number of iterations defined for each step.

Table II.9: Summary of all numerical schemes and models are used to solve actual problems.

Variable case	RANS
Multiphasic models	VOF
Turbulence models	K-ε RNG with wall treatment
Radiation models	DO
Solver	Segregated
Pressure-velocity coupling	SIMPLE
Spatial Discretization transports equations(continuity, momentum, energy)	Third-order MUSCL scheme Third-order MUSCL scheme
Turbulence scheme of turbulence	Second order upwind

Implemented fixed parameters scheme, models and method are reported in the Table II.9 in this study.

Table II.10: The boundary conditions for numerical simulations implemented in the present work.

place	Type	Description
PV module surface	Wall	$T=T_{PV,}$ $Q''=I_g * A_{PV} * \alpha\tau_w * \alpha\tau_g * (1-\eta_O)$
Insulation wall	Wall	$Q=0W/m^2$
Entrance sloped channel	Wall	$Q=0W/m^2$
Aluminum Flat plate	Wall	Thermal coupled
Inlet channel	Pressure inlet Velocity inlet	Gauge total pressure =0Pa T=T€=300k Turbulent intensity of 5%
Outlet channel	Pressure outlet Velocity outlet	Gauge total pressure =0Pa Back flow temperature T=T€=300k Turbulent intensity of 5% Backflow turbulent viscosity ratio =4

The boundary conditions used to model our physical problem for the three configurations, whether passive air-cooling, active air-cooling, or the configuration with active air and water-cooling for the new hybrid PV/T Bi-fluid system are summarized in **table II.10.**

d) Convergence criterion

The initialization procedure of the VOF model in an open channel analysis is critical (ANSYS 2016). In addition, the convergence criterion of the VOF model is stricter than the models for closed conduit or pressure flow. The standard initialization was accomplished with the computed values from the inlet.

The most important convergence criterion for steady flow in the VOF model was considered the difference between the mass flow rates at the inlet and the outlet. The solution was manually stopped and considered to be converged when the difference between the mass flow rates at the inlet and outlet was less than 0.5%. To speed up early convergence, the monitoring residual for the velocity in the y-direction was set at 10^{-7}. Other monitoring residuals were set at 0.1s.

II.5 Conclusion

In the first part of the study, generalities have been presented to provide the reader with the basics and principles of CFD digital modeling. This section of the study is also considered as the best guide for the student or researcher to be able to understand everything related to numerical modeling and use it in the best way.

As for the second part of this section, It is a statement of the methodology used in relation to the current study, by providing all the carefully explained steps so that the reader will be able to comprehend and benefiting as much as possible.

Based on what presented in this section of the current study, the next chapter will present a detailed three-dimensional numerical study to optimize the geometric and dynamic parameters of the new hybrid PVT system, using the only passive air-cooling technique.

References

[1] Dictionary, Collins English. Complete & unabridged 10th edition." Missiology." HarperCollins Publishers. (2012). http://dictionary. reference. Com/browse/missiology (2012).

[2] L. F. Richardson. IX The approximate arithmetical solution by finite differences of physical problems involving differential equations, with an application to the stresses in a masonry dam, Philosophical Transactions of the Royal Society of London. Series A, Containing Papers of a Mathematical or Physical Character. 210 (1911) 307-357.

[3] P. V. Nielsen, F. Allard, H. B. Awbi, L. Davidson, A. Schälin. Computational fluid dynamics in ventilation design REHVA guidebook. (2007) 291-294. https://doi.org/10.1080/14733315.2007.11683784

[4] Y. Li, P. V. Nielsen. CFD and ventilation research. Indoor Air. 21 (2011) 442-453.

[5] M. Hajdukiewicz, M. Geron, M. Keane. Formal calibration methodology for CFD models of naturally ventilated indoor environments, Building and Environment. 59 (2013) 290-302. https://doi.org/10.1016/j.buildenv.2012.08.027

[6] B. Andersson, R. Andersson, L. Håkansson, M. Mortensen, R. Sudiyo, B. Van Wachem. Computational fluid dynamics for engineers. Cambridge university press. (2011)

[7] H. K. Versteeg, W. Malalasekera. An introduction to computational fluid dynamics: the finite volume method. Pearson education. (2007).

[8] K. Inthavong, E. Wong, J. Tu, N. Singh. Clinical and Biomedical Engineering in the Human Nose. In Clinical and Biomedical Engineering in the Human Nose, Springer, Singapore. (2021) 1-8. https://doi.org/10.1007/978-981-15-6716-2_1

[9] Y. He, M. A. Schnabel, Y. Mei. (2019, December). A novel methodology for architectural wind environment study by integrating CFD simulation, multiple parametric tools and evaluation criteria, In Building Simulation, Tsinghua University Press. (2019) 1-17. doi.org/10.1007/s12273-019-0591-8

[10] S. Cao. (2013). CFD applications in structural wind engineering. In Advanced Structural Wind Engineering, Springer, Tokyo. (2013) 301-324. doi.org/10.1007/978-4-431-54337-4_11

[11] L. Tang, M. Nikolopoulou, F. Y. Zhao, N. Zhang. (2012). CFD modeling of the built environment in Chinese historic settlements, Energy and buildings. 55 (2012) 601-606. doi.org/10.1016/j.enbuild.2012.09.025

[12] H. Montazeri, B. Blocken. CFD simulation of wind-induced pressure coefficients on buildings with and without balconies: validation and sensitivity analysis, Building and Environment. 60 (2013) 137-149. doi.org/10.1016/j.buildenv.2012.11.012

[13] E. I. Basri, A. A. Basri, V. N. Riazuddin, S. F. Shahwir, Z. Mohammad, K. A. Ahmad. Computational fluid dynamics study in biomedical applications: a review, International Journal of Fluids and Heat Transfer. 1 (2016) 2-14.

[14] S. Golshan, R. Sotudeh-Gharebagh, R. Zarghami, N. Mostoufi, B. Blais, J. A. M. Kuipers. Review and implementation of CFD-DEM applied to chemical process systems. Chemical Engineering Science. 221 (2020) 115646. doi.org/10.1016/j.ces.2020.115646

[15] P. J. Jones, G. E. Whittle. Computational fluid dynamics for building air flow prediction—current status and capabilities, Building and Environment. 27 (1992) 321-338. doi.org/10.1016/0360-1323(92)90033-L

[16] L. Yang, M. Ye. CFD simulation research on residential indoor air quality, Science of the Total Environment. 472 (2014) 1137-1144. doi.org/10.1016/j.scitotenv.2013.11.118

[17] E. Cuce, F. Sher, H. Sadiq, P. M. Cuce, T. Guclu, A. B. Besir. Sustainable ventilation strategies in buildings: CFD research, Sustainable Energy Technologies and Assessments. 36 (2019) 100540. doi.org/10.1016/j.seta.2019.100540

[18] P.E. Bournet, T. Boulard. Effect of ventilator configuration on the distributed climate of greenhouses: A review of experimental and CFD studies, Computers and Electronics in Agriculture. 74 (2010) 195-217. doi.org/10.1016/j.compag.2010.08.007

[19] B. Xia, D. W. Sun. Applications of computational fluid dynamics (CFD) in the food industry: a review, Computers and electronics in agriculture. 34 (2002) 5-24. doi.org/10.1016/S0168-1699(01)00177-6

[20] H. K. Versteeg, W. Malalasekera. An introduction to computational fluid dynamics: the finite volume method, Pearson education. (2007).

[21] E. Dick. (1992). Introduction to finite volume techniques in computational fluid dynamics, In Computational fluid dynamics, Springer, Berlin, Heidelberg. (1992) 261-288. https://doi.org/10.1007/978-3-662-11350-9_11

[22] R. Löhner. Applied computational fluid dynamics techniques: an introduction based on finite element methods, John Wiley & Sons. (2008).

[23] J. W. Thomas. Numerical partial differential equations: finite difference methods, Springer Science & Business Media. 22 (2013).

[24] A. Stylianos. The process of heat transfer and fluid flow in CFD problems, American Journal of Science and Technology. 1 (2014) 36-49.

[25] S. Patankar. Numerical heat transfer and fluid flow, Taylor & Francis. (2018).

[26] R. J. LeVeque, R. J. Leveque. Numerical methods for conservation laws. Basel: Birkhäuser. 132 (1992) IX, 214. https://doi.org/10.1007/978-3-0348-5116-9

[27] E. F. Toro. Riemann solvers and numerical methods for fluid dynamics: a practical introduction, Springer Science & Business Media. (2013).

[28] M. K. Thompson, J. M. Thompson. Introduction to ANSYS and Finite Element Modeling, ANSYS Mech. APDL Finite Elem. Anal. (2017)1-9.

[29] L. K. Fung, A. D. Hiebert, L. X. Nghiem. Reservoir simulation with a control-volume finite-element method, SPE Reservoir Engineering. 7 (1992) 349-357. https://doi.org/10.2118/21224-PA

[30] D. V Hutton. Fundamentals of finite element analysis. McGraw-Hill Education. (2003).

[31] J. D. Ramshaw, C. H. Chang. Computational fluid dynamics modeling of multicomponent thermal plasmas, Plasma chemistry and plasma processing. 12 (1992) 299-325. doi.org/10.1007/BF01447028

[32] O. C Zienkiewicz, Y. K Cheung. Finite elements in the solution of field problems, The Engineer. 220 (1965) 507-510.

[33] C. H. Suh, C. W. Radcliffe. Kinematics and mechanisms design, Wiley. (1978).

[34] J. T. Oden, L. C. Wellford Jr. Analysis of flow of viscous fluids by the finite-element method, AIAA Journal. 10 (1972) 1590-1599.

[35] R. H. Pletcher, J. C. Tannehill, D. Anderson. Computational fluid mechanics and heat transfer. CRC press. (2012).

[36] M. N. Özişik, H. R. Orlande, M. J. Colaço, R. M. Cotta. Finite difference methods in heat transfer, CRC press. (2017).

[37] F. Moukalled, L. Mangani, M. Darwish. The finite volume method in computational fluid dynamics, Berlin, Germany: Springer. 113 (2016) 10-1007.

[38] J. Peiró, S. Sherwin. Finite difference, finite element and finite volume methods for partial differential equations. In Handbook of materials modeling, Springer, Dordrecht. (2005) 2415-2446. doi.org/10.1007/978-1-4020-3286-8_127

[39] J. Blazek. Computational fluid dynamics: principles and applications. Butterworth-Heinemann. (2015).

[40] J. H. Ferziger, M. Perić, R. L. Street. Computational methods for fluid dynamics, Berlin: springer. 3 (2002) 196-200. https://doi.org/10.1007/978-3-319-99693-6

[41] B. E. Launder, D. B. Spalding. The numerical computation of turbulent flows. In Numerical prediction of flow, heat transfer, turbulence and combustion Pergamon. (1983) 96-116. https://doi.org/10.1016/B978-0-08-030937-8.50016-7

[42] D. Spalding, S. Patankar. Heat and mass transfer. Morgan-Grampian, London, England. (1967).

[43] A. D. Gosman. Heat and mass transfer in recirculating flows, Academic press. (1969).

[44] K. Nordlund. Historical review of computer simulation of radiation effects in materials, Journal of Nuclear Materials. 520(2019). 273-295. doi.org/10.1016/j.jnucmat.2019.04.028

[45] P. Cardiff, I. Demirdžić. Thirty Years of the Finite Volume Method for Solid Mechanics. Arch Computat Methods Eng. (2021). doi.org/10.1007/s11831-020-09523-0

[46] J. F. Macián Pérez. Numerical and physical modelling approaches to the study of the hydraulic jump and its application in large-dam stilling basins, Doctoral dissertation. (2020). http://hdl.handle.net/10251/149565

[47] Eggenspieler, G. (2011). Turbulence modeling. ANSYS Inc.

[48] W. Rodi. Turbulence modeling and simulation in hydraulics: A historical review,Journal of Hydraulic Engineering.143(2017) 03117001.

[49] Morinishi, Y., Tamano, S., & Nakabayashi, K. (2004). Direct numerical simulation of compressible turbulent channel flow between adiabatic and isothermal walls, J. Fluid Mech. 502(2004) 273–308. DOI: 10.1017/S0022112003007705

[50] Y. Bazilevs, V. M. Calo, J. A. Cottrell, T. J. R. Hughes, A. Reali, G. Scovazzi. (2007). Variational multiscale residual-based turbulence modeling for large eddy simulation of incompressible flows, Computer methods in applied mechanics and engineering. 197(2007) 173-201. doi.org/10.1016/j.cma.2007.07.016

[51] G. Alfonsi. Reynolds-averaged Navier–Stokes equations for turbulence modeling, Applied Mechanics Reviews. 62(2009) 040802-040822. https://doi.org/10.1115/1.3124648

[52] W. Liu, J. Fang, S. Rolfo, C. Moulinec, D. R. Emerson. An Iterative Machine-Learning Framework for Turbulence Modeling in RANS. (2019). DOI:10.1016/j.ijheatfluidflow.2021.108822

[53] F. R. Menter. Two-equation eddy-viscosity turbulence models for engineering applications, AIAA journal. 32(1994) 1598-1605.

[54] A. Keshmiri, A. Revell, H. G. Darabkhani. Assessment of a common nonlinear eddy-viscosity turbulence model in capturing laminarization in mixed convection flows,

Numerical Heat Transfer, Part A: Applications. 69(2016)146-165. doi.org/10.1080/10407782.2015.1069672

[55] D. Cokljat, M. Slack, S. A. Vasquez, A. Bakker, G. Montante. Reynolds-stress model for Eulerian multiphase. Progress in Computational Fluid Dynamics, An International Journal. 6(2006) 168-178. doi.org/10.1504/PCFD.2006.009494

[56] S. Catris, & B. Aupoix. Density corrections for turbulence models, Aerospace Science and Technology. 4(2000) 1-11. doi.org/10.1016/S1270-9638(00)00112-7

[57] H. W. Stock, W. Haase. Determination of length scales in algebraic turbulence models for Navier-Stokes methods, AIAA journal. 27(1989) 5-14.

[58] W. M. Lazeroms, G. Svensson, E. Bazile, G. Brethouwer, S. Wallin, A. V. Johansson. Study of transitions in the atmospheric boundary layer using explicit algebraic turbulence models, Boundary-Layer Meteorology.161 (2016) 19-47. doi.org/10.1007/s10546-016-0194-1

[59] T. J. Wray, R. K. Agarwal. Low-Reynolds-Number One-Equation Turbulence Model Based on k-ω Closure, AIAA Journal. 53(2015)2216-2227.

[60] H. Burchard, O. Petersen. Models of turbulence in the marine environment—A comparative study of two-equation turbulence models, Journal of Marine Systems. 21(1999) 29-53. doi.org/10.1016/S0924-7963(99)00004-4

[61] N. J. Georgiadis, D. A. Yoder, W. A. Engblom. Evaluation of modified two-equation turbulence models for jet flow predictions, AIAA journal.44 (2006) 3107-3114.

[62] Machulskaya, E., & Mironov, D. V. (2020). The Stability Functions and Realizability of the Turbulent Kinetic Energy–Scalar Variance Closure for Moist Atmospheric Boundary-Layer Turbulence, Boundary-Layer Meteorology. 176(2020)197-228. doi.org/10.1007/s10546-020-00528-7

[63] T. Brüning. Improvements in turbulence model realizability for enhanced stability of ocean forecast and its importance for downstream components, Ocean Dynamics. 70(2020)693-700. doi.org/10.1007/s10236-020-01353-9

[64] V. B. Zalesny, S. N. Moshonkin, V. L. Perov, A. V. Gusev. Ocean Circulation Modeling with K-Omega and K-Epsilon Parameterizations of Vertical Turbulent Exchange, Physical Oceanography. 35(2019).

[65] L. Könözsy. The Anisotropic Hybrid k- ω SST/Stochastic Turbulence Model. In A New Hypothesis on the Anisotropic Reynolds Stress Tensor for Turbulent Flows. Springer, Cham. 125 (2021)115-140. doi.org/10.1007/978-3-030-60603-9_2

[66] P. A. Durbin. (1995). Separated flow computations with the k-epsilon-v-squared model, AIAA journal.33 (1995) 659-664.

[67] S. H. Shih, A. Hamed, J. Yeuan. Unsteady supersonic cavity flow simulations using coupled k-epsilon and Navier-Stokes equations, AIAA journal. 32(1994) 2015-2021.

[68] F. H. Harlow, P. I. Nakayama. Transport of turbulence energy decay rate, Los Alamos Scientific Lab., N. Mex. (No. LA-3854). (1968).

[69] B. E. Launder, D. B. Spalding. Lectures in mathematical models of turbulence. (1972).

[70] D. C. Wilcox, Turbulence modeling for CFD, La Canada, CA: DCW industries. 2 (1998)103-217.

[71] P. J. Richards, S. E. Norris. Appropriate boundary conditions for computational wind engineering: Still an issue after 25 years, Journal of Wind Engineering and Industrial Aerodynamics. 190(2019) 245-255. doi.org/10.1016/j.jweia.2019.05.012

[72] K. W. Stapleton, E. Guentsch, M. K. Hoskinson, W. H. Finlay. On the suitability of k–ε turbulence modeling for aerosol deposition in the mouth and throat: a comparison with experiment, Journal of Aerosol Science. 31(2000)739-749.doi.org/10.1016/S0021-8502(99)00547-9

[73] V. C. Patel, W. Rodi, G. Scheuerer. Turbulence models for near-wall and low Reynolds number flows-a review, AIAA journal. 23(1985)1308-1319.

[74] R. A. W. M. Henkes, F. F. Van Der Vlugt, C. J. Hoogendoorn. Natural-convection flow in a square cavity calculated with low-Reynolds-number turbulence models. International Journal of Heat and Mass Transfer.34 (1991) 377-388. https://doi.org/10.1016/0017-9310(91)90258-G

[75] Y. Cheng, F. S. Lien, E. Yee, R. Sinclair, A comparison of large eddy simulations with a standard k–ε Reynolds-averaged Navier–Stokes model for the prediction of a fully developed turbulent flow over a matrix of cubes, Journal of Wind Engineering and Industrial Aerodynamics. 91 (2003)1301-1328. doi.org/10.1016/j.jweia.2003.08.001

[76] B. N. Murthy, J. B. Joshi. Assessment of standard k–ε, RSM and LES turbulence models in a baffled stirred vessel agitated by various impeller designs, Chemical engineering science. 63(2008)5468-5495. https://doi.org/10.1016/j.ces.2008.06.019

[77] D. B. Spalding, Mathematical models of turbulent flames; a review, Combustion Science and Technology. 13 (1976), 3-25. https://doi.org/10.1080/00102207608946727

[78] A. Kumar, A. Ghobadian, J. M Nouri. Assessment of cavitation models for compressible flows inside a nozzle, Fluids. 5 (2020) 134. doi.org/10.3390/fluids5030134

[79] S. W. Choi, H. S. Kim. Predicting turbulent flows in butterfly valves with the nonlinear eddy viscosity and explicit algebraic Reynolds stress models, Physics of Fluids. 32(2020) 085105. doi.org/10.1063/5.0006896

[80] X. Zhang, A. U. Weerasuriya, K. T. Tse. CFD simulation of natural ventilation of a generic building in various incident wind directions: Comparison of turbulence modelling, evaluation methods, and ventilation mechanisms, Energy and Buildings. 229(2020)110516. doi.org/10.1016/j.enbuild.2020.110516

[81] M. E. Nakhchi, J. A. Esfahani. Entropy generation of turbulent Cu–water nanofluid flow in a heat exchanger tube fitted with perforated conical rings, Journal of Thermal Analysis and Calorimetry. 138(2019) 1423-1436. doi.org/10.1007/s10973-019-08169-w

[82] T. H. Shih, W. W. Liou, A. Shabbir, Z. Yang, J. Zhu. A new k-ϵ eddy viscosity model for high reynolds number turbulent flows, Computers & fluids. 24(1995)227-238. doi.org/10.1016/0045-7930(94)00032-T

[83] V. Yakhot, S. A. Orszag, Renormalization group analysis of turbulence. I. Basic theory, Journal of scientific computing. 1 (1986) 3-51. doi.org/10.1007/BF01061452

[84] Y. Liu, H. Li, G. Feng. February). Simulation of inhalable aerosol particle distribution generated from cooking by Eulerian approach with RNG k–epsilon turbulence model and pollution exposure in a residential kitchen space. In Building Simulation. Tsinghua University Press. 10 (2017) 135-144. doi.org/10.1007/s12273-016-0313-4

[85] F. Perini, K. Zha, S. Busch, R. Reitz. Comparison of linear, non-linear and generalized RNG-based k-epsilon models for turbulent diesel engine flows, SAE Technical Paper. (2017). https://doi.org/10.4271/2017-01-0561.

[86] K. Hanjalić, S. Kenjereš. Some developments in turbulence modeling for wind and environmental engineering, Journal of Wind Engineering and Industrial Aerodynamics. 96 (2008) 1537-1570. doi.org/10.1016/j.jweia.2008.02.054

[87] M. Sheikholeslami, S. A. Farshad, A. Shafee, H. Babazadeh. Performance of solar collector with turbulator involving nanomaterial turbulent regime, Renewable Energy. 163 (2021) 1222-1237. doi.org/10.1016/j.renene.2020.08.144

[88] X. Zhang, A. U. Weerasuriya, K. T. Tse. CFD simulation of natural ventilation of a generic building in various incident wind directions: Comparison of turbulence modelling, evaluation methods, and ventilation mechanisms, Energy and Buildings. 229 (2020) 110516. doi.org/10.1016/j.enbuild.2020.110516

[89] R. Shen, Z. Jiao, T. Parker, Y. Sun, Q. Wang. Recent application of Computational Fluid Dynamics (CFD) in process safety and loss prevention: A review, Journal of Loss Prevention in the Process Industries. (2020) 104252. doi.org/10.1016/j.jlp.2020.104252

[90] Turbulence Modeling. Introductory FLUENT, https://imechanica.org/files/fluent_13.0_lecture06-turbulence.pdf.

[91] M. D. G. Carvalho, T. Farias, P. Fontes. Radiative heat transfer in absorbing, emitting, and scattering media, Journal of heat transfer. 87 (1991) 161-162. doi:10.1115/1.3689065

[92] N. G. Shah. A new method of computation of radiant heat transfer in combustion chambers, Doctoral dissertation, University of London. (1979).

[93] R. H. J. R. Siegel, J. R. Howell. Thermal radiation heat transfer, Hemisphere Pub. Corp., Washing ton DC. (1992).

[94] P. Cheng. (1964). Two-dimensional radiating gas flow by a moment method. AIAA journal. 2 (1964) 1662-1664.

[95] E. H. Chui, G. D. Raithby. Computation of radiant heat transfer on a nonorthogonal mesh using the finite-volume method, Numerical Heat Transfer. 23 (1993), 269-288. https://doi.org/10.1080/10407799308914901

[96] G. D. Raithby, E. H. Chui. (1990). A finite-volume method for predicting a radiant heat transfer in enclosures with participating media, *J. Heat Transfer*. 112 (1990) 415-423. https://doi.org/10.1115/1.2910394

[97] Overview and Limitations, https://www.afs.enea.it/project/neptunius/docs/fluent/html/th/node110.htm

[98] A. Farhadi, A. Mayrhofer, M. Tritthart, M. Glas, H. Habersack. Accuracy and comparison of standard k-ϵ with two variants of k-ω turbulence models in fluvial applications. Engineering Applications of Computational Fluid Mechanics, 12 (2018) 216-235. doi.org/10.1080/19942060.2017.1393006

[99] V. R. Gopala, B. G. van Wachem. (2008). Volume of fluid methods for immiscible-fluid and free-surface flows, Chemical Engineering Journal. 141 (2008) 204-221. doi.org/10.1016/j.cej.2007.12.035

[100] I. R. Park. A volume of fluid method for free surface flows around ship hulls, Journal of computational fluids engineering. 20 (2015) 57-64. https://doi.org/10.6112/kscfe.2015.20.1.057

[101] D. M. Hargreaves, H. P. Morvan, N. G. Wright. Validation of the volume of fluid method for free surface calculation: the broad-crested weir. Engineering Applications of

Computational Fluid Mechanics, 1 (2007), 136-146. doi.org/10.1080/19942060.2007.11015188

[102] F. Losasso, R. Fedkiw, S. Osher. Spatially adaptive techniques for level set methods and incompressible flow, Computers & Fluids. 35 (2006) 995-1010. doi.org/10.1016/j.compfluid.2005.01.006

[103] L. Wu, M. Gong, J. Wang. Development of a DEM–VOF model for the turbulent free-surface flows with particles and its application to stirred mixing system, Industrial & Engineering Chemistry Research. 57 (2018) 1714-1725. doi.org/10.1021/acs.iecr.7b04833

[104] Y. L. Li, C. P. Ma, X. H. Zhang, K. P. Wang, D. P. Jiang.Three-dimensional numerical simulation of violent free surface deformation based on a coupled level set and volume of fluid method. Ocean Engineering. 210 (2020) 106794. doi.org/10.1016/j.oceaneng.2019.106794

[105] S. Banerjee, R. K. Agarwal. An Eulerian approach to computational fluid dynamics simulation of a chemical-looping combustion reactor with chemical reactions, Journal of Energy Resources Technology. 138 (2016). doi.org/10.1115/1.4031968

[106] R. Safa, A. S. Goharrizi. CFD simulation of an industrial hydrocyclone with Eulerian–Eulerian approach: A case study, International Journal of Mining Science and Technology. 24 (2014) 643-648. doi.org/10.1016/j.ijmst.2014.07.010

[107] T. S. Zaripov, A. K. Gilfanov, S. M. Begg, O. Rybdylova, S. S. Sazhin, M. R. Heikal. The fully lagrangian approach to the analysis of particle/droplet dynamics: Implementation into ansys fluent and application to gasoline sprays, Atomization and Sprays. 27 (2017) 493-510. DOI:10.1615/ATOMIZSPR.2017019354

[108] R. Danchin, P. B. Mucha. (2017). Compressible Navier–Stokes system: large solutions and incompressible limit, Advances in Mathematics. 320 (2017) 904-925. doi.org/10.1016/j.aim.2017.09.025

[109] A. Klimanek, W. Adamczyk, A. Katelbach-Woźniak, G. Węcel, A. Szlęk. Towards a hybrid Eulerian–Lagrangian CFD modeling of coal gasification in a circulating fluidized bed reactor. Fuel. 152 (2015) 131-137. doi.org/10.1016/j.fuel.2014.10.058

[110] O. Z. Sharaf, A. N. Al-Khateeb, D. C. Kyritsis, E. Abu-Nada. Direct absorption solar collector (DASC) modeling and simulation using a novel Eulerian-Lagrangian hybrid approach: Optical, thermal, and hydrodynamic interactions. Applied energy, 231 (2018) 1132-1145. doi.org/10.1016/j.apenergy.2018.09.191

[111] D. I. Kolaitis, M. A. Founti. A comparative study of numerical models for Eulerian–Lagrangian simulations of turbulent evaporating sprays. International Journal of Heat and Fluid Flow. 27 (2006) 424-435. doi.org/10.1016/j.ijheatfluidflow.2006.01.002

[112] L. Malan. Direct numerical simulation of free-surface and interfacial flow using the VOF method: cavitating bubble clouds and phase change. Mechanics of the fluids, Université Pierre et Marie Curie – Paris. (2018).

[113] Y. Shen, C. Shi, L. Zhang, S. Bu, W. Xu, Z. Zhang, X. Liu. (2021). Falling film evaporation in a vertical tube with a new type of liquid distributor designed using the brachistochrone principle, Vacuum. 187 (2021) 110023. doi.org/10.1016/j.vacuum.2020.110023

[114] M. Mahdavi, M. Sharifpur, J. P. Meyer. Fluid flow and heat transfer analysis of nanofluid jet cooling on a hot surface with various roughness. International Communications in Heat and Mass Transfer, 118 (2020) 104842. doi.org/10.1016/j.icheatmasstransfer.2020.104842

[115] D. L. Youngs. Time-dependent multi-material flow with large fluid distortion, Numerical methods for fluid dynamics. (1982).

[116] D. L. Youngs. An interface tracking method for a 3D Eulerian hydrodynamics code, Atomic Weapons Research Establishment (AWRE) Technical Report. 44 (1984) 35.

[117] F. Xiao, Y. Honma, T. Kono. (2005). A simple algebraic interface capturing scheme using hyperbolic tangent function, International Journal for Numerical Methods in Fluids. 48 (2005) 1023-1040.

[118] J. P. Fürstenau, C. Weißenfels, P. Wriggers. Free surface tension in incompressible smoothed particle hydrodynamcis (ISPH), Computational Mechanics. 65 (2020) 487-502. doi.org/10.1007/s00466-019-01780-6

[119] S. Bagheri, A. Kabiri-Samani. Simulation of free surface flow over the streamlined weirs, Flow Measurement and Instrumentation. 71 (2020) 101680. doi.org/10.1016/j.flowmeasinst.2019.101680

[120] A. Franci, I. de-Pouplana, G. Casas, M. Á. Celigueta, J. González-Usúa, E. Oñate. PFEM–DEM for particle-laden flows with free surface, Computational Particle Mechanics. 7 (2020) 101-120. doi.org/10.1007/s40571-019-00244-1

[121] T. Frank, S. Jain, A. A. Matyushenko, A. V. Garbaruk. (2012, September). The OECD/NEA MATIS-H benchmark-CFD analysis of the water flow through a 5× 5 rod bundle with spacer grids using ANSYS Fluent and ANSYS CFX, In Conference on

Experimental Validation and Application of CFD and CMFD Codes in Nuclear Reactor Technology, OECD/NEA and IAEA Workshop. 10 (2012) 12.

[122] S. F. Hosseinizadeh, A. R. Darzi, F. L. Tan. Numerical investigations of unconstrained melting of nano-enhanced phase change material (NEPCM) inside a spherical container, International Journal of Thermal Sciences. 51 (2012) 77-83. doi.org/10.1016/j.ijthermalsci.2011.08.006

[123] M. D. Muhammad, O. Badr, H. Yeung. Validation of a CFD melting and solidification model for phase change in vertical cylinders, Numerical Heat Transfer, Part A: Applications. 68 (2015) 501-511. doi.org/10.1080/10407782.2014.994432

[124] J. M. Cascón, E. Rodríguez, J. M. Escobar, R. Montenegro. Comparison of the meccano method with standard mesh generation techniques, Engineering with Computers. 31 (2015), 161-174. doi.org/10.1007/s00366-013-0338-6

[125] S. V. Patankar, D. B. Spalding. A calculation procedure for heat, mass and momentum transfer in three-dimensional, Numerical prediction of flow, heat transfer, turbulence and combustion. 54 (2015).

[126] H. K. Versteeg, W. Malalasekera. Computational fluid dynamics: the finite volume method, Harlow, England: Longman Scientific & Technical. (1995).

[127] R. Eymard, T. Gallouët, R. Herbin. (2000). Finite volume methods. Handbook of numerical analysis. 7 (2000) 713-1018.

[128] H. K. Versteeg, W. Malalasekera. An introduction to computational fluid dynamics: the finite volume method. Pearson education. (2007).

[129] C. Zhang, H. Chen, G. Zhao, L. Zhang, S. Lou. Optimization of porthole extrusion dies with the developed algorithm based on finite volume method, The International Journal of Advanced Manufacturing Technology. 85 (2016) 1901-1913. doi.org/10.1007/s00170-016-8522-7

Chapter III

Numerical modeling of hybrid PV/ T system with passive air-cooling

III.1 Introduction

Hybrid photovoltaic/thermal systems are an important energy technology due to their efficiency in producing both electrical and thermal energy, and their ease of incorporation into the roofs of buildings.

The rising of solar photovoltaic modules operating temperature is a major problem, which affects negatively their performance. The present study focused in detail on the turbulent natural air circulation (passive technique) of a new hybrid PV/T system to reduce their operating temperature and achieve an optimal design able to cool efficiently the PV module backside.

The finite volume method is used to solve the governing transport equations and the standard k-ε turbulence model is implemented for describing the turbulent fluctuations of natural convection. A sloped entrance channel (SEC) and aluminum flat plate (AFP) are installed to improve the heat transfer of a new hybrid PV/T system. Influences of SEC geometric parameters, AFP number, and their distance to the PV module on average Nusselt number are examining.

Besides, the impact of the PV/T system tilted angle and Rayleigh number on the thermo-hydrodynamic flow behavior.

The main aims of the present CFD analysis are:

1. Investigating the effect of the sloped entrance channel dimension on the heat transfer rate.
2. Rayleigh number and tilted angle effects on thermo-hydrodynamic flow behavior.
3. Proposing correlations of average Nusselt number versus of SEC dimension and Rayleigh numbers for industry engineering use.
4. Developing numerically an optimal geometry of a new solar hybrid PV/T system with high performance.

This part of the study is organized as follows: Section 2 describes the physical model. Section 3, thermal and hydrodynamic parameters are assessed. Discussion of the main results is presented in Section 4. Section 5 shows the main conclusions and perspectives.

III.2 Physical model description

Figure III. 1 represents both considered configurations of the hybrid PV/T air system in the case by using a passive air cooling technique.

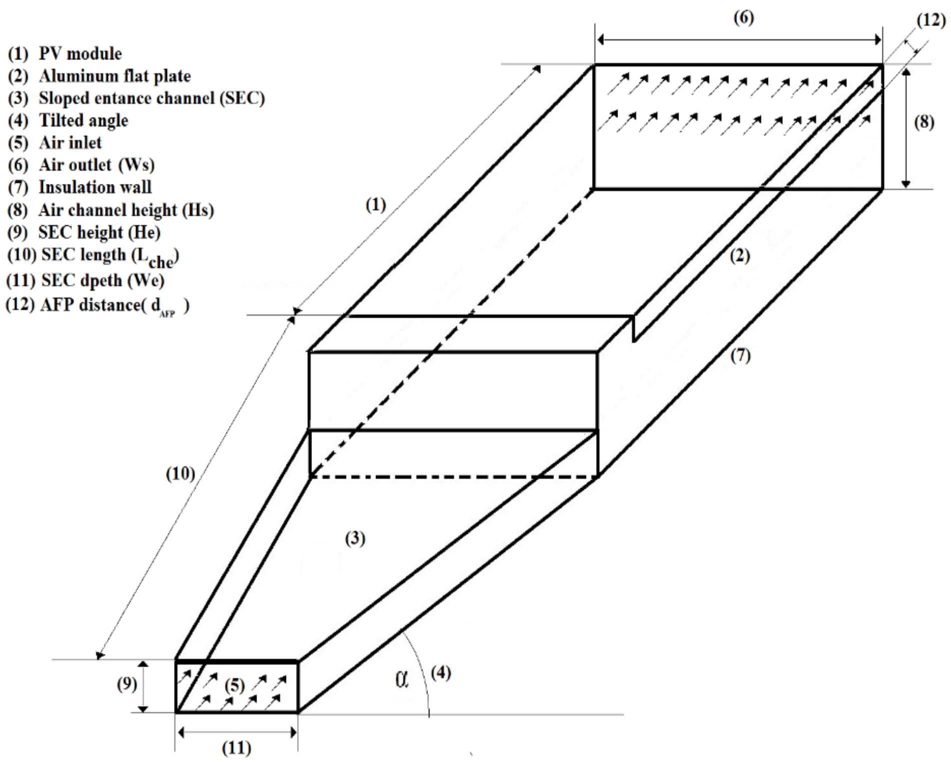

Figure III.1 *Sketch of the physical model of the studied configurations using passive air cooling*

The first step is designed in a manner to cool the PV module from the backside with natural air circulation for fixed a tilted angle to optimize the geometric parameters. The second step is focused to study the hydrodynamic parameters such as tilted angle and modified Rayleigh number on the average Nusselt number and heat gain.

Moreover, an aluminum flat plate AFP is installed in the air channel at different positions to enhance the heat transfer of the PV module (see **figure III.1**). **Table III. 1** summaries All geometric parameters, symbols and their values of studied configurations.

Table. III. 1 : Dimensions of the considered configurations of New hybrid PV/T system solar collector

Geometric parameters	**Symbol**	**Values**
PV module length	L_{PV}	1.2
Air channel gap	S	0.14
Air channel length	L_{ch}	1.2
Entrance sloped air channel length	L_{che}	0-1.2
Entrance channel Depth	W_e	0.15-0.57
Entrance channel size	H_e	0.01-0.14
Aluminum Flat plate Length	L_{afp}	1.17
Aluminum Flat plate depth	W_{afp}	0.57
Aluminum Flat plate thickness	E_{afp}	0.001
Aluminum Flat plate Number	N_{afp}	0-6
Aluminum Flat plate distance to PV	d_{afp}	0-0.13

Table III .2 shows the studied scenarios in this work. For the first time, the air channel tilted angle is fixed to α =30° and carried the SEC dimensions to optimize the geometry and subject for three Rayleigh numbers.

Table. III. 2 : Studied cases in this work

Studied cases	Ra_m, Ra_L	L_{che}(m)	He (m)	We(m)	N_{AFP}	d_{AFP}(m)	α
Case 1	$Ra_m = 8.12*10^8$ $Ra_m = 2.44*10^9$ $Ra_m = 4.06*10^9$	$0 \le L_{Che} \le 1.2$	0.01-0.14	0.15-0.57	1	0.07	30°
Case 2	$Ra_m = 8.12*10^8$ $Ra_m = 2.44*10^9$ $Ra_m = 4.06*10^9$	L_{Che}=0.735	He=0.05	0.3	0-4	0.01-0.13	30°
Case 3	$1.62*10^8 \le Ra_L \le 8.12*10^9$	L_{che}*=0.625	He*=0.36	We*=0.52	1	d_{AFP}= 0.03	$0° \le \alpha \le 90°$
Case 4	$1.62*10^8 \le Ra_L \le 8.12*10^9$	L_{che}*=0.625	He*=0.36	We*=0.52	1	d_{AFP}= 0.03	$0° \le \alpha \le 90°$

After that, the optimal AFP number and distance to the PV module surface are obtained. The third step of the new optimal geometry is tested for different tilted angles such as (0 =<α =<90°) and for different Rayleigh numbers.

III.3 Computational method

3D Dimensional numerical simulations are used to compute the thermal and hydrodynamic flow behavior of the PV/T system. The numerical solution of the governing equations presented above with the associated boundary conditions is based on the finite volume technique.

The SIMPLE algorithm treats the pressure-velocity coupling. The standard k-ε turbulence model used for modeling the turbulent properties of the flow. Convergence criteria have declared when the maximum relative change between two consecutive iterations fell below for momentum and energy and mentioned as 10^{-5} and 10^{-6}, respectively.

III.3 .1 Numerical procedure

ANSYS FLUENT 16 is a CFD code based on the finite volume method and is a well-established commercial software used in various fields including fluid dynamics .The steady pressure-based solver is used to solve governing equations. A SIMPLE algorithm is used for pressure and velocity terms coupling.

The central difference scheme is used for the discretization of momentum and energy equations, whereas discretization of convective terms is done using a second-order upwind scheme. The present investigation is carried out in an Intel 5-core CPU with a RAM size of 8GB, 3.60 Hz, and 64-bit Windows 7.

III.3 .2 Simplifying assumptions

Several assumptions were prepared before performing numerical simulations, these assumptions, which are imposed for the first application (passive air-cooling), second application (active-air cooling), and third application (active hybrid PV/T Bi-fluid) were as follows:

1. **First application (passive air cooling)**
   - The flow regime is a steady-state, turbulent regime.
   - The geometry is created in three-dimensional with a symmetry plane
   - The air channel walls are homogeneous and isotropic.
   - The working fluid (air) is assumed to be incompressible and Newtonian.
   - No-slip boundary condition is assigned to all walls.
   - Negligible radiation heat transfer.
2. **Second application (active air cooling)**
   - The flow regime is a steady-state, turbulent regime.
   - The geometry is created in three-dimensional with a symmetry plane
   - The air channel walls are homogeneous and isotropic.
   - The working fluid (air) is assumed to be incompressible and Newtonian.
   - No-slip boundary condition is assigned to all walls.
   - Negligible radiation heat transfer.
   - The air inlet velocity is sopposed as uniform

III.3 .3 Governing equations

Three-dimensional numerical simulation was performed by CFD ANSYS to understand thermo-hydrodynamic flow behaviors in a new hybrid PV/T system. The simulation was carried out to calculate and explain the experimental conditions. It involves mathematical solutions of the conservation equations for mass, momentum, and energy. Steady-state flow in the new hybrid PV/T air solar collector was simulated in this study.

The mass conservation, momentum, and energy equations (III.1) - (III.4) are solved numerically using the finite volume method evaluated by Patankar. Because of the small temperature difference in the air that occurs between the heated wall and the openings, the Navier-Stokes equations and energy have been expressed with the Boussinesq approximation.

The fluid is Newtonian, incompressible and its constant thermophysical properties (ρ, Cp, k, μ. These governing equations for incompressible fluid expressed as follows **[1, 2]**:

Continuity equation

$$\frac{\partial \rho}{\partial x_j}\left(\rho u_j\right)=0 \quad \text{(III.1)}$$

Momentum equations

$$\frac{\partial \rho}{\partial x_j}\left(\rho u_i u_j\right)=-\frac{\partial P}{\partial x_i}+\frac{\partial}{\partial x_i}\left[u\left(\frac{\partial u_i}{\partial x_j}+\frac{\partial u_j}{\partial x_i}\right)\right]-\left(\overline{\rho u'_i u'_j}\right) \quad \text{(III.2)}$$

Energy equation

$$\frac{\partial}{\partial x_j}\left(\rho u_i T\right)=\frac{\partial}{\partial x_j}\left[\left(\frac{u_i}{Pr}+\frac{u_t}{\sigma_t}\right)\frac{\partial T}{\partial x_j}\right] \quad \text{(III.3)}$$

Where ρ is the air density, P static pressure, σ_t is the stress tensor, u is velocity. The governing equations are discretized using the finite volume method, which is to convert the transport equations to algebraic equations which are solved by an iterative process using CFD software.The Reynolds-averaged techniques of turbulence modeling require suitable modeling of the Reynolds stresses, $\overline{\rho u'_i u'_j}$.

One common technique uses the Boussinesq approximation to relate Reynolds strains to average velocity gradients.

$$\overline{\rho u'_i u'_j}=u_t\left(\frac{\partial u_i}{\partial x_j}+\frac{\partial u_j}{\partial x_i}\right)-\frac{2}{3}k\delta_{ij} \quad \text{(III.4)}$$

The turbulent viscosity term μ_t can be calculated from a suitable turbulence model. The appearance of the turbulent viscosity is specified as.

$$\mu_t=\rho C_\mu \frac{k^2}{\varepsilon} \quad \text{(III.5)}$$

III.3 .4 Turbulence models

The k-ε model is a turbulent viscosity group model, based on the Boussinesq gradient hypothesis, which relates the turbulent stresses to the mean-field, as in the case of viscous stresses. The constraints, which appear in the preceding equations. One of the advantages of this method is taking into account the spatial variability of turbulent agitation and its simplicity of implementation. Its turbulent kinetic energy and its dissipation rate are given by **[3]**:

$$\frac{\partial \rho}{\partial x_i}(\rho k u_i)=\frac{\partial \rho}{\partial x_j}\left[\left(\mu+\frac{\mu_t}{\sigma_k}\right)\frac{\partial k}{\partial x_j}\right]+G_k-\rho\varepsilon \quad \text{(III.6)}$$

$$\frac{\partial \rho}{\partial x_i}(\rho \varepsilon u_i)=\frac{\partial \rho}{\partial x_j}\left(\left(\mu+\frac{\mu_t}{\sigma_\varepsilon}\right)\frac{\partial \varepsilon}{\partial x_j}\right)+C_{1\varepsilon}\frac{\varepsilon}{k}(G_k)-C_{2\varepsilon}\rho\frac{\varepsilon^2}{k} \quad \text{(III.7)}$$

Where $G_k=-\rho\overline{u'u'}\frac{\partial ui}{\partial uj}$ represents the production of turbulent kinetic energy.

Where k represents the generation of turbulence kinetic energy due to the mean velocity gradients, ε and are the inverse effective Prandtl numbers for k, and, ε respectively.

Table. III. 3 summerizes the different constant for the standard turbulent model.

Table. III. 3:Turbulent constant for k-ε standard models

Constant	C_1	C_2	C_u	f_1	f_2	Pr_t	σ_k	σ_ε
Value	1.44	1.92	0.09	1.0	1.0	0.85	1.0	1.3

III.3 .5 Boundary conditions applied for computational domain

Firstly, it considers a three-dimensional open channel asymmetrically heated by a constant temperature imposed on the two PV modules and absorber (see **Table. III 4**).

All walls in this system have no-slip and impermeable boundary conditions. The working fluid applied to the interior domain is the air. The ambient temperature considered with constant physical proprieties in the air channel. The following boundary conditions are implemented on the CFD model:

- No-slip boundary condition for all the walls
- Fully developed air with non-uniform velocity enters at an inlet temperature and turbulent intensity of 300 K and 5 % respectively.
- A pressure outlet is imposed at the outlet air channel.
- Pressure inlet is imposed at the sloped entrance air channel.
- A constant, uniform temperature is imposed uniformly on the PV module surface.
- Right sidewalls are imposed with symmetry boundary conditions, due to symmetrical geometry.
- Adiabatic boundary conditions were imposed for the Left sidewall and base sidewall.

➢ All these boundary conditions were localized in detail in the **figure. III.2.**

Table III. 4: Boundary conditions used in the present simulation for the fluid and solid

Wall surface	**Boundary conditions**	**Mathematical expression**
SEC inlet	Pressure inlet	$\Delta P_{in} = 0,$ (gauge pressure), $T = T_{amb}$
Air channel outlet	Pressure Outlet	$P = P_{atm}, T = T_{amb}$
PV module surface	Wall	$u = v = 0, \mathrm{T} = \mathrm{T}_{\mathrm{PV}}$
Lateral side wall	adiabatic	$\partial T/\partial x = \partial T/\partial y = 0,$
Base wall	adiabatic	$\partial T/\partial y = \partial T/\partial z = 0,$
SEC surface	adiabatic	$\partial T/\partial x = \partial T/\partial z = 0,$
Aluminum Flat plate **(AFP)**	Thermal coupled	$k_{al} \nabla T_{\sup} = k_{al} \nabla T_{\inf} = \mathrm{T}_{\mathrm{AFP}},$

Figure III. 2 represents the computational domain of both configuration and implemented boundary conditions. It is noticed that, boundary conditions, which implemented to describe the current problem to solve it numerically.

In the numerical simulation, the mesh form has obeyed to the best distribution of volumes in the domain, with the possibility of refining the details wherever necessary.

As an example, **figure III.3** shows the mesh detail for computational domain calculation of the new hybrid PV/T system. The structured mesh type is the best grid for the CPU calculator and the reliability of the solution.

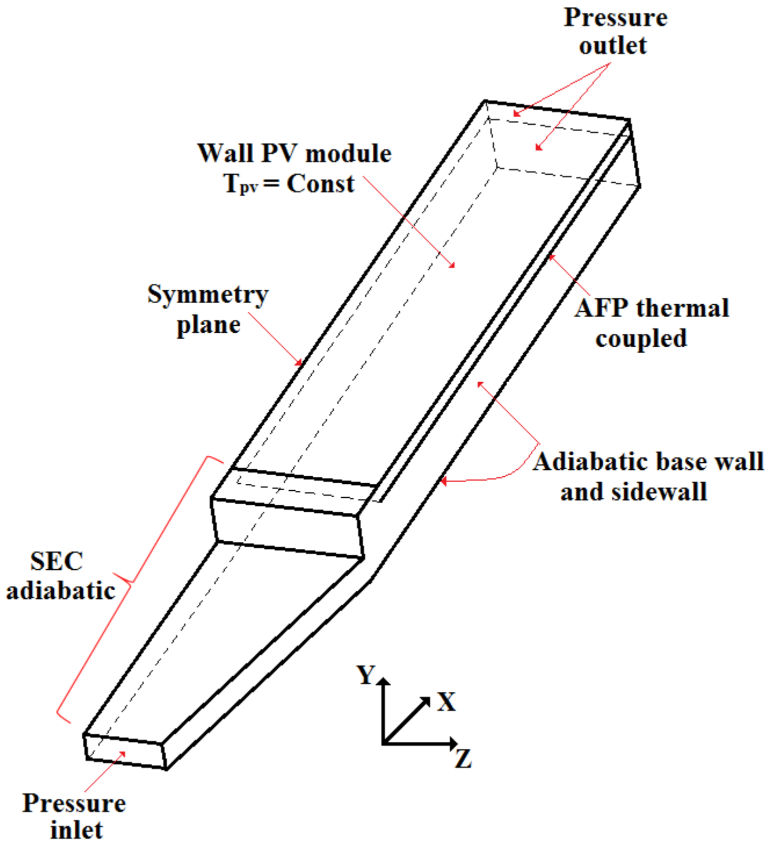

Figure III. 2: *The computational domain and Boundary conditions of both configurations of PV/T system for passive air cooling case*

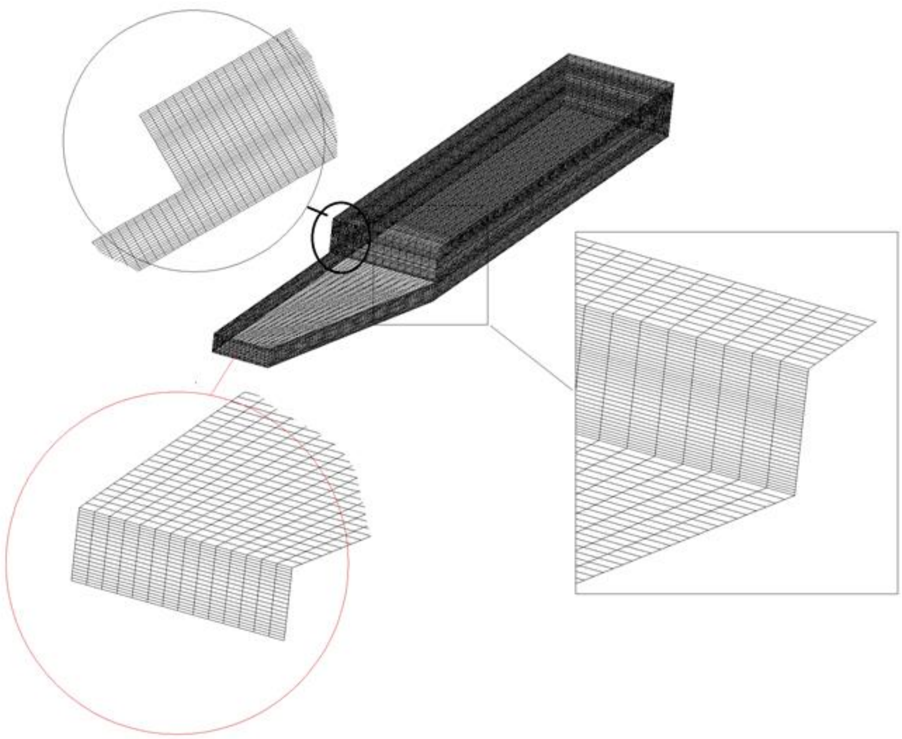

Figure III. 3: *Mesh generation and computational domain calculating of PV/T air solar collector*

III.4 Thermo-hydrodynamic parameters assessment

- **Grashof number**

The Grashof number based on PV module length, $Gr_{L_{PV}}$ is defined as follows:

$$Gr_{L_{PV}} = \frac{g\beta(T_{PV} - T_{amb})L_{PV}^{3}}{\nu^{2}} \quad \text{(III. 8)}$$

Where β is the thermal expansion coefficient, T_{PV} is the PV module average temperature, T_{amb} is ambient air temperature, ν is the kinematic viscosity of air, and g is the acceleration of gravity.

- **Prandtl number**

$$Pr = \frac{\nu}{\delta} \quad \text{(III. 9)}$$

Here ν is fluid viscosity and thermal diffusivity.

- **Rayleigh number**

The Rayleigh number based on PV length, Ra is defined as follows:

$$Ra_L = Pr.Gr = \frac{g\beta(T_{PV} - T_{amb})L^3}{\nu\delta} \quad \text{(III. 10)}$$

Where β is the thermal expansion coefficient, T_{PV} is the PV module surface temperature, T_{amb} is ambient air temperature, ν is kinematics viscosity of air, δ is thermal diffusivity of air and g is the acceleration of gravity.

Modified Rayleigh number is expressed by following equation.

$$Ra_m = Ra_L \cos(\alpha) \quad \text{(III. 11)}$$

- **Nusselt number**

The average Nusselt number of the solar panels is presented as [**4**]:

$$Nu_{L\_avg} = \frac{h_{c\_avg} \times L_{PV}}{k_f} \quad \text{(III. 12)}$$

Where k_f is thermal conductivity of fluid (air), the heat transfer coefficient h, and L the length of PV module. *Where; h_{avg_c} represents the average convective heat transfer coefficient is expressed:*

$$\bar{h} = \int_{\substack{exposed\\surface}} h_{conv} \times dn \quad \text{(III. 13)}$$

➢ **Airflow consideration**

The average air velocity inside the air channel depends on the difference in interior air temperature between and entrance air ambient to the friction of the wall and drops pressure. In addition, the average air velocity is mentioned by equations **[5]**:

$$f\,\frac{L_{PV}}{D_H}\frac{\rho_a V^2}{2}+k_{in}\frac{\rho_a V^2}{2}+k_{out}\frac{\rho_a V^2}{2}=H_{ch}.\mathrm{g}.\sin\alpha.(\rho_0-\rho_a) \qquad \text{(III. 14)}$$

With H_{ch} is the height $H_{ch}=L_{PV}.\sin\alpha$

Correspondingly, the equation for the velocity of the air inside the air channel is obtained as follows.

$$v=\left[\frac{2g.L_{PV}.(\sin\alpha)^2(\rho_o-\rho_a)}{(f.\frac{L_{PV}}{D_h}+k_{in}+k_{out}).\rho_a}\right]^{1/2} \qquad \text{(III. 15)}$$

Where f is the coefficient of friction (f = 0.056), k_{in} and k_{out} are the input and output pressure drops (1.5 and 1.0), **[6]**, L is the length of the channel, D_H is the hydraulic diameter of the rectangular channel (Dh = 2wS /(w + S), ρ_o is the density of the ambient air, ρ_a is the density of the air, V is the average air velocity, H_{ch} is the difference of height between the inlet and the outlet of the channel, W is the width of the channel and S is their spacing.

III.5 Results and discussions

In this section, firstly the effect of geometric parameters by passive air cooling and hydrodynamic parameters for active air-cooling has been presented.

Secondly, the impact of geometric parameters of the sloped entrance air channel such as length, depth, and height on the transfer rate was performed.

Thirdly, the number of aluminum flat plates and their distance to the PV module on the heat transfer rate is evaluated in this section.

Fourthly, the influence of Rayleigh number and tilted angle on the temperature and velocity field was presented. Moreover, tilted angle and Rayleigh number effects on the mass flow rate, heat gain rate, skin friction coefficient, pressure drop, and average Nusselt number were treated in detail.

Finally, a comparison with previous works concerning the correlations of the average Nusselt number against to the Rayleigh number for natural convection is carried out.

III.5.1 Solver code validation

The validation of the numerical model is carried out under the same conditions of experimental studies examined by Onur et al. **[7]**. **Figure III. 4** presents the average Nusselt number evolution for fixed channel gap size as a function of Rayleigh numbers, Ra.

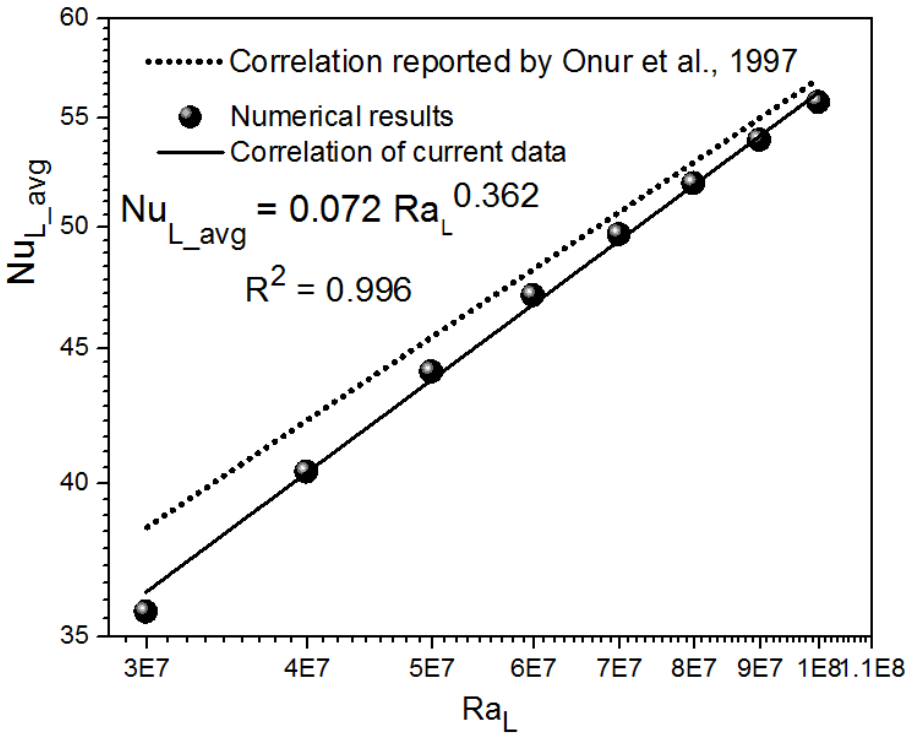

Figure III. 4: *Variation of average Nusselt number versus Rayleigh number for S = 10mm*

From **figure III. 4** appears that the numerical results are in good agreement with the experimental data reported by the ref. **[7].** It noticed also that the average Nusselt number is very performed for high values Rayleigh number and with a maximum error of about ε = 7%. The correlation of the average Nusselt number against the Rayleigh number is fitted by the following equation:

$$Nu_{H\_avg} = 0.072(Ra)^{0.362}, \qquad \text{(III. 16)}$$

III.5.2 Grid generation and dependence study

Figure III. 5 displays the average Nusselt number evolution versus nodes number for a fixed modified Rayleigh, Ra_m. The mesh test study is used to ensure that the numerical solution is independent of the grille nodes.

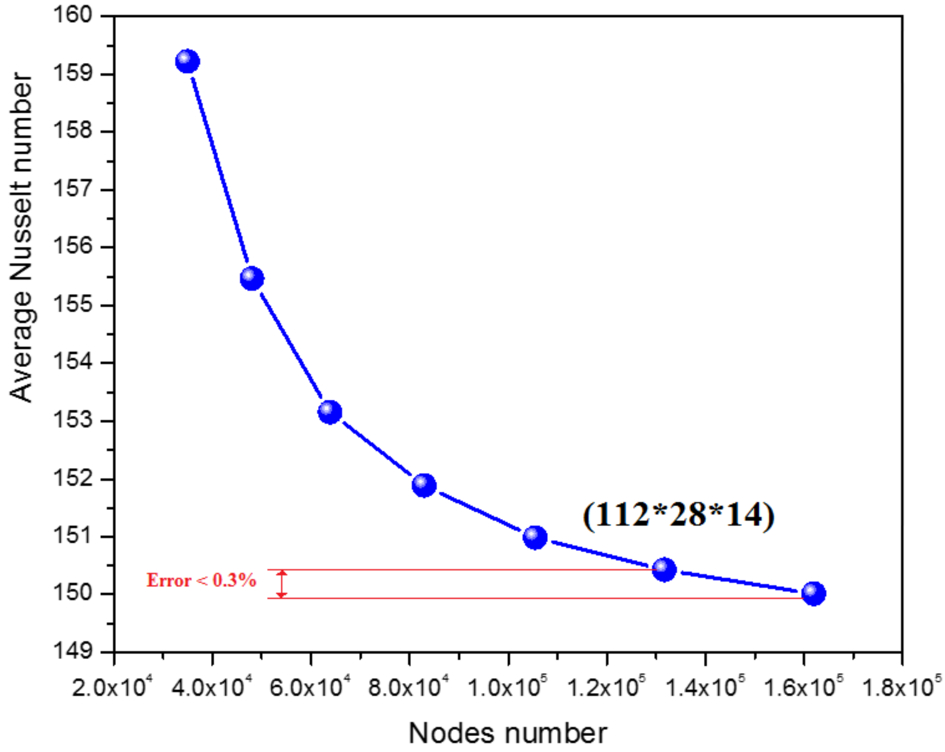

Figure III. 5: *Nodes number effect on the average Nusselt number for α=30° and with AFP configuration for fixed Rayleigh at* $Ra_m=4.06x10^9$

It is clear that the mesh (112*28*14) nodes, present a better solution, to optimize the CPU time(2Hours) and the cost of the running calculations.

III.5.3 Sloped entrance air channel dimensions effect on the average Nusselt number

In this sub-section, geometric parameters of SEC such as length, height, and depth for the fixed tilted angle (α=30°) with AFP case were analyzed. **Figure III.6** displays the average Nusselt number distribution as a function of the sloped entrance channel length for different Rayleigh numbers and for the fixed tilted angle of the hybrid system (α=30°).

It seems from **figure.6 (a)** that the average Nusselt number decreases in the range of SEC against the length (10<L_{ch}e<60). Whereas, in the range of 10<L_{che}<60 of SEC length the average Nusselt number stays constant. **Figure III.6 (b)** displays the average Nusselt number which decreases until L_{che}=60cm, after this value the Nu_{L_avg} starts to increase where the pant becomes important. It also appears in **figure III.6 (c)** that Nu_{L_avg} increases by three phases as a function of SEC length. The decreasing of the average Nusselt number versus SEC length for the first phases **for figure III.6 (a)** and **figure III.6 (b)** can be explained by the fact that bouncy forces are weaker than friction forces. Therefore, the average Nusselt number is more efficient for high SEC length and for high Rayleigh number. From these previous plotted profiles, several correlations have been fitted by Origin software, as follows:

- *For the minimum* $Ra_m = 8.12*10^8$

$$Nu_{L\_avg} = (100.5672)*\mathrm{L_{che}}^{(-0.00278)} \; ; 0 \le \mathrm{L_{che}} \le 60cm; \quad \text{(III.17)}$$

$$Nu_{L\_avg} = (99.16228)*\mathrm{L_{che}}^{(7.052*10^{-04})} \; ; 60 \le \mathrm{L_{che}} \le 120cm; \quad \text{(III.18)}$$

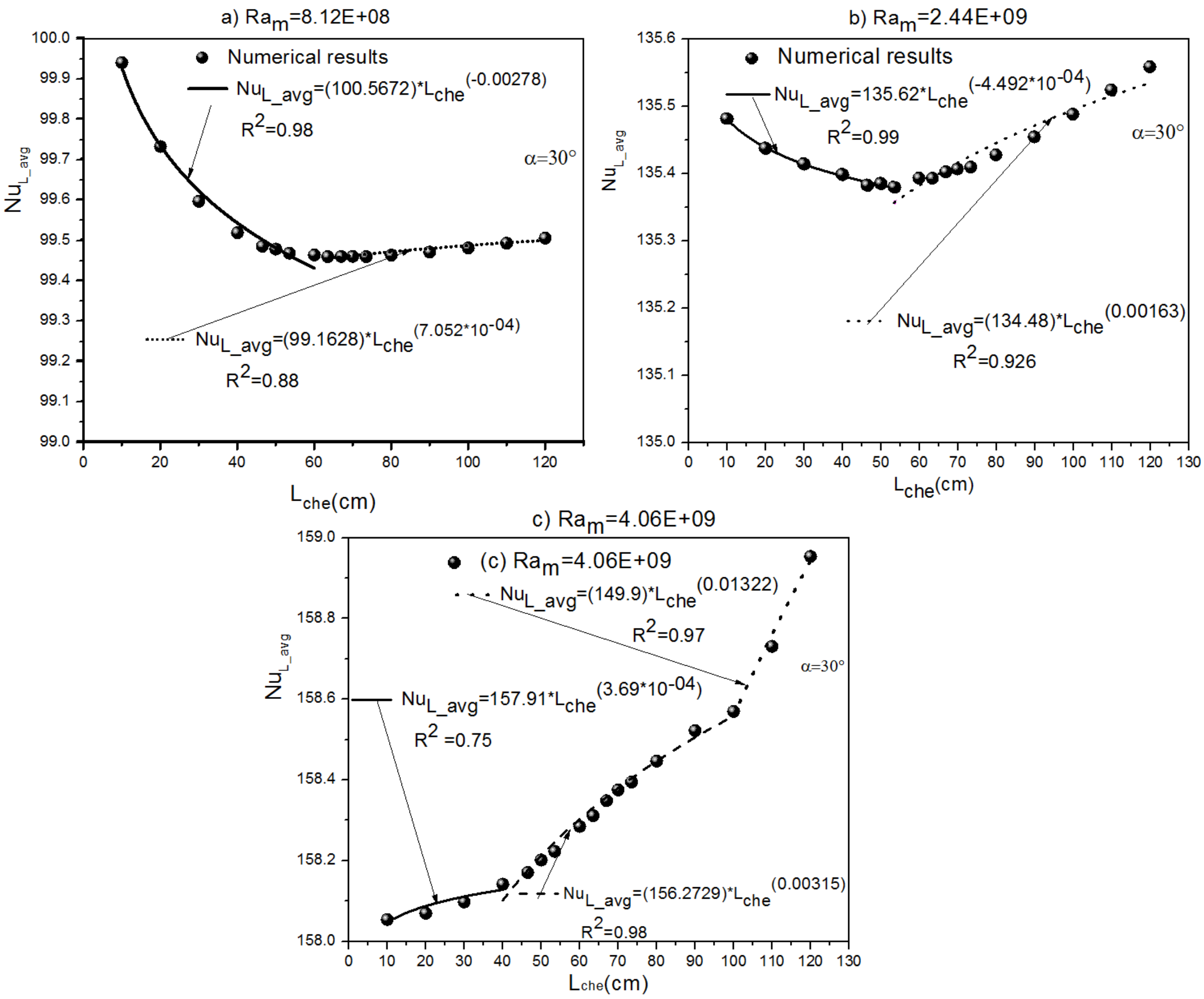

Figure III. 6: *Average Nusselt number distribution versus SEC length for three modified Rayleigh numbers values, and tilted angle α=30°.*

- *For the intermediate* $Ra_m = 2.44*10^9$

$$Nu_{L\_avg} = (135.62)*\mathrm{L_{che}}^{(-4.492*10^{-04})} \; ; 0 \le \mathrm{L_{che}} \le 60cm; \quad \text{(III.19)}$$

$$Nu_{L\_avg} = (134.48)*\mathrm{L_{che}}^{(0.00163)} \; ; 60 \le \mathrm{L_{che}} \le 120cm; \quad \text{(III.20)}$$

- *For the maximum* $Ra_m = 4.06*10^9$

$$Nu_{L\_avg} = (157.91)*\mathrm{L_{che}}^{(-3.69*10^{-04})} \; ; 0 \le \mathrm{L_{che}} \le 40cm; \quad \text{(III.21)}$$

$$Nu_{L\_avg} = (156.2729) * L_{che}^{(0.00315)} \ ; 40 \le L_{che} \le 100cm; \quad \text{(III.22)}$$

$$Nu_{L\_avg} = (149.9) * L_{che}^{(0.01322)} \ ; 100 \le L_{che} \le 120cm; \quad \text{(III.23)}$$

Figure III.7 (a-b) Illustrations the variation of the average Nusselt number with respect to SEC height for three fixed Ra_m ($8.12*10^8$, $2.44*10^9$, $4.06*10^9$) and fixed tilted angle (α=30°).

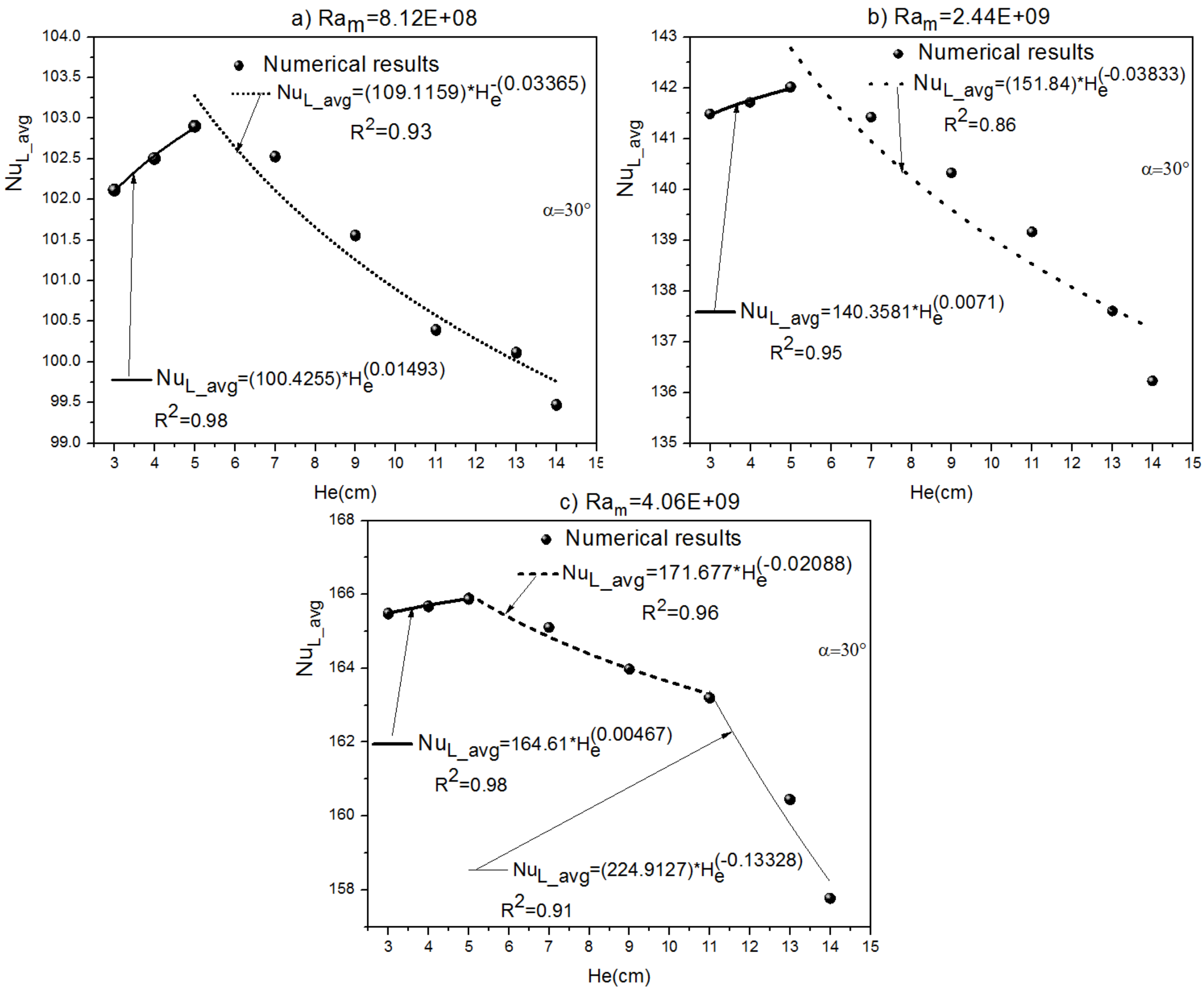

Figure III. 7: ***(a-c)*** *Nusselt number evolution on the sloped air channel height for different Rayleigh number, α=30°.*

From He=5cm, a great decrease in the average Nusselt number with an increase in SEC height is noticed. In more, for SEC height low than 5 cm, high average Nusselt number values are recorded, especially for high Ra_m **(figure III. 7(c))** where Nu_{L_avg} values are around 166. As result, for SEC height greater than He=5cm The Nu_{L_avg} improved by about 3%, 4.1%, and 5.1% for Ra_m take values $8.12*10^8$, $2.44*10^9$, and $4.06*10^9$, respectively.

Regarding to fitted correlations of average Nusselt numbers as a function of modified Rayleigh numbers, the different equations are writen as follows:

- *For the minimum* $Ra_m = 8.12*10^8$

$$Nu_{L\_avg} = (100.4255)*H_e^{(0.01493)} \ ; 3 \le H_e \le 5cm; \tag{III.24}$$

$$Nu_{L\_avg} = (109.1159)*H_e^{(-0.03365)} \ ; 5 \le H_e \le 14cm; \tag{III.25}$$

- *For the intermediate* $Ra_m = 2.44*10^9$

$$Nu_{L\_avg} = (140.3581)*H_e^{(0.0071)} \ ; 3 \le H_e \le 5cm; \tag{III.26}$$

$$Nu_{L\_avg} = (151.84)*H_e^{(-0.03833)} \ ; 5 \le H_e \le 14cm; \tag{III.27}$$

- *For the maximum* $Ra_m = 4.06*10^9$

$$Nu_{L\_avg} = (164.61)*H_e^{(0.00467)} \ ; 3 \le H_e \le 5cm; \tag{III.28}$$

$$Nu_{L\_avg} = (171.677)*H_e^{(-0.02088)} \ ; 5 \le H_e \le 11cm; \tag{III.29}$$

$$Nu_{L\_avg} = (224.9127)*H_e^{(-0.13328)} \ ; 11 \le H_e \le 14cm; \tag{III.30}$$

Figure III.8 (a-c) illustrates average Nusselt number development as a function of the SEC depth for three fixed R_{am}, α=30°. It is recorded that there is a little increase in the average Nusselt number against the SEC depth of about 0.39%,0.38%, and 0.25%, respectively.

The SEC depth has a negligible effect on the average Nusselt number. The average Nusselt numbers on the PV module surface for several Ra_m are fitted in **figure III.8 (a-c)**, and were correlated by the following equations:

- *For the minimum* $Ra_m = 8.12*10^8$

$$Nu_{L\_avg} = (100.5976)*W_e^{(0.0048)} \ ; 22 \le W_e \le 57cm; \tag{III.31}$$

- *For the intermediate* $Ra_m = 2.44*10^9$

$$Nu_{L\_avg} = (139.39)*W_e^{(0.0033)} \ ; 0 \le W_e \le 60cm; \ Ra_m = 2.44*10^9 \tag{III.32}$$

- *For the maximum* $Ra_m = 4.06*10^9$

$$Nu_{L\_avg} = (162.8604)*W_e^{(0.00297)} \ ; 22 \le W_e \le 57cm; \ Ra_m = 4.06*10^9 \tag{III.33}$$

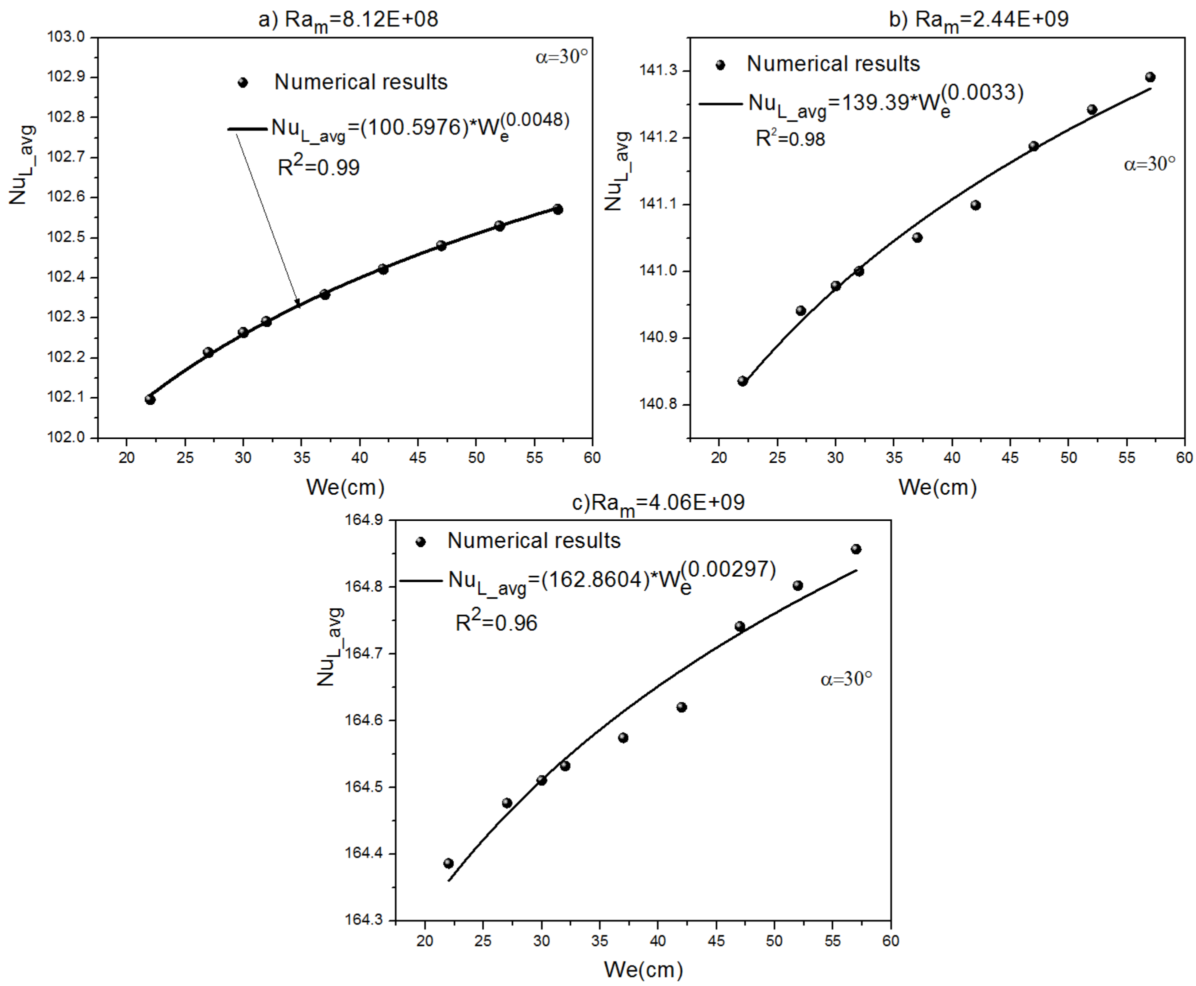

Figure III. 8: ***(a-c)*** *Average Nusselt number variation versus the SEC depth for Three fixed* Ra_m *,* $\alpha=30°$*.*

III.5.4 AFP distance and number effect on the average Nusselt number

Figure III.9 (a-c) presents the influence of AFP distance on the average Nusselt number for various Ra_m, $\alpha=30°$. It observes that for low values of AFP distance the heat transfer is more improved.

Besides, the values of AFP distance, in the range, which reaches between 0.02 to 0.04 m and have optimum values of the average Nusselt number. The heat transfer rate is improved when the AFP is installed near the surface of the PV module. This can be explained by the fact of the air passage section is reduced; consequently, the heat transfer rate is increased.

This can be explained by the fact of the air passage section is reduced consequently the heat transfer rate is increased.

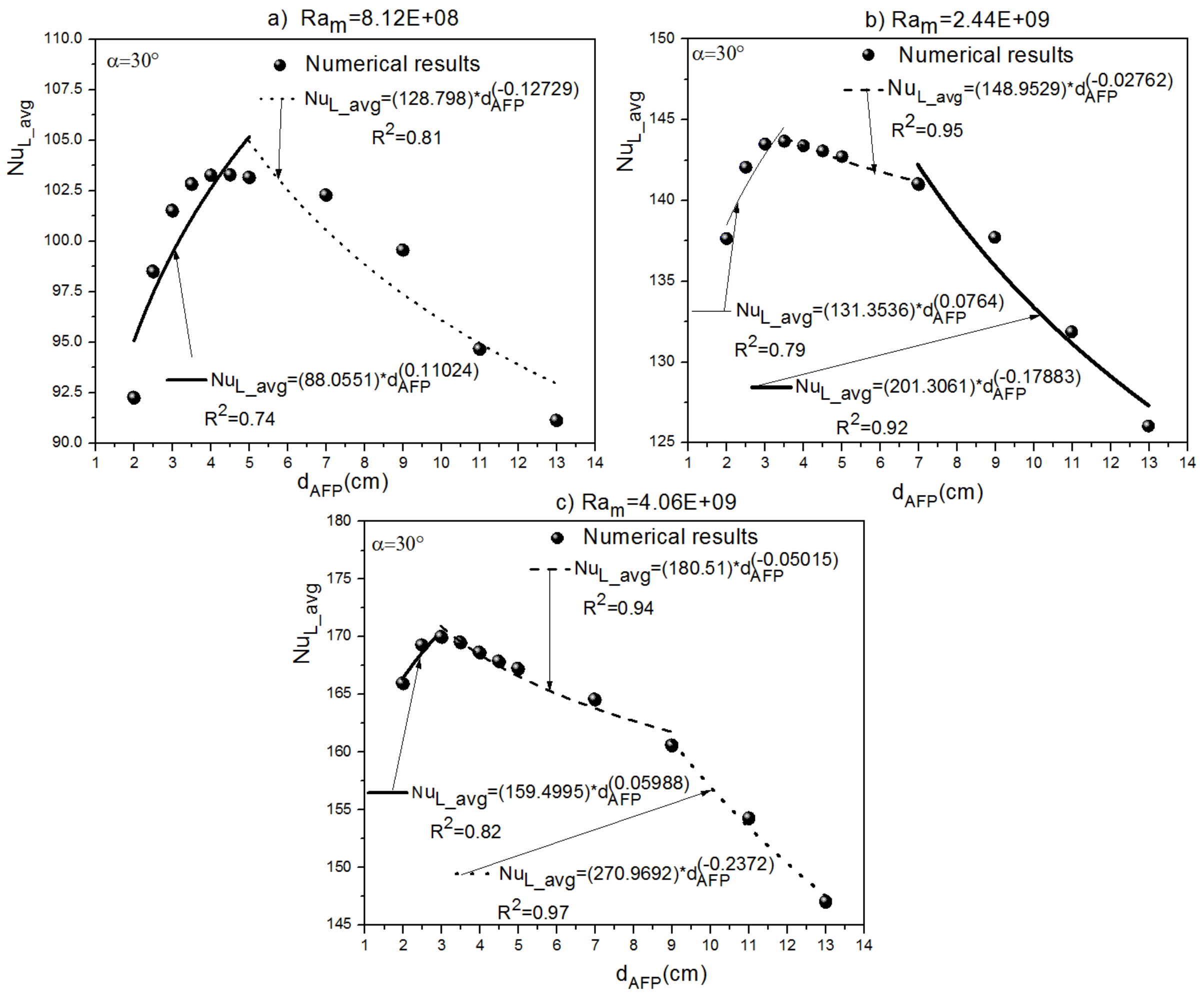

Figure III. 9 (a-c) : *Average Nusselt number distribution versus the AFP distance to PV module for various Ra_m, $\alpha=30°$.*

Finally, the insertion of AFP closed to the PV module is more recommended for enhancing the heat transfer rate, and were correlated by the following equations:

- *For the minimum* $Ra_m = 8.12*10^8$

$$Nu_{L\_avg} = (88.0551)*d_{AFP}^{(0.11024)} \;;\; 2 \le d_{AFP} \le 5cm; \quad \text{(III. 34)}$$

$$Nu_{L\_avg} = (128.798)*d_{AFP}^{(-0.12729)} \;;\; 5 \le d_{AFP} \le 13cm; \quad \text{(III.35)}$$

- *For the intermediate* $Ra_m = 2.44*10^9$

$$Nu_{L\_avg} = (131.3536)*d_{AFP}^{(0.0764)} \;;\; 2 \le d_{AFP} \le 3.5cm; \quad \text{(III.36)}$$

$$Nu_{L\_avg} = (148.9529)*d_{AFP}^{(-0.012762)} \;;\; 3.5 \le d_{AFP} \le 7cm; \quad \text{(III.37)}$$

$$Nu_{L\_avg} = (201.3061)*d_{AFP}^{(-0.17883)} \;;\; 7 \le d_{AFP} \le 13cm; \quad \text{(III.38)}$$

- *For the maximum* $Ra_m = 4.06*10^9$

$$Nu_{L\_avg} = (159.4995)*d_{AFP}^{(0.05988)} \; ; 2 \le d_{AFP} \le 3cm; \tag{III.39}$$

$$Nu_{L\_avg} = (180.51)*d_{AFP}^{(-0.05015)} \; ; 3 \le d_{AFP} \le 9cm; \tag{III.40}$$

$$Nu_{L\_avg} = (270.9692)*d_{AFP}^{(-0.2372)} \; ; 9 \le d_{AFP} \le 13cm; \tag{III.41}$$

Figure III. 10 presents the average Nusselt number evolution as a function of the AFP distance d_{AFP}, for different values of the modified Rayleigh number. A better heat transfer rate (maximum average Nusselt number) is obtained for an optimal value of the AFP distance around 3 cm.

As the AFP closes to the PV module, the average Nusselt number becomes more significant. The average Nusselt number as a function of d_{AFP} and Ra_m is fitted and expressed in the following equations:

$$Nu_{L\_avg} = \left(-6.53 + (6.63*\exp^{(-0.0136*\times d_{AFP})}\right) \times \mathrm{Ra_m}^{0.328} \; ; \; 8.12*10^8 \le Ra_m \le 4.06*10^9 \tag{III.42}$$

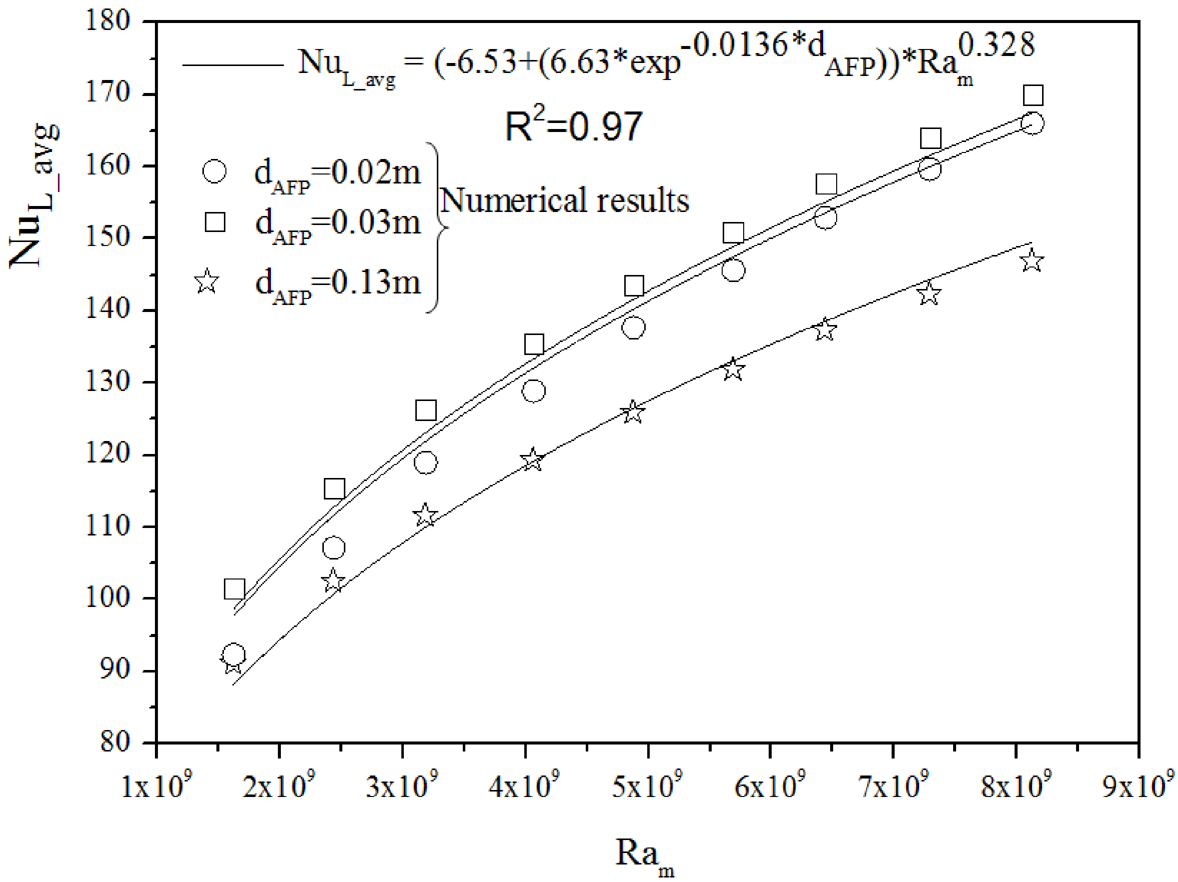

Figure III. 10: *Average Nusselt number variation versus Ra_m and d_{AFP}, for fixed α=30°.*

Figure III.11 displays the average Nusselt number distribution as a function of the AFP number for three fixed Ram. It seems that since integrating AFP, the average Nusselt number was improved for the whole Ra_m.

However, for the same Ra_m, the AFP number rising has no effect on the average Nusselt number. It is also clear that the heat transfer rate is enhanced compared to the case without AFP. Consequently, the integration of AFP has a positive effect to improve the heat transfer rate, especially for high R_{am}.

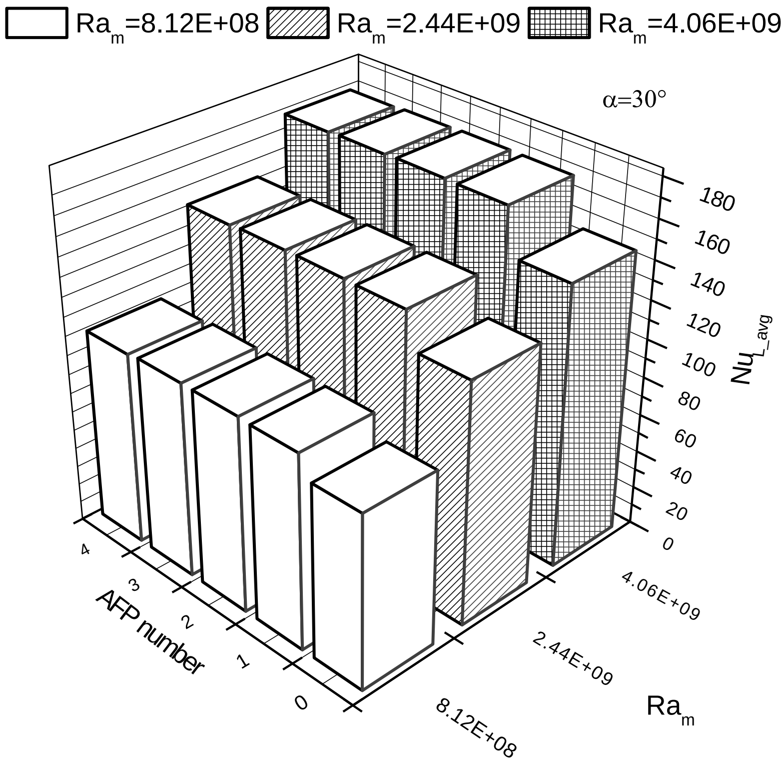

Figure III. 11: Average Nusselt number evolution as a function of AFP number with d_{AFP}=0.03m for various Ra_m number, α=30°.

III.5.5 Influence of Rayleigh number and tilted angle on the temperature filed

Figure III. 12 (a, b) illustrates the isotherms contours inside the air channel with various tilted angles and for fixed Rayleigh numbers for both cases. It noticed that the maximum temperature inside the air channel is reduced with increasing the tilted angles.

For each angle, it appears that the temperature increase more in more when near the PV module surface. The thermal boundary layer thickness is reduced against the augmentation of tilted angles.

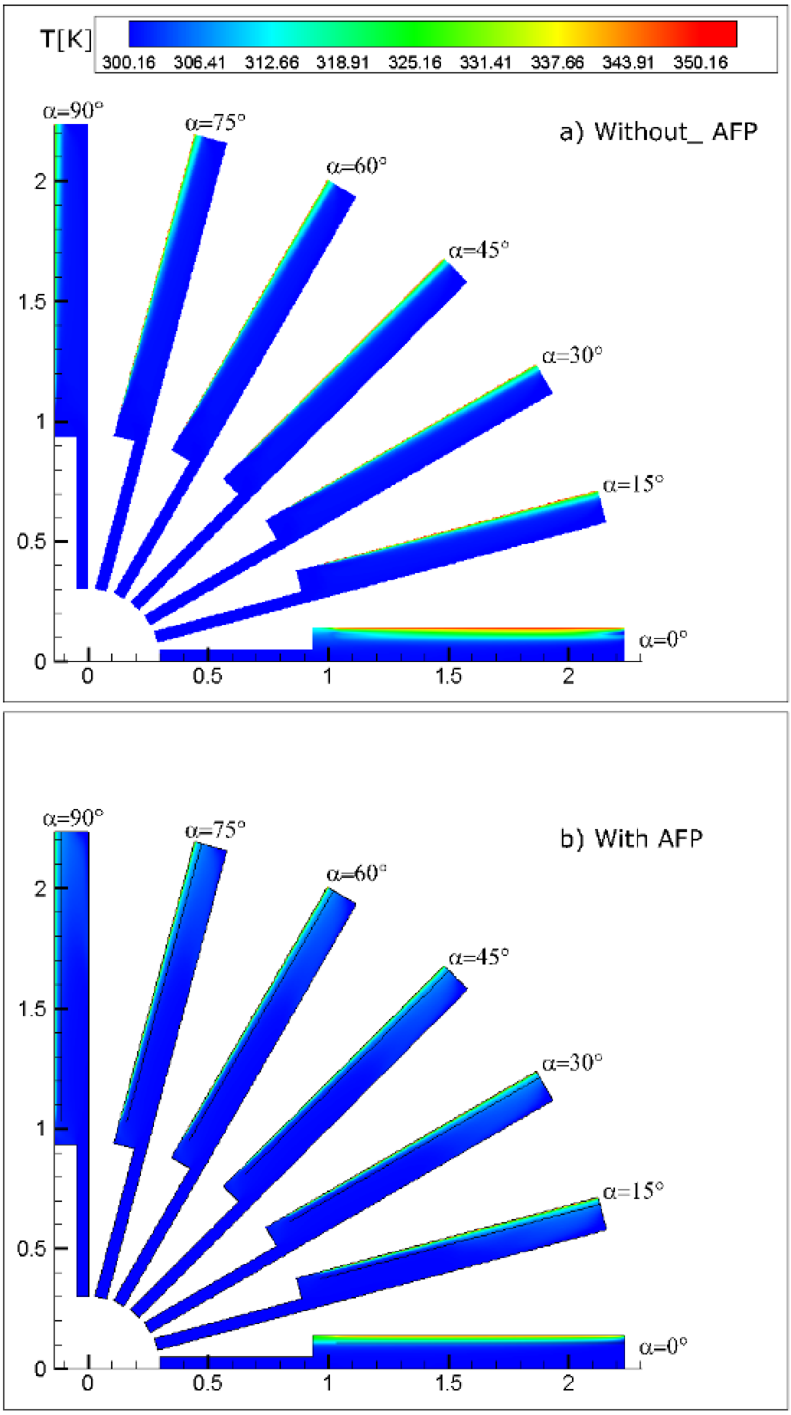

***Figure III. 12* (a,b) :** *Isothermal contours versus tilted angle for fixed Rayleigh number.*

In more, these configurations give more local characteristics to the thermo-hydrodynamic flow behaviors. The stratification zone is attenuated with increase-tilted angles. For both cases, and then more noted for horizontal configuration (α=0°).

Hence, the PV module becomes colder, **Figure III. 12b** shows that a distinct vertical thermal boundary layer is formed adjacent to the heated wall for all three Rayleigh numbers. Over this range of the Rayleigh numbers, the thickness of the thermal boundary layer, which decreases as the Rayleigh number increases, is much smaller than the channel air gap size.

The absence of isotherms near the insulation wall suggests that convection is strong and predominant near the PV module, as expected.

Figure III. 13 (a, b) displays the temperature evolution profile against the dimensionless position along the air channel for several tilted angles and Ra_L=8.12E^{+08}at distance to the PV module of 1.5 cm for both cases.

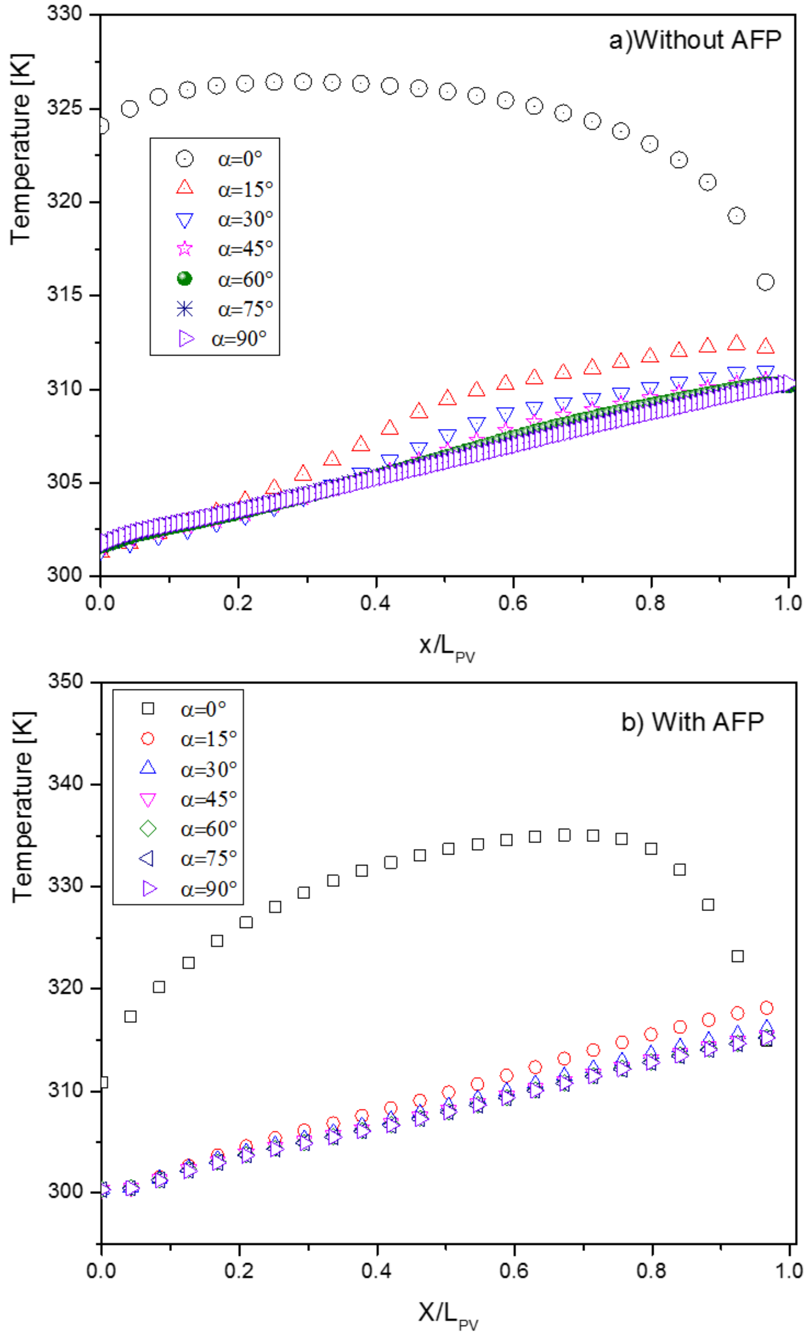

Figure III. 13 (a,b): *Temperature evolution versus long position at distance to y=0.1cm to PV module for various tilt angle and for fixed Rayleigh number for the of without and with AFP*

The temperature in the air channel decreases with the increase of the tilted angles. In more, for the vertical PV system (a=90°) the temperature is lowest compared to the other tilted angles for both cases. For tilted angles different from zero, it seems that with AFP configuration, the temperature values are nearest compared to those for the case without AFP.

Figure III. 14 (a, b) represents the temperature difference as a function of Rayleigh numbers and tilted angles in both cases (with and without AFP).

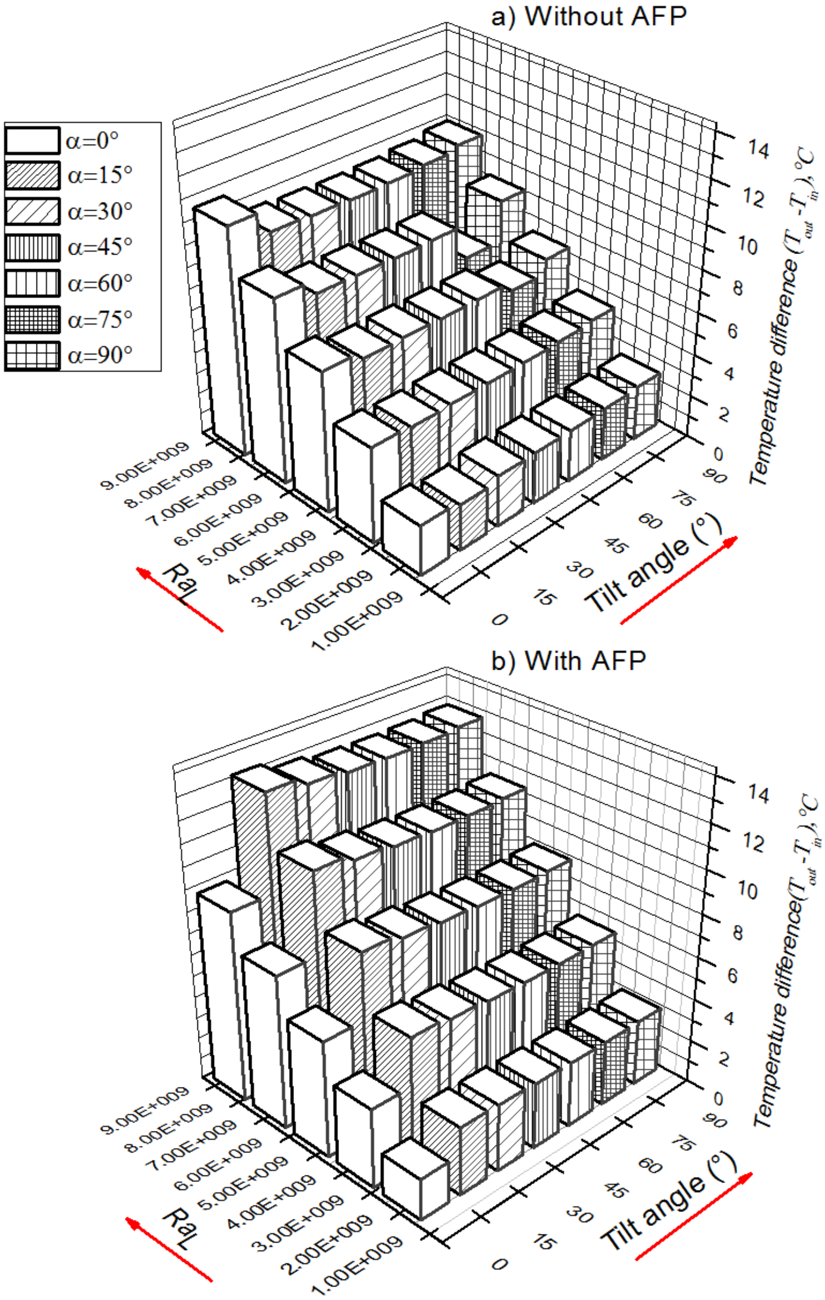

Figure III. 14 (a,b): *Difference temperature evolution as a function of Rayleigh number for various tilted angle for the case without and with AFP*

It is noticed that the temperature difference is more significant for the case of AFP than without. According to these figures, the tilted angles have not affected the temperature difference, except for the horizontal configurations. On the contrary, the Rayleigh number has a high impact on the temperature difference.

III.5.6 Influence of Rayleigh number and tilted angle on the velocity filed

The velocity contours distribution inside the air channel with various tilted angles and for fixed Rayleigh number is clarified in **Figure III.15 (a, b)**.

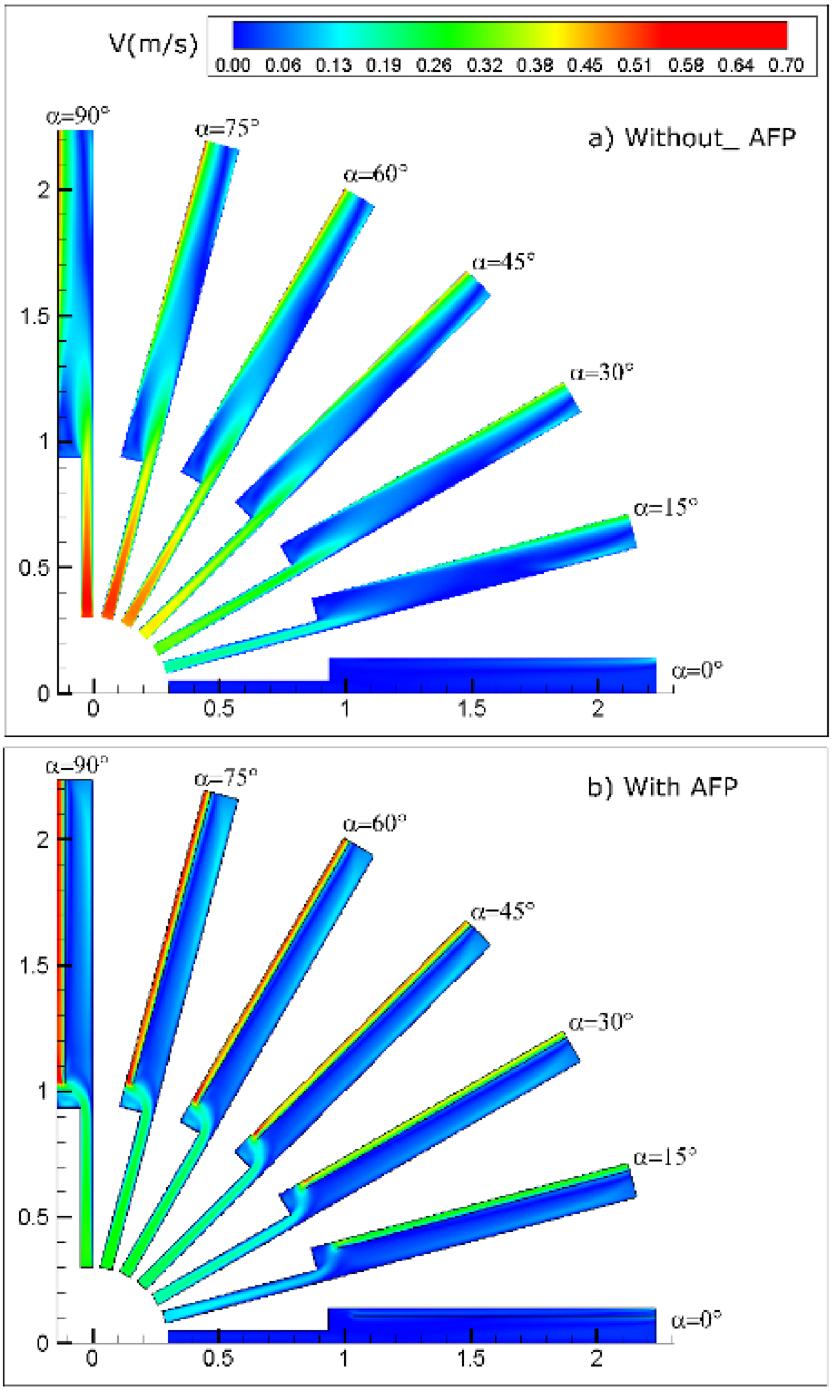

Figure III. 15 (a,b): *Magnitude velocity contours versus tilted angle for fixed Rayleigh numbers.*

It is observed that rising tilted angles produce an increase in the magnitude velocity in the air channel for both cases. For the case with AFP, the maximum velocity was concentrated in the gap between AFP and the PV module surface due the passage section is reduced.

While for the case without AFP, the maximum distribution velocity is localized at the SEC. In more, the maximum velocity for both cases is significant for high tilted angles (α>=60°). **Figure III. 16 (a, b)** shows velocity magnitude evolution along the air channel at the level of the PV module versus normalized length(X=x/LPV) for different tilted angles and for fixed distance to PV surface (Y=y/H).

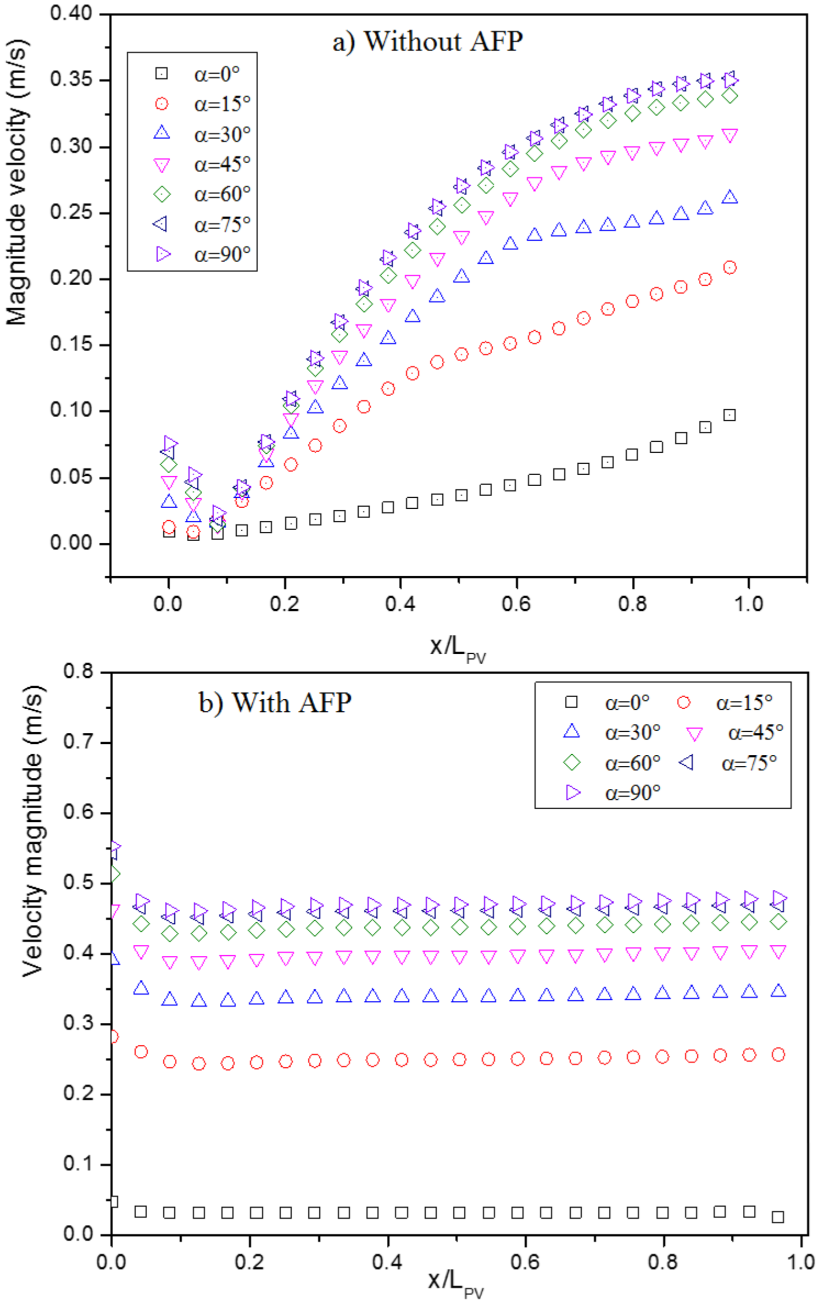

Figure III. 16 (a,b): *Magnitude velocity profile evolution as a function of position at distance to PV module of about y=0.0125 for various tilted angle and fixed Rayleigh number for the case with and without AFP*

It is noticed that augmentation of the magnitude velocity in the air channel with increasing of tilted angles for both cases (with and without). The magnitude velocity is more important in the case with AFP (**Figure III.16b**) compared to them without (see **Figure III.16a**). For each tilted angle, magnitude velocity appears constant with the AFP case.

In both cases, the maximum velocities vary versus the Rayleigh number and the tilted angle, as shown in **Figure III. 17 (a, b).** It is noticed that the maximum velocities values increase as rising tilted angles and Rayleigh numbers, for cases with and without AFP. The optimum angles for best enhancing of maximum velocity are superior to α=30°, where percentage enhanced take values.

The maximum enhancement value is recorded for the tilted angle of α=45° reached 22% for Ra_L=9.0E+9. Finally, it can be concluded that integrating AFP has been improved the maximum magnitude velocity in the PV/T system.

III.5.7 Influence of tilted angle and Rayleigh number on the heat gain rate

The changing of heat gain rate at the air channel outlet against the Rayleigh numbers and tilted angles for both cases (with and without AFP) is plotted in **Figure III.18 (a, b).**

The rate of heat removal by the natural air cooling system is calculated as follows [8]:

$$\dot{Q} = M_{air} Cp\left(T_{out} - T_{in}\right) \quad \text{(III.43)}$$

Where M_{air}, T_{out}, T_{in}, and Cp are the mass flow rate, outlet temperature, inlet temperature, and specific heat coefficient of the cooling air, respectively. The mass flow rate is calculated using following equations.

$$M_{air} = \rho * V * A_{ch} \quad \text{(III.44)}$$

It notes that an increase in the heat gain is more significant for the case with AFP compared to another case.

Figure III.18 (a, b) shows heat gain variation as a function of Rayleigh numbers for various air channel tilted angle for both cases with and without AFP. The heat gain is improved by increasing Rayleigh number and air channel tilted angles for both cases without and with AFP. On the other hand, the heat gain for the case with AFP is more enhanced compared to another case. It appears clearly that the heat gain is more significant for high Rayleigh and for high tilted angles.

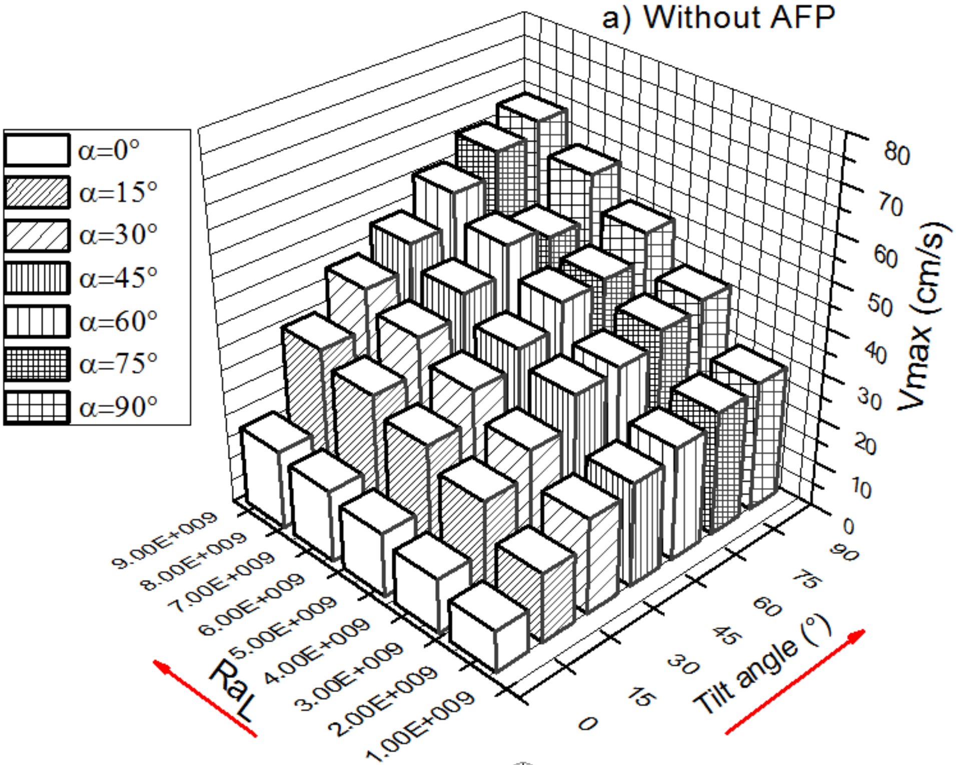

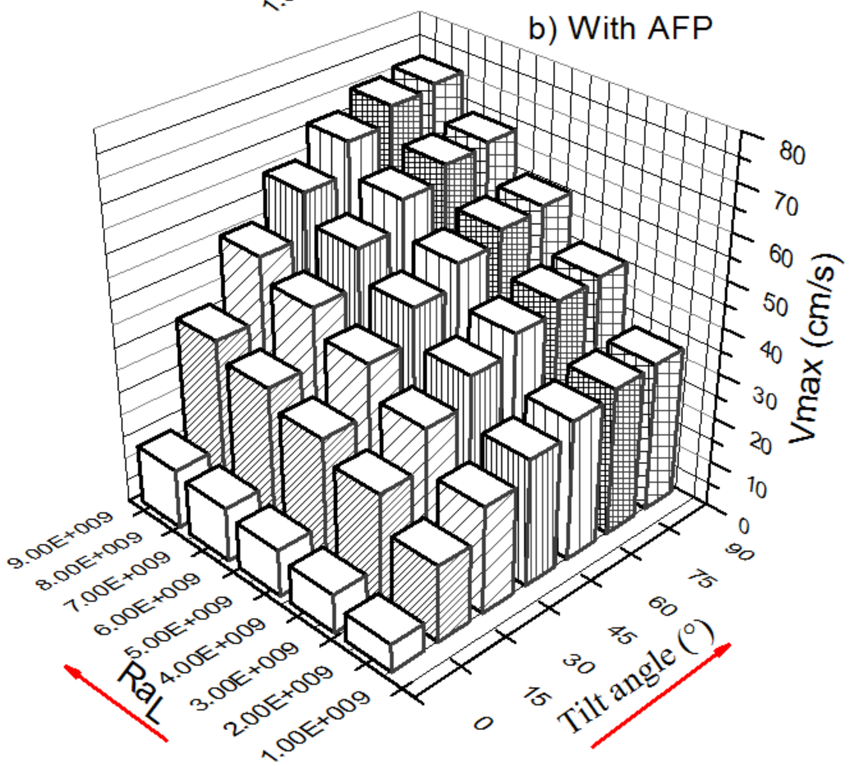

Figure III. 17 (a,b): *Maximum magnitude velocity evolution versus Rayleigh number and for various tilted angle for the case without and with AFP*

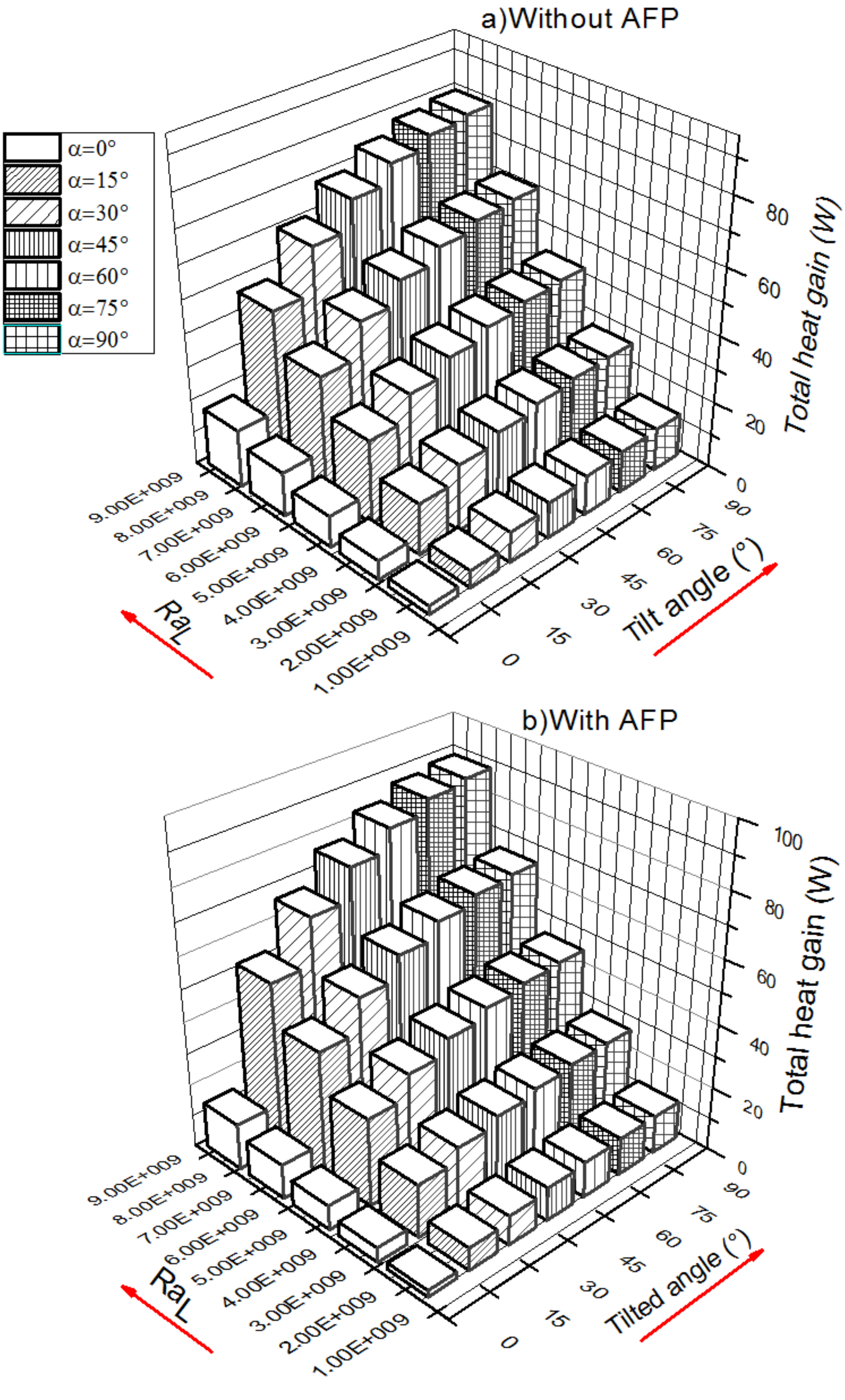

Figure III. 18 (a,b): Total h*eat gain evolution versus Rayleigh number for various tilted angle at the case with and without AFP*

III.5.8 Influence of air channel tilted angle on the average Nusselt number

Figure III.19 shows average Nusselt number growth as a function of Rayleigh numbers for various air channel tilted angles for both cases with and without AFP.

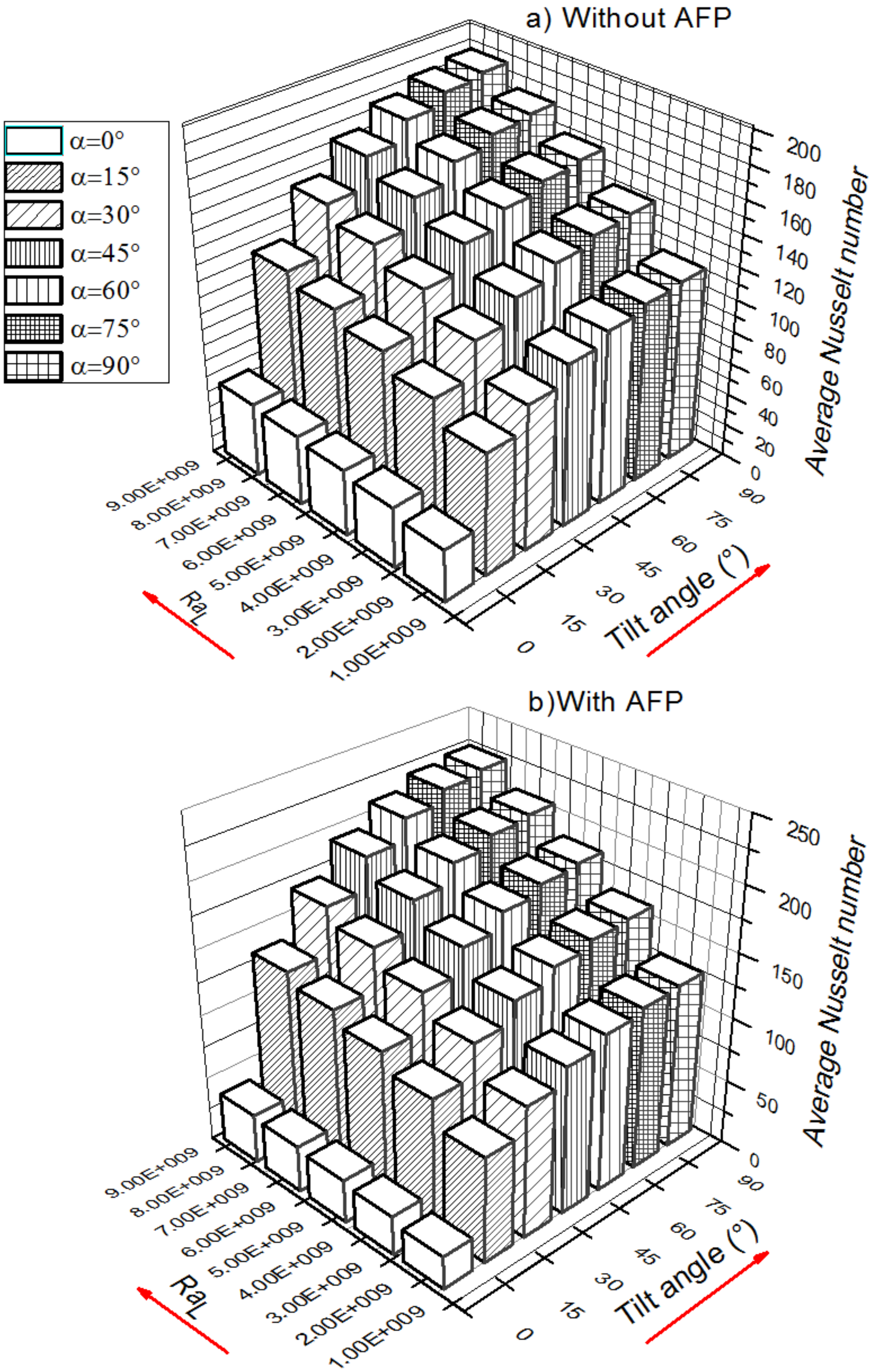

Figure III. 19 (a,b): *Average Nusselt number variation versus Rayleigh number for different tilted air channel*

The average Nusselt number is enhanced by the progression of the air channel tilted angle.

It observes that an increase in the average Nusselt number of the PV module surface for the case with AFP compared to another case.

From **Figure III. 19**, it appears clearly that the heat transfer rate is enhanced by increasing the sloped air channel.

Consequently, the rising in the sloped air channel length produces a high buoyancy force for various Rayleigh numbers.

Figure III.20 illustrates average Nusselt number changing versus Ra_m for the optimal geometry obtained with (L_{che}=0.735m,We=0.3m,He=0.05m,d_{AFP}=0.03m,N_{AFP} =1,α=30°) for the case with AFP.

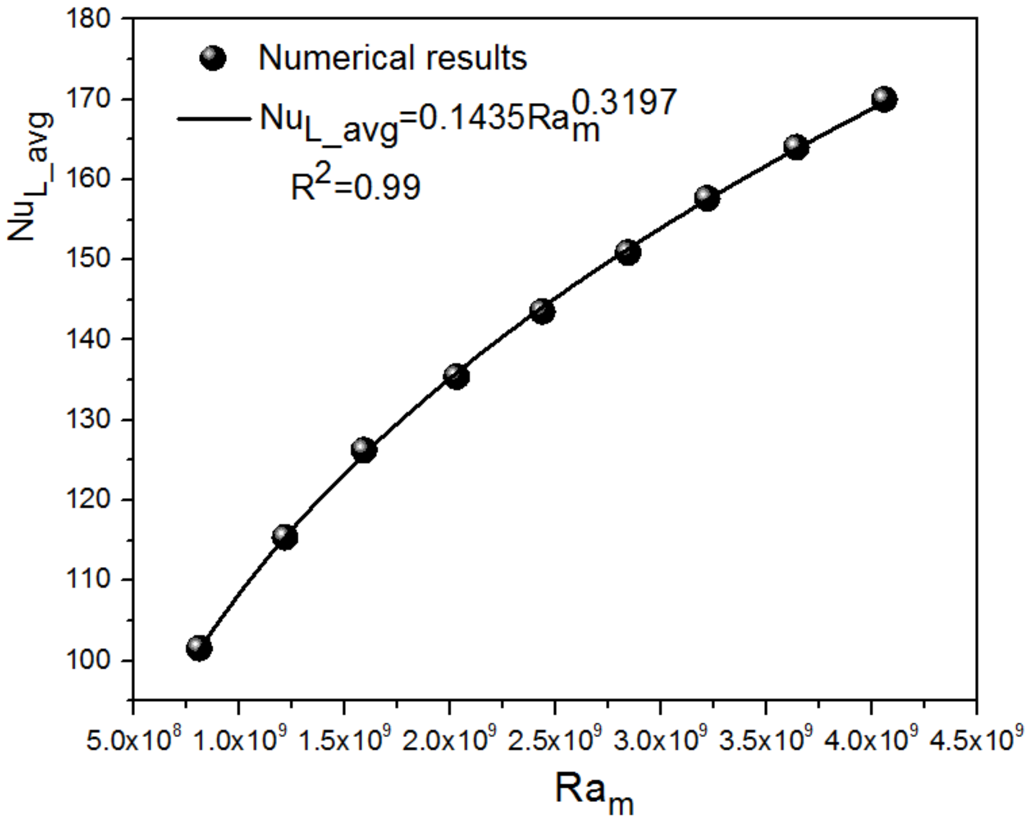

Figure III. 20: *Nusselt number variation versus Rayleigh number and AFP distance for fixed tilted angle,α=30°*

It observes that an increase in the average Nusselt number of the PV module surface versus Ra_m. A correlation is fitted of Average Nusselt number versus modified Rayleigh number, is fitted and expressed in the following equations:

$$Nu_{L\_avg} = 0.1435 Ra_m^{0.3197} \; ; \; 8.12*10^8 \le Ra_m \le 4.06*10^9 \quad \text{(III.45)}$$

This correlation with multivariable can be used to calculate the average Nusselt number of PV modules for different modified Rayleigh numbers.

III.5.9 Comparison with previous works

Table. III. 5 collects some correlations employed in the air channel to calculate the average Nusselt number for analyzed the heat transfer. The geometric parameters such as spacing size effect on the heat transfer filed in laminar or turbulent natural convection are presented.

Table. III. 5: A Comparison of average Nusselt number correlations versus Rayleigh number of natural convection in a channel.

Authors	Correlations	Flow regime
Onur et al. (1997)[7]	$Nu_{S\_avg} = 0.669Ra^{0.232}$ $(Ra \leq 10^8,\ 15 \leq L/s \leq 50\ and\ \alpha = 30°$	Turbulent
Millteman et al. [9]	$Nu_{S\_avg} = F(L/S) \times (Ra \sin\alpha)^{0.203}$ $F(L/S) = -3.38\times10^{-6}(L/S)^3 + 0.000687\ (L/S)^2$ $-0.04419(L/S) + 1.833$ $(Ra \leq 10^8,\ 15 \leq L/s \leq 50\ and\ 30° \leq \alpha \leq 90°)$	combined Turbulent convection/Radiation
Phiraphat et al.,(2017) [5]	$Nu_{S\_avg} = 0.3282(Ra_s \sin 30)^{0.2249}$ $(S = 15cm, S/L = 0.125$	Turbulent
Boutina et al. (2018)[4]	$Nu_{S\_avg} = (0.04889 * La * 0.1914)Ra_s^{0.368}$ $(10^6 \leq Ra_s \leq 5*10^6,\ (S/L) = 0.0192,$ $\alpha = 30°$	Turbulent
Present study	$Nu_{L\_avg} = \times 0.1435 \mathrm{Ra_m}^{0.3197}$; $8.12*10^8 \leq Ra_m \leq 4.06*10^9$	Turbulent

These authors suggested correlations to calculate the average Nusselt number for vertical and tilted air channels.

III.6 Conclusions

In this three-dimensional numerical study, the improvement of heat transfer by passive air-cooling of an innovative concept of the hybrid photovoltaic/thermal system is presented. The effects of the geometric parameters of the SEC inlet air channel, the integration of the aluminum flat plate on the heat transfer rate were analyzed. In addition, the impact of the PVT system tilt angle and Rayleigh number on the thermo-hydrodynamic flow behavior is performed.

The analysis of the results obtained allows us to achieve the following main conclusions:

- ✓ The obtained results have best agreement with experiment results of Onur et al. **[7]**.
- ✓ For He = 0.05 m, the average Nusselt number is improved by about 5.1 % .
- ✓ AFP improving the heat transfer rate by about 20% compared to case without
- ✓ An optimal value of the AFP distance (d_{AFP} optimal = 3 cm).
- ✓ Increasing the system tilt angle improved the maximum airflow velocity
- ✓ Correlations of average Nusselt numbers versus modified Rayleigh numbers reported.

References

[1] W. Li X, J. A. Meng, Z. Y. Guo. Turbulent flow and heat transfer in discrete double inclined ribs tube. International Journal of Heat and Mass Transfer. 52 (2009)962-970. doi.org/10.1016/j.ijheatmasstransfer.2008.07.027

[2] G. Xie, S. Zheng, W. Zhang, B. Sundén. A numerical study of flow structure and heat transfer in a square channel with ribs combined downstream half-size or same-size ribs, Applied Thermal Engineering.61 (2013)289-300. doi.org/10.1016/j.applthermaleng.2013.07.054

[3] Kumar A, Kim M. H. Effect of roughness width ratios in discrete multi V-rib with staggered rib roughness on overall thermal performance of solar air channel. Solar Energy. 2015; 119: 399-414. doi.org/10.1016/j.solener.2015.06.030

[4] L. Boutina, A. Khelifa, K. Touafek, M. lebbi, M. T. Baissi. Improvement of PVT air-cooling by the integration of a chimney tower (CT/PVT), Applied Thermal Engineering. 129 (2018)1181–1188. Doi.org/10.1016/j.applthermaleng.2017.10.097

[5] S. Phiraphat, R. Prommas, W. Puangsombut. Experimental study of natural convection in PV roof solar collector. International Communications in Heat and Mass Transfer. 89 (2017) 31-38. https://doi.org/10.1016/j.icheatmasstransfer.2017.09.022

[6] G. E. Lau Sanvicente, G. H. Yeoh, V. Timchenko, M. Fossa, C. Ménézo, S. Giroux-Julien. Modelling of natural convection in vertical and tilted photovoltaic applications. Energy and Buildings. 55 (2012)810-822. doi.org/10.1016/j.enbuild.2012.10.014

[7] N. Onur, M. Sivrioğlu, M. K. Aktaş. An experimental study on the natural convection heat transfer between inclined plates (Lower plate isothermally heated and the upper plate thermally insulated as well as unheated). Heat and Mass transfer. 32 (1997)471-476. doi.org/10.1007/s002310050147

[8] Lau G. E, Sanvicente E, Yeoh G. H, Timchenko V, Fossa M., Ménézo C, Giroux-Julien S. Modelling of natural convection in vertical and tilted photovoltaic applications. Energy and Buildings. 2012; 55: 810-822. doi.org/10.1016/j.enbuild.2012.10.014

[9] G. Mittelman, A. Aiman, J. H. Davidson. A model and heat transfer correlation for rooftop-integrated photovoltaics with a passive air-cooling channel, Solar Energy. 83 (2009)1150-1160. doi.org/10.1016/j.solener.2009.01.015

Chapter IV

A novel concept of active Bi-fluid cooling system for photovoltaic modules

IV.1 Introduction

After presented a numerical study on the passive air-cooling effect on the dimensions of the new hybrid system in the previous chapter.

This part of the study is divided into two sections, the first includes a three-dimensional numerical study on the air-cooling effect ensured by two fans to improve the heat transfer rate, friction coefficient, and total heat gain.

Another section concerning a comparison between the results of the numerical simulation of new solar hybrid PV/T Bi-fluid collector, with the experimental data in order to verify the validity of the proposed numerical model.

The finite volume method is used to solve the governing transport equations and the RNG k-ε turbulence model is elaborate for describing the turbulent mixed convection.

This new system hybrid PV/T Bi-fluid able to cool the PV module from their two sides and cleaner their front side from the soiling and pollution. The main objectives of this contribution are to achieve these principal important points:

- ✓ Influence of tilt angle and Grashof number on the average Nusselt number
- ✓ Influence of co-current and counter-current on the average Nusselt number
- ✓ Investigating the effect of air Reynolds number on heat transfer rate and friction coefficient, and total heat gain
- ✓ Compared the new solar hybrid PV/T Bi-fluid collector with present experimental data reported in Ref. [1] in terms of average electrical efficiency during the daytime.

IV.2 Physical model description

Figure IV.1 represents both considered configurations of the hybrid PV/T air system in the case by using an active air cooling technique. The first step is designed in a manner to cool the PV module from the backside with forced air circulation for different tilt angles to improve the heat transfer rate. The second step is focused to study the effect of the hydrodynamic parameters such as tilted angle and Reynolds number on the average Nusselt number and heat gain.

The **figure. IV. 2** represents the physical model sketch of both configurations of PV/T Bi-fluid solar collector considered for active cooling case.

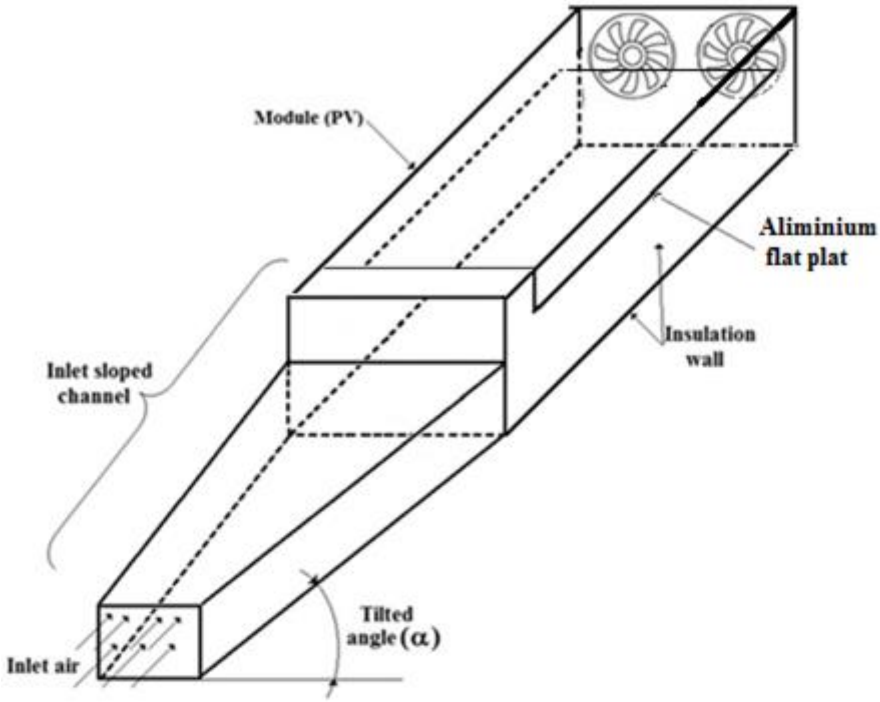

Figure. IV. 1: *Physical model sketch of configuration for active air-cooling PV/T air Config (A).*

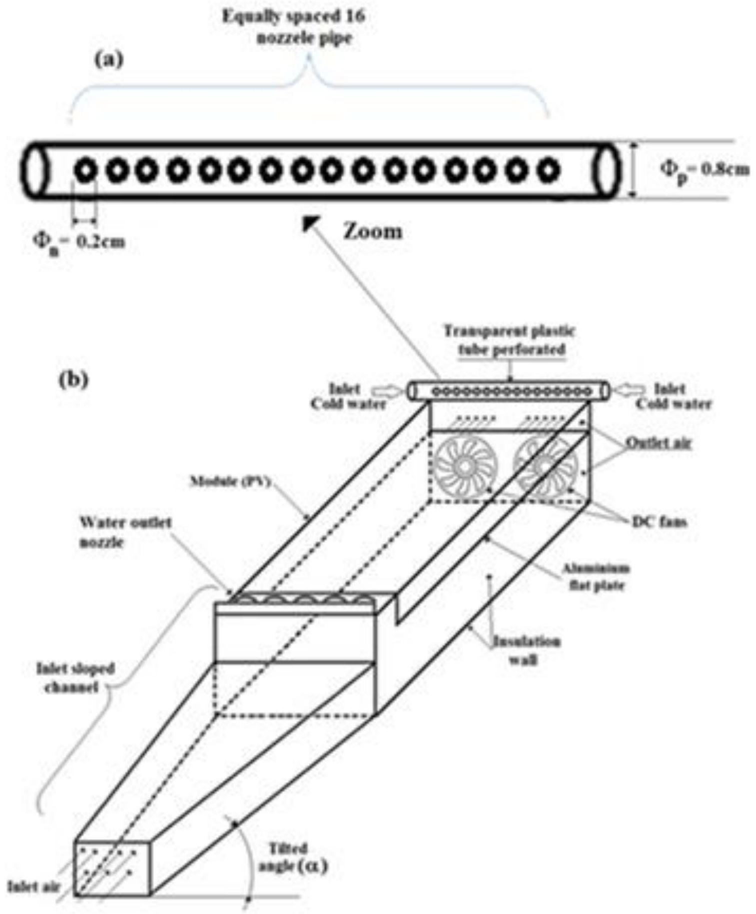

Figure. IV. 2: *Physical model sketch of PV/T Bi-fluid solar collector configuration considered for cooling case, Config (B) [1].*

In Table. IV. 1 All summarizes geometric parameters, symbols and their values of studied configurations. **Table. IV .2** shows Present different scenario studied for Config (A) and Config (B).

Table. IV. 1: Dimensions of the considered configurations Config (A) and Config (B) of New hybrid PV/T air and PV/T Bi-fluid system solar collector respectively.

Geometric parameter	**Symbol**	**Values**
PV module length	L_{PV}	1.2
Air channel gap	S	0.14
Air channel length	L_{ch}	1.2
Entrance sloped air channel length	L_{che}	0.735
Entrance channel Depth	W_e	0.3
Entrance channel size	H_e	0.14
Aluminum Flat plate Length	L_{afp}	1.2
Aluminum Flat plate depth	W_{afp}	0.57
Aluminum Flat plate thickness	E_{afp}	0.001
Aluminum Flat plate Number	N_{afp}	1
Aluminum Flat plate distance to PV	d_{afp}	0.03
Plastic perforated tube	ϕp	0.008
Inlet water nozzle	ϕn	0.002
Outlet water nozzle	ϕn_{out}	0.006

Table. IV. 2: Considered cases of active cooling by using air and water fluid as working flow

Studied cases	Reynolds number	L_{che}^*	He^*	We^*	N_{AFP}	d_{AFP} (m)	α	ϕ_P	ϕ_n
Config(A)	$2500 \leq Re_{air} \leq 10000$	0.625	0.36	0.52	1	0.03	$0° \leq \alpha \leq 90°$	////	////
Config(B)	$Re_{water} = 500$	0.625	0.36	0.52	1	0.03	$0° \leq \alpha \leq 90°$	0.008	0.002

IV.3 Computational method

Three-dimensional numerical simulations are used to compute the thermal and hydrodynamic flow behavior of the PV/T Bi-fluid system. The numerical solution of the governing equations presented above with the associated boundary conditions is based on the finite volume technique. The standard k-ε turbulence model is used for modeling the turbulent properties of the flow. Convergence criteria have declared when the maximum relative change between two consecutive iterations fell below 10^{-5}, for velocity and temperature

IV. 3.1 Numerical procedure

ANSYS FLUENT 16 is a CFD code based on the finite volume method and is a well-established commercial software used in various fields including fluid dynamics. The steady pressure-based solver is applied to solve governing equations. A SIMPLE algorithm is used for pressure and velocity terms coupling. The central difference scheme is involved for the discretization of momentum and energy equations, whereas discretization of convective terms is done using a second-order upwind scheme. The present investigation is carried out in an Intel 5-core CPU with a RAM size of 8 GB, 3.60 Hz, and 64-bit Windows 7.

IV. 3. 2 Simplifying assumptions

For obtaining a simple mathematical model, the following simplifying assumptions are adopted:

- The flow regime is forced turbulent for both configuration
- The geometry is created in three-dimensional with a symmetry plane
- The working fluid (air) and water are assumed to be Newtonian and incompressible.
- No-slip boundary condition is assigned to the walls
- Negligible radiation heat transfer mod in the wall.
- The flow regime is assumed permanent for config (A) and transient for config (B).
- The physical properties of the fluid are constant for config(A) and varied for config(B).

IV. 3. 3 Water and air physical properties

The physical properties of water are affected by the changing of water temperature. The next correlations provide respectively the water density, dynamic viscosity, thermal conductivity, thermal expansion coefficient, and specific heat capacity **[2, 3]**.

Table VI.3 Thermo-physical properties of air and water correlations between (0 to 100°C, 273.15- to 373.15)**[2,3]**

Thermo-physical quantities	Air	Water
Density	$\rho = 353/(\theta + 273)$	$\rho = -0.00380 * \theta^2 - 0.0505 + 1002.6$
Heat capacity	$C_p = 1.0057 + 0.000066(\theta - 27$	$C_p = 5631.3 - 9.2262T + 1.4622 \times 10^{-2} T^2$
Thermal conductivity	$\lambda = 7.57 * 10^{-05} \theta + 0.0242$	$\lambda = -9.87 * 10^{-6} * \theta^2 + 2.238 * 10^{-3} \theta + 0.5536$
Dynamic viscosity	$\mu = 10^{-5} \times (0.0046 * \theta + 1.7176)$	$\mu = 10^{-4}(0.00200 * \theta^2 - 0.3389\theta + 17.199$
Thermal expansion coefficient (1/k)	$\beta(T) = \frac{1}{(\theta + 273)}$	$\beta(T) = -1.908 \times 10^{-3} + 7.318 \times 10^{-6} T$
Diffusivity	$\chi = 10^{-5} \times (0.0046 * \theta + 1.8343)$	$\chi = 10^{-7}(-0.00360 * \theta + 1.34)$
Prandtl number	$\Pr = -2.54.10^{-4} \theta + 0.7147$	$\Pr = 1.577 * 10^{-3} * \theta^2 - 0.261 * \theta + 12.501$

IV. 3.4 Governing equations

The CFD software Flow Simulation Ansys Fluent solves the Navier-Stokes equations. It consists of mass, momentum, and energy conservation laws. It is supplemented by fluid state equations defining the nature of the fluid.

The Reynolds-averaged Navier-Stokes equations are used for the prediction of turbulence flow. These are the equations of fluid mechanics in the general case of turbulent flow: conservation of mass conservation of momentum, conservation of energy, and for a simple formulation of the problem.

These equations describe the behavior of the fluid and are the basis of all thermo-hydrodynamic considerations, whether physical or numerical.

Taking into account the incompressible flow, where the density is constant, the Navier-Stokes equations for the three-dimensional flow are shown in equations (IV1– IV5). Here, body forces have not been included **[4]**.

- ✓ **Continuity equation**

$$\frac{\partial(\rho u)}{\partial x}+\frac{\partial(\rho v)}{\partial y}+\frac{\partial(\rho w)}{\partial z}=0 \quad \text{(IV.1)}$$

- ✓ **Momentum equations in x-direction**

$$\frac{\partial(\rho u)}{\partial t}+\frac{\partial(\rho uu)}{\partial x}+\frac{\partial(\rho vu)}{\partial y}+\frac{\partial(\rho wu)}{\partial z}=-\frac{\partial p}{\partial x}+\mu\left(\frac{\partial^2 u}{\partial x^2}+\frac{\partial^2 u}{\partial y^2}+\frac{\partial^2 u}{\partial z^2}\right) \quad \text{(IV.2)}$$

- ✓ **Momentum equations in y-direction**

$$\frac{\partial(\rho v)}{\partial t}+\frac{\partial(\rho uv)}{\partial x}+\frac{\partial(\rho vv)}{\partial y}+\frac{\partial(\rho wv)}{\partial z}=-\frac{\partial p}{\partial y}+\mu\left(\frac{\partial^2 v}{\partial x^2}+\frac{\partial^2 v}{\partial y^2}+\frac{\partial^2 v}{\partial z^2}\right)-\rho g\beta(T_{amb}-T) \quad \text{(IV.3)}$$

- ✓ **Momentum equations in z-direction**

$$\frac{\partial(\rho w)}{\partial t}+\frac{\partial(\rho uw)}{\partial x}+\frac{\partial(\rho vw)}{\partial y}+\frac{\partial(\rho ww)}{\partial z}=-\frac{\partial p}{\partial z}+\mu\left(\frac{\partial^2 w}{\partial x^2}+\frac{\partial^2 w}{\partial y^2}+\frac{\partial^2 w}{\partial z^2}\right) \quad \text{(IV.4)}$$

✓ **Energy equations**

$$\frac{\partial\left(\rho c_p T\right)}{\partial t}+\frac{\partial\left(\rho u c_p T\right)}{\partial x}+\frac{\partial\left(\rho v c_p T\right)}{\partial y}+\frac{\partial\left(\rho w c_p T\right)}{\partial z}=k\left(\frac{\partial^2 T}{\partial x^2}+\frac{\partial^2 T}{\partial y^2}+\frac{\partial^2 T}{\partial z^2}\right)+q''' \quad \text{(IV.5)}$$

✓ **Boussinesq approximation**

It consists in considering that the density (ρ) of the fluid varies only in the term of the volume forces (gravity), whose variations with temperature, assumed linear, generate natural convection. These variations are then translated by an equation of state that relates density to temperature. However, the Boussinesq approximation is applied to the buoyancy term in the averaged momentum equations Eqs. (IV.6-11) where the density is calculated from Eq. (IV.6) as **[5]**:

$$\rho=\rho_0\left(1-\beta(T-T_0)\right) \quad \text{(IV.6)}$$

The Boussinesq approximation is valid when [6]:

$$\left(\beta(T-T_0)\right)\ll 1 \quad \text{(IV.7)}$$

✓ **K-epsilon RNG Turbulence model equations**

$$\frac{\partial\left(\rho k\right)}{\partial t}+\frac{\partial}{\partial x_i}\left(\rho k u_i\right)=\frac{\partial}{\partial x_j}\left[\left(\mu+\frac{\mu_t}{\sigma_k}\right)\frac{\partial k}{\partial x_j}\right]+P_k-\rho\varepsilon \quad \text{(IV.8)}$$

$$\frac{\partial\left(\rho\varepsilon\right)}{\partial t}+\frac{\partial}{\partial x_i}\left(\rho\varepsilon u_i\right)=\frac{\partial}{\partial x_j}\left[\left(\mu+\frac{\mu_t}{\sigma_\varepsilon}\right)\frac{\partial\varepsilon}{\partial x_j}\right]+C_{1\varepsilon}\frac{\varepsilon}{k}P_k-\rho C^*_{2\varepsilon}\frac{\varepsilon^2}{k} \quad \text{(IV.9)}$$

Where $C^*_{2\varepsilon}$ is calculate by the following equation:

$$C^*_{2\varepsilon}=C_{2\varepsilon}+\frac{C_u\eta^3(1-\eta/\eta_0)}{1+\beta\eta^3} \quad \text{(IV.10)}$$

And η is calculate by the following expressions

$$\eta=Sk/\varepsilon \quad \text{(IV.11)}$$

In addition, S is calculate by the formulate:

$$S=\sqrt{2S_{ij}S_{ij}} \quad \text{(IV.12)}$$

It is interesting to note that the values of all of the constants (except β) are derived explicitly in the RNG procedure. Variable and constant that used in RNG k-e are summarized in the **Table. IV.4**

Table. IV. 4: Presentations of the turbulent variable and constant appears in each equation

Symbol	Signification	Formulation
G_k	Represents the generation of turbulent kinetic energy that arises due to mean velocity gradients.	$G_k = \rho \overline{u_i u_j} \frac{\partial u_j}{\partial x_j}$
G_b	Represents generation of turbulent kinetic energy the arises due to buoyancy	$G_b = \beta g_j \frac{\mu_t}{\Pr_t} \frac{\partial T}{\partial x_i}$
Y_M	represents the fluctuating dilation in compressible turbulence that contributes to the overall dissipation rate	$Y_M = 2\rho\varepsilon M_t^2$
S_ε	source terms defined by the user dissipation	$S_\varepsilon = \sqrt{2S_{ij}S_{ij}}$
S_k	source terms defined by the user kinetic energy	$S_k = \sqrt{2S_{ij}S_{ij}}$
$C_{1\varepsilon}$	Constant determined experimentally	$C_{1\varepsilon} = 1.42$
$C_{2\varepsilon}$	Constant determined experimentally	$C_{2\varepsilon} = 1.68$
C_μ	Constant determined experimentally	0.0845
C_v	Constant determined experimentally	100
σ_ε	Inverse effective Prandtl numbers for the turbulent kinetic energy	$\sigma_\varepsilon = 1.2$
σ_k	Inverse effective Prandtl numbers for the turbulent kinetic energy dissipation rate	$\sigma_k = 1.0$
μ_t	Turbulent kinetic energy and its dissipation rate	$\mu_t = \rho C_\mu \frac{k^2}{\varepsilon}$

✓ **VOF model equations**

As none of the earlier investigators used the volume of fluid (VOF) model as an appropriate model for open channel flow, in the present study, a 3D CFD analysis using the VOF model. ANSYS Fluent 16 software, and Gambit 2.4.6 preprocessor software, were used to predict the for modeling an open channel geometry using of the model. In this present work, the VOF model of Eulerian-Eulerian multiphase models was used.

A methodology for the numerical simulation and prediction of the water following over the front surface of the PV module with free air was developed and subsequently used to simulate the flow. In the actual work, Re is greater than 1, and it is also greater than 1. Therefore, the surface tension effect was neglected. Other variables were given default values.

For the current model, the movement of the water surface is captured using the VOF method. A step function F (x, y, z, t) is defined as unity at any cell occupied by fluid (liquid cells) and zero in cells occupied by air (empty cells). Cells with an F function between zero and one contain the water surface (surface cells).

For incompressible flows, the VOF method solves the following advection equation, which is in the conservative form, to calculate the time evolution of the function F:

$$\frac{\partial F}{\partial t} + \nabla.(uF) = 0 \qquad \text{(IV.13)}$$

In the VOF model, all properties are calculated using the volume the fraction in each cell. In a two-phase system, if the phases are represented by the subscripts 12 and 13, and of the volume fraction of the second phase is being tracked, the density in each cell is determined as follows.

$$\rho = \alpha_2 \rho_2 + (1 - \alpha_2)\rho_1 \qquad \text{(IV.14)}$$

IV. 3. 5 Boundary conditions applied for computational domain

Figure. IV.3 represents the computational domain of both configuration and implemented boundary conditions.

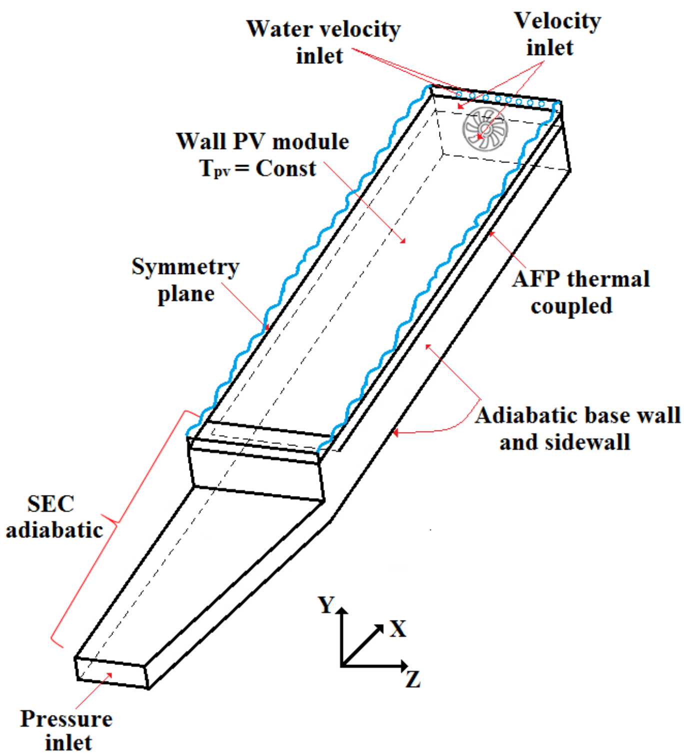

Figure. IV. 3: *The computational domain and Boundary conditions of both configurations of PV/T Bi-fluid system for active air and water cooling case*

It is noticed that, boundary conditions, which implemented to describe the current problem to solve it numerically. Firstly, we consider a Three-dimensional open channel asymmetrically heated by a constant temperature imposed on the two PV modules and absorbers (see **Table IV.5**). All walls in this system have no-slip and impermeable boundary conditions. The working fluid applied to the interior domain is the air. The ambient temperature considered with constant physical proprieties in the air channel. For modeling, the fluid, a free surface in Ansys Fluent a short program (UDF) was used (see Annex A) to set all physical proprieties varied as a function of air and water temperature and flow time. The time step was calculated by used the courant number and expressed by the following equations:

$$\Delta t = \frac{C\Delta x}{V} \qquad \text{(IV.15)}$$

Where Δt is the time step, Δx is the minimal grid size and V is mean velocity of water flow.

Following boundary conditions are implemented on the CFD model:

- No-slip boundary condition for all the walls
- Fully developed air with non-uniform velocity enters at an inlet temperature and turbulent intensity of 300 K and 5 % respectively.
- A pressure outlet is executed at the outlet air channel.
- Pressure inlet is fixed at the sloped entrance air channel.
- A constant, uniform temperature is imposed uniformly on the PV module surface.
- Right sidewalls are implicated with symmetry boundary conditions, due to symmetrical geometry.
- Adiabatic boundary conditions were implemented for the Left sidewall and base sidewall.

Table. IV. 5: Boundary conditions used in the present simulation for the fluid and solid phases

Wall surface	**Boundary conditions**	**Mathematical expression**
SEC inlet	Pressure inlet	$\Delta P_{in} = 0$, (gauge pressure), $T = T_{amb}$
Air channel outlet	Pressure Outlet	$P = P_{atm}, T = T_{amb}$
PV module surface	Wall	$u = v = 0, \mathrm{T} = \mathrm{T_{PV}}$
Lateral side wall	adiabatic	$\partial T/\partial x = \partial T/\partial y = 0,$
Base wall	adiabatic	$\partial T/\partial y = \partial T/\partial z = 0,$
SEC surface	adiabatic	$\partial T/\partial x = \partial T/\partial z = 0,$
Aluminum Flat plate (AFP)	Thermal coupled	$kal\nabla T_{\sup} = kal\nabla T_{\inf} = \mathrm{T_{AFP}},$

All these boundary conditions were summarized in detail on the **table. IV.5.**

In the numerical simulation, the mesh form has obeyed to the best distribution of volumes in the domain, with the possibility of refining the details wherever necessary. As an example, **figure. IV.4** shows the mesh detail for computational domain calculation of new hybrid PV/T system. The structured mesh type is the best grid for CPU calculator and the reliability of solution.

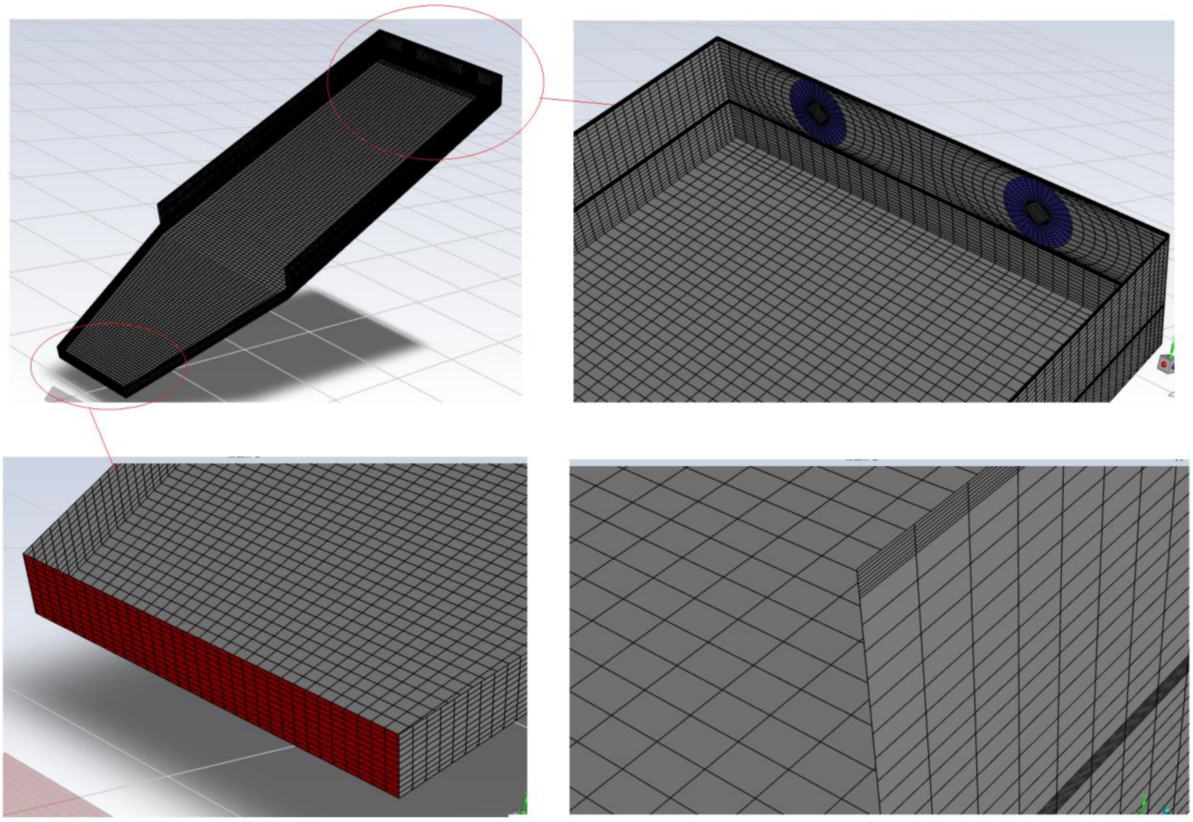

Figure. IV. 4: *Mesh generation and computational domain calculating of PV/T Bi-fluid solar collector*

IV.4 Thermo-hydrodynamic parameters assessment and airflow velocity consideration

- **Grashof number**

The Grashof number based on PV module length, Gr_L is defined as follows **[7]**:

$$Gr_{L_{PV}} = \frac{g\beta(T_{PV} - T_{amb})L_{PV}^{3}}{\nu^{2}} \quad \text{(IV.16)}$$

Where β is the thermal expansion coefficient, T_W is the PV module surface temperature, T_{amb} is ambient air temperature, ν is the kinematic viscosity of air, α is the thermal diffusivity of air and g is the acceleration of gravity.

- **Prandtl number**

$$Pr. = \frac{\nu}{\delta} \tag{IV.17}$$

Here, ν: is fluid viscosity and thermal diffusivity.

- **Water Reynolds number**

$$\mathrm{Re}_w = \frac{VD_{hw}}{\nu} \tag{IV.18}$$

- **Air Reynolds number**

$$\mathrm{Re}_a = \frac{VD_{ha}}{\nu} \tag{IV.19}$$

- **Nusselt number**

The average Nusselt number of the solar panels is presented as:

$$Nu_{L\_avg} = \frac{h_{c\_avg} \times L_{PV}}{k_f} \tag{IV.20}$$

Where k_f is thermal conductivity of fluid (air), the heat transfer coefficient h, and L the length of PV module. *Where;* h_{c_avg} represents the average convective heat transfer coefficient is expressed:

$$\bar{h} = \int_{\substack{\text{exposed}\\ \text{surface}}} h_{conv} \times dn \tag{IV.21}$$

The thermal energy heat gain from air stream produced by the PV/T Bi-fluid is calculated by using the Eqs. (IV.22), **[8]**:

$$Q_{air} = m_{air}.Cp_{air}(T_{air,out} - T_{air,in}) \tag{IV.22}$$

Where $\dot{m}_{air}$ is the air mass flow rate in kg/s; Cp_{air} is air specific heat in J/(kg.K), $T_{air,out}$ and $T_{air,in}$ are the outlet and inlet tempertaures of air flow, respectivly.

The formula for calculating air mass flow rate is:

$$m_{air} = \rho_{air}.V_{air}.A_{in} \tag{IV.23}$$

Where, V_{air} is the air velocity inside the air channel. For forced convection V_{air} is calculated by Eq.(IV.24) according to Ref.**[9]:**

$$V_{air}=\sqrt{\frac{0.5.g.\beta.Lc(T_{air,out}-T_{air,in})+(\Delta p/\rho_{air})}{C_f(L_C/D_h)+C_{in}.(A_d^2/A_{in}^2)+C_{out}.(A_d^2/A_{out}^2)}} \quad (IV.24)$$

Where β is the thermal expansion of the air fluid and calculated by the expression (IV.25):

$$\beta=\frac{1}{Tm}=\frac{2}{(T_{air,out}+T_{air,in})} \quad (IV.25)$$

D_H is the air channel's hydraulic diameter, i.e.

$$D_h=2.\left(\frac{Wc.SC}{Wc+SC}\right) \quad (IV.26)$$

Δp is the pressure difference created by the DC fan provided by the manufacturer.

$$\Delta p=f(P_{Fan}) \quad (IV.27)$$

A_d is the cross-sectional area of the air duct (m^2), $A_d=Wc.SC$. $A_{in;}A_{out;}$. The friction factors of the air channel's walls, entrance, and exhaust loss coefficients are $C_f, C_{in};\text{and}\, C_{out}$ respectively, and are calculated as follows:

$$C_f=0.3*1.368.G_x^{0.084}, C_{in}=1.5; C_{out}=1.5 \quad (IV.28)$$

For forced convection, the air velocity is conveniently correlated to global solar irradiation (G), as follows **[10]**

$$V_{air}=C_{Fan}.G \quad (IV.29)$$

Where C_{Fan} is a coefficient that represents the slope of the linear correlation, which is plotted according to the experimental data of the present study of the air velocity through the air channel with two DC fans compared to the global solar irradiation.

The thermal energy gain from the water stream generated by the PV/T Bi-fluid solar collector is calculated using Eq. (IV.30) **[11]**:

$$Q_w=m_w.Cp_w(T_{w,out}-T_{w,in}) \quad (IV.30)$$

Where $\dot{m}_w$ is the water mass flow rate at the inlet nozzle pipe.

In this study, the hybrid PV/T Bi-fluid system is cooled down using both air and water working fluids. This is, the total thermal energy of the system is the sum between that generated by air and water. Thus, the total thermal efficiency η_{th}, is calculated according to the relation given by Duffie and Beckman **[12]**:

$$\eta_{th} = \frac{(Q_{air} + Q_w)}{GA_c} \tag{IV.31}$$

The overall efficiency $\eta_{overall}$ has been widely used in the performance evaluation of hybrid PV/T system, according to Ref. **[13]** $\eta_{overall}$ is assessed as follow:

$$\eta_{ovrall} = \eta_{th} + \eta_{el} / \eta_{power} \tag{IV.32}$$

where η_{th} and η_{el} are respectively the thermal efficiency and electrical efficiency of the PV/T Bi-fluid system, η_{power} is a conversion factor often assigned a value of 38%, which is the second law efficiency of a conventional thermal power plant.

Exergy analysis is a practical thermodynamic tool to evaluate the effectiveness of an energy system under irreversible conditions. In this study, the exergy efficiency of the system is the sum of electrical efficiency and exergy efficiency of water and air stream, as expressed by Eq. (IV.31) as cited in the **[14]:**

$$\eta_{ex,overall} = \eta_{el,PVT} + \eta_{th,air}\left[1 - \frac{To}{T_{air,out}}\right] + \eta_{th,w}\left[1 - \frac{To}{T_{w,out}}\right] \tag{IV.33}$$

IV. 5 Results and discussions

In this section, the effect of air and water Reynolds numbers, and system tilt angle on the heat transfer rate has been achieved. Moreover, the co-current and counter-current cooling flow direction effect on the average Nusselt number was adopted. A comparison of new hybrid PV/T Bi-fluid system performance in terms of energy with the present experimental setup was examined and validated.

IV. 5. 1 Influence of Reynolds number on the average Nusselt number

Figure IV.5 displays the average Nusselt number evolution as a function of the Grashof number for different air Reynolds numbers of three tilt angles. It seems from f**igure (IV.5 a)** that the average Nusselt number improved versus the Reynolds number increasing.

The tilt angles affect positively the average Nusselt numbers, especially for low Reynolds numbers values. However, for the high Reynolds number, the average Nusselt number stays constant.

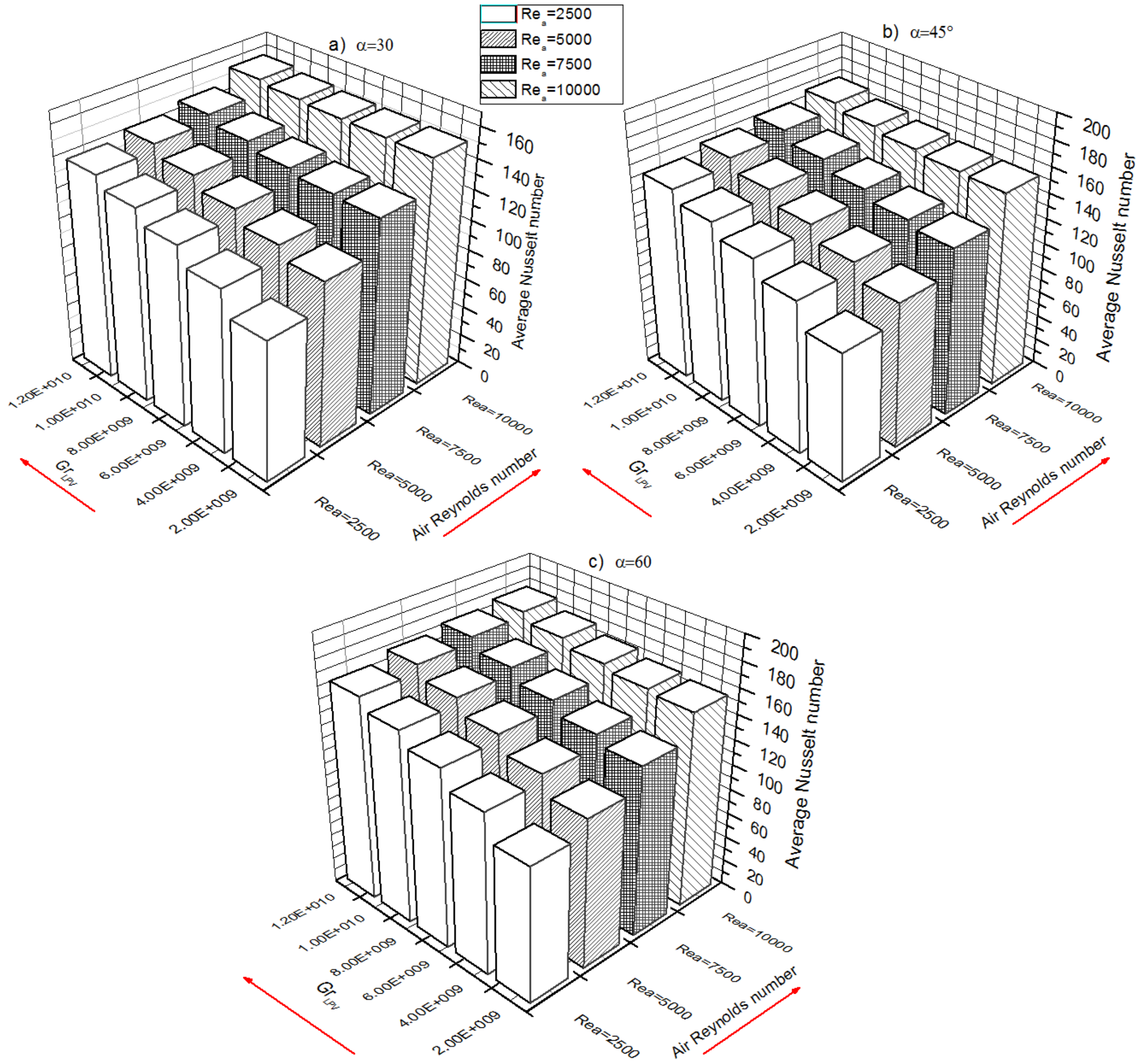

***Figure. IV. 5 (a-c):** Average Nusselt number evolution versus Grashof number and Reynolds number for different tilted angle*

IV. 5. 2 Influence of tilt angle and Grashof number on the average Nusselt number

Figure IV.6 shows average Nusselt number growth as a function of Grashof numbers and tilt angles for both cases of various air channel tilted angles for both cases with and without AFP. From **figure IV. 6 (a, b)** it is observed that the average Nusselt number is enhanced by the progression of the air channel tilted angle for tilt angles carried in the range, $15° \le \alpha \le 60°$. Contrary, for up to $60° \le \alpha \le 90°$, the average, Nusselt numbers stay constant.

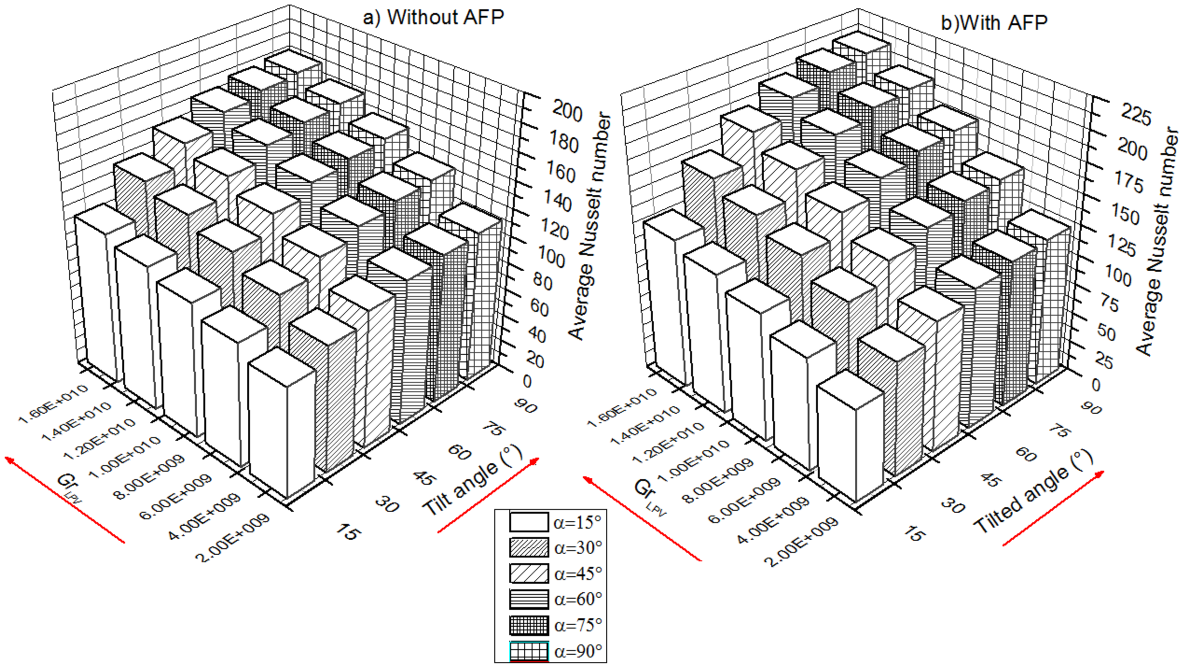

Figure. IV. 6 (a, b): *Average Nusselt number evolution versus tilted angle and GrL for the case with AFP and without AFP for Re_a=2500*

IV. 5. 3 Influence of co-current and counter-current on the average Nusselt number

Figure IV.7 (a, b) displays the average Nusselt number as a function of evolution Grashof number and air Reynolds numbers for both cases co-current and contra-current.

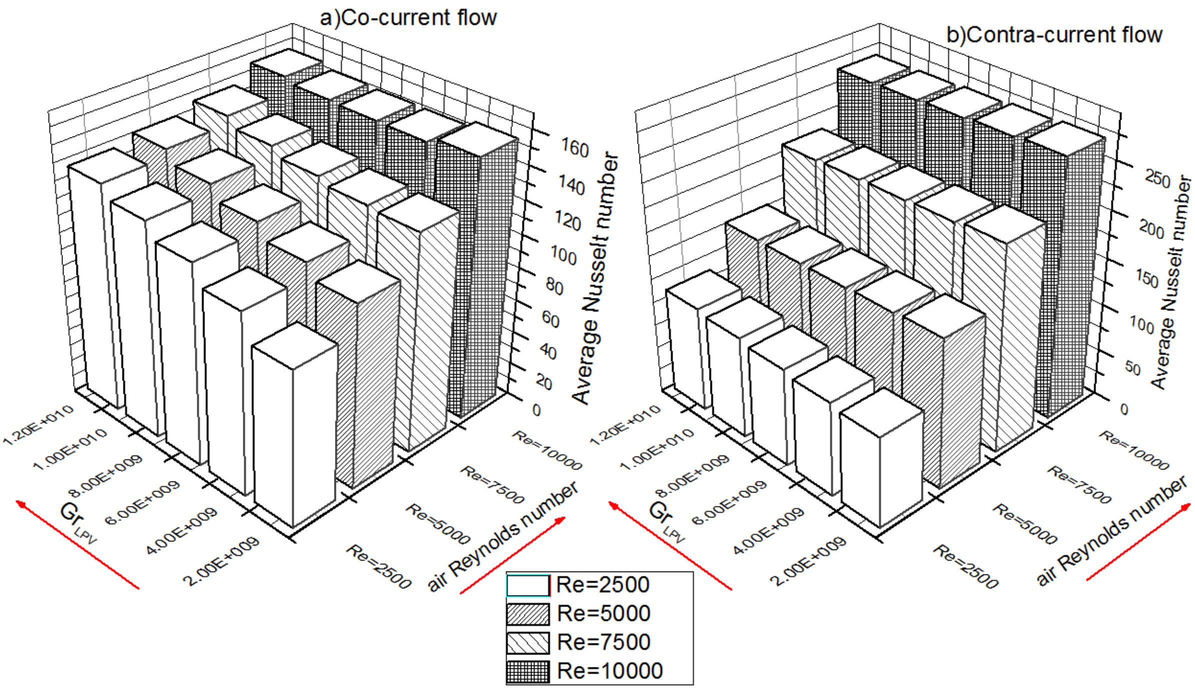

Figure. IV. 7 (a, b): *Average Nusselt number evolution versus tilted angle and for various Gr L_{PV} for the case with co-current and counter-current.*

It noticed that the average Nusselt numbers are more enhanced for the case contra-current than the other case. On the other hand, the average Nusselt number is improved by about **80%** for high Reynolds numbers.

IV. 5. 4 Influence Reynolds number on the friction coefficient

Figure VI.8 illustrates friction coefficient distribution as a function of the Reynolds number for different Grashof numbers at, α=60°. It is recorded that there is a little increase in the average friction coefficient against the air Reynolds number.

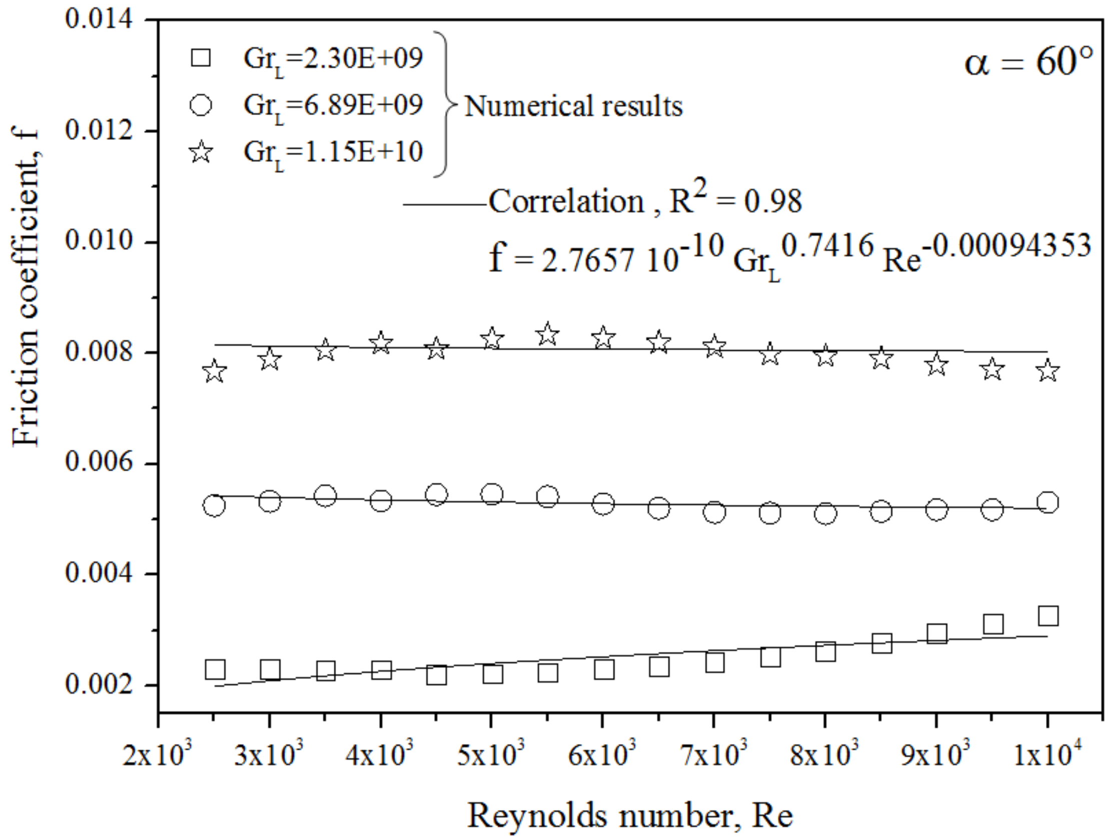

Figure. IV. 8: *Friction coefficient evolution versus air Reynolds number for various Gr_L for the case with AFP.*

However, except for low Grashof numbers, it is observed that is the friction coefficient is increase.

The friction coefficient on the PV module surface versus air Reynolds number are fitted as the following correlations :

$$f = 2.7657 * 10^{-10} \mathrm{Gr}^{0.7416} \mathrm{Re}^{-0.00094353} \;;\; 2.310^{9} \le Gr_L \le 1.1510^{9};\; 2500 \le \mathrm{Re}_a \le 10000 \quad \text{(IV.34)}$$

IV. 5. 5 Influence Reynolds number on the total heat transfer gain

Figure IV.9 demonstrates total heat transfer gain distribution as a function of the Reynolds number for different Grashof numbers at, α=60°. It is noted that the improveing of the total heat tansfer rate against air Reynolds number.

The total heat transfer rate evolution versus Reynolds number are fitted by following correlation:

$$Q = 7.96*10^{-8} Gr^{0.7416} Re^{0.8079} \; ; 2.310^{9} \leq Gr_L \leq 1.1510^{9}; \; 2500 \leq Re_a \leq 10000 \qquad \text{(IV.35)}$$

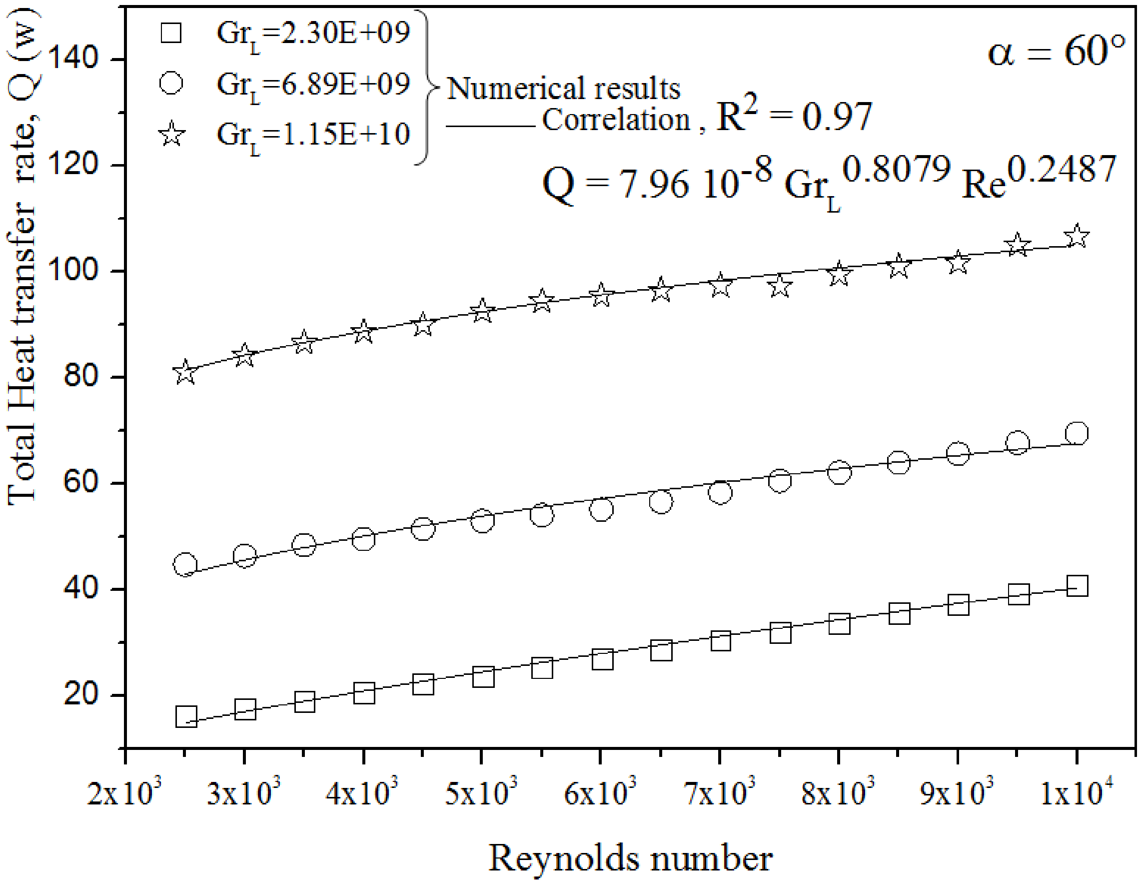

Figure. IV. 9: *Total Heat transfer rate evolution versus tilt angle and for various Gr_L for the case with AFP.*

V. 5. 6 Influence of Reynolds number on the average Nusselt number

The average Nusselt number distribution as a function of the Reynolds number for different Grashof numbers at, α=60° is presented in **figure IV.10**. It is recorded that the enhancement of the average Nusselt number versus the increasing of air Reynolds number.

The average Nusselt number evolution versus Reynolds number is fitted by the following correlation :

$$Nu_{L\_avg} = 0.1516 Gr^{0.2919} \mathrm{Re}^{0.0498} \;;\; 2.310^{9} \leq Gr_L \leq 1.1510^{9};\; 2500 \leq \mathrm{Re}_a \leq 10000$$

(IV.36)

V. 5. 7 Comparison of the New hybrid PV/T Bi-fluid with experimental current data

It is noticed that the numerical results is very agreement with experimental data.
A comparative analysis on the average thermal energy, electrical power, and overall efficiency between the present works against similar researches works reported in the literature is depicted in **Figure IV.11.**

It is noticed that the numerical results are very agreement with experimental data.

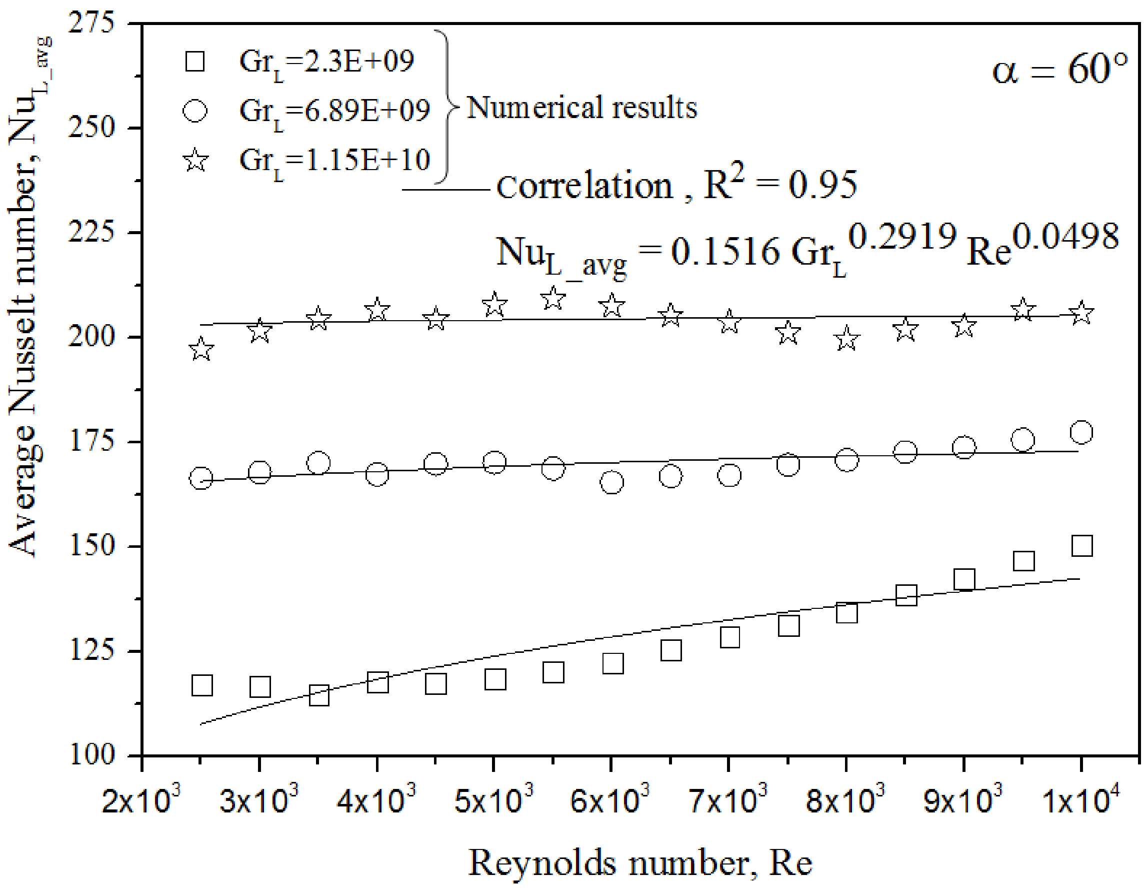

Figure. IV. 10: *Average Nusselt number evolution versus tilted angle and for various Gr_L for the case with*

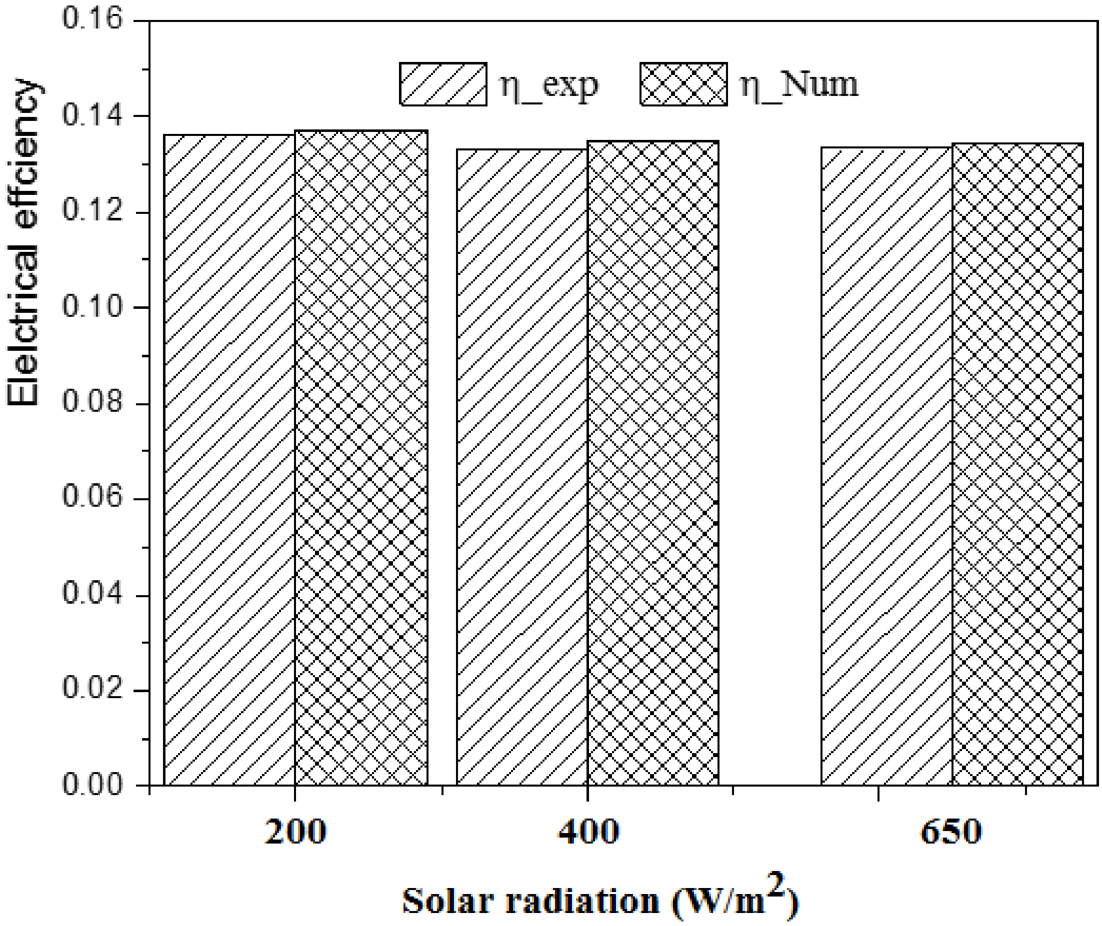

Figure. IV. 11: *Comparison of the average electrical efficiency of experimental and numerical data for current study*

IV.6 Conclusions

In this numerical works, the improvement of heat transfer by active air and water-cooling of a new concept of hybrid photovoltaic/thermal system is presented. The influence of air Reynolds numbers, tilt angles and Grashof numbers on the average Nusselt number ,friction coefficient and heat gain were studied.

In addition, a comparison of numerical simulation with current experimental data is performed. The obtained results allows us to achieve the following main conclusions:

- ✓ The tilt angles affect positively the average Nusselt numbers especially for low Reynolds numbers values. However, for high Reynolds number the average Nusselt number stay constant.

- ✓ A little increase in the average friction coefficient against air Reynolds number, while for low Grashof numbers it is observed that is the friction coefficient is increase.
- ✓ Average Nusselt number affected by the increasing of air Reynolds number.
- ✓ The average Nusselt number is improved by about 80% for high Reynolds numbers, for the case of contra-current compared with the case of co-current flow direction.

As future work, a new air channel and water channel was proposed over the front side of PV module to enhance the heat transfer consequently the system performance. Besides, the effect of different position of DC fans and different tube plastic diameters will be proposed.

References

[1] M. Lebbi, K. Touafek, A. Benchatti, L. Boutina, A. Khelifa, M. T. Baissi, S. Hassani. Energy performance improvement of a new hybrid PV/T Bi-fluid system using active cooling and self-cleaning: Experimental study, Applied Thermal Engineering. 182 (2021) 116033. https://doi.org/10.1016/j.applthermaleng.2020.116033

[2] M. T. Bouzaher, N. Bouchahm, B. Guerira, C. E. Bensaci, M. Lebbi. On the thermal stratification inside a spherical water storage tank during dynamic mode. Applied Thermal Engineering, 159(2019) 113821. doi.org/10.1016/j.applthermaleng.2019.113821

[3] W. Al Hadad, Y. Jannot, D. Maillet. Modélisation du transfert de chaleur dans un demi-échangeur, In Congrès Français de Thermique SFT 2015. (2015).

[4] M. Cable. An evaluation of turbulence models for the numerical study of forced and natural convective flow in Atria (Doctoral dissertation, Queen's University). (2009).

[5] D. D. Gray, A. Giorgini. The validity of the Boussinesq approximation for liquids and gases. International Journal of Heat and Mass Transfer, 19 (1976)545-551. doi.org/10.1016/0017-9310(76)90168-X

[6] https://www.afs.enea.it/project/neptunius/docs/fluent/html/ug/node470.htm#eq-boussinesq

[7] L. Boutina A. Khelifa, K. Touafek, M. lebbi, M. T. Baissi. Improvement of PVT air-cooling by the integration of a chimney tower (CT/PVT), Applied Thermal Engineering. 129(2018) 1181–1188. Doi.org/10.1016/j.applthermaleng.2017.10.097

[8] R. Kumar, M.A. Rosen. Performance evaluation of a double pass PV/T solar air heater with and without fins, Appl. Therm. Eng, 31 (2011)1402-1410. doi.org/10.1016/j.applthermaleng.2010.12.037

[9] H. U. Choi, Y. B. Kim, C. H. Son, J. I. Yoon, K. H. Choi. Experimental study on the performance of heat pump water heating system coupled with air type PV/T

collector, Applied Thermal Engineering. 178 (2020) 115427. doi.org/10.1016/j.applthermaleng.2020.115427

[10] J. Jie, Y. Hua, P. Gang, J. Bin, H. Wei. Study of PV-Trombe wall assisted with DC fan, Building and Environment. 42 (2007)3529-3539. doi.org/10.1016/j.buildenv.2006.10.038

[11] H. Yi, J. Jie, H. Hanfeng, J. Aiguo, H. Chongwei, L. Chenglong. Optimized simulation for PV-TW system using DC fan. In Proceedings of ISES World Congress 2007 Springer, Berlin, Heidelberg. (2008) 1617-1622. doi.org/10.1007/978-3-540-75997-3_332

[12] J.A. Dufe, W.A. Beckman. Solar engineering of thermal processes, 2nd edn, Wiley, New York. (1991).

[13] B. J. Huang, T. H. Lin, W. C. Hung, F. S. Sun. Performance evaluation of solar photovoltaic/thermal systems, solar energy. 70(2001)443-448. doi.org/10.1016/S0038-092X(00)00153-5

[14] S. Hassani, R. Saidur, S. Mekhilef, R. A. Taylor. Environmental and exergy benefit of Nanofluid-based hybrid PV/T systems, Energy Conversion and Management. 123(2016), 431-444. doi.org/10.1016/j.enconman.2016.06.061.

Chapter V

Study, Design and experiment of a new hybrid PV/T Bi-fluid system

V.1 Introduction

The operating temperature rise and the dust accumulation on the front side of solar panels especially in arid and semi-arid desert areas is a major issue that causes low performance and damage to photovoltaic cells.

This experimental investigation aimed to improve the solar panel electrical performance mounted in new hybrid system PV/T Bi-fluid that combines both active cooling and self-cleaning technique simultaneously.

This new hybrid system was actively cooled from the backside of the PV module by forced air circulation, while its front side was cooled and cleaned by flowing water. The impact of the operating temperature and global solar radiation intensity on the PV module output voltage, electrical current, electrical power output, and electrical efficiency was evaluated experimentally.

Experimental results showed a decreasing linear relationship between electrical efficiency and the increase in PV module's temperature i.e. reference case without cooling.

V.2 System description

Figure V.1 (a, b) shows the air channel installed behind the PV module with and without the integration of an aluminum plate at a well-determined distance from the PV module. The installation of the aluminum plate serves to increase the transfer rate and therefore to maximize the heat extraction from the back surface of the PV module.

To address experimentally the operating temperature rise issue as well as dust accumulation in the PV/T system, an outdoor test platform is required to set up. **Figure V.2** depicts the experimental hybrid Bi-fluid PV/T prototype. The basic principle of the self-cleaning technique SC used in this design is based on the formation of spherical drops of water flowing out from small holes of a perforated pipe mounted on the front surface of the PV module. When these droplets roll on the inclined PV surface, dust particles are pulled out and the surface become clean. It is worthy to mention that the water used is tap water without adding any cleaning agent. Experimental tests were performed in the Applied Research Unit for Renewable Energy, at Ghardaïa province, Algeria, during a typical day (October 12 th, 2019).

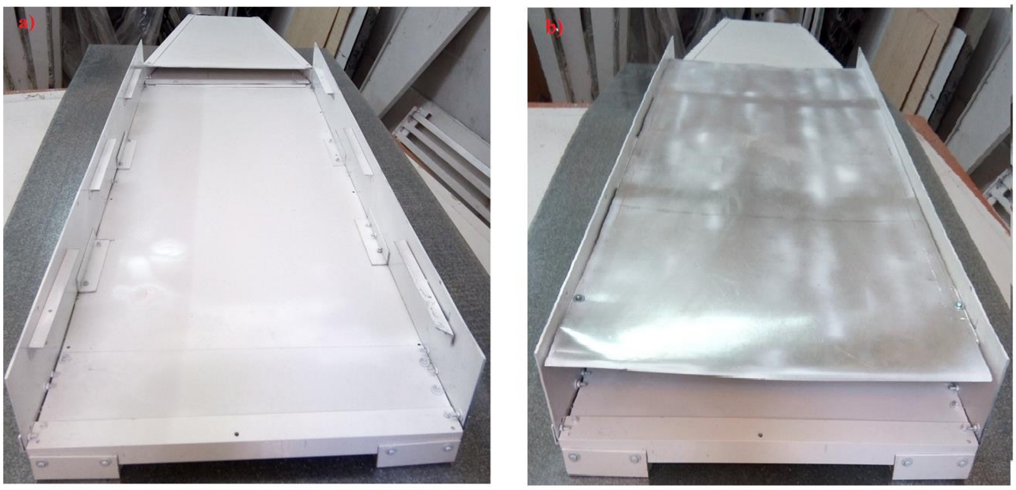

Figure. V. 1: a) *Photograph of the experimental prototype with integrated of insulation air channel at the bottom part of PV module,* ***b)*** *Insulation air channel with integrated of aluminium flat plat*

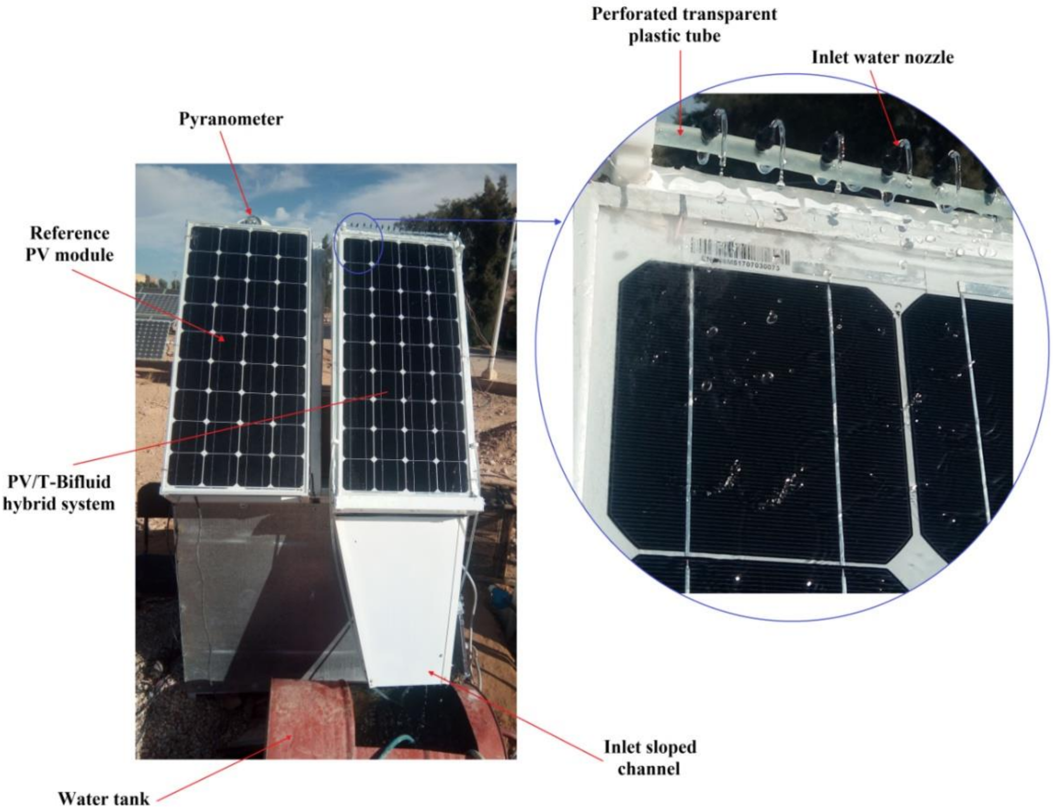

Figure. V. 2: *Photograph of the experimental prototype.*

The Specification of the PV module reference under standard testing conditions (STC) (G_{STC}= 1000 W/m2, T_{ref}=25 °C, AM= 1.5) is shown in **Table. V. 1.**

All components of the hybrid Bi-fluid PV/T system are presented in detail in the schematic diagram as shown in **Figure V. 2**, and listed down in **Table. V. 2.**

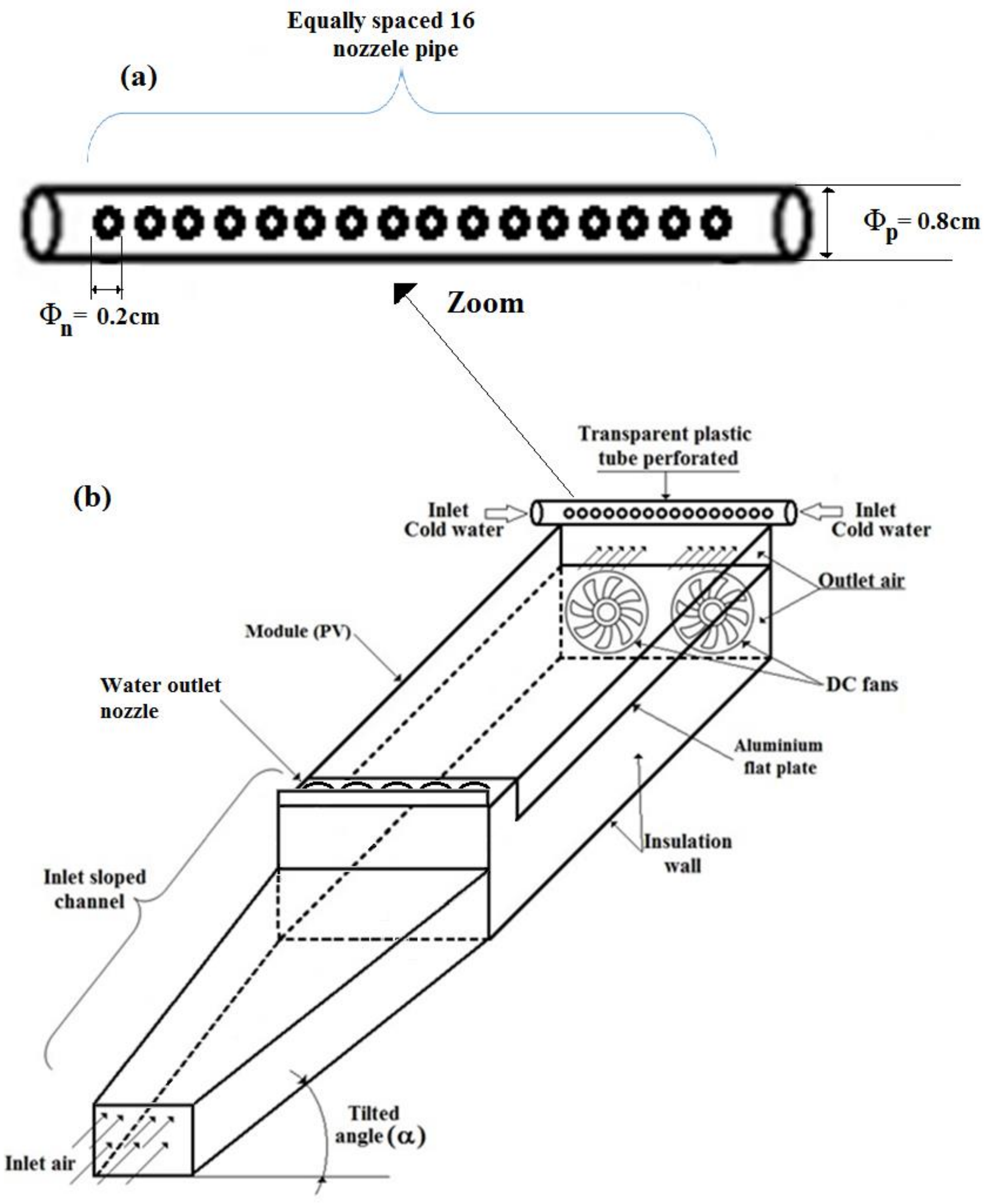

Figure. V. 3: ***a)*** *Zoom of transparent pipe nozzle,* ***b)*** *Illustration diagram of the new hybrid system PV/T Bi-fluid components.*

Table V. 1: Specification of the PV module under standard testing conditions (STC).

Components	Symbol	Properties
Nominal electrical power	P_m	90 W
Hail resistance	-	Max. φ25mm,at 23 m/s
Open circuit voltage	V_{oc}	22.45 V
Short-circuit current	I_{sc}	5.19 A
Voltage at max power	V_{mp}	18.74 V
Current at max power	I_{mp}	4.8 A
Filling factor	FF	77.24 %
PV module standard electrical efficiency	η_o	13.62 %
Dimensions of the PV module	L_{PV}, W_{PV}, h_{PV}	1200x550x30 mm
Glass thickness	eg	3.2 mm
Cell number	Nc	36
Weight	-	5.78 kg
Transmittance absorbance Product	-	0.9
Specification (mm)	Mono 125x/4*9	-
Temperature at standard testing conditions	T_{ref}	25°C
Global solar irradiation	G_{STC}	1000W/m^2
Air mass	AM	1.5

An aluminum flat plate was installed rear of the PV module at an offset distance of d = 3cm. Two DC fans were installed at the collector's outlet to extract hot air out of the system. In the purpose to ensure active cooling and self-cleaning of the PV module, a perforated plastic tube with 16 nozzles was installed at the top edge of the PV module as shown in f**igure V.3**.

Table V. 2: Specifications of the new hybrid PV/T Bi-fluid solar collector.

Components	Symbol	Specification
PV module dimensions (length, depth, thickness)	L_{PV}*W_{PV}*h_{PV}	1200*550*30 mm
Insulator thickness	e	5mm
Water transparent plastic tube diameter	Φ_p	8mm
diameter of the water pipe nozzle inlet	Φ_{in}	2mm
diameter of the water Outlet water nozzle	Φ_{out}	5mm
Collector channel height	Sc	140mm
Collector channel depth	Wc	570mm
Collector channel length	Lc	1300mm
Entrance sloped channel length	Le	750mm
Entrance sloped channel depth from the inlet	We	300mm
Entrance sloped channel depth from the outlet	Ws	570mm
Entrance sloped channel height	Se	50mm
Aluminum flat plat length	L_{alm}	1200mm
Aluminum flat plat depth	W_{alm}	570mm
Aluminum flat plat thickness	E_{alm}	8mm
Aluminum flat plat distance to the PV module	d_{alm}	30mm

The hybrid system PV/T Bi-fluid includes an air channel mounted at the back of the PV module to cool the rear surface via forced convection using two DC air fans. In order to pull in cold air and to increase vortex inside the main air channel, a sloped inlet channel was attached to the collector entrance.

Table V. 3: Characteristic and operating conditions of the DC Fans

Description	**Parameter**	**Value**
DC air fan maximum power	P_{Fan}	3.6W
Dimension of air fan	$L_{fan} x\ w_{fan} x\ h_{fan}$	92x92x25mm
Operating voltage	V_{fan}	24V
Operating current	I_{fan}	150mA

The characteristics and specifications of the DC fan and water pump are listed in **Table. V.3** and **Table V. 4,** respectively.

Table V. 4: Characteristic and operating conditions of the DC water pump

Description	**Parameter**	**Value**
DC Water pump maximum power	Pw	4.2W
Dimension of water pump	$l_{pump} x\ w_{pump} x\ h_{pump}$	54x37x42mm
Operating voltage	V_{pump}	12V
Operating current	I_{pump}	375mA
Volumetric flow rate	Q_{pump}	240 L / H
Inlet diameter	$\phi_{in,\ pump}$	8 mm
Outlet diameter	$\phi_{out,\ pump}$	8mm

V.3 Measuring instrument and procedure

Equipment and measuring instruments used to collect experimental data output are shown in **Figure V. 4 (a-f),** the following response parameters were measured during the experiment:

- Temperature in the inlet air entrance channel.
- Temperature in the air channel behind the PV.
- Water inlet temperature.
- Water outlet temperature.
- Temperature air collector outlet
- Water tank temperature.
- Temperature of the PV module forward and backward.
- Ambient temperature.
- Solar intensity, G on the PV module.
- Charging current, I_ PV, I_PVT L and charging voltage, PV and PVT.
- Short circuit current, Isc and open-circuit voltage, Voc

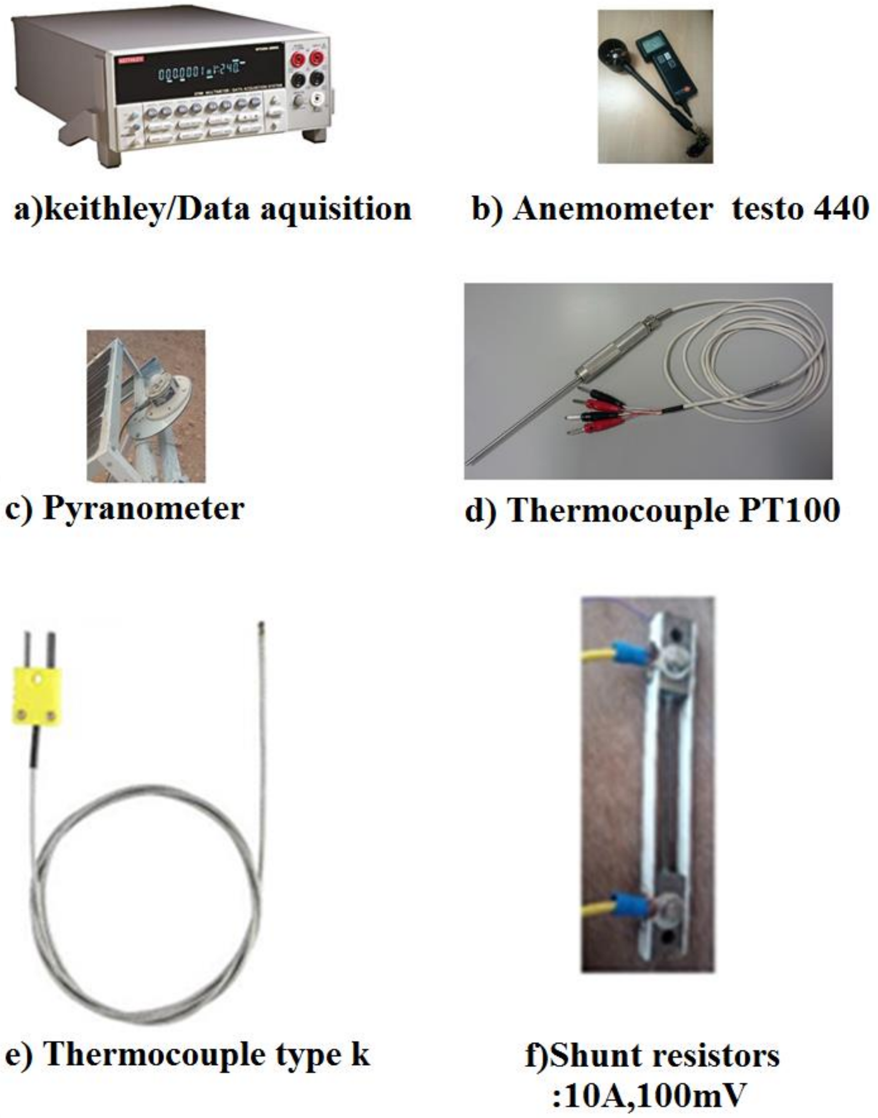

Figure. V. 4 (a-f): *Equipment used for data acquisition.*

V.3.1 Temperature measurement

Many temperatures were measured using a type k or type pt100 thermocouple sensor connected to the data acquisition device. These thermocouples are placed on both systems, whether control or PVT / Bi-fluid in well-defined situations as shown in **figure V.5 (a, b)**.

We installed three type k thermocouples on the front surface and three on the last surface for each PV module.

There are also three thermocouples are placed at the inlet and three on the outlet of the air manifold in order to measure the average temperature of the airflow at the inlet and outlet.

There are two other thermocouples that have been installed at the inlet and outlet of the water in order to measure the temperature of the water entering and leaving the PV / T collector.

The other three type k thermocouples are placed in a shaded right to measure the average ambient temperature. Setup design, system dimensions, and temperature sensors' locations (see **Figure V.5 (a, b)**.

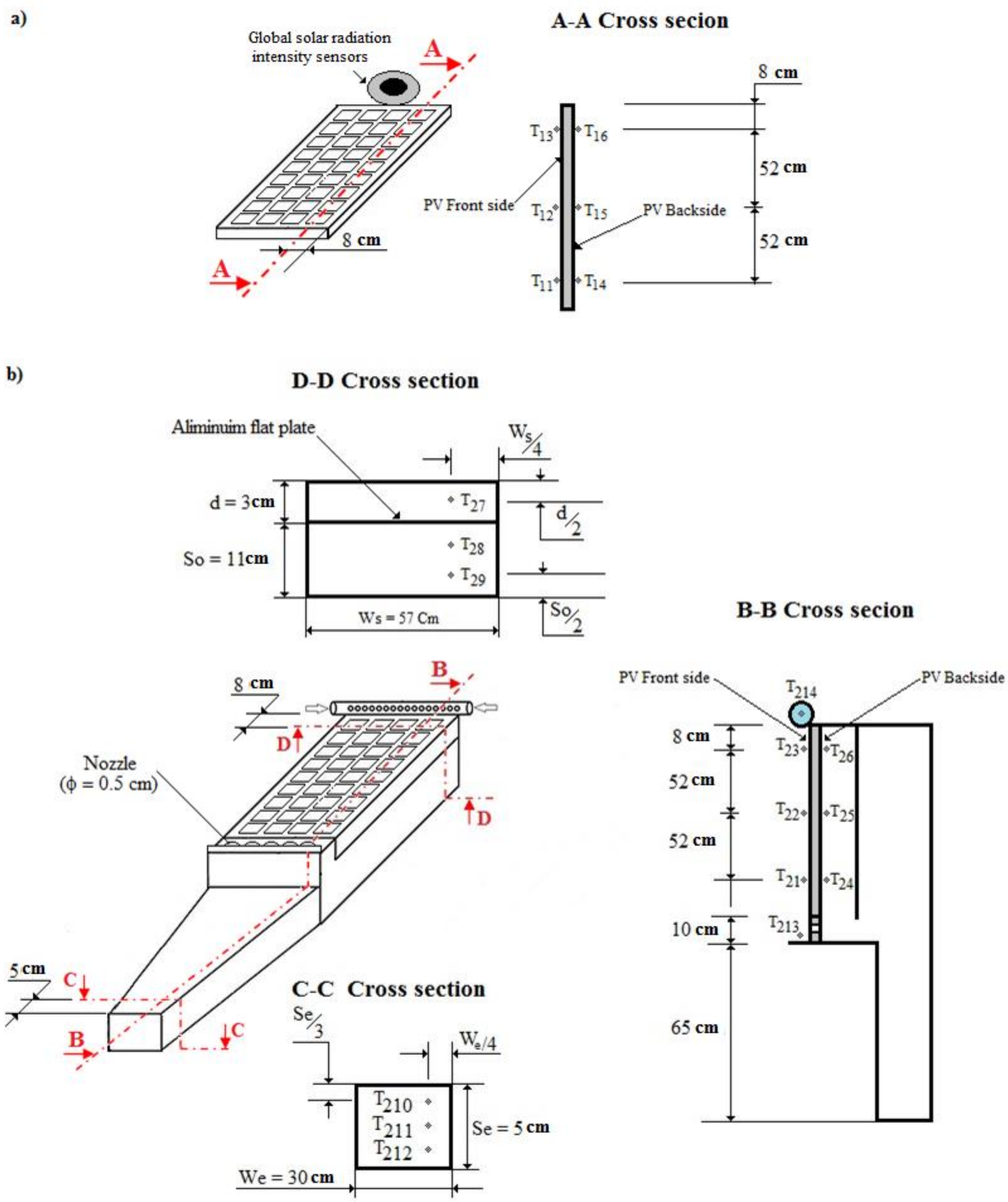

Figure. V. 5 (a, b): *Systems dimensions and the temperature sensors locations, a) PV module (reference case), b) PV/T Bi-fluid solar collector.*

Three thermocouple sensors were installed on the front and backside of each PV module in both systems. Three other thermocouple sensors were added at the inlet and outlet air channel, and two water thermocouple sensors were placed at the inlet of the perforated transparent tube and the water outlet nozzle is represented in **figure V.5 (a, b).**

Experimental test platform dimensions are 0.57 m width, 1.87 m length, and an air-gap height of 0.14 m. The slopped entrance channel length of 0.735 m. Before proceeding to the experimental test, the thermocouples are calibrated by a water bath with a sensitivity of ± 0.2 °C between 10 and 70 °C. A thermal data logger collects the thermocouple readings.

V .3.2 Global solar radiation intensity measurement

In designing the PV system, it is essential to know how much sunlight is available in a particular location at any given time. Solar radiation is an instantaneous power density in units of kW/m^2.

Solar radiation varies throughout the day from 0 kW/m^2 at night to a maximum of around 1 kW/ m^2. Global solar radiation is highly dependent on location and local weather. It consists of global or direct radiation measurements taken periodically throughout the day. The measurements are carried out either using a pyranometer for the measurement of global solar radiation.

V .3.3 Air channel and wind speed measurement

The TESTO 440 anemometer measures the average velocity of the airflow at the inlet air channel, connected to two DC Fans at its outlet to extract the air outside the system. During outdoor experimental tests, the electrical circuit of the photovoltaic modules is connected to an electrical load consists of two lamps 60W and two DC fans as shown in figure 5. The mass flow rate of air is $m_{air} = 0.028\ kg/s$, and the average air velocity calculated using Eq. 13 equal to $V_a = 0.31\ m/s$.

V .3.4 Water mass flow rate measurement

The water pump volumetric flow rate Q_{pump} is set to 2 L/min, and knowing the number of water nozzles in the perforated tube is equal to 16 nozzles, hence the volumetric flow rate for each nozzle Q_{vn} is equal to 0.125 L/min. We have set this value in such a way that we ensure that the water film must cover the entire surface of the PV module with a very thin thickness reaching up to one millimeter.

V .3.5 Voltage and current measurement

The measurement of the voltage produced by the two separate photovoltaic panels is done directly using two wires placed at the positive and negative terminals of the panels and connected directly with the data collection device.

For both systems, either reference PV module or hybrid PV/T Bi-fluid system, the measurement of electric current intensity was carried out every five minutes through a shunt resistor.

During outdoor experimental tests, the electrical circuit of the photovoltaic modules is connected to an electrical load consists of two lamps 60W and two DC fans as shown in f**igure V. 6, the** mass flow rate of air is $m_{air} = 0.028\ kg/s$, and the average air velocity calculated using Eq. 13 equal to $V_a = 0.31\ m/s$.

All experiment results were collected at a time resolution of one hour. Finally, all sensors (temperature, solar radiation intensity, and resistors shunt) were connected to a data acquisition apparatus Keithley 2700 monitored via personal computer i.e. PC.

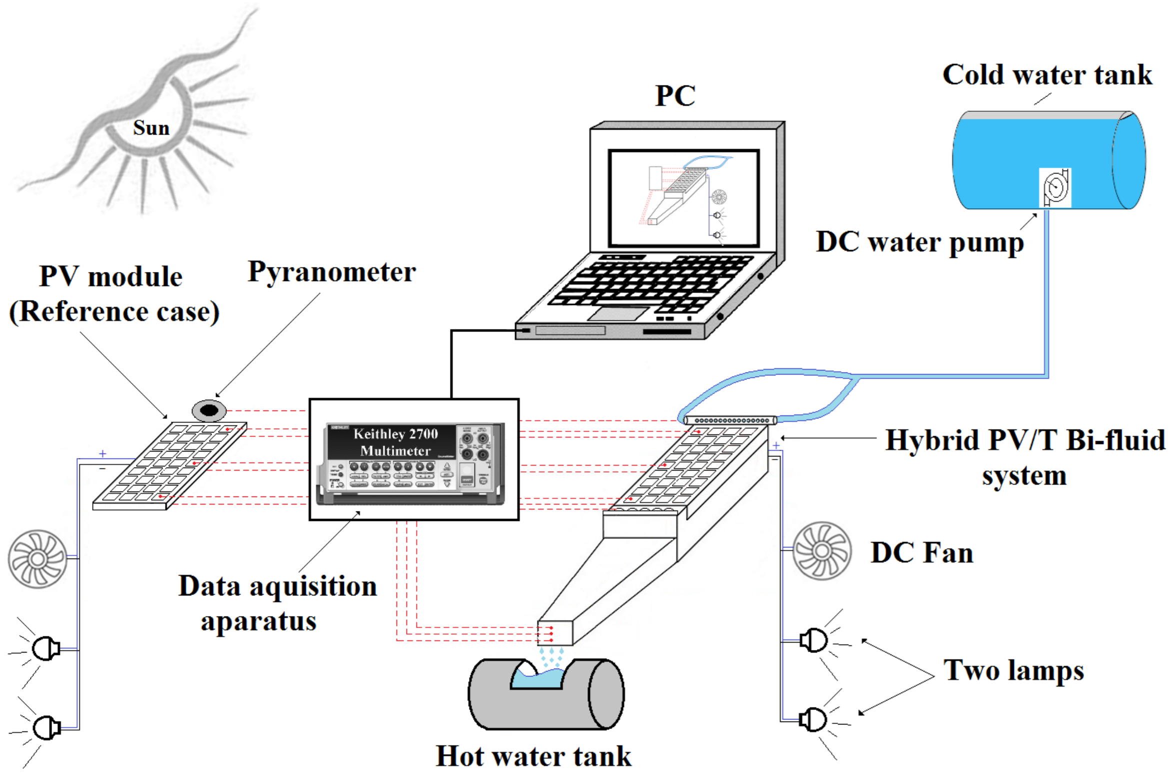

Figure. V. 6 (a, b): *A representative diagram of the experimental test procedure.*

V.4 Uncertainty analysis

Uncertainty and errors in data measurement are inevitable due to the accuracy level of used equipment, and the manner in which results are taken, either by notes or by reading.

Therefore, it is important to calculate the uncertainty of all used measuring instruments and variables.

The uncertainty of the measuring instruments was calculated according to the Holman method **[1]** using the following equation:

$$w_R = \left[\left(\frac{\partial R}{\partial V_1} w_1 \right)^2 + \left(\frac{\partial R}{\partial V_2} w_2 \right)^2 + \cdots + \left(\frac{\partial R}{\partial V_n} w_n \right)^2 \right]^{1/2} \quad \text{(V.1)}$$

Where $R = R\,(V_1, V_2 \ldots V_n)$, and it is a function of n variables $(V_1,\, V_2 \ldots V_n)$ normally distributed, and $w_1, w_2 \ldots w_n$ correspond to the uncertainty intervals for each single variable. The uncertainty interval for the result is w_R.

In instance, the total uncertainty for temperature measurements T can be derived from uncertainty interval of thermocouples, Data Acquisition, and cable connection as follow;

$$W_{R,total} = \left[\left(w_{thermocouple} \right)^2 + \left(w_{dataaquision} \right)^2 + \left(w_{Connection} \right)^2 \right]^{1/2}$$
$$W_{R},_{total} = \left[(0.5)^2 + (0.5)^2 + (0.5)^2 \right]^{1/2} = 0.8°C \quad \text{(V.2)}$$

The calculated uncertainty values for each measuring instrument are depicted in **Table V. 5.**

Table V. 5: Operating range and uncertainty of the measurement instruments**.**

Nu.	Instruments	Measured parameter	Uncertainty (%)	Operating range
1	Steel scale	Air channel dimensions	± 0.001m	-
2	Thermocouple Type , K and Type PT100	Temperatures	±0.8°C	-50 ~ +400 °C
4	Pyranometer	Global solar radiation intensity	±10 W/m^2	0~2000W/m2
5	Shunt Resistors	Current intensity	±0.5%	0 ~ 10A
6	Multifunction anemometer Testo 440	Wind speed and air flow velocity	±0.5 %	0 ~ 25 m/s
7	Keithley 2700 Data Acquisition	Collect measured data	± 0.1%	-

V.5 Performance computations

V.5.1 Electrical performance

Electrical performance of the new hybrid PV/T Bi-fluid system is compared to that obtained for the PV reference panel. For both cases, the PV module supplies an electrical load likewise a real operational system, where the current was measured using shunt resistors. Calculation of the maximum electrical power output of the PV module, defined as follows **[2]**:

$$P_{mP} = I_{mP} . V_{mP} \tag{V.3}$$

The net electric power of the system $P_{net,PVT}$ is obtained after subtracting the total power consumed by the pump and DC fans from the total gross power generated by the PV module.

$$P_{net,PVT} = P_{mp} - P_{consumed} \tag{V.4}$$

Where $P_{consumed}$ is the total power consumed by the water pump and DC fans in case of hybrid PV/T Bi-fluid system, which expressed by Eq (5):

$$P_{consumed} = 2P_{Fan} + P_{pump} \tag{V.5}$$

Where the power DC fan calculated by formula:

$$P_{Fan} = I_{Fan} . V_{Fan} \tag{V.6}$$

The instantaneous electrical efficiency defined as the ratio of the maximum net power to the global solar irradiation received by the PV module area **[3]**:

$$\eta_{el,PVT} = \frac{P_{net,PVT}}{G.A_{PV}} \tag{V.7}$$

G is the global solar radiation intensity, and A_{PV} is the PV module area.

The instantaneous efficiency for the PV reference panel is calculated by the following formula **[4]**:

$$\eta_{el,PV} = \frac{P_{mp,PV}}{G.A_{PV}} \tag{V.8}$$

Alternatively, electrical efficiency of the PV module can be expressed as function of operating PV cells temperature as follow, Zondag et al. [**4**]:

$$\eta_{el,PV} = \eta_o \left(1 - \beta_{ref} (T_{PV} - 25°C\right) \tag{V.9}$$

Where β_{ref} is temperature coefficient, [1/K], and η_0 is the standard electrical efficiency evaluated under standard test condition (STC) reported in Ref. **[5]** as follow;

$$\eta_o = \frac{V_{mp}.I_{mp}}{G_{STC}.A_{PV}} \tag{V.10}$$

V .5.2 Thermal performance calculation

The thermal energy gain from air stream produced by the PV/T Bi-fluid is calculated using Eqs. (12), **[6]**:

$$Q_{air} = m_{air}.Cp_{air}(T_{air,out} - T_{air,in}) \tag{V.11}$$

Where $\dot{m}_{air}$ is the air mass flow rate in kg/s; Cp_{air} is air specific heat in J/(kg.K), $T_{air,out}$ and $T_{air,in}$ are the outlet and inlet tempertaures of air flow, respectivly.

The formula for calculating air mass flow rate is:

$$m_{air} = \rho_{air}.V_{air}.A_{in} \tag{V.12}$$

Where, V_{air} is the air velocity inside the air channel. For forced convection $V_{air}$is calculated by Eq(14) according to Ref.**[7]**:

$$V_{air} = \sqrt{\frac{0.5.g.\beta.Lc(T_{air,out} - T_{air,in}) + (\Delta p / \rho_{air})}{C_f(L_C / D_h) + C_{in}.(A_d^2 / A_{in}^2) + C_{out}.(A_d^2 / A_{out}^2)}} \tag{V.13}$$

Where β is the thermal expansion of the air fluid and calculated by the expression (14):

$$\beta = \frac{1}{Tm} = \frac{2}{(T_{air,out} + T_{air,in})} \tag{V.14}$$

D_H is the air channel's hydraulic diameter, i.e.

$$D_h = 2.\left(\frac{Wc.SC}{Wc + SC}\right) \tag{V.15}$$

Δp is the pressure difference created by the DC fan provided by the manufacturer.

$$\Delta p = f(P_{Fan}) \tag{V.16}$$

A_d is the cross-sectional area of the air duct (m^2), $A_d = Wc.SC$. $A_{in;}A_{out;}$. The friction factors of the air channel's walls, entrance, and exhaust loss coefficients are $C_f, C_{in};$ and C_{out} respectively, and are calculated as follow:

$$C_f = 0.3*1.368.G_x^{0.084}, C_{in} = 1.5; C_{out} = 1.5 \tag{V.17}$$

For forced convection, the air velocity is conveniently correlated to global solar irradiation (G), as follows **[8]:**

$$V_{air} = C_{Fan}.G \tag{V.18}$$

C_{Fan} is a coefficient represents the slope of the linear correlation, which is plotted according to the experimental data of the present study of the air velocity through the air channel with two DC fans compared to the global solar radiation.

The thermal energy gain from the water stream generated by the PV/T Bi-fluid solar collector is calculated using Eq. (20) **[9]**:

$$Q_w = m_w.Cp_w(T_{w,out} - T_{w,in}) \qquad (V.19)$$

Where $\dot{m}_w$ is the water mass flow rate at the inlet nozzle pipe.

In this study, the hybrid PV/T Bi-fluid system is cooled down using both air and water working fluids. This is, the total thermal energy of the system is the sum between that generated by air and water. Thus, the total thermal efficiency $\eta_{th,}$ is calculated according to the relation given by Duffie and Beckman **[10]**:

$$\eta_{th} = \frac{(Q_{air} + Q_w)}{GA_c} \qquad (V.20)$$

The overall efficiency $\eta_{overall}$ has been widely used in the performance evaluation of hybrid PV/T system, according to Ref. **[11]** $\eta_{overall}$ is assessed as follow:

$$\eta_{ovrall} = \eta_{th} + \eta_{el} / \eta_{power} \qquad (V.21)$$

where η_{th} and η_{el} are respectively the thermal efficiency and electrical efficiency of the PV/T Bi-fluid system, η_{power} is a conversion factor often assigned a value of 38%, which is the second law efficiency of a conventional thermal power plant.

V .5.3 Exergy analysis

Exergy analysis is a practical thermodynamic tool to evaluate the effectiveness of an energy system under irreversible conditions.

In this study, the exergy efficiency of the system is the sum of electrical efficiency and exergy efficiency of water and air stream, as expressed by Eq. (22) as cited in the **[12]:**

$$\eta_{ex,overall} = \eta_{el,PVT} + \eta_{th,air}\left[1 - \frac{To}{T_{air,out}}\right] + \eta_{th,w}\left[1 - \frac{To}{T_{w,out}}\right] \qquad (V.22)$$

V.6 Results and discussion

V.6.1 Weather data

In this experimental study, a typical day was chosen to inspect the effect of the climatic conditions on the PV module energy performance. After several experimental tests, the most effective day chosen was characterized by climatic conditions.

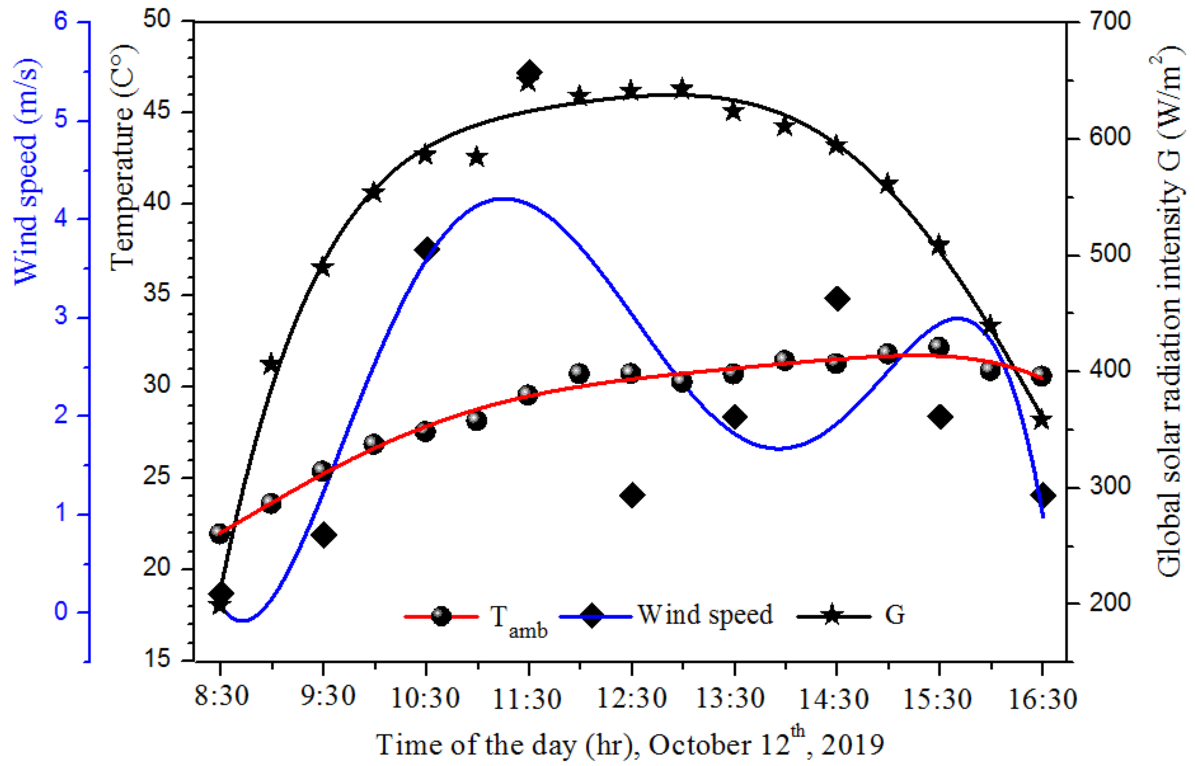

Figure. V. 7: *Evolution of global solar radiation intensity, wind speed, and ambient temperature during time of the day.*

Figure V.7 presented the ambient temperature, wind speed, and global solar radiation intensity during the day. The sky is semi-clear and partially cloudy, it was noticed that the maximum ambient temperature, solar intensity, and wind speed was about 33 °C, 650 W/m^2 and 5.5 m/s, respectively.

V.6 .2 Temperatures profiles evolution

Figure V.8 shows the evolution of the average air and water temperature at the inlet and outlet of the hybrid PV/T Bi-fluid system.

During the test period from 8:30 am to 12:00 pm, it was noted that the average outlet water temperature was slightly below the average inlet water temperature.

This is justified by the fact that the flowing water was cooled by wind motion, whose speed was about 5.5 m/s.

A similar observation was recorded for the air temperature. In contrast, in the evening period, the outlet water temperature is mostly greater than the inlet.

This is due to the noticeable decrease in wind speed and the high intensity of global incident solar radiation.

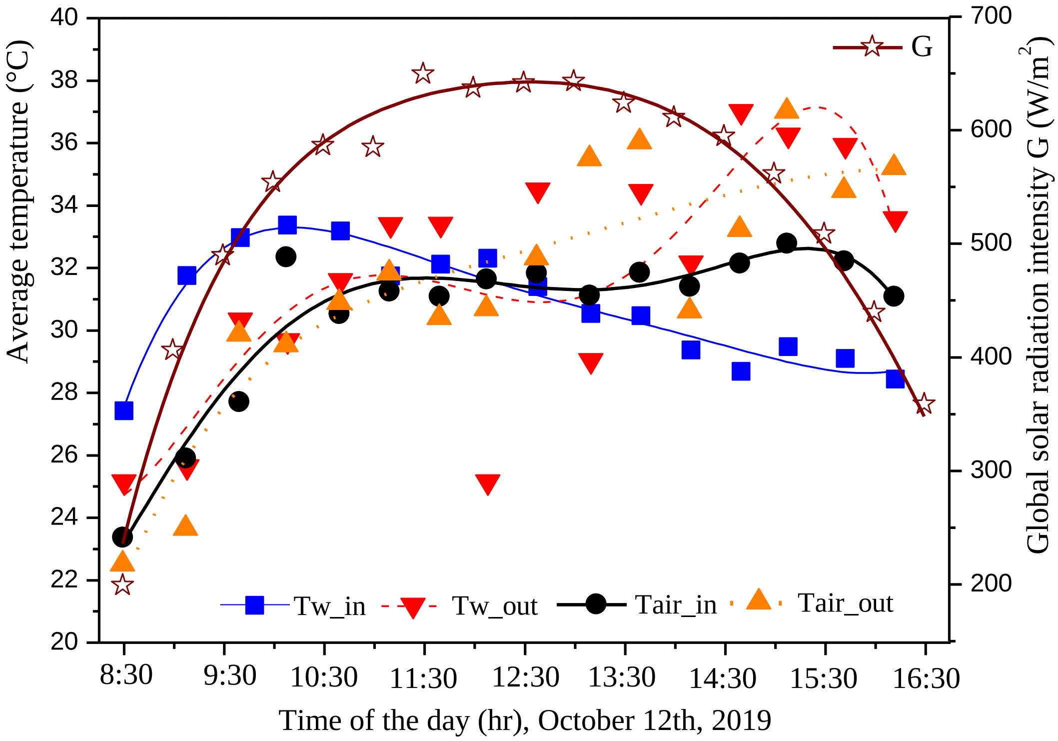

Figure. V. 8: *Evolution of water and air temperature profiles at the inlet and outlet of hybrid system PV/T Bi-fluid solar collector, during the time of the day.*

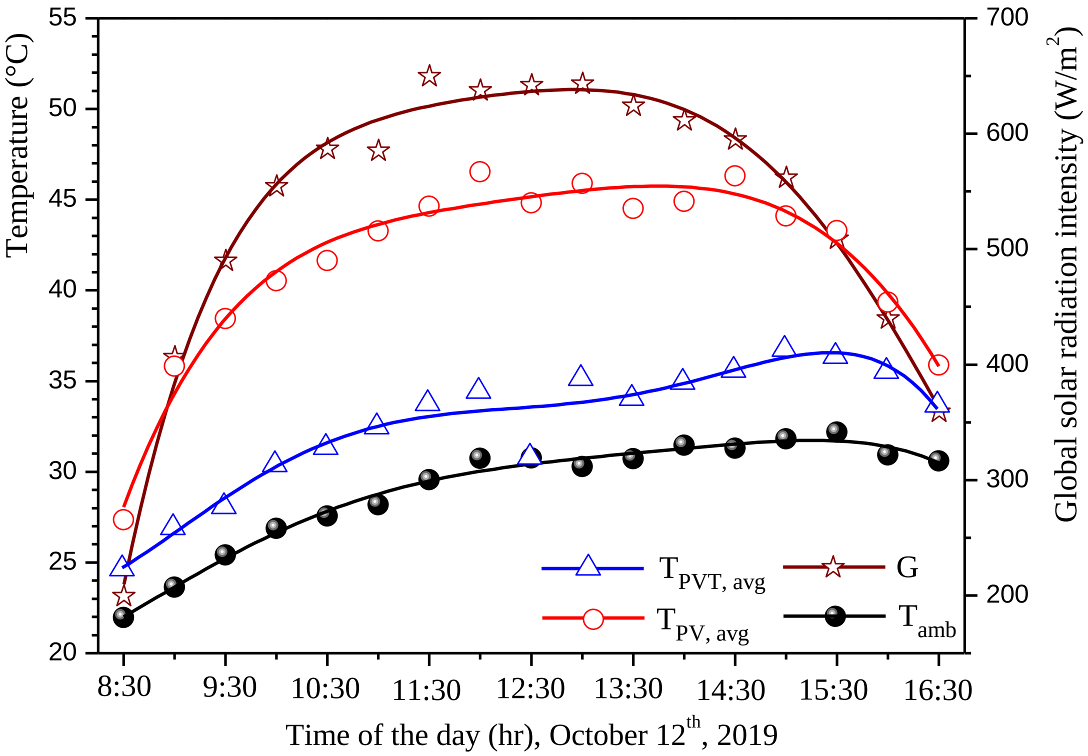

Figure. V. 9: *Evolution of average temperature profiles of the PV module in hybrid PV/T Bi-fluid system and in PV reference panel during full daylight time.*

Figure V.9 shows the full day evolution of average PV module temperature for both cases; new hybrid PV/T Bi-fluid system and PV reference panel. It can be seen that the reference PV module's temperature is higher than the average temperature of the hybrid PV/T Bi-fluid.

Therefore, the concept of the proposed hybrid PV/T Bi-fluid system induces a reduction of up to 15 °C in the average PV module temperature compared to the PV reference panel.

From figure V.10, it is obvious that the PV module's average temperature evolves linearly with the global solar radiation intensity. It is clear that using an active cooling and self-cleaning concept in the new hybrid PV/T Bi-fluid system the PV module average temperature increases by 1.5 °C for every 100 W/m^2 increments in solar radiation intensity, whereas this is 3 °C per 100 W / m^2 in case of PV reference panel.

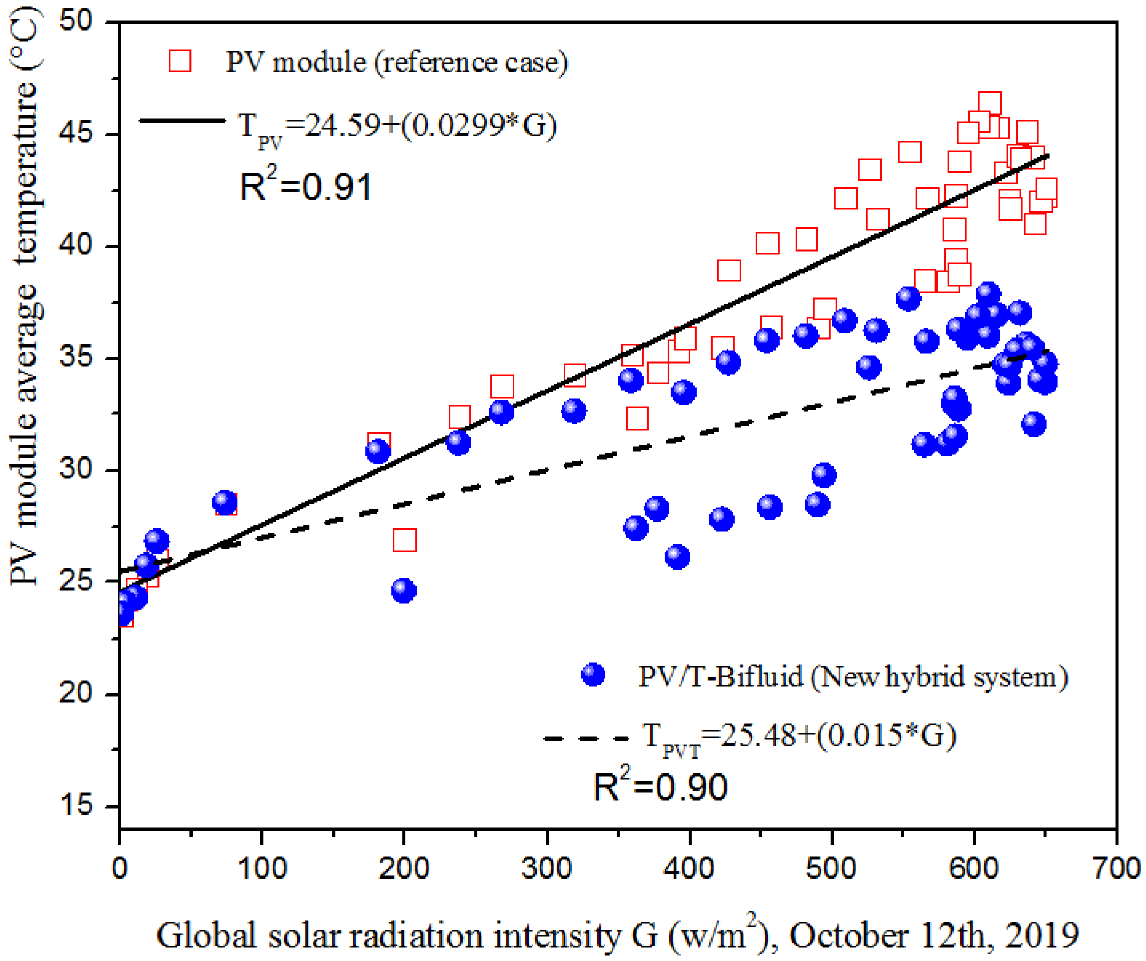

***Figure. V. 10:** PV module average temperature as a function of global solar radiation intensity.*

Correlations of the average temperature evolution of PV modules as a function of global solar radiation intensity for both systems are proposed in this study.

- For PV module (Reference case):

$$T_{PV} = 24.59 + 0.0299G \qquad (V.23)$$

- For new hybrid PV/T Bi-fluid system:

$$T_{PVT} = 25.48 + 0.015G \qquad (V.24)$$

V. 6. 3 Electrical performance analysis

Figure V.11 illustrates the closed-circuit voltage throughout the day for both the proposed hybrid system and PV reference panel. A maximum voltage value of 18.35 V has been noticed for the proposed hybrid system, whereas only 16.8 V for the PV reference panel case. Consequently, an improvement of about 9.22% was observed.

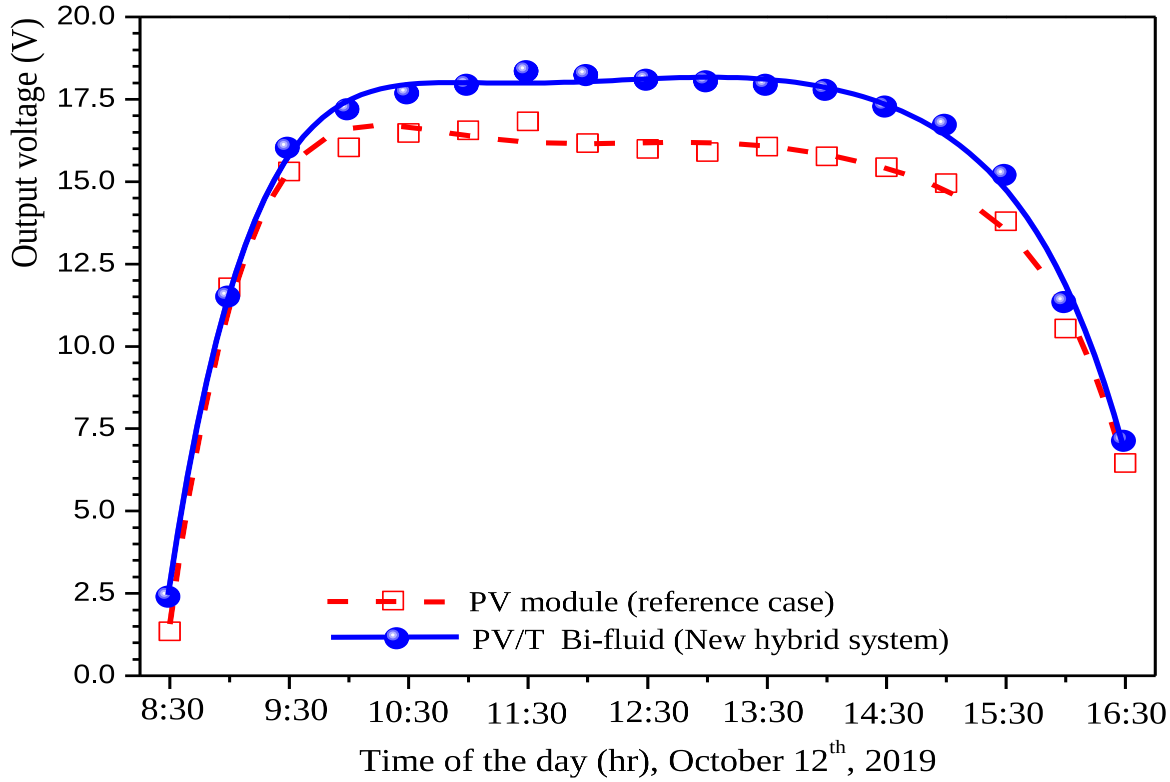

Figure. V. 11: *Output voltage evolution in closed circuit, during the time of the day.*

From **figure V.12**, it is evident that electric current increases proportionally with the intensity of global solar radiation. Under similar solar radiation intensity i.e. 650W/m^2, the electrical current in the hybrid system has been found higher by 6.19% compared to the PV reference panel.

Finally, correlations for electric current intensity as a function of the global solar radiation were developed.

- For PV reference panel:

$$I_{PV} = 0.64543 + 0.00497G \qquad (V.25)$$

- For new hybrid PV/T Bi-fluid system:

$$I_{PVT} = 0.7889 + 0.00513G \tag{V.26}$$

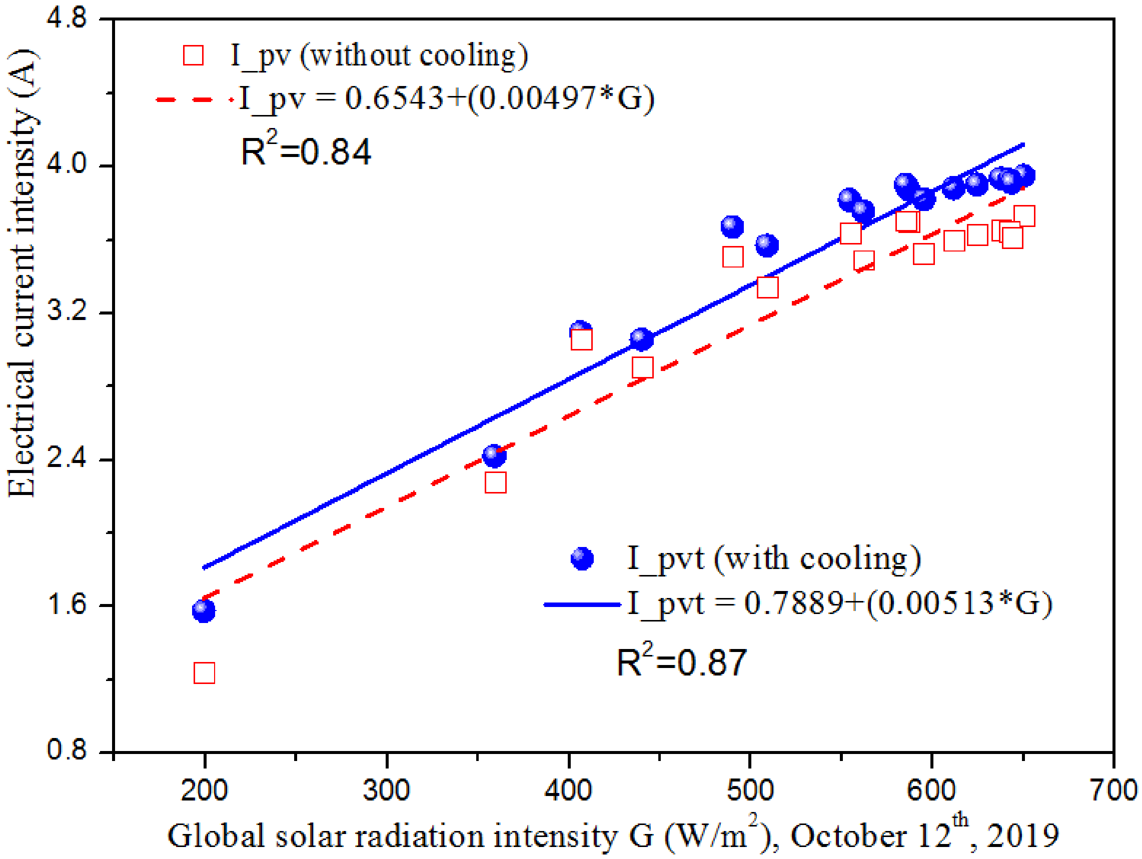

Figure. V. 12: *Electrical current intensity evolution as a function of the global solar radiation intensity*

The daily evolution of electrical power produced by both systems and the power consumed by DC fans and water pump in the hybrid system is presented in **figure V.13**. It is to be noted that the power consumed by DC fans, and water pump have been evaluated by measuring their currents and voltages.

In addition, since the mass flow rate of the cooling water is fixed throughout the experiment, hence it comes out with a pumping power of 3.8W. Furthermore, it has been found that both DC fans and water pump their average power consumption is 4.6W.

A maximum improvement in net electrical power output has been obtained at 13:00 am, where the new hybrid system outperforms the PV reference panel by 13.17%.

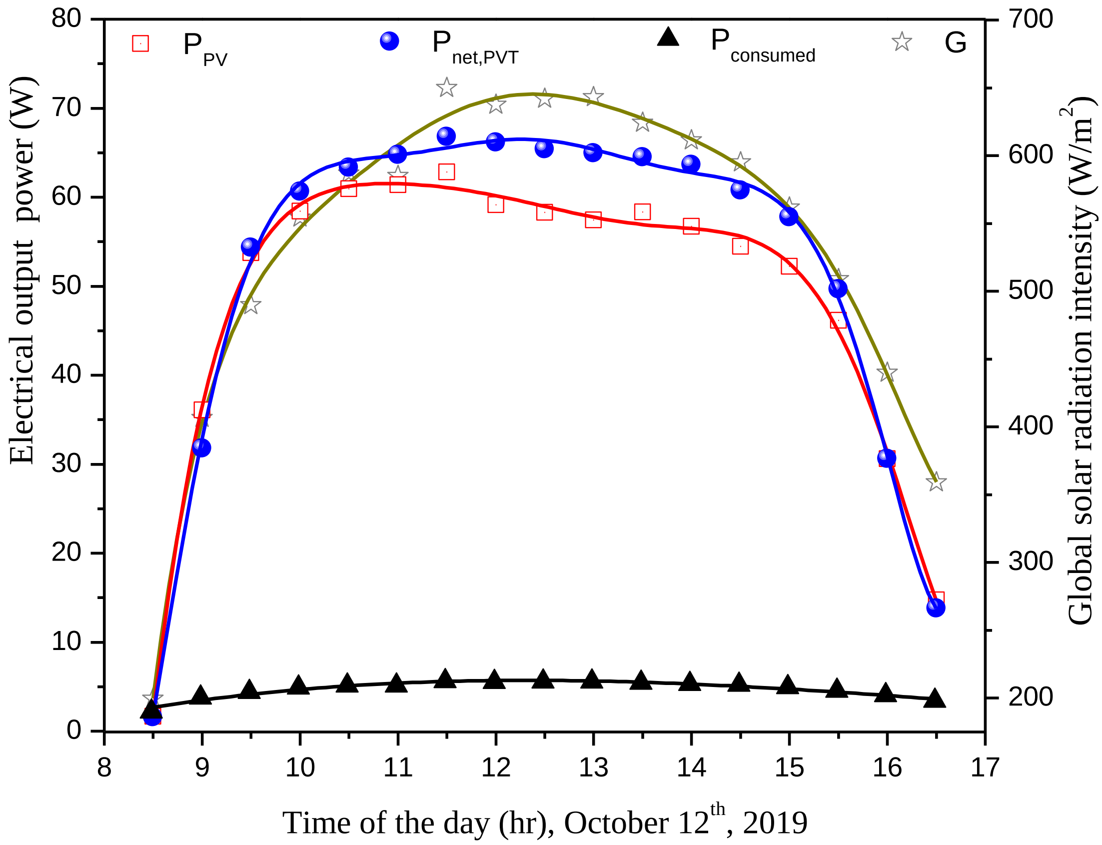

Figure. V. 13: *Electrical output power of the PV module and PV/T Bi-fluid hybrid system, during the time of the day.*

Figure V.14 shows a comparison between the output electrical power of the PV reference panel and the proposed hybrid PV/T Bi-fluid system as a function of the global solar radiation intensity. It's observed that the electrical output power curve increases linearly with the progression of solar radiation, which has a similar trend to current values evolution.

In addition, it is clear that under the value of solar radiation of 400W/m^2 the hybrid system has lower competitiveness compared to the PV reference panel.

This is due to the supplementary electric load i.e. 2 DC fans, in the hybrid system, however, from 400W/m^2 onward the hybrid system compensates for all extra electrical load and mainly performs better than the PV reference panel.

For instance, at 650 W/m^2, the power produced in PV/T Bi-fluid was superior to that produced in the PV reference panel by 13.17%. Correlations for electric power as a function of incident solar radiation are proposed for both systems, see Eqs. 27 and 28.

- For PV module (Reference case):

$$P_{PV} = -20.4926 + 0.1298G \quad \text{(V.27)}$$

- For PV/T Bi-fluid new hybrid system:

$$P_{net,PVT} = -32.7884 + 0.1585G \quad (V.28)$$

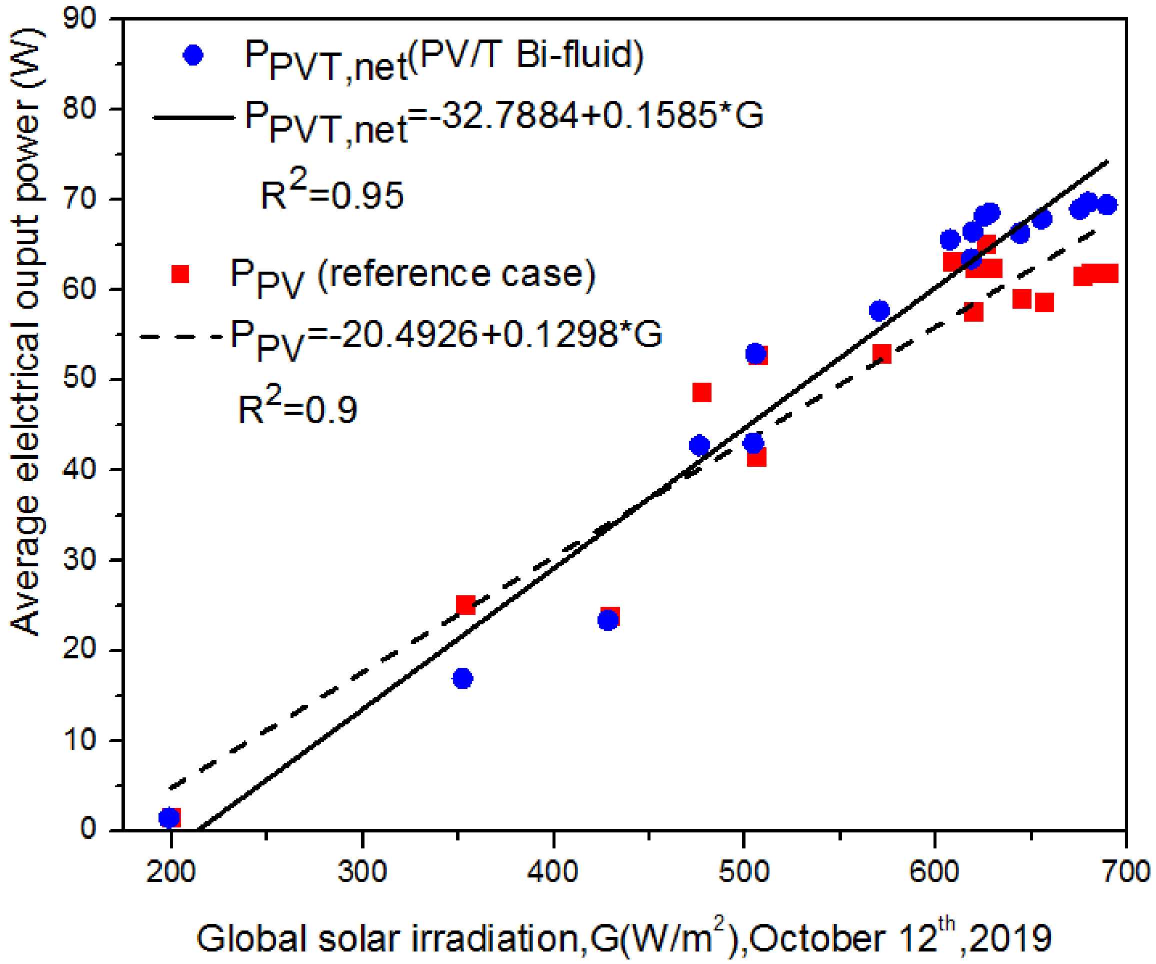

Figure. V. 14: *Evolution of electrical power output of the PV reference panel and the new hybrid system PV/T Bi-fluid, as a function of the global solar radiation intensity.*

The PV module electrical efficiencies varied for both systems are plotted in **Figure V.15**. Straightforwardly, in both systems, the electrical efficiencies decrease during morning hours from 8h00 to 12h00. This is due essentially to the increase in solar radiation intensity, which induces a rise in PV cells temperature, leading to a drop in their efficiencies.

However, it is clear view the decrease slope in the PV reference panel is drastic compared to the hybrid system. For instance, an improvement in daily average electrical efficiency of 3.7% was recorded in the hybrid system against PV reference panel under daily average solar radiation of 524.3 W/m^2.

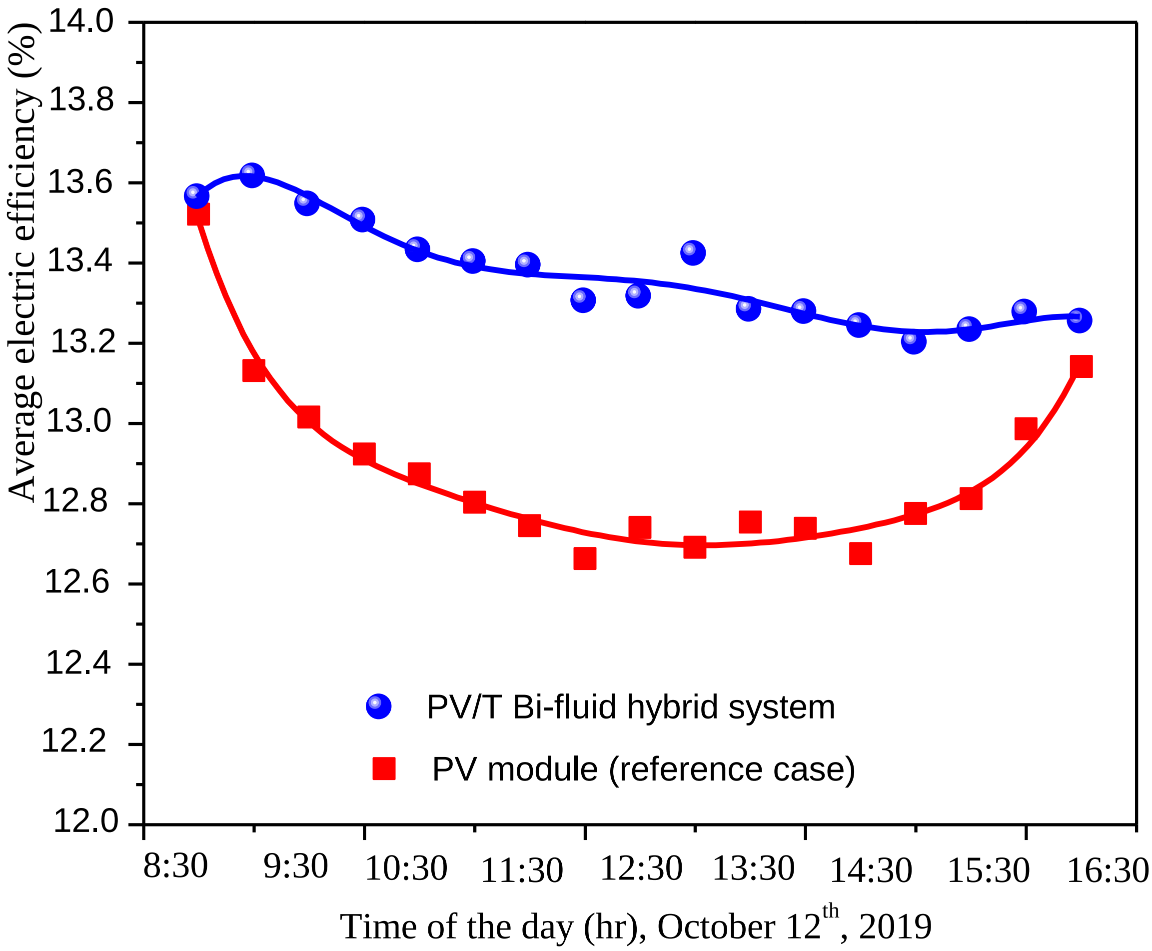

Figure. V. 15: *Electrical efficiency evolution during time of the day*

Figure V.16 depicts the average electrical efficiencies versus the PV module average temperature. A linear progression of the electrical efficiency was noted for both systems. As discussed previously in **Figure 14**, electrical efficiency decreases in both cases when PV module temperature increases. However, due to the efficient active cooling and self-cleaning mechanism implemented in the hybrid system, the latter largely exceed the PV reference panel's performance.

For instance, at the peak value of solar radiation of 650W/m^2, a rate increase in electrical efficiency of 5.7% has been observed in the hybrid systems compared to PV reference panels. Correlations for electric efficiencies as a function of the PV module average temperature were correlated for both systems.

- For PV reference panel:

$$\eta_{el,PV} = -0.1475 - 0.00044 T_{PV,avg} \tag{V.29}$$

- For new hybrid PV/T Bi-fluid system:

$$\eta_{el,PVT} = -0.1422 - 0.0003 T_{PV,avg} \qquad (V.30)$$

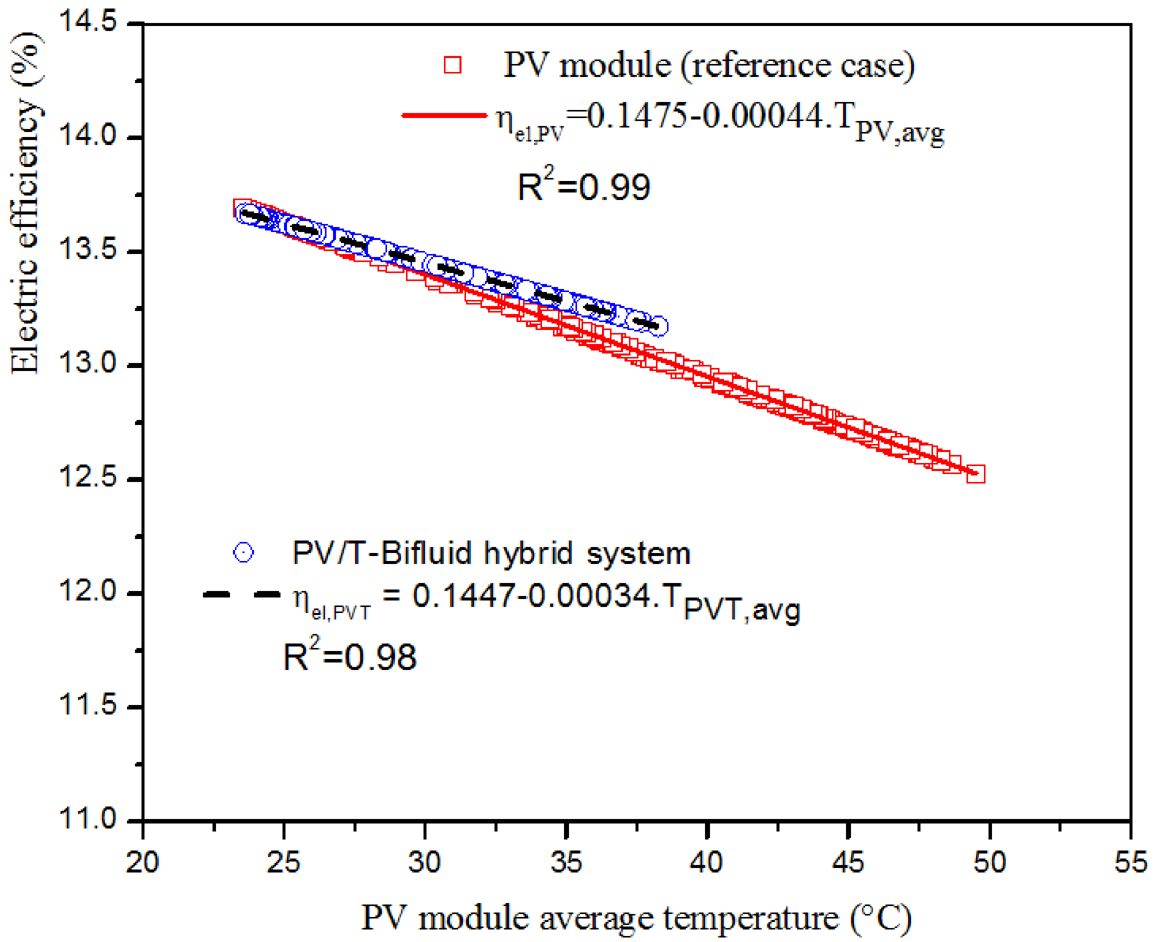

Figure. V. 16: *Electrical efficiency evolution as a function of the PV module average temperature*

V. 6. 4 Comparison of Electrical efficiency of the present study with previous works

In order to assess the competitiveness of the proposed hybrid PV/T Bi-fluid system in terms of electrical power output performance, a comparative study has been carried out between the proposed hybrid system against existing other systems reported in the literature.

Therefore, **figure V.17** shows the evolution of electrical efficiencies for several systems as a function of PV module temperature.

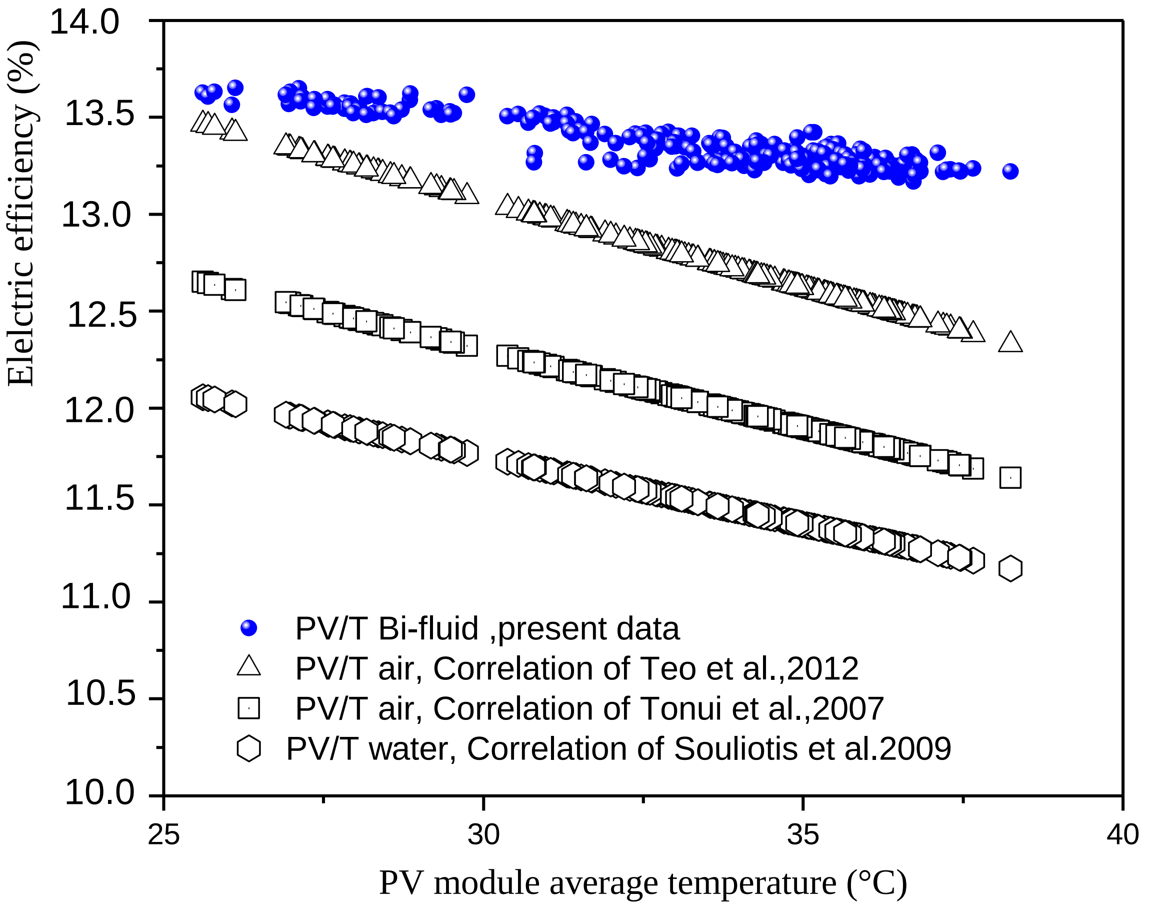

Figure. V. 17: *Electrical efficiency evolution as a function of the PV module average temperature, compared to existing works from literature*

It is obvious that all electrical efficiency curves from the literature's works linearly decrease with a steep slope, whereas the present hybrid PV/T Bi-fluid system's efficiency decreases with a gentle slope.

This clearly proves the effectiveness of our System.

For instance, at PV module average temperatures varying from 24 °C to 39 °C the electrical efficiency in our hybrid PV/T Bi-fluid system drops by 3.5%, in contrast, this is 10.7% in Teo et al., [**13**], 10.1% in Tounui et al., [**14**], and 7.33% in Souliotis et al. [**15**], respectively.

Experimental linear correlations of the electrical efficiencies as a function of PV module average temperature reported by authors [**13, 14, and 15**] are respectively as follows:

$$\eta_{el,PVT} = -0.1577 - 0.0009.T_{PV,avg} \quad (V.31)$$

$$\eta_{el,PVT} = -0.147 - 0.0008.T_{PV,avg} \quad (V.32)$$

$$\eta_{el,PVT} = -0.1385 - 0.0007.T_{PV,avg} \quad (V.33)$$

V. 6. 5. Thermal Energy performance analysis

A comparative analysis on the average thermal energy, electrical power, and overall efficiency between the present works against similar researches works reported in the literature is depicted in f**igure V.18**.

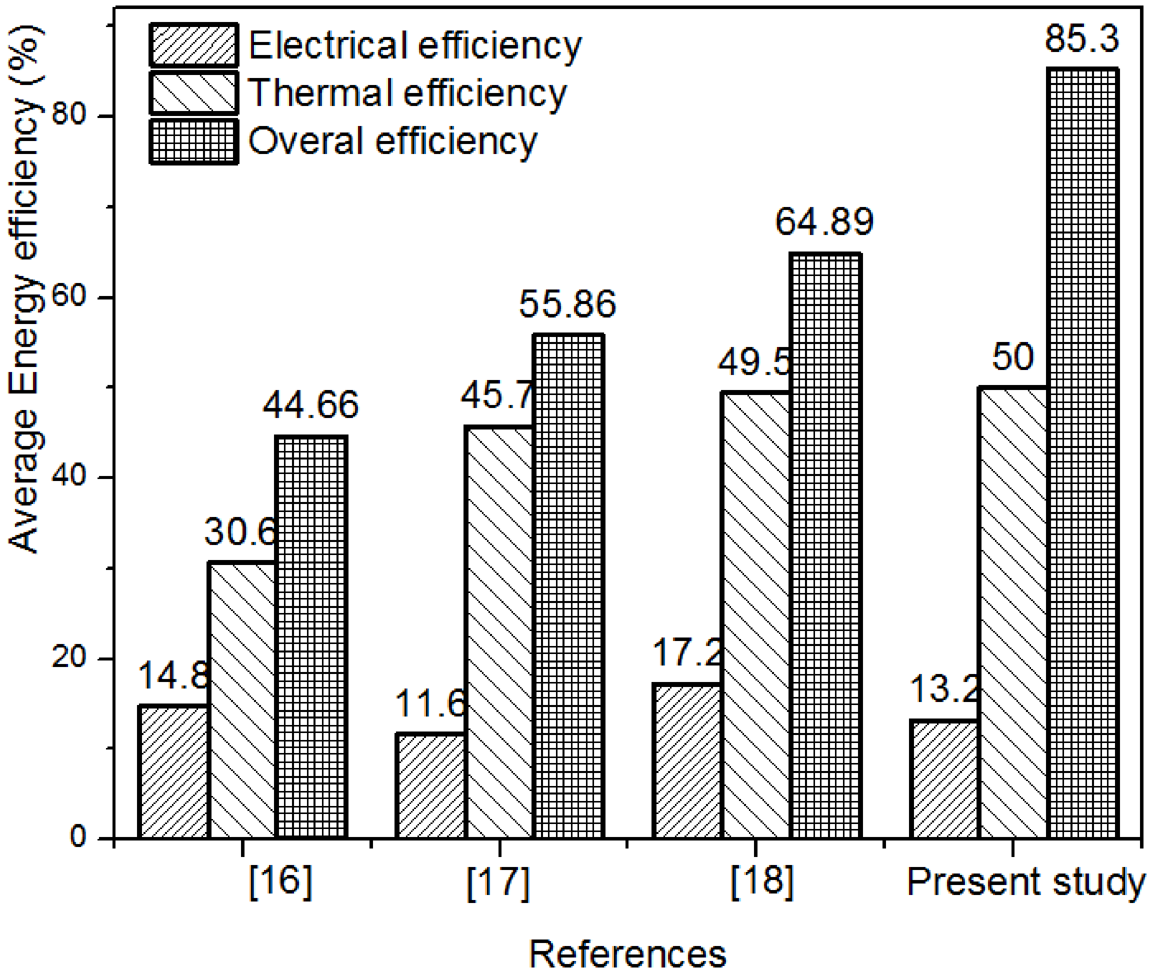

Figure. V. 18: *Comparison of the average energy efficiency for different design types of PV/T found in previous studies.*

The daily average thermal efficiency of the hybrid system is calculated by using Eq. 34:

$$\eta_{th,avg} = \frac{\sum_{J=1}^{N} \eta_j}{N} \tag{V.34}$$

where η_j is the instantaneous efficiency measured every 1h and N is the number of readings.

Hence, a peak in thermal efficiency of the hybrid system has been found to be 50 %, and the overall efficiency i.e. Eq. 21, equal to ~85.3%. In contrast, overall efficiencies for the reported works vary between 44.66-64.89%, and they are remarkably below the performance of the present hybrid system.

V. 6. 6. Average exergy efficiency

Figure V.19 shows the daily average exergy efficiency of the hybrid PV/T Bi-fluid system compared to similar studies brought from literature. It is obvious that our system hybrid PV/T Bi-fluid holds the highest record in terms of exergy efficiency compared to the rest of the other systems. This confirms the performance of the proposed design of using Bi-fluid as coolants and combining cooling & self-cleaning mechanism simultaneously in a PV/T system.

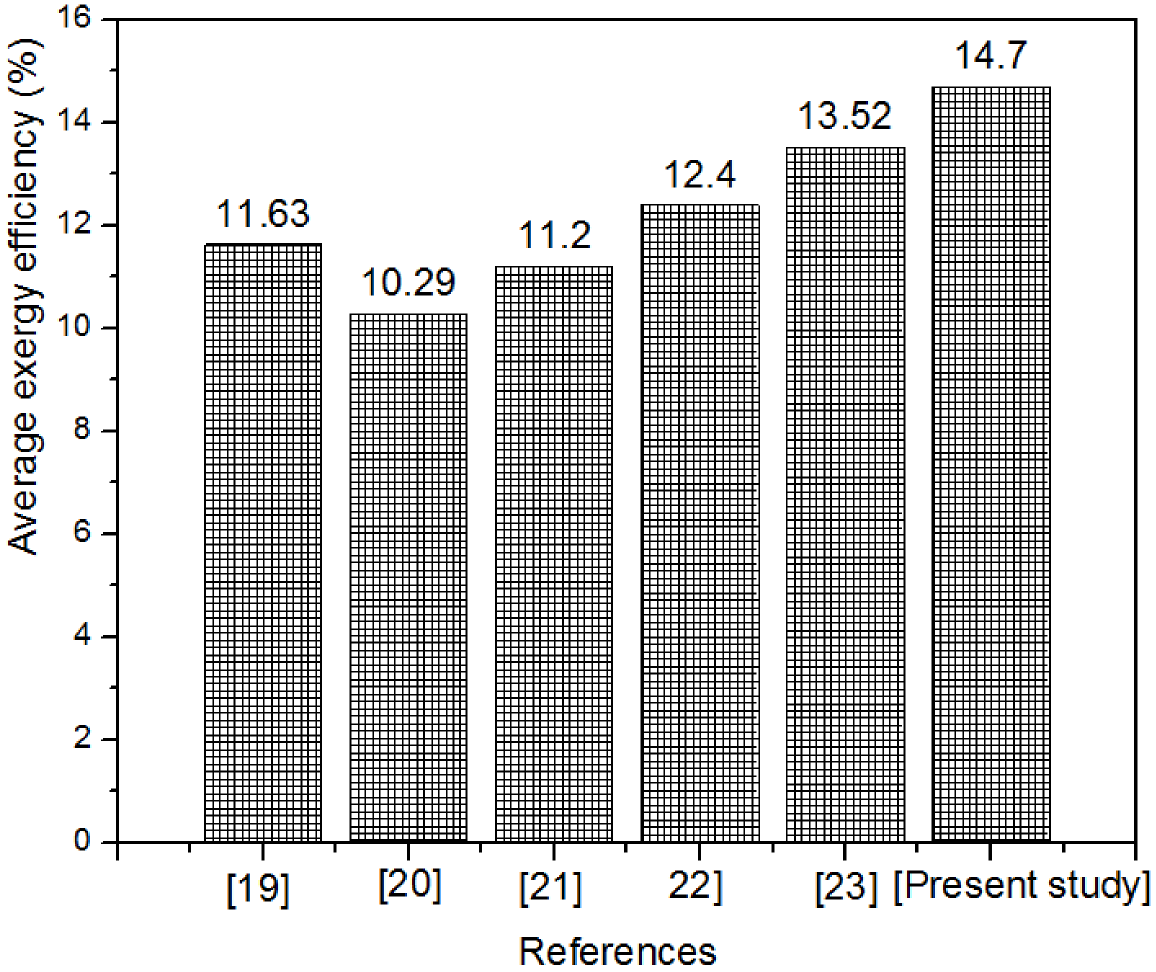

Figure. V. 19: *Comparison of the average exergy efficiency for different system types of PV/T in previous works.*

V.7 Conclusion

The experimental study carried out is based on the geometric parameters obtained during the simulation. A parametric study made it possible to find the expected trends concerning the performance of the hybrid system as a function of time and solar irradiation.

A new hybrid PV/T Bi-fluid system has been designed, built, and tested experimentally under outdoor operating conditions. The proposed hybrid system endowed by a combined mechanism of active cooling and self-cleaning. All apparatus and measuring instruments used during the experimental test presented in this chapter.

This chapter has recalled some formulations to calculate the efficiency and the uncertainty to perform during the measurement of values experimentally. The performance of the new hybrid system, as a function of operating temperature and solar radiation intensity, has been assessed and discussed.

The main concluding remarks extracted from this current study are as follows:

- PV module's average temperature in the new hybrid system has been decreased by about 15°C compared to the PV reference panel.
- PV module average temperature of the hybrid system increases by 1.5°C for every 100W/m^2 increments in solar radiation intensity, whereas this is 3 °C per 100 W / m^2 in the case of PV reference panel. This is, the hybrid system is effective to maintain the stability of the PV module's electrical efficiency.
- An improvement in the output voltage, and electrical current by 9.22% and 6.19%, respectively, compared to the reference case.
- A gain of up to 13.17% in electrical power output for the new hybrid system was recorded compared to the reference case.
- Correlations for electric current intensity, electrical power output, and electrical efficiency as functions of average PV module temperature, or global solar radiation intensity, were correlated and presented.
- The overall energy efficiency of 85.3% has been registered, while 14.7% was the average exergy efficiency for the hybrid PV/T Bi-fluid system.
- A comparative study against similar works from literature certifies the effectiveness of the proposed new design hybrid system.

To sum up, the active cooling and self-cleaning combination and the utilization of Bi-Fluid coolants has proved the design efficacy of the hybrid PV/T Bi-fluids system in terms of yield either electrical and/or thermal energy.

Therefore, as future work, an application of the present hybrid system to enhance solar pumping irrigation for large applications in the agricultural field, as well as the detailed economic feasibility of the project is intended.

References

[1] J. P. Holman. Experimental methods for engineers. (2001).

[2] E. Skoplaki, J. A. Palyvos. On the temperature dependence of photovoltaic module electrical performance: A review of efficiency/power correlations, solar energy. 83(2009)614-624. doi.org/10.1016/j.solener.2008.10.008

[3] A. A. Abed, O. K. Ahmed, M. M. Weis, K. I. Hamada. Performance augmentation of a PV/Trombe wall using Al2O3/Water nano-fluid: An experimental investigation, Renewable Energy. 157 (2020)515-529. doi.org/10.1016/j.renene.2020.05.052

[4] K. Luo, J. Ji, L. Xu, Z. Li, Seasonal experimental study of a hybrid photovoltaic-water/air solar wall system, Applied Thermal Engineering. 169(2020) 114853. doi.org/10.1016/j.applthermaleng.2019.114853

[5] H.A. Zondag, D.W. Vries, W.G.J. Van Hendel, R.J.C. Van Zolingen, A.A. Van Steenhoven, The yield of different combined PV–thermal collector designs, Solar Energy. 74 (2003) 253–269. doi.org/10.1016/S0038-092X(03)00121-X

[6] R. Kumar, M.A. Rosen. Performance evaluation of a double pass PV/T solar air heater with and without fins, Appl. Therm. Eng. 31 (2011) 1402-1410. doi.org/10.1016/j.applthermaleng.2010.12.037

[7] H. U. Choi, Y. B. Kim, C. H. Son, J. I. Yoon, K. H. Choi. Experimental study on the performance of heat pump water heating system coupled with air type PV/T collector, Applied Thermal Engineering. (2020) 115427. doi.org/10.1016/j.applthermaleng.2020.115427

[8] J. Jie, Y. Hua, P. Gang, J. Bin, H. Wei. Study of PV-Trombe wall assisted with DC fan. Building and Environment, 42 (2007)3529-3539. doi.org/10.1016/j.buildenv.2006.10.038

[9] V. Badescu, P.T. Landsberg, A. Devos, Statistical thermodynamic foundation for photovoltaic and photothermal conversion III: application to hybrid solar converters, J. Appl. Phys.81 (1997) 3692-3699. doi.org/10.1063/1.365490

[10] J.A. Dufe, W.A. Beckman. Solar engineering of thermal processes, 2nd edn. Wiley, New York. (1991).

[11] Huang, B. J., Lin, T. H., Hung, W. C., Sun, F. S. Performance evaluation of solar photovoltaic/thermal systems, Solar energy. 70(2001)443-448. doi.org/10.1016/S0038-092X(00)00153-5

[12] S. Hassani, R. Saidur, S. Mekhilef, R. A. Taylor. Environmental and exergy benefit of Nanofluid-based hybrid PV/T systems, Energy Conversion and Management. 123(2016) 431-444. doi.org/10.1016/j.enconman.2016.06.061

[13] H.G. Teo, P.S. Lee, M.N.A. Hawlader, An active cooling system for photovoltaic modules, Appl. Energy 90 (1) (2012) 309–315.

[14] J.K. Tonui, Y. Tripanagnostopoulos, Air-cooled PV/T solar collectors with low cost performance improvements, Sol. Energy 81 (2007) 498–511, https://doi.org/10.1016/j.solener.2006.08.002

[15] M. Souliotis, Y. Tripanagnostopoulos, S.A. Kalogirou, Thermosiphonic hybrid PV/T solar systems, Polska Energetyka Słoneczna. 1 (2009) 1–4.

[16] C. Cristofari, J.L. Canaletti, G. Notton, Patented twintex hybrid PV/T collector: Level of performances and comparison with thermal solar collector, in: Proc. 2011 Int. Conf. Util. Exhib. Power Energy Syst. Issues Prospect. Asia, ICUE 2011; 2012. https://doi.org/10.1109/ICUEPES.2011.6497769

[17] J. Lv, Z. He, G. Zhao, X. Li, Z. Hu, J. Zhang, Analysis on the performance of photovoltaic/thermal solar system, in: ICMREE 2013 - Proc. 2013 Int. Conf. Mater.

[18] I.E. Haber, Energy transport modeling of PV/T collectors, in: Renew Energy Res Appl (ICRERA), 2015 Int Conf, vol. 5. 2015, p. 1615–1617.

[19] Ranjana Arora, Rajesh Arora, Experimental Investigations and Exergetic Assessment of 1 kW Solar PV Plant, Pertanika J. Sci. Technol. 26 (2018) 4.

[20] M. Sardarabadi, M. Hosseinzadeh, A. Kazemian, M. Passandideh-Fard, Experimental investigation of the effects of using metal-oxides/water nanofluids on a photovoltaic thermal system (PVT) from energy and exergy viewpoints, Energy 138 (2017) 682–695.

[21] H. Saitoh, Y. Hamada, H. Kubota, M. Nakamura, K. Ochifuji, S. Yokoyama, K. Nagano, Field experiments and analyses on a hybrid solar collector, Appl. Therm. Eng. 23 (16) (2003) 2089–2105, https://doi.org/10.1016/S1359-4311(03)00166-2.

[22] M. Sardarabadi, M. Passandideh-Fard, M.J. Maghrebi, M. Ghazikhani, Experimental study of using both ZnO/water nanofluid and phase change material (PCM) in photovoltaic thermal systems, Sol. Energy Mater. Sol. Cells 161 (2017) 62–69, https://doi.org/10.1016/j.solmat.2016.11.032.

[23] K. Sopian, A.H. Al-Waeli, H.A. Kazem, Energy, exergy and effciency of four photovoltaic thermal collectors with different energy storage material, J. Storage Mater. 29 (2020), 101245, https://doi.org/10.1016/j.est.2020.101245.

General conclusion

1. Conclusions

In the present dissertation, most efforts in this study were devoted to demonstrating the need for cooling and self-cleaning to improve the performance of photovoltaic panels. Application of two cooling techniques passive or active by using two heat transfer working fluids in optimized geometry concept of hybrid PV/T Bi-fluid system helps to improve PV panels' performance. During this study, generalities on CFD numerical modeling were presented, as well as the methods used systematically so that the reader could understand them and re-work them in order to improve them if necessary. To achieve this purpose, passive air-cooling technology was used to improve the geometric and hydrodynamic parameters in a new hybrid system by means of turbulent natural air circulation. The geometry parameters effect of the SEC air inlet duct and the installation of a flat aluminum plat (AFP) near the back surface of the photovoltaic panel on the heat transfer rate was analyzed. In addition, the effect of the tilt angle of the PV/T system and Rayleigh number on the thermo-hydrodynamic flow behavior and the average heat transfer rate was examined. The second part of this work has been approached numerically using active cooling, but this time two coolants used, which are air and water. The back surface of the PV module is air-cooled, while the front face is cleaned and cooled with flowing water. Based on the optimum design obtained in the first part of our study, a three-dimensional numerical study was carried out, including active cooling by installing two DC fans at the system outlet. Furthermore, in the same system, a transparent perforated plastic tube was installed to allow water to flow over the entire front face of the PV module.

A new hybrid PV/T Bi-fluid system has been designed, built, and tested experimentally under outdoor operating conditions. The proposed hybrid system endowed by a combined mechanism of active cooling and self-cleaning. In addition, the different performances of the hybrid system, as a function of PV modules operating temperature and solar radiation intensity, have been assessed and discussed. As a reminder, the main objective of this contribution is to obtain a new solar hybrid PV/T Bi-fluid system, realized and then outdoor experimentally tested under the real climatic conditions of Ghardaïa city, in order to improve its performance. The main conclusions based on the numerical results and outdoor experimental data of the present study can be summarized as follows:

- The obtained numerical results are in very agreement with the experiment results of Onur et al. [49], for the case of passive air-cooling.

For passive air-cooling of hybrid PV/T air collector:

- For high modified Rayleigh numbers, an improvement by about 6 % has been registered for an optimal value of sloped entrance channel dimensions, (He =0.05m, L_{che}=0.735m, and We=0.3m).
- The integration of aluminum flat plat with an optimal value of the AFP distance to the PV module backsides surface (d_{AFP} optimal = 3 cm), has a positive effect on improving the heat transfer rate by about 20%, contrary to their number which no effect on the average Nusselt number.
- Increasing the system tilt angle improved the maximum airflow velocity, in particular for high Rayleigh number values (with and without AFP).
- Correlations of average Nusselt numbers versus modified Rayleigh numbers and sloped entrance air channel dimensions are presented and discussed.

For active air-cooling of hybrid PV/T air collector:

- The tilt angles affect positively the average Nusselt numbers, especially for low Reynolds numbers values.
- An increase in the air Reynolds number leads to a low increase in the average friction coefficient, while increases significantly as a function of the Grashoff number.
- Average Nusselt number affected by the increase of air Reynolds number.
- The average Nusselt number is improved by about 80% for high Reynolds numbers, for the case of contra-current compared with the case of co-current flow direction.

For active cooling of the new hybrid PV/T Bi-fluid collector (numeric and experimental results):

- PV modules' average temperature in the new hybrid system by about 15°C compared to the PV reference panel has been dropped.
- PV module average temperature of the hybrid system increases by 1.5°C for every 100 W/m2 increments in solar radiation intensity, whereas this is 3 °C per 100 W / m2 in the case of PV reference panel.
- For this reason, this hybrid system has been shown to be effective in maintaining the stability of the electrical efficiency of the PV modules shown.
- An improvement in the output voltage and mains was recorded by 9.22% and 6.19%, respectively, compared to the reference condition.

➢ A gain of up to 13.17% in electrical power output for the new hybrid system was registered compared to the reference case.

➢ Correlations for electric current intensity, electrical power output, and electrical efficiency as functions of average PV module temperature, or global solar radiation intensity, were proposed and presented.

➢ An overall energy efficiency increase of about 85.3% has been recorded, while the average exergy efficiency is estimated at around 14.7%.

2. Recommendations and suggested perspectives works

In this contribution, a new solar optimal hybrid PV/T Bi-fluid system with the ability to cool and self-cleaning has been obtained and tested under outdoor climatic conditions. It can be recommended that the proposed new hybrid of PV/T Bi-fluid system will be a favorable green solution to satisfy the energy demand at large scale applications such as in the residential industry-building, hotel, as well remote off-grid regions. To improve the performance of photovoltaic panels and significantly extend their lifespan, are proposed, the works mentioned below.

➢ To improve the performance of photovoltaic panels and significantly extend their lifespan, are proposed, the works mentioned below.

➢ The effect of the integration of a new absorber behind the hybrid PV/T Bi-fluid system to improve the energy performance will be proposed.

➢ The influence of different shapes and materials of the plate integrated under the PV module on the heat transfer rate will be studied.

➢ Proposed a new hybrid system used to enhance solar pumping irrigation for large applications in the agricultural field, due to its low cost, especially in this field.

➢ The use of the Canadian wells technique (geothermal energy) to cool with a lower temperature, resulting in an increase in the heat transfer rate.

➢ The integration of different shapes of chimney towers to increase the heat transfer of PV modules by using the passive air-cooling technique.

Annex

UDF for calculate physical proprieties of air and water versus time and temperature

```
/*********************************************************************/
/* UDF for het flux profil_____NEW */
/*********************************************************************/
#include "udf.h"
DEFINE_PROFILE(heat_flux,thread,i)
{
face_t f;
begin_f_loop(f, thread)
{
real t = CURRENT_TIME;
real b1=-80945.79042;
real b2=47553.25075;
real b3=-12046.74669;
real b4=1715.25113;
real b5=-149.69946;
real b6=8.16904;
real b7=-0.27068;
real b8=0.00494;
real b9=-3.76675*pow(10,-5);
F_PROFILE(f, thread, i)
=(b9*pow(t,9))+(b8*pow(t,8))+(b7*pow(t,7))+(b6*pow(t,6))+(b5*pow(t,5))+(b4*pow(t,4))+(b3
*pow(t,3))+(b2*pow(t,2))+(b1*t)+82.1309423267143;
}
end_f_loop(f, thread);
}

/*********************************************************************/
/* UDF for AIR density property_____NEW */
/*********************************************************************/
#include "udf.h"
DEFINE_PROPERTY(cell_density_air,cell,thread)
{
real t=CURRENT_TIME;
real b1=22482.24132;
real b2=-14528.36168;
real b3=4064.64828;
real b4=-643.42052;
real b5=63.0692;
real b6=-3.92243;
real b7=0.15124;
real b8=-0.00331;
real b9=3.1422*pow(10,-5);
real Tamb;
```

```
real density;
real den;
Tamb=(b9*pow(t,9))+(b8*pow(t,8))+(b7*pow(t,7))+(b6*pow(t,6))+(b5*pow(t,5))+(b4*pow(t,4)
)+(b3*pow(t,3))+(b2*pow(t,2))+(b1*t)+293.8300268;
den=(1.1774-(0.00359*((Tamb-273.16)-27)));
density=den;
return density;
}
/********************************************************************/
/* UDF for AIR SPECIFIC HEAT property_____NEW  */
/********************************************************************/
#include "udf.h"
DEFINE_SPECIFIC_HEAT(SPECIFIC_HEAT_air, T, Tref, h, yi)
{
real t=CURRENT_TIME;
real b1=22482.24132;
real b2=-14528.36168;
real b3=4064.64828;
real b4=-643.42052;
real b5=63.0692;
real b6=-3.92243;
real b7=0.15124;
real b8=-0.00331;
real b9=3.1422*pow(10,-5);
real Tamb;
real cp;
Tamb=(b9*pow(t,9))+(b8*pow(t,8))+(b7*pow(t,7))+(b6*pow(t,6))+(b5*pow(t,5))+(b4*pow(t,4)
)+(b3*pow(t,3))+(b2*pow(t,2))+(b1*t)+293.8300268;
cp=1005.7+(0.066*((Tamb-273.16)-27));
*h =cp*(T-Tamb);
return cp;
}
/********************************************************************/
/* UDF for AIR conductivity property_____NEW  */
/********************************************************************/
#include "udf.h"
DEFINE_PROPERTY(cell_conductivity_air,cell,thread)
{
real t=CURRENT_TIME;
real b1=22482.24132;
real b2=-14528.36168;
real b3=4064.64828;
real b4=-643.42052;
real b5=63.0692;
real b6=-3.92243;
real b7=0.15124;
```

```
real b8=-0.00331;
real b9=3.1422*pow(10,-5);
real Tamb;
real conductivity;
real cond;
Tamb=(b9*pow(t,9))+(b8*pow(t,8))+(b7*pow(t,7))+(b6*pow(t,6))+(b5*pow(t,5))+(b4*pow(t,4)
)+(b3*pow(t,3))+(b2*pow(t,2))+(b1*t)+293.8300268;
cond=(0.02624+(0.0000758*((Tamb-273.16)-27)));
conductivity=cond;
return conductivity;
}
/**********************************************************************/
/* UDF for AIR viscosity property_____NEW  */
/**********************************************************************/
#include "udf.h"
DEFINE_PROPERTY(cell_viscosity_air,cell,thread)
{
real t=CURRENT_TIME;
real b1=22482.24132;
real b2=-14528.36168;
real b3=4064.64828;
real b4=-643.42052;
real b5=63.0692;
real b6=-3.92243;
real b7=0.15124;
real b8=-0.00331;
real b9=3.1422*pow(10,-5);
real Tamb;
real viscosity;
real visc;
Tamb=(b9*pow(t,9))+(b8*pow(t,8))+(b7*pow(t,7))+(b6*pow(t,6))+(b5*pow(t,5))+(b4*pow(t,4)
)+(b3*pow(t,3))+(b2*pow(t,2))+(b1*t)+293.8300268;
visc=(1.983+(0.00184*((Tamb-273.16)-27)))*pow(10,-5);
viscosity=visc;
return viscosity;
}
/**********************************************************************/
/* UDF for water density property_____NEW */
/**********************************************************************/
#include "udf.h"
DEFINE_PROPERTY(cell_density_water,cell,thread)
{
real t=CURRENT_TIME;
real b1=-265.33808;
real b2=100.0293;
real b3=-14.85769;
```

```
real b4=1.09303;
real b5=-0.03992;
real b6=5.79541*pow(10,-4);
real Tamb;
real density;
real den;
Tamb=(b6*pow(t,6))+(b5*pow(t,5))+(b4*pow(t,4))+(b3*pow(t,3))+(b2*pow(t,2))+(b1*t)+295.9
974271;
den=756.42+(1.8595*Tamb)-(0.0035360*pow(Tamb,2));
density=den;
return density;
}
/*******************************************************************/
/* UDF for water SPECIFIC HEAT property_____NEW */
/*******************************************************************/
#include "udf.h"
DEFINE_SPECIFIC_HEAT(SPECIFIC_HEAT_water, T, Tref, h, yi)
{
real t=CURRENT_TIME;
real b1=-265.33808;
real b2=100.0293;
real b3=-14.85769;
real b4=1.09303;
real b5=-0.03992;
real b6=5.79541*pow(10,-4);
real Tamb;
real cp;
Tamb=(b6*pow(t,6))+(b5*pow(t,5))+(b4*pow(t,4))+(b3*pow(t,3))+(b2*pow(t,2))+(b1*t)+295.9
974271;
cp=5631.3-(9.2262*Tamb)+(0.014622*pow(Tamb,2));
*h =cp*(T-Tamb);
return cp;
}
/*******************************************************************/
/* UDF for water conductivity property_____NEW */
/*******************************************************************/
#include "udf.h"
DEFINE_PROPERTY(cell_conductivity_water,cell,thread)
{
real t=CURRENT_TIME;
real b1=-265.33808;
real b2=100.0293;
real b3=-14.85769;
real b4=1.09303;
real b5=-0.03992;
real b6=5.79541*pow(10,-4);
```

```
real Tamb;
real conductivity;
real cond;
Tamb=(b6*pow(t,6))+(b5*pow(t,5))+(b4*pow(t,4))+(b3*pow(t,3))+(b2*pow(t,2))+(b1*t)+295.9
974271;
cond=-0.581798+(0.00635704*Tamb)-(0.00000796625*pow(Tamb,2));
conductivity=cond;
return conductivity;
}
/***********************************************************************/
/* UDF for water viscosity property_____NEW */
/***********************************************************************/
#include "udf.h"
DEFINE_PROPERTY(cell_viscosity_water,cell,thread)
{
real t=CURRENT_TIME;
real b1=-265.33808;
real b2=100.0293;
real b3=-14.85769;
real b4=1.09303;
real b5=-0.03992;
real b6=5.79541*pow(10,-4);
real Tamb;
real viscosity;
real visc;
real nn;
Tamb=(b6*pow(t,6))+(b5*pow(t,5))+(b4*pow(t,4))+(b3*pow(t,3))+(b2*pow(t,2))+(b1*t)+295.9
974271;
nn=(247.8/(Tamb-140));
visc=0.00002414*pow(10,nn);
viscosity=visc;
return viscosity;
}

/***********************************************************************/
/* UDF for temperature_air_in profil_____NEW */
/***********************************************************************/
#include "udf.h"
DEFINE_PROFILE(temperature_air_in,thread,i)
{
face_t f;
begin_f_loop(f, thread)
{
real t = CURRENT_TIME;
real b1=22482.24132;
real b2=-14528.36168;
```

```
real b3=4064.64828;
real b4=-643.42052;
real b5=63.0692;
real b6=-3.92243;
real b7=0.15124;
real b8=-0.00331;
real b9=3.1422*pow(10,-5);
F_PROFILE(f, thread,
i)=(b9*pow(t,9))+(b8*pow(t,8))+(b7*pow(t,7))+(b6*pow(t,6))+(b5*pow(t,5))+(b4*pow(t,4))+(b
3*pow(t,3))+(b2*pow(t,2))+(b1*t)+293.8300268;
}
end_f_loop(f, thread);
}

/*****************************************************************************/
/* UDF for temperature_ambiante profil_____NEW */
/*****************************************************************************/
#include "udf.h"
DEFINE_PROFILE(temperature_ambiante,thread,i)
{
face_t f;
begin_f_loop(f, thread)
{
real t = CURRENT_TIME;
real b1=63.16335;
real b2=-29.74396;
real b3=5.3492;
real b4=-0.4635;
real b5=0.01955;
real b6=-3.23145*pow(10,-4);
F_PROFILE(f, thread, i)
=(b6*pow(t,6))+(b5*pow(t,5))+(b4*pow(t,4))+(b3*pow(t,3))+(b2*pow(t,2))+(b1*t)+295.12456
34;
}
end_f_loop(f, thread);
}
/*****************************************************************************/
/* UDF for temperature_water_in profil_____NEW   */
/*****************************************************************************/
#include "udf.h"
DEFINE_PROFILE(temperature_water_in,thread,i)
{
face_t f;
begin_f_loop(f, thread)
{
real t = CURRENT_TIME;
```

```
real b1=-265.33808;
real b2=100.0293;
real b3=-14.85769;
real b4=1.09303;
real b5=-0.03992;
real b6=5.79541*pow(10,-4);
F_PROFILE(f, thread, i)
=(b6*pow(t,6))+(b5*pow(t,5))+(b4*pow(t,4))+(b3*pow(t,3))+(b2*pow(t,2))+(b1*t)+295.99742
71;
}
end_f_loop(f, thread);
}
/*********************************************************************/
/* UDF for velocity_fan profil_____NEW  */
/*********************************************************************/
#include "udf.h"
DEFINE_PROFILE(velocity_fan,thread,i)
{
face_t f;
begin_f_loop(f, thread)
{
real t = CURRENT_TIME;
real b1=-9381.74803;
real b2=5885.95905;
real b3=-1599.35913;
real b4=245.87147;
real b5=-23.39215;
real b6=1.41049;
real b7=-0.05264;
real b8=0.00111;
real b9=-1.01735*pow(10,-5);
F_PROFILE(f, thread, i) =-
((b9*pow(t,9))+(b8*pow(t,8))+(b7*pow(t,7))+(b6*pow(t,6))+(b5*pow(t,5))+(b4*pow(t,4))+(b3
*pow(t,3))+(b2*pow(t,2))+(b1*t)+1.8);
}
end_f_loop(f, thread);
}
/*********************************************************************/
/* UDF for wind-speed profil_____NEW  */
/*********************************************************************/
#include "udf.h"
DEFINE_PROFILE(wind_speed,thread,i)
{
face_t f;
begin_f_loop(f, thread)
{
```

```
real t = CURRENT_TIME;
real b1=-55163.97396;
real b2=36978.55319;
real b3=-10747.91586;
real b4=1769.20291;
real b5=-180.41496;
real b6=11.67291;
real b7=-0.46805;
real b8=0.01064;
real b9=-1.0491*pow(10,-4);
F_PROFILE(f, thread, i)
=(b9*pow(t,9))+(b8*pow(t,8))+(b7*pow(t,7))+(b6*pow(t,6))+(b5*pow(t,5))+(b4*pow(t,4))+(b3
*pow(t,3))+(b2*pow(t,2))+(b1*t)+1.2;
}
end_f_loop(f, thread);
}
```

ملخص: يعتبر تراكم الغبار على الوجوه الأمامية للألواح الشمسية، وارتفاع درجة حرارة تشغيل الخلايا الكهروضوئية، وانخفاض مستويات الرطوبة المسجلة في المناطق شبه القاحلة من المشاكل الرئيسية التي تؤثر سلباً على أدائها. لذلك مما يؤدي بمرور الوقت إلى تدهور حالة وحتى تلف الخلايا الكهروضوئية. تهدف هذه المساهمة إلى الحصول على نظام هجين جديد قادر على تقليل درجة حرارة تشغيل الخلية الكهروضوئية باستخدام تقنيات التبريد السلبي والنشط. كما تم ادراج تقنية تنظيف ذاتية مناسبة للوجه الأمامي. تم إجراء دراسة عددية لتحسين المعلمات الهندسية والحرارية الهيدروديناميكية باستخدام برنامج CFD Ansys Fluent. بعد عملية المحاكاة والتحسين، تم تحقيق واختبار هذا النظام الهجين الجديد في ظل ظروف مناخية حقيقية في منطقة غرداية. وبالتالي، يتم تبريد الجزء الخلفي من الوحدة الكهروضوئية عن طريق الهواء، وتدفق طبقة رقيقة من الماء على جانبها الأمامي لتبريد النظام وتنظيفه. أظهرت النتائج العددية أن المعلمات الهندسية المثلى لنظام الهواء الهجين الجديد PV / T (He = 0.05 m، We = 0.3 m، L_{che} = 0.735 m، d_{afp} = 0.03 m) تعزيزًا لمتوسط رقم Nusselt بحوالي 20٪ مقارنة للقضية دون تكامل وكالة فرانس برس. تعمل زيادة زاوية إمالة نظام الهواء PV / T على تحسين سرعة التدفق القصوى، خاصة لقيم رقم Rayleigh العالية (مع وبدون AFP). يؤدي استخدام تقنية تبريد الهواء النشط وتدفق التيار المعاكس إلى تحسين متوسط عدد نسلت بحوالي 80٪ مقارنة بحالة التيار المشترك. تم الحصول على تحسن بنسبة 5.7 ٪ تقريبًا في الكفاءة الكهربائية مقارنة بالحالة المرجعية في نفس ظروف التشغيل وفي ذروة الإشعاع الشمسي الاجمالي، ($G = 650\ W/m^2$). تبلغ الكفاءة الكلية للطاقة ومتوسط كفاءة الطاقة حوالي 85.3٪ و14.7٪ على التوالي.

الكلمات المفتاحية :
جمع الطاقة الشمسية الكهروضوئية/حرارية ثنائي السوائل، الحمل الحراري الطبيعي والمختلط المضطرب، نظام التبريد، زاوية الميل، متوسط عدد نوسيلت، عدد رايليغ،
تساب الحرارة الشمسية، الوحدة الكهروضوئية، النمذجة العددية، أداء الطاقة، كفاءة الطاقة، دراسة تجريبية، التنظيف الذاتي للوحدة الكهروضوئية.

Abstract: The accumulation of dust on the front faces of solar panels, the rise in the operating temperature of photovoltaic cells, and the low humidity levels recorded in semi-arid regions are considered major problems affecting negatively their performance. Therefore, over time, this leads to deteriorating and damaging PV cells. Hybrid photovoltaic/thermal systems are considered among the important technologies due to their efficiency in producing mainly electrical and thermal energy. This contribution is aimed to get a new hybrid system capable to reduce the PV cell's operating temperature with the use of passive and active cooling techniques. A self-cleaning technique suitable for the front face has also been incorporated. A numerical study of optimization of the geometrical and Thermo-hydrodynamic parameters using the CFD software Ansys Fluent was performed. After the simulation and optimization process, this new hybrid system was realized and tested under real climatic conditions in the Ghardaïa region. Thus, the PV module's backside is cooled by air, and flowing a thin film of water over its front side to cool and clean the system. The numerical results show that the optimal geometric parameters of the new hybrid PV / T air system (H_e = 0.05 m, W_e = 0.3 m, L_{che} = 0.735 m and d_{afp} = 0.03 m) enhancement of the average Nusselt number by about 20% compared to the case without AFP integration. Increasing the tilt angle of the PV / T air system improves the maximum flow velocity, especially for high Rayleigh number values (with and without AFP). Using the active air-cooling technique and counter-current flow improves the average Nusselt number by about 80% compared to the co-current case. The experimental results showed a reduction of the PV module average temperature measured for the new hybrid system of around 15 °C, against the reference PV module. An improvement of approximately 5.7% in electrical efficiency compared to the reference case was obtained under the same operating conditions and at the peak of global solar irradiation, ($G = 650\ W / m^2$). The overall energy efficiency and the average exergy efficiency are approximately 85.3% and 14.7%, respectively.

Keywords: Hybrid PV / T Bi-fluid system, Natural convection, cooling system, tilt angle, average Nusselt number, Rayleigh number, Solar heat gain, CFD, Energy performance, Experimental study, and Photovoltaic self-cleaning.

Résumé : L'accumulation de poussière sur les faces avant des panneaux solaires, l'élévation de la température de fonctionnement des cellules photovoltaïques et les faibles taux d'humidité enregistrées dans les régions semi-arides sont considérées comme des problèmes majeurs affectant négativement leurs performances. Par conséquent, cela peut entrainer des dégradations au cours du temps et même l'endommagement des cellules photovoltaïques. Les systèmes photovoltaïques/thermiques hybrides sont considérés parmi les technologies importantes en raison de leur efficacité à produire essentiellement de l'énergie électrique et thermique. L'objectif principal de cette contribution est d'obtenir un nouveau système hybride capable de réduire la température de fonctionnement des cellules photovoltaïques par des techniques de refroidissement passives et actives. Une technique de nettoyage appropriée de leurs faces avant a été également effectué. Une étude numérique d'optimisation des paramètres géométriques et thermo-hydrodynamiques utilisant le logiciel CFD Ansys Fluent a été abordée. Après les étapes de simulation et l'optimisation, ce système est réalisé et testé dans des conditions climatiques réelles de la région de Ghardaïa. Ainsi, la face arrière du module photovoltaïque est refroidi par l'air, et un écoulement d'un film d'eau sur sa face avant ont servi à refroidir et nettoyer le système. Les principaux résultats numériques montrent que les paramètres géométriques optimaux du nouveau système hybride PV/T air (He = 0,05 m, We = 0,3 m, L_{che} = 0,735 m et d_{afp}=0,03 m) ont amélioré le nombre moyen de Nusselt d'environ 20% par rapport au cas sans intégration AFP. En plus, l'augmentation de l'angle d'inclinaison du système PV/T air améliore la vitesse maximale de l'écoulement, en particulier pour les valeurs élevées du nombre de Rayleigh (avec et sans AFP. L'utilisation de la technique de refroidissement actif par air, et dans le cas d'écoulement à contre-courant améliore du nombre de Nusselt moyen d'environ 80% comparativement au cas co-courant. Les résultats expérimentaux obtenus ont montré une réduction de la température moyenne mesurée pour le nouveau système hybride d'environ 15 °C, par rapport au module PV témoins (cas de référence). Une amélioration d'environ 5,7 % du rendement électrique par rapport au cas de référence a été obtenue dans les mêmes conditions de fonctionnement et au pic de l'irradiation solaire globale, ($G = 650\ W/m^2$). L'efficacité énergétique globale et l'efficacité éxergétique moyenne ont été respectivement d'environ 85,3 % et 14,7 % respectivement.

Mots clés : Système hybride PV/T Bi-fluide, Convection naturelle, Système de refroidissement, Angle d'inclinaison, Nombre moyen de Nusselt, Nombre de Rayleigh, Gain de chaleur solaire, CFD, Performance énergétique, Étude expérimentale, Auto-nettoyage photovoltaïque.